Technische Universität München
TUM School of Computation, Information and Technology

Dynamical Systems on Large Networks and Their Limits

Tobias Böhle

Vollständiger Abdruck der von der TUM School of Computation, Information and Technology

der Technischen Universität München zur Erlangung eines

Doktors der Naturwissenschaften (Dr. rer. nat.)

genehmigten Dissertation.

Vorsitz: Prof. Dr. Oliver Junge

Prüfer der Dissertation:

1.   Prof. Christian Kuehn, Ph.D.
2.   Prof. Dr. Christian Bick
3.   Prof. Michael T. Schaub, Ph.D.

Die Dissertation wurde am 28.06.2023 bei der Technischen Universität München eingereicht

und durch die TUM School of Computation, Information and Technology am 27.10.2023

angenommen.

Abstract

Many real-world systems can be elegantly modeled by dynamical systems on networks. In this dissertation we analyze network dynamical systems and their induced dynamical effects in a variety of instances. First, we study a discrete-time dynamical system on a graph. Even though this system exhibits chaotic behavior, we find solutions that show synchrony among the nodes, analyze the stability of these solutions and confirm the results numerically. We conduct the analysis and perform simulations for both regular coupling on graphs as well as for systems with generalized coupling structure. Next, we focus on continuous-time dynamical systems on networks, specifically, ones for which each node of the network represents an oscillator. While these oscillations can occur in a general high-dimensional phase space, a phase reduction can help to reduce the dynamics to a lower dimensional system, where each oscillator is represented by just a phase from the unit circle. We derive such phase reductions as a second-order expansion in the coupling strength and compare the stability of states of collective dynamics in phase-reduced systems with those in the unreduced system. Subsequently, we take a higher-order phase oscillator model with a nontrivial coupling structure, which causes interesting equilibria—so called twisted states—to exist. We analyze the bifurcation at which these states gain or lose their stability upon variation of system parameters and approximate emanating branches of equilibria. In general, network dynamical systems can show complicated behavior. Thus, to get an intuition for their dynamics, numerical simulations are often helpful. We develop algorithms that can efficiently integrate a wide range of dynamical systems on networks.

Titel in deutscher Sprache:
Dynamische Systeme auf großen Netzwerken und deren Grenzwerten

Zusammenfassung
Viele dynamische Systeme, die in der Natur auftreten, lassen sich elegant durch dynamische Systeme auf Netzwerken beschreiben. In dieser Doktorarbeit analysieren wir verschiedene dynamische Systeme auf Netzwerken und die von ihnen erzeugten dynamischen Effekte. Zuerst betrachten wir ein zeitdiskretes dynamisches System auf einem Graphen. Auch wenn dieses System chaotische Dynamik zeigt, gibt es eine Lösung, die trotz ihres chaotischen Verhaltens Synchronisation zwischen verschiedenen Knoten des Graphen zulässt. Wir analysieren die Stabilität dieser speziellen Lösung und überprüfen unsere Resultate anhand von numerischen Simulationen. Dann weiten wir unsere Analyse auf ein System mit generalisierter Kopplungsstruktur aus und überprüfen, inwiefern die Resultate sich anpassen lassen. Als Nächstes betrachten wir ein zeitkontinuierliches dynamisches System auf Netzwerken, in dem jeder Knoten des Netzwerkes einen generellen Oszillator darstellt. Selbst wenn diese Oszillationen in einem hoch-dimensionalen Raum stattfinden, ist es möglich, diese mittels einer Phasenreduktion durch jeweils eine Phase zu beschreiben. Wir berechnen eine Annäherung zweiter Ordnung einer solchen Phasenreduktion und vergleichen Stabilitätseigenschaften wichtiger Gleichgewichtspunkte und periodischer Orbits im phasenreduzierten System mit den entsprechenden Eigenschaften im nicht-reduzierten System. Des Weiteren betrachten wir ein System von gekoppelten Phasenoszillatoren auf einem nicht-trivialen Netzwerk, auf dem interessante Gleichgewichtszustände existieren. Wir analysieren die Bifurkation, in der diese Zustände stabil oder instabil werden, wenn man die Kopplungsstruktur verändert, und beschreiben Annäherungsverfahren für zusätzliche Gleichgewichtspunkte, die in der Bifurkation entstehen. Da dynamische Systeme auf Netzwerken komplizierte dynamische Effekte aufweisen können, sind numerische Simulationen oft sehr hilfreich, um eine Intuition für das Verhalten dieser Systeme zu bekommen. Wir entwickeln effiziente numerische Algorithmen, die Simulationen auf großen Netzwerken ermöglichen.

Acknowledgments

Publications by the Author

During my doctoral research I have worked on articles that were published or are to be published. The content of the following articles is covered in this thesis.

[35]   Tobias Böhle, Christian Kuehn, Raffaella Mulas, and Jürgen Jost. Coupled hypergraph maps and chaotic cluster synchronization. *Europhysics Letters*, 136(4):40005, nov 2021.

[131]   Raffaella Mulas, Christian Kuehn, Tobias Böhle and Jürgen Jost. Random walks and Laplacians on hypergraphs: When do they match? *Discrete Applied Mathematics*, 317:26–41, aug 2022.

[36]   Tobias Böhle, Christian Kuehn, and Mechthild Thalhammer. On the reliable and efficient numerical integration of the Kuramoto model and related dynamical systems on graphs. *International Journal of Computer Mathematics*, 99(1):31–57, jan 2021.

[37]   Tobias Böhle, Mechthild Thalhammer, and Christian Kuehn. Community integration algorithms (CIAs) for dynamical systems on networks. *Journal of Computational Physics*, 469:111524, nov 2022.

[22]   Christian Bick, Tobias Böhle, and Christian Kuehn. Phase Oscillator Networks with Nonlocal Higher-Order Interactions: Twisted States, Stability and Bifurcations. Accepted for publication in SIAM Journal on Applied Dynamical Systems, available as preprint on arXiv https://arxiv.org/abs/2206.01951 pages 1–38, jun 2022.

[20]   Christian Bick, Tobias Böhle, and Christian Kuehn. Higher-Order Interactions in Phase Oscillator Networks through Phase Reductions of Oscillators with Phase Dependent Amplitude. pages 1–29, may 2023. Currently under review, available as preprint on arXiv https://arxiv.org/abs/2305.04277

Moreover, I have also worked on other articles, whose content is not covered in this thesis. These are listed below:

[34] Tobias Böhle and Christian Kuehn. Mathematical analysis of nonlocal PDEs for network generation. *Mathematical Modelling of Natural Phenomena*, 14(5):506, dec 2019.

[21] Christian Bick, Tobias Böhle, and Christian Kuehn. Multi-population phase oscillator networks with higher-order interactions. *Nonlinear Differential Equations and Applications NoDEA*, 29(6):64, nov 2022.

June 26th, 2023

Contents

Chapter 1

Introduction

Many real-world dynamical systems consist of interacting particles. These particles can, for example, be celestial bodies, human beings [115], animals [118] or microscopic particles such as cells [166], neurons [174] or molecules [99]. They interact with each other via the gravitational force, communication, predator-prey effects, protein production, electrical currents and physical forces, respectively. In many areas, the attempt to infer the macroscopic dynamics of the system based on the behavior of individual particles is an ongoing challenge. For example, some species of fireflies have the ability to flash in unison [44, 46, 45, 43, 179], even though there seems to be no leading firefly that can initiate a flash of all the others. Rather, each firefly observes the flashes of many other individuals and corrects its own flashing behavior accordingly. From a biological perspective it is still active research to investigate how a single firefly adopts its own flashing frequency such that synchronization with the others can occur.

This phenomenon of synchronization is not limited to flashing fireflies, but it can be found in many other dynamical systems. In fact, synchronization is so prominent that it is its own area of research [144, 149, 163]. Synchronization and many variants thereof has been studied in previous works; see [52, 41, 166, 117, 38, 156, 69, 83, 8, 35, 162, 160, 138, 44, 132, 158, 47] and many more. For example, it can be applied to crickets chirping in unison [174], soldiers marching in lock-step [164], neuron clusters in the brain [38, 168], pacemaker cells in the heart [64, 140, 178], constituents of the global electric power grid [27, 150, 105] and many more. One of the most prominent examples for synchronization is when many mechanical metronomes are placed on a board which can move to counteract the metronomes' momentum. When they are set to a similar frequency, they start to synchronize [139]. A prototypical mathematical model that describes synchronization of oscillatory units is the Kuramoto model [107, 108], which is known since at least 1975. In this model, each of the finitely many oscillators is represented by just a phase $\phi_k \in \mathbb{T} = \mathbb{R}/(2\pi\mathbb{Z})$, which can be thought of an

1

element on the unit circle. These phases then evolve according to

$$\dot{\phi}_k = \omega_k + \frac{K}{M} \sum_{l=1}^{M} \sin(\phi_l - \phi_k), \quad k = 1, \dots, M, \qquad (1.1.1)$$

if there are a total of M oscillators. Moreover, $\omega_k \in \mathbb{R}$ is the intrinsic frequency of oscillator k and $K \in \mathbb{R}$, typically $K \geq 0$, is a parameter which describes the coupling strength. In the classical Kuramoto model, the oscillators are nonidentical and they can be distinguished by their intrinsic frequencies ω_k. In fact, these frequencies are sampled from a symmetric probability distribution that has a unimodal probability density, typically a Gaussian distribution. The randomness of these frequencies makes it hard to study the dynamics of the Kuramoto model for finite M as the occurrence of dynamical effects depends on the specific samples ω_k. To overcome this obstacle, one can consider a limit as $M \to \infty$, where the law of large number helps to get rid of the randomness. The dynamical effects that appear in this limit have been extensively studied [165, 162, 63, 127]. If the infinitely many oscillators are uncoupled, i.e., $K = 0$, each oscillator moves according to its own intrinsic frequency. Thus, each oscillator's evolution is independent of the state of other oscillators, so there is no tendency to synchronize. For very small coupling strengths $K > 0$, one still observes no tendency towards synchronization. If one increases K beyond a critical coupling strength K_c, a positive proportion of the oscillators begins to gather at one side of the circle; one says that the oscillators partially synchronize. Increasing K even further makes this proportion bigger and bigger such that finally in the limit as $K \to \infty$, all oscillators synchronize.

While the classical Kuramoto model only shows no synchronization, partial synchronization or complete synchronization (in the limit as $K \to \infty$), only slight modifications cause fundamentally different phenomena to appear. For example, one can replace the sin function, that describes how one oscillator is coupled to another, with a general 2π periodic coupling function. Then, one obtains a general phase oscillator model, in which more dynamical effects can occur. For example, already when the coupling function contains only two Fourier modes, cluster states can occur, where the oscillators split into two groups, and oscillators synchronize within a group, but two oscillators from different groups do not [100, 161]. Even more harmonics in the coupling function allow for general cluster states with an arbitrary number of clusters. More harmonics can also cause the system to become chaotic, even if the number of oscillators M is small; see [25] for identical oscillators (all intrinsic frequencies are the same) and [119] for nonidentical oscillators.

Note that in the classical Kuramoto model, each oscillator is influenced by every other. Another possible generalization one can make to this model is to break this structure and allow for a non all-to-all coupling. Of course, this generalization is not made out of pure mathematical interest. Rather, non all-to-all coupling can

be motivated by many real-world examples. Mathematically one can describe a non all-to-all coupling structure by a network or more specifically by a graph, in which each node represents an oscillator. Two nodes in this graph are connected by an edge if the corresponding oscillators influence each other. This non all-to-all coupling can induce interesting dynamical effects [149], such as chimera states, where the oscillators in one part of the network are synchronized, whereas oscillators in other parts are not [109, 135]. Especially when the oscillators are identical, non all-to-all coupling can also yield interesting equilibria such as regular twisted states [177, 122, 126, 22] or general patterns [62].

When modeling real-world systems as dynamical systems on networks, such as the Kuramoto model, one realizes that a graph is not always sufficient to model the network structure, as a graph can only encode pairwise interactions. Instead, one often needs to include group or higher-order interactions, which describe the interplay of three or more particles simultaneously. Mathematically, these higher-order interactions are modeled by a hypergraph consisting of nodes and a set of hyperedges, each of which can contain more than just two nodes. For example, the reaction of two (bio-)chemical elements can depend on a catalyst, which would result in an interaction of three elements [99]. Such an interaction cannot be represented by a superposition of interactions in every group of two particles, as all three elements have to be present to start the reaction. Another example where higher-order interactions are useful arises when modeling the spread of an epidemic on a network. Classically, one assumes that an infection from one person to another happens along an edge in a graph, where each individual is connected to another if they are in contact with each other. As an individual human is typically part of multiple groups of people, such as the household he or she lives in or the group of colleagues he or she works with, it makes sense to take this group structure into account by studying the spread of the epidemic with higher-order interactions [53, 89, 31, 120]. Further examples include collaboration networks [173] or cell models in ecology [157]. Incorporating higher-order interaction in existing models has shown to yield interesting dynamical effects and influence the stability of existing equilibria [181, 160, 22, 167, 21, 183, 80].

Of course, the generalizations presented above apply not only to the Kuramoto model, but to general dynamical systems on networks. In this thesis we consider different network dynamical systems with non all-to-all coupling structure and higher-order interactions. We derive higher-order interactions in the Kuramoto model, study these models and their bifurcations in the thermodynamic limit as the particle size goes to infinity. Moreover, we elucidate synchrony in chaotic network dynamical systems with higher-order interactions and present numerical algorithms to efficiently integrate a wide range of network dynamical systems.

This thesis is organized as follows:

Chapter 2 provides a brief overview of the mathematical concepts of dynamical systems on networks and gives basic definitions. First, we introduce basic notation and conventions that are used throughout the thesis. After stating many examples of continuous-time dynamical systems on networks, we formalize the limit of these systems as the size of the system tends to infinity. Next, we explain how these systems can be generalized using higher-order interactions. We describe the mathematical basics of these higher-order interactions and illustrate how they are combined with ordinary (pairwise) interactions. The chapter concludes with some examples of discrete-time dynamical systems, their limits as the network size goes to infinity and examples of how to incorporate higher-order interactions.

Chapter 3 is split into two parts. In the first part, we review the concept of coupled map lattices (CMLs), which are a prototypical class of dynamical systems on graphs, that can exhibit complex patterns such as the synchronization of chaos. These patterns are generated by combining the iteration of a one-dimensional map at each node and the diffusive property of a graph Laplacian. We introduce CMLs in detail by explaining each of these two parts individually. Next, we analyze how the stability of a synchronized solution depends on the main parameters in the system and use this information to detect regions of synchronized chaos, whose existence we confirm numerically. In the second part of this chapter, we propose a class of higher-order coupled dynamical systems, that we call coupled hypergraph maps (CHMs). These CHMs generalize the concept of CMLs to hypergraphs, by including Laplacians on higher-order networks. We extend our analysis from the first part to find regions of chaotic cluster synchronization occurring in the parameter space upon varying the main system parameters. Furthermore, we find key differences between Laplacian and hypergraph Laplacian coupling and detect various other patterns. The results show the high complexity of CHMs and indicate that they might be an excellent universal model class to understand the similarities and differences between dynamics on classical graphs and dynamics on hypergraphs.

Chapter 3 is based on publications [35, 131], which are joint work with Raffaella Mulas, Jürgen Jost and Christian Kuehn.

In Chapter 4 we derive and study phase oscillator models, such as the Kuramoto model (1.1.1), from general coupled oscillator systems. The technique used to describe coupled oscillators just in terms of their phases is called phase reduction. Since phase reductions are typically derived as an expansion in the coupling strength, one can obtain phase reductions of different order by truncating this expansion after a specified amount of terms. For example, a first-order phase reduction can result in the Kuramoto model (1.1.1). In this chapter we first introduce the basics of phase reductions and illustrate how one can derive phase

reductions for coupled Stuart–Landau oscillators. As these Stuart–Landau oscillators are a special type of oscillators with a circular limit cycle, which is rarely the case in real-world scenarios, we then derive phase reductions up to second order for coupled Stuart–Landau oscillators in which the limit cycle has been deformed. Next, we compare the stability of special periodic orbits, in phase-reduced systems with the stability of these orbits in unreduced systems. Thereby, we answer questions about when one can assume to have circular limit cycles and when second-order phase reductions are required. We conclude this chapter by identifying terms in the second-order phase reduction with hyperedges of a hypergraph to obtain a natural class of hypergraphs that adequately capture the dynamics of coupled oscillators.

Chapter 4 is based on the publication [20], which is joint work with Christian Bick and Christian Kuehn.

Motivated by the higher-order phase equations derived in Chapter 4 we move on to consider a higher-order variant of the Kuramoto model with identical oscillators and a special ring-like nonlocal coupling structure in Chapter 5. Apart from full phase synchrony where all oscillators behave identically, this model can exhibit more interesting patterns, such as twisted states, as equilibria. It was discovered by Wiley, Strogatz and Girvan in 2006 that the stability of these twisted states depends on the coupling range of each oscillator [177]. We study their stability and develop a general bifurcation theory by conducting a Lyapunov–Schmidt reduction in the infinite particle limit. We then apply our results to a few special cases: First, we show that equilibria that emanate from twisted states at a bifurcation are always unstable if one only considers traditional pairwise interactions. Second, the stability of twisted states itself can be controlled by higher-order interactions and third, suitably combining different higher-order interaction terms can stabilize emerging equilibria branches.

Chapter 5 is based on the publication [22], which is joint work with Christian Bick and Christian Kuehn.

In Chapter 6 we develop efficient numerical algorithms to forward integrate the dynamics of large-scale network dynamical systems. A forward integration of high-dimensional dynamical systems on networks can be helpful to get an intuition of the dynamical behavior or to approximate the infinite particle limit. However, such an integration of large network models is often computationally prohibitive as the right-hand side of these models typically consist of large sums, e.g., in (1.1.1). Yet, most networks have intrinsic community structure that we exploit to propose fast community integration algorithms (CIAs) for network dynamical systems. By aggregating the inputs, a node receives, these CIAs can significantly reduce function evaluations to get from polynomial to linear computational complexity. We illustrate these results by applying our algorithms to

many network dynamical systems including Kuramoto-type models, used to study synchronization, and Cucker–Smale models describing flocking behavior of birds. A numerical comparison of our algorithms confirm their accuracy and efficiency.

Chapter 6 is based on publications [36, 37], which are joint work with Mechthild Thalhammer and Christian Kuehn.

Finally, Chapter 7 contains a brief conclusion and an outlook for future research.

Chapter 2

Mathematical Foundations of Network Dynamical Systems

This chapter contains an overview of network dynamical systems (NDS) including many examples. Network dynamical systems are made up of the constituents (or nodes) of the network, which can represent very general entities, the coupling structure of the network that describes which entity influences which other, and an evolution law, that governs how the states of each entity evolve over time. For example, the entities can be given by molecules, biological cells, individual animals or humans, populations of animals or celestial bodies. The structure of the network can be given in terms of pairs or groups, as described below, and the evolution law is typically given by a differential equation or an iterated map. Here, we restrict ourselves to dynamical systems on networks, meaning that only the states of the nodes evolve over time, but the network itself is assumed to be constant in time.

A dynamical system on a network is a very broad term and there does not exist one general evolution law that describes all possible dynamical systems on a network. However, these systems can be grouped into certain classes based on their properties. For example, one can distinguish between network dynamical systems posed in continuous time and discrete time. Moreover, at each time the state of a node can be in a set of discrete states or in a continuous state space. Then, one can further group these systems based on if they are deterministic or if stochastic processes are involved. However, stochastic dynamical systems and dynamical systems posed on a discrete state space are not discussed in this thesis. Instead, we consider deterministic dynamical systems on a continuous state space.

The rest of this chapter is organized as follows: First, we introduce some basic definitions and notation and provide a list of graphs that often appear in network dynamical systems. Then, we provide examples of network dynamical systems in continuous time. Next, we present two basic concepts about how to derive infinite particle dynamical systems that can approximate large but finite dimensional

models. Moreover, we introduce higher-order interactions and illustrate how they can be incorporated in finite dimensional continuous-time network dynamical systems and why it makes sense to do that. Finally, we also mention a few examples of discrete-time network dynamical systems and describe infinite particle limits thereof.

2.1   Basic Definitions and Notation

Many real-world dynamical systems have the property that they consist of many linked particles or particles that behave in a similar way. Not only is their intrinsic behavior similar, but also their reaction to other particles. In this case, we can interpret the dynamical system as one posed on a network. Such a network describes the general topology of connections between particles and groups of particles. As networks have been studied in other fields of mathematics, there are many powerful tools and concepts to understand them. Thus, such an interpretation can help to study the dynamics as one has access to many more tools. Of course a network can be very general, but the easiest variant of one is a graph $G = (V, E)$, where V is the node set and we shall always denote M for the cardinality of V, i.e., $M = |V|$. Typically, the nodes do not have a specific label, so we just assume $V = \{1, \ldots, M\}$. Moreover, E is a set of unordered pairs of elements of V and these pairs are called edges. Such a graph can be represented by its adjacency matrix $A \in \mathbb{R}^{M \times M}$ and we denote the entries of A by a_{kl} for $k, l = 1, \ldots, M$. An edge between two nodes k, l is present if $a_{kl} \neq 0$ and the value of a_{kl} can be seen as a weight associated with this edge. In case of an unweighted graph we have $a_{kl} \in \{0, 1\}$. Furthermore, a graph is undirected if $a_{kl} = a_{lk}$ for all $k, l = 1, \ldots, M$ and directed otherwise. If there is an edge between any two nodes in the graph, one says that the coupling is all-to-all or global. If the graph is empty, i.e., there is no edge at all, the particles are called uncoupled. Otherwise, the coupling structure is nontrivial and one often refers to such a coupling as nonlocal. More complicated networks can be described by hypergraphs. Such hypergraphs also consist of a node set V and a set E of hyperedges, that is a collection of subsets of V.

The rest of this section lists a few important classes of graphs, that appear in many real-world dynamical systems. Particular hypergraphs will be introduced later, when needed.

Full graph   The most trivial graph is one in which every node is connected to every other node. Such a graph is called a full graph and the only parameter is the number of nodes M. Coupling in a full graph is also referred to as all-to-all. A full graph can be seen in Figure 2.1(a).

k-nearest neighbor graphs and ring graphs Given a set of M nodes and a coupling range parameter $\Bbbk \in \mathbb{N}$ with $1 \leq \Bbbk \leq \lfloor (M-1)/2 \rfloor$, one can imagine a $\Bbbk$-nearest neighbor graph by placing all M nodes uniformly distributed on the unit circle. Then, one connects every node to $\Bbbk$ of its neighbors in one direction and to $\Bbbk$ of its neighbors in the other direction such that the degree of every node is $2\Bbbk$. Moreover, if M is even and $\Bbbk = M/2$, we define the $\Bbbk$-nearest neighbor graph as the full graph on M nodes. In this special case, the degree of every node is just $M - 1 = 2\Bbbk - 1$. An example of a 4-nearest neighbor graph can be seen in Figure 2.1(b). In the special case $\Bbbk = 1$, this is also called a ring graph.

Erdös–Rényi graphs Apart from the previously introduced graph classes, an Erdös–Rényi graph [65] is a random graph, that is determined by the size of the graph M and a parameter $p \in [0, 1]$. First, one starts with an empty graph of M nodes. Then, to obtain an Erdös–Rényi graph with parameters M and p one independently includes each of the $M(M-1)/2$ possible edges with probability p. An example of an Erdös–Rényi graph can be seen in Figure 2.1(c).
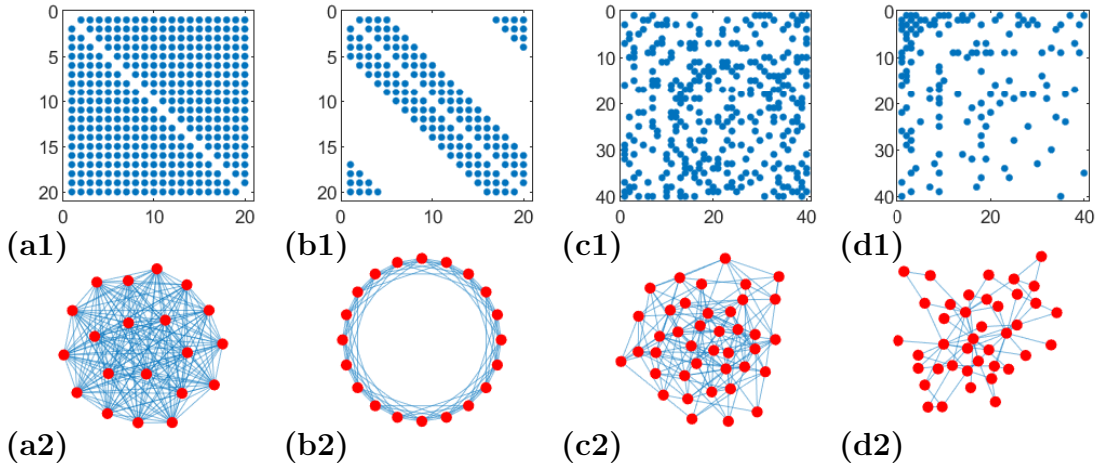
Figure 2.1: List of a few common types of graphs. Part (a1) shows the adjacency matrix of a full graph of $M = 20$ nodes. A blue dot represents an entry of $+1$ in the adjacency matrix and no dot corresponds to a 0 at the respective position in the adjacency matrix. Part (a2) depicts the full graph, that corresponds to this adjacency matrix. Similarly, parts (b1) and (b2) depict the adjacency matrix of a 4-nearest neighbor graph on $M = 20$ nodes and the graph itself, respectively. Then, (c1) and (c2) show one sample of an Erdös–Rényi graph on $M = 40$ nodes with $p = 0.2$. Finally, part (d) depicts a sample of a scale-free graph created using the Barabási–Albert model with $m = 2$. The graph sequence has been terminated at $M = 40$ nodes.

Scale-free graphs   Scale-free graphs are typically created using the Barabási–Albert model [13]. However, it is important to note that this model does not describe a single graph of a given size M but rather creates a sequence of random graphs, that grow in size. Given a parameter $m \in \mathbb{N}$, typically $m = 1, 2, 3$, one starts with a full graph of m nodes. Next, one adds a node to the graph and connects it to m other nodes that are chosen with a probability proportional to their degree. Then, one repeats this process over and over again to obtain a sequence of Barabási–Albert graphs. Of course, one can terminate this procedure when the size of the graphs has reached a predetermined parameter M. There are many variants of this model, e.g., one can allow multi-edges, directed edges, start with a different initial graph, ect., but in the limit, the degree distribution of these sequences converges to $\mathcal{N}_k \sim k^{-\alpha}$ for some $\alpha > 0$, where $\mathcal{N}_k$ is the amount of nodes with degree k. Therefore, these networks are also called power-law graphs. An example of a scale-free graph can be seen in Figure 2.1(d).

2.2   Continuous-Time Network Dynamical Systems

In this section, we present a few prominent examples of continuous-time dynamical systems, whose coupling structure can be described by a graph. Note that this graph can also be weighted and directed. The examples listed below are presented in a simple form. In particular, there are many ways to derive variants thereof or to generalize them.

Population Models   In ecology, one can model the growth of a species with N individuals as

$$\dot{N} = r\frac{N}{S}(S - N),$$

where $N = N(t)$ is a function of time $t \in \mathbb{R}$ that we usually suppress in the notation and $\dot{N} = \frac{\mathrm{d}}{\mathrm{d}t}N(t)$. Moreover, r is the intrinsic growth rate of the population and $S > 0$ is a saturation capacity. If $r > 0$, the size of the population N grows but always stays bounded, which can, for example, model the limited availability of a resource. The presence of M different species in predator-prey systems can then be modeled as

$$\dot{N}_k = r_k\frac{N_k}{S_k}\left(S_k - N_k - \sum_{l=1}^{M} a_{kl}N_l\right), \quad k = 1, \ldots, M, \qquad (2.2.1)$$

where N_k is the number of individuals in population k, r_k is the intrinsic growth rate of population k and S_k is its saturation capacity [118]. Moreover, the coefficients $a_{kl} \in \mathbb{R}$ for $k, l = 1, \ldots, M$ describe the effect of population l on population k. The parameter a_{kl} is positive whenever the presence of many individuals of population l inhibits the growth of population k and negative if the opposite applies. These parameters $(a_{kl})_{k,l=1,\ldots,M}$ can be interpreted as the adjacency matrix of a directed and weighted graph.

Phase Oscillators   A phase oscillator model describes the evolution of M coupled oscillators, which are represented just by their phase $\phi_k \in \mathbb{T}$ for $k = 1, \ldots, M$. An example of a phase oscillator model is

$$\dot{\phi}_k = \omega_k + \frac{K}{M} \sum_{l=1}^{M} a_{kl} \ g(\phi_l, \phi_k), \qquad (2.2.2)$$

where $\omega_k \in \mathbb{R}$ is the intrinsic frequency of oscillator k. Moreover, $K \in \mathbb{R}$ is the coupling strength and $g \colon \mathbb{T} \times \mathbb{T} \to \mathbb{R}$ is a coupling function. For the special case of $g(\phi_l, \phi_k) = \sin(\phi_l - \phi_k)$ and $a_{kl} \equiv 1$, this agrees with the classical Kuramoto model (1.1.1). A frequently used observable that measures the level of synchrony in phase oscillator models is the complex order parameter $Z \in \mathbb{C}$ defined by

$$Z = \frac{1}{M} \sum_{k=1}^{M} e^{\mathrm{i}\phi_k},$$

where $\mathrm{i} = \sqrt{-1}$ is the imaginary unit. On the one hand, we have $|Z| = 1$ if and only if the oscillators are synchronized, i.e., $\phi_1 = \cdots = \phi_M$. On the other hand, states with $|Z| = 0$ are called incoherent. For example, the state in which all oscillators are equidistantly distributed on $\mathbb{T}$ is incoherent.

Cucker–Smale Model   The Cucker–Smale model [57, 58] describes the interactions of birds that lead to the emergence of flocks. Each bird is modeled by its position $s_k \in \mathbb{R}^d$ and its velocity $v_k \in \mathbb{R}^d$. Then, the governing equations of the Cucker–Smale model are given by

$$\dot{s}_k = v_k,$$

$$\dot{v}_k = \frac{K}{M} \sum_{l=1}^{M} \frac{a_{kl}}{(\sigma^2 + \|s_l - s_k\|^2)^\beta} (v_l - v_k),$$

where M is the number of birds, $\sigma, \beta > 0$ are parameters and $K \in \mathbb{R}$ is the coupling strength. Thus, each bird adopts its velocity to match the velocities of

other birds. The influence of two birds k, l decreases with the distance $\|s_k - s_l\|$ between them, if $a_{kl} > 0$. Depending on the system parameters, this model can show flocking behavior, i.e., the separation of the birds into groups that move with the same velocity, even for global coupling $a_{kl} \equiv 1$.

Epidemic Spreading   There are many models of epidemic spreading on networks [98]. We assume that the epidemic spreads on a graph $G = (V, E)$ where $V = \{1, \ldots, M\}$ is the set of individuals, e.g., humans or animals. An edge between two individuals is present whenever they are in contact with each other such that an infection of one can cause an infection of the other. In a simple SIS-model each individual can be susceptible (S) or infected (I) and an individual can change its state from S to I by infection and vice versa by recovery. One can, for example, describe the probability that individual k is infected as $\langle I_k \rangle$ and the probability of individual k being susceptible as $\langle S_k \rangle$. Since there are only these two possibilities, we have $\langle S_k \rangle = 1 - \langle I_k \rangle$. Moreover, $\langle I_k \rangle$ then satisfies

$$\langle \dot{I}_k \rangle = -\gamma_k \langle I_k \rangle + \tau \sum_{l=1}^{M} a_{kl} \langle S_k I_l \rangle,$$

where $\tau > 0$ is the infection rate, γ_k the recovery rate of individual k and $\langle S_k I_k \rangle$ the probability that k is susceptible and l is infected. Note that this system is not closed as we do not know the evolution of $\langle S_k I_l \rangle$. If the state of two neighboring individuals k and l was independent one could write $\langle S_k I_l \rangle = \langle S_k \rangle \langle I_l \rangle$. However, since an infection occurs along an edge, the state of two neighboring individuals is not independent. It is an ongoing challenge to find suitable methods to close the system [98, 101].

2.3   Limits of Continuous-Time Network Dynamical Systems

The derivation of analytic results about network dynamical systems as those presented in Section 2.2 is often very difficult, especially if the number of particles M is large, which is the case in many applications. Moreover, a heterogeneous graph G further complicates the analysis. For example, the position of equilibria, if they even exist, can nonlinearly depend on system parameters, such as the frequencies ω_k in the Kuramoto model (1.1.1). Here, not even an analytic expression for all equilibria is known, which makes the analysis of this model particularly complicated. To overcome this problem, one can consider the limit as $M \to \infty$. Even though it first seems counter-intuitive to analyze an infinite particle system,

when one cannot even understand its finite dimensional analog, it turns out that there are useful tools from nonlinear analysis that can be used to study the infinite particle limit. Then, one can infer dynamical properties of the finite system from the infinite particle limit. Yet, sending $M \to \infty$ in a network dynamical system is not easy. In particular, this requires a sequence of finite dimensional dynamical systems, whose sizes tend to infinity. Then, one has to establish limits of all the finite dimensional objects that appear in the system and derive an equation that governs the dynamics of the limiting infinite dimensional dynamical system. We demonstrate this at the example of the phase oscillator model (2.2.2), as this model is particularly relevant for this thesis. To make the dependence on the system size clear, we include the index M for the system size and write

$$\dot{\phi}_k^M = \omega_k^M + \frac{K}{M} \sum_{l=1}^{M} a_{kl}^M \ g(\phi_l^M, \phi_k^M), \quad k = 1, \ldots, M. \tag{2.3.1}$$

Now, one has to derive limit objects of $\omega^M \in \mathbb{R}^M$, $\phi^M \in \mathbb{T}^M$ and $(a_{kl}^M)_{k,l=1,\ldots,M}$, as $M \to \infty$, which is not easy as the dimension of the space itself, where these objects are in, increases. There are two fundamentally different concepts to achieve that, which differ from each other by the way of representing the state variable ϕ in the limit. Both of these concepts assume that the graph sequence G^M, represented by the adjacency matrices $(a_{kl}^M)_{k,l=1,\ldots,M}$, is dense. We assume that this is the case and later explain why such an assumption is necessary. Another important point when deriving limiting dynamical systems is to ensure that the limiting equation has a unique solution and that it approximates the finite dimensional systems reasonably well. These questions have been answered for both concepts presented below [49, 94, 124].

The first concept is the continuum limit. While the oscillators ϕ_k^M are indexed by $k = 1, \ldots, M$ for finite M, the idea of the continuum limit is to index the oscillators in the limit by a continuous variable $x \in I := [0, 1]$. To achieve that, one first defines a function $\Theta^M \colon \mathbb{R}_{\geq 0} \times I \to \mathbb{T}$ with

$$\Theta^M(t, x) := \phi_k^M(t) \qquad \text{if } x \in \left[\frac{k-1}{M}, \frac{k}{M}\right), \tag{2.3.2}$$

where $\phi_k^M(t)$ solve (2.3.1) and the value at $x = 1$ can be defined arbitrarily. For every fixed time t, this is a step function on the unit interval I. Moreover, note that a_{kl}^M are the coefficients of an adjacency matrix of a graph G^M with M nodes. Thus, we can also define a two dimensional step function $W^M \colon I^2 \to \mathbb{R}$ as

$$W^M(x, y) = a_{kl}^M \qquad \text{if } x \in \left[\frac{k-1}{M}, \frac{k}{M}\right) \text{ and } y \in \left[\frac{l-1}{M}, \frac{l}{M}\right). \tag{2.3.3}$$

Again, the value of W^M at $x = 1$ and $y = 1$ can be defined arbitrarily. Now, if $\omega_k^M \equiv \omega$ for some given $\omega \in \mathbb{R}$, one can immediately see that the function $\Theta^M(t, x)$ satisfies

$$\frac{\partial}{\partial t}\Theta^M(t, x) = \omega + K \int_I W^M(x, y) \, g(\Theta^M(t, y), \Theta^M(t, x)) \, \mathrm{d}y, \qquad (2.3.4)$$

whenever $\phi_k^M(t)$ solve (2.3.1). Since $\Theta^M(t, \cdot) \colon I \to \mathbb{T}$ and $W^M \colon I^2 \to \mathbb{R}$ are objects in a space that is independent of M, one can transition to the limit by lifting the requirement that they are step-functions and allowing them to be arbitrary measurable functions in a suitable function space on I and I^2, respectively. A limit Θ of Θ^M then satisfies the continuum limit equation

$$\frac{\partial}{\partial t}\Theta(t, x) = \omega + K \int_I W(x, y) \, g(\Theta(t, y), \Theta(t, x)) \, \mathrm{d}y, \qquad (2.3.5)$$

where $W \colon I^2 \to \mathbb{R}$ is the limit of the function W^M defined in (2.3.3) in a suitable metric. This function W is also called a graphon. Generally, this type of graph limit is suitable if the graph sequence G^M is dense. Otherwise, the functions W^M converge to the zero function, and thus information about the structure of the graph is lost in the $M \to \infty$ limit. In these cases, one has to consider other types of graph limits, see e.g., [85, 12]. When working with the continuum limit (2.3.5), it is often useful to know how close a solution of the continuum limit is to one of the finite dimensional system. For this reason approximation results have been established, which state when $d(\Theta^M(t, \cdot), \Theta(t, \cdot)) \to 0$ as $M \to \infty$, where Θ^M solves (2.3.4), Θ solves (2.3.5) and d is a distance of functions on $\mathbb{T}$. In fact, this is the case when $\left\|W^M - W\right\| \to 0$ in a suitable norm and the initial conditions converge in the sense that $d(\Theta^M(0, \cdot), \Theta(0, \cdot)) \to 0$, see e.g. [124]. A drawback of the continuum limit is the assumption of identical oscillators, i.e., $\omega_k^M \equiv \omega$, which prevents us considering limits of heterogeneous particles. Of course, one can try to derive a continuum limit without this assumption and make the constant ω in (2.3.5) dependent on x. This, however, might result in convergence issues, in particular when considering the Kuramoto model, where the intrinsic frequencies ω_k are samples from a probability distribution that can have unbounded support. To get around this problem there is a second way of transitioning to the limit as $M \to \infty$.

A second way of deriving an infinite particle limit of (2.2.2) is the mean-field limit. This mean-field limit still relies on the existence of a graphon W that represents the limit of the dense graph sequence G^M. If this is not the case, one has to consider other kinds of limits, see e.g., [72, 106]. A node in this (dense) graph limit is then described by a value $x \in I$. However, instead of having a function that describes the exact position of each oscillator in the continuum, one

here only has a probability density $\rho(t, \theta, x, \omega)$ with $\int_{\mathbb{T} \times I \times \mathbb{R}} \rho(t, \theta, x, \omega) \mathrm{d}\theta \mathrm{d}x \mathrm{d}\omega = 1$ that describes the likelihood of finding an oscillator at time t at the position $\theta \in \mathbb{T}$ with intrinsic frequency $\omega \in \mathbb{R}$, when this oscillator is on a node $x \in I$ in the graph limit. Note, however, that there is no randomness involved. Rather, the probability density only denotes a normalized mass distribution. Apart from the continuum limit, where each infinitesimal oscillator is located at node $x \in I$ in the graph limit and has one intrinsic frequency, the idea of the mean-field limit is that at almost every pair (x, ω), where $x \in I$ is a position in the graph limit and $\omega \in \mathbb{R}$ is an intrinsic frequency, there is a whole distribution of oscillators with density $\rho(t, \cdot, x, \omega)$ up to a normalization factor. This density evolves according to the continuity equation

$$\frac{\partial}{\partial t} \rho(t, \theta, x, \omega) + \frac{\partial}{\partial \theta} \Big(\rho(t, \theta, x, \omega) V[\rho](t, \theta, x, \omega) \Big) = 0, \qquad (2.3.6)$$

where $V[\rho]$ is the velocity field defined by

$$V[\rho](t, \theta, x, \omega) = \omega + K \int_I \int_{\mathbb{R}} \int_{\mathbb{T}} W(x, y) g(\xi, \theta) \rho(t, \xi, y, \lambda) \, \mathrm{d}\xi \mathrm{d}\lambda \mathrm{d}y,$$

and the function W is the same graphon that appears in the continuum limit. It was shown in [76, 94, 49] that this mean-field limit has a unique solution. As in the continuum limit, it is important to know how well the mean-field limit approximates a finite dimensional system. Since the mean-field limit (2.3.6) describes the evolution of a density, but the finite dimensional system (2.2.2) gives the position of the oscillators, one cannot directly compare the two. However, one can generalize (2.3.6) to track the evolution of general measures μ_t on $\mathbb{T} \times I \times \mathbb{R}$. Then, a probability distribution with density $\rho(t, \cdot, \cdot, \cdot)$ can also be represented by a measure $\mu_t[\rho]$. Furthermore, the state of the finite dimensional system can also be represented by a discrete measure

$$\mu_t^M = \frac{1}{M} \sum_{k=1}^{M} \delta_{(\phi_k(t), (k-1)/M, \omega_k)},$$

where $\delta_{(\phi, x, \omega)}$ is the dirac-distribution centered at $(\phi, x, \omega) \in \mathbb{T} \times I \times \mathbb{R}$. Whenever the functions $\phi_k(t)$ solve the finite dimensional system (2.3.1) one can check that the measures μ_t^M solve the generalized continuity equation. Now, that we can describe both systems with a probability measure we can compare the two in a suitable metric, usually a bounded-Lipschitz or Wasserstein metric. It was shown that whenever $\mu_0^M \to \mu_0[\rho]$ and $W^M \to W$ as $M \to \infty$, then also $\mu_t^M \to \mu_t[\rho]$ for fixed $t \geq 0$ as $M \to \infty$ and one can even estimate the rate of convergence [76, 94].

2.4   Higher-Order Interactions for Continuous-Time Network Dynamical Systems

The systems presented in Section 2.2 and the resulting continuum and mean-field limits derived in Section 2.3 are made up of pairwise interactions, which is a type of an interaction between exactly two particles. In particular, the right-hand side of the systems considered in Section 2.2 are sums of interactions between two particles. Similarly, the right-hand sides of their limits consist of integrals over the interaction between two particles. Other types of interactions might involve more than just two particles. If, for example, the interaction between two particles depends on a third one, one speaks of a triplet interaction. In general, any interaction that involves three or more particles is called a higher-order interaction.

Historically, higher-order interactions have first appeared in ecology [172, 1, 26], where the interaction between three or more species occurs in predator-prey systems due to various competitive or parasitic effects. In particular, it has been shown that just the pairwise effect of one population on another, see (2.2.1), is sometimes insufficient to describe the dynamics of coexisting populations. Instead, when modeling the growth of M coexisting populations, with N_k individuals for $k = 1, \ldots, M$, one needs to consider systems of the form

$$\dot{N}_k = r_k \frac{N_k}{S_k} \left(S_k - N_k - \sum_{l=1}^{M} a_{kl} N_l - \sum_{l=1}^{M} \sum_{i=1}^{M} b_{kli} N_l N_i \right), \quad k = 1, \ldots, M,$$

where the parameters r_k, S_k and a_{kl} are as in (2.2.1) and $b_{kli} \in \mathbb{R}$ for $k, l, i = 1, \ldots, M$ model triplet or 3-way interactions between the populations [172]. Sometimes, one also has to include quadruplet or even higher-order interactions [172]. These higher-order interactions can, for example, describe coalitions that are formed by a few species against another species [172, 118, 26].

Since then, it was discovered that higher-order interactions can also be included in other type of network models and they lead to interesting effects, see for example [161, 160, 4, 19, 18, 183]. A prototypical class of dynamical systems that generalizes pairwise phase oscillator models to higher-order models is given by

$$\dot{\phi}_k(t) = \omega_k + \frac{K_2}{M} \sum_{l=1}^{M} a_{kl} \, g_2(\phi_l(t), \phi_k(t)) + \frac{K_3}{M^2} \sum_{l,i=1}^{M} b_{kli} \, g_3(\phi_k(t), \phi_l(t), \phi_i(t)).$$

$$(2.4.1)$$

As in the pairwise phase oscillator model (2.2.2), a_{kl} are the coefficients of an adjacency matrix corresponding to a graph that describes the pairwise coupling and we specifically include the index 2 in the coupling function g_2 to highlight

that this is the pairwise coupling function. Moreover, $K_2 \in \mathbb{R}$ is the strength of the pairwise coupling. The last term on the right-hand side describes triplet interactions: b_{kli} are the coefficients of a 3-tensor that represents a higher-order coupling, and similarly, g_3 is the three-way interaction function and $K_3 \in \mathbb{R}$ is its strength.

Mathematically, this higher-order coupling structure can be represented by a hypergraph. In general, a hypergraph consists of a node set $V = \{1, \ldots, M\}$ and a set of hyperedges E, whose elements are subsets of V. One can generalize this definition by assigning weights to each hyperedge or considering ordered tuples instead of sets as hyperedges to make the hypergraph directed. In our case, the coefficients $(b_{kli})_{k,l,i=1,\ldots,M}$ define a 3-tensor, which can represent a hypergraph with special properties. First, the hypergraph is 3-uniform, meaning that every hyperedge in this hypergraph consists of three nodes. Second the hypergraph is undirected, when b_{kli} are invariant under a permutation of the indices k, l, i and finally, the hypergraph is weighted, as the coefficients b_{kli} are not restricted to $\{0, 1\}$. Analogously, one can add 4-way interactions and even higher-order interactions. The coupling structure of an ℓ-way interaction would then be given by an ℓ-uniform hypergraph, represented by an ℓ-tensor and a coupling function $g_\ell \colon \mathbb{T}^\ell \to \mathbb{R}$. In general, dynamical properties of higher-order systems are more challenging to study since the right-hand side of (2.4.1) involves many sums and thus numerical simulations become intractable starting at much smaller system size M.

A simple model up to 4-way interactions, in which all the coefficients from the adjacency matrix and higher-order coupling tensors are equal to 1 and coupling functions are sinusoidal, was proposed in [160]. Even in this simple model, the higher-order interactions can lead to the creation of new equilibria and influence their bifurcation behavior.

2.5 Discrete-Time Network Dynamical Systems

Having discussed many continuous-time network dynamical systems, their limits, and generalizations to higher-order interactions, we now want to consider network dynamical systems in discrete time. A lot of discrete-time network dynamical systems emerge from discretizing continuous-time network dynamical systems using an Euler scheme or a general Runge–Kutta method. Below, we present two examples of discrete-time network dynamical systems; the first of which has an analog in continuous-time and second of which does not.

Opinion Dynamics   An opinion dynamics model consists of a number M of agents who have their own opinion about some subject. Each agent can react to

the opinions of other agents to form their own opinion, but an agent does not need to be influenced by all others in the same way. In fact, an agent might only react to a few other agents. Such a reaction structure can be represented by a directed (and possibly weighted) graph, that is represented by an adjacency matrix $A = (a_{kl})_{k,l=1,\dots,M}$. If the opinion of agent k at discrete time $n \in \mathbb{N}$ can be represented by a real number x_k^n for $k = 1, \dots, M$, the opinion at time $n+1$ is given by

$$x_k^{n+1} = \sum_{l=1}^{M} a_{kl}\ x_l^n, \qquad k = 1, \dots, M,$$

or just $x^{n+1} = Ax^n$, where $x^n = (x_1^n, \dots, x_M^n)^\top$. Usually, the matrix A is stochastic, i.e., $\sum_{l=1}^{M} a_{kl} = 1$ and $a_{kl} \geq 0$ for all k, l, see [86]. If agent k disrespects the opinion of agent l we have $a_{kl} = 0$. If an agent k disrespects the opinions of all other agents, we have $a_{kl} = 0$ for all $l \neq k$ and $a_{kk} = 1$. If the contrary is true and an agent k imitates the opinion of an agent l we have $a_{kl} = 1$ and $a_{ki} = 0$ for all $i \neq l$.

Coupled Map Lattices   Coupled map lattices (CMLs) can consist of a smooth map $f \colon \mathbb{R}^d \to \mathbb{R}^d$ and some coupling structure, for example a coupling function $g \colon \mathbb{R}^d \times \mathbb{R}^d \to \mathbb{R}^d$, usually with $d = 1$, such that

$$x_k^{n+1} = f(x_k^n) + \frac{K}{M} \sum_{l=1}^{M} a_{kl}\ g(x_l^n, x_k^n), \qquad k = 1, \dots, M, \qquad (2.5.1)$$

where x_k^n is the state of particle k at the discrete time $n \in \mathbb{N}$ and $K \in \mathbb{R}$ is the coupling strength. Without coupling, i.e., $K = 0$, the state of each particle evolves by iterating the map f. Depending on the specific choice of f there might be invariant regions in which interesting dynamics, such as chaos can appear. Already for globally coupled maps, interesting dynamical effects, such as chaos and pattern formation, were observed; see [143, 93, 95] and Chapter 3.

Similarly to the continuous-time examples, that we presented, infinite particle limits for discrete-time dynamical systems can also be derived. For example in [159], the authors study a discrete-time variant of the mean-field limit of (2.5.1), where the coupling is global. In particular, as (2.5.1) with global coupling, i.e., $a_{kl} \equiv 1$, is equivariant under a permutation of the particles [11], it is sufficient to use a discrete measure μ_n to represent the state of all particles at time n. Such a measure is then defined by

$$\mu_n = \frac{1}{M} \sum_{l=1}^{M} \delta_{x_l^n}.$$

Using such a measure, one can also rewrite (2.5.1) as an iteration procedure for measures. This iteration procedure can then also be applied to general measures, not only to those which are a finite convex combination of dirac measures. Thereby, the authors of [159] derived a mean-field limit for discrete-time network dynamical systems. If the map f in (2.5.1) is expanding, one can find chaos in this mean-field limit [169].

Chapter 3

From Coupled Map Lattices to Coupled Hypergraph Maps

The content of this chapter is based on publications [35] and [131], which are both joint work together with Raffaella Mulas, Jürgen Jost and Christian Kuehn.

3.1 Background

Synchronization of interacting particle systems is a ubiquitous phenomenon that is observed in many real-world systems. However, synchronization can not only occur among particles with "simple" dynamics, such as coupled oscillators with a stable limit cycle, but also in chaotic systems [141]. Since chaotic systems feature sensitive dependence on initial conditions, two trajectories that start close to each other eventually drift away and become uncorrelated. Therefore, the synchronization of chaotic systems seems counter-intuitive and its discovery came as a surprise [68]. However, due to many possible applications, the study of synchronization in chaos has been an active area of research [91, 110, 144]. A prototypical mathematical framework that is often used to study this phenomenon are coupled map lattices (CMLs) [91, 95].

Generally speaking, CMLs are a discrete-time dynamical system of particles, where the intrinsic dynamics at each node is given by an iterated map and the interactions between the nodes are specified by a simple graph $G = (V, E)$. Then, the state of a particle at time $n + 1$ only depends on the state of the particle itself and the states of all neighboring particles at time n. In this chapter we denote $x_k^n \in \mathbb{R}$ for the state of vertex $k = 1, \ldots, M = |V|$ at discrete time $n \in \mathbb{N}$. Classically, one has considered ring graphs [95] or complete graphs [175] on M nodes; both classes already display very surprising phenomena.

For example, one of the systems considered in [95] is given by

$$x_k^{n+1} = f(x_k^n) + \varepsilon\Big((f(x_{k-1}^n) + f(x_{k+1}^n))/2 - f(x_k^n)\Big),$$

where $n \in \mathbb{N}$ is the discrete time, $k = 1, \ldots, M$ labels the nodes of the graph, $\varepsilon \in \mathbb{R}$ is the coupling strength and $f(x) = 1 - ax^2$ with $a \in \mathbb{R}$. Moreover, there is a periodic boundary condition of the form $x_{M+1}^n = x_1^n$ such that the underlying graph has a ring structure. Even though the author called this system a "coupled logistic lattice", it belongs to the later introduced broader class of CMLs. Starting from the initial condition $x_k^0 = \sin(2\pi k/M)$, the author conducted numerical simulations for different parameters a, ε and graph sizes M. He found that in some parameter regimes the trajectories converge to a stable periodic orbit, that consists of patterns, which are relatively flat in some regions of $k = 1, \ldots, M$ but then have some sudden jumps to other flat regions. Varying the parameters can change the profile of these patterns, lead to period doubling bifurcations or can even make the system chaotic.

Motivated by these findings on ring graphs and further results about CMLs on complete graphs, many scientists began to study CMLs when the graph is not complete or a ring and it was discovered that new effects may arise in these cases [91, 116, 175].

For example, the authors of [175] considered CMLs on scale-free graphs $G = (V, E)$ with $|V| = M$ nodes, which reads as

$$x_k^{n+1} = (1 - \varepsilon)f(x_k^n) + \varepsilon\frac{1}{\mathcal{N}_k}\sum_{k=1}^{M} a_{kl}\deg(l)^{\alpha}f(x_l^n),$$

where a_{kl} are the coefficients of the adjacency matrix of the graph G, $\varepsilon \in [0, 1]$ is the coupling strength, $f(x) = 1 - ax^2$ is the same map as in the last example, $\alpha \in [-\frac{1}{4}, 2]$ and $\mathcal{N}_k = \sum_{k=1}^{M} a_{kl}\deg(l)^{\alpha}$ normalizes the sum. In this system, the authors focus in particular on the synchronized solution, for which $x_1^n = \cdots = x_M^n$. They study random scale-free network sequences, see Section 2.1 and deterministic scale-free network sequences derived thereof. They found that the tendency towards synchronization is mainly controlled by the parameter m that describes the connectivity in these graph sequences, see Section 2.1. Moreover, even when $a = 2$, i.e., when $[-1, 1]$ is mapped onto itself under the application of f, and when the one-dimensional logistic system $y^{n+1} = f(y^n)$ is maximally chaotic, synchronized solutions do appear as stable limits.

However, all of the previous studies only consider pairwise interactions by nodes, even though it was shown that this graph coupling is insufficient in many applications, see Section 2.4. In this chapter we are interested in the dynamical effects that can occur when replacing the pairwise graph coupling in CMLs by higher-order coupling.

   This chapter is organized as follows: First, we review a subclass of CMLs, in which the coupling is given by a Laplacian. We introduce the Laplacian and the dynamics of the subclass of CMLs in Section 3.2. Moreover, we analyze the stability of the synchronized solution. Next, we propose a very general extension of CMLs that includes higher-order interactions by replacing the graph by a hypergraph. In Section 3.3 we therefore introduce Laplacians on Hypergraphs and then generalize CMLs to coupled hypergraph maps (CHMs). Section 3.4 first analyzes the dynamics of such a CHM on a special class of hypergraphs in detail and then gives a numerical summary of new effects discovered in CHMs on further classes of hypergraphs. Finally, Section 3.5 consists of a summary and concluding remarks.

3.2   Coupled Map Lattices

Given a graph $G = (V, E)$, with vertex set $V = \{1, \ldots, M\}$ we denote $x^n = (x_1^n, \ldots, x_M^n)^\top \in \mathbb{R}^M$ for the state of the CML at time $n \in \mathbb{N}$. The dynamics of the class of CMLs that we consider and then want to generalize to hypergraphs in Section 3.3, is made up of two separate parts that induce different dynamical effects. One of them is the iteration of a one-dimensional map that induces chaos and the other part is the application of a graph Laplacian that creates diffusion. We introduce these two parts individually in Sections 3.2.1 and 3.2.2 and then combine the two parts in Section 3.2.3. Combining two parts that induce different dynamical effects, raises the question whether one of these effects dominates the other or if the resulting dynamics shows a combination of the two effects. We tackle this question by a stability analysis of a certain type of solutions in Section 3.2.4 and numerical simulations in Section 3.2.5.

3.2.1   First Part: Iterated Map

The first part is based on a one-dimensional real valued map f_μ that induces a dynamical system via the iteration

$$y^{n+1} = f_\mu(y^n), \tag{3.2.1}$$

where $y^n \in \mathbb{R}$ and $\mu \in \mathbb{R}$ is a parameter. Typical examples of f_μ are the logistic map

$$f_\mu(x) = \mu x(1 - x) \tag{3.2.2}$$

or the tent map

$$f_\mu(x) = \frac{\mu}{2} \min(x, 1 - x), \tag{3.2.3}$$

both with parameter $\mu \in [0, 4]$, which makes the unit interval $[0, 1]$ invariant. Moreover, since upon increasing μ the dynamical system (3.2.1) first undergoes many period doubling bifurcations and then transitions to chaos (see first row of Figure 3.1), we also call μ the main bifurcation parameter. A method to determine if the system is chaotic or not, is to evaluate the Lyapunov coefficient [3], which is given by

$$\mu_0 = \lim_{N \to \infty} \frac{1}{N} \sum_{n=0}^{N-1} \log |f'_\mu(y^n)|. \tag{3.2.4}$$

If $\mu_0 > 0$, the system is chaotic and if $\mu_0 < 0$ it is not. For the tent map and the logistic map, the second row of Figure 3.1 depicts how the Lyapunov coefficient depends on μ.
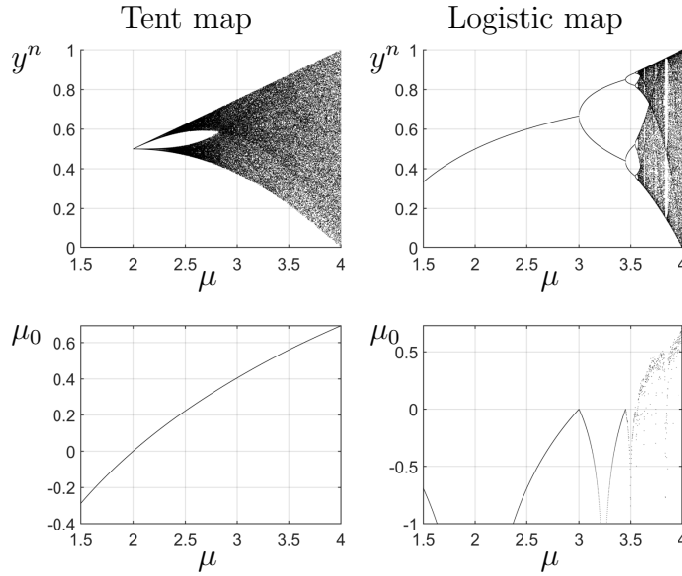
Figure 3.1: Simulation of the system (3.2.1) for the tent map (3.2.3) (left column) and the logistic map (3.2.2) (right column). The first row shows y^n for $10000 \leq n \leq 10050$ for different values of μ and a random initial condition. The second row depicts the Lyapunov coefficient μ_0.

This one-dimensional dynamical system trivially induces a dynamical system on a graph by simply applying f_μ to the state of each vertex, such that

$$x_k^{n+1} = f_\mu(x_k^n), \tag{3.2.5}$$

which we also denote by $x^{n+1} = f_\mu(x^n)$ in vector notation. Here, $f_\mu(x^n)$ is the vector of element-wise applications of f_μ to the elements of $x^n = (x_1^n, \ldots, x_M^n)^\top \in \mathbb{R}^M$.

In general, we write y^n for the state of the one-dimensional system (3.2.1) and x^n to denote the vector valued state of (3.2.5). Note that (3.2.5) basically represents M independent dynamical systems that are governed by the same iterated map, since there is no interaction among the different vertices. In parameter regions of μ, where the system exhibits chaos, there is sensitive dependence on initial conditions, i.e., even if x_k^0 is close to x_l^0, for some $k \neq l$, the two trajectories x_k^n and x_l^n drift apart and quickly become uncorrelated as n increases. Therefore, this step defies the synchronization among the different vertices.

3.2.2 Second Part: Diffusive Process

A diffusive process on a graph is typically defined by a graph Laplacian. To define a Laplacian, we need the adjacency matrix $A \in \{0,1\}^{M \times M}$ of the graph, which we assume to be symmetric. Moreover, we define the degree matrix $D = (d_{kl})_{kl} \in \mathbb{N}_0^{M \times M}$ as the matrix with $d_{kl} = 0$ if $k \neq l$ and $d_{kk} = \deg(k)$. Then, the normalized graph Laplacian is an operator given by the matrix $L = \mathrm{Id}_M - D^{-1}A$, where Id_M is the M-dimensional identity matrix. If the graph is connected, which we assume, the degree matrix D is indeed invertible and as a consequence L is well defined. To indicate that we are using a graph Laplacian we also denote L_G for this operator. A diffusive process on the graph is then given by the application of the normalized graph Laplacian L_G to the state x^n. Thereby, this step couples the individual vertices. In particular, we consider the dynamics of

$$x^{n+1} = x^n - \varepsilon(L_G x^n), \tag{3.2.6}$$

where $\varepsilon \in \mathbb{R}$ is a parameter that controls the coupling strength. Thus, we call ε the coupling parameter. Such a process can, for example, be obtained by the discretization of the continuous-time heat equation where ε is the time step. If the time step ε is in $(0,1)$, this process inherits the diffusive property from the heat equation. In particular, this means that the state x_k^n of the node k is attracted towards a mean of the state of neighboring nodes of k. Moreover, if $\varepsilon \in (0,1)$, the process (3.2.6) satisfies a maximum principle, i.e., $\max_k x_k^{n+1} \leq \max_k x_k^n$ and $\min_k x_k^{n+1} \geq \min_k x_k^n$. Eventually, as the graph is connected, the process converges to an equilibrium, in which the states of the nodes are synchronized among each other. Figure 3.2 shows a simulation of the diffusive process (3.2.6) on a ring graph of 5 nodes with parameter $\varepsilon = 0.3$. The initial condition at time $n = 1$ is depicted in Figure 3.2(a). The tip of the red arrows, that originate from the state of vertex k, corresponds to the mean of the states of neighboring nodes. Since $\varepsilon = 0.3$, the state of the vertex at time $n = 2$ can be obtained by moving the state of the vertex at time $n = 1$ exactly $\frac{3}{10}$ along this arrow, which then results in the state depicted in Figure 3.2(b). Figure 3.2(c) shows another iteration and after a

few more iterations the states of the vertices synchronize more and more, as seen in Figure 3.2(d).
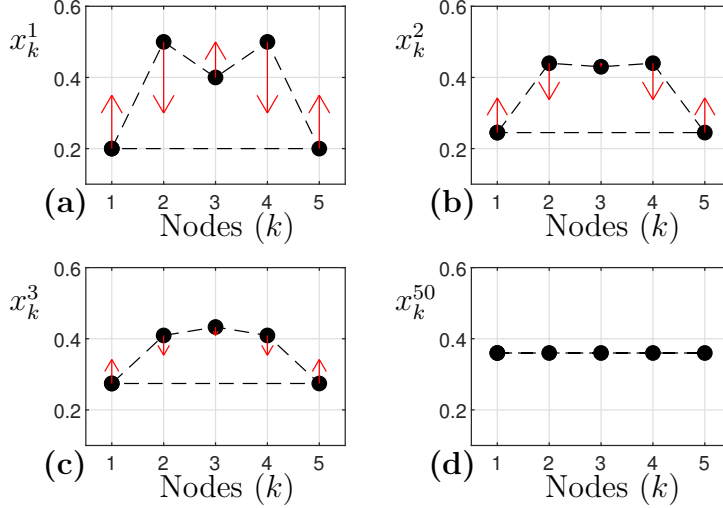
Figure 3.2: Visualization of the diffusive process (3.2.6) on a ring graph with 5 nodes, see Section 2.1. Part (a)-(d) show the state of the vertices at time $n = 1$, $n = 2$, $n = 3$ and $n = 50$, respectively. The dashed lines indicate which node is coupled to which. The red arrows point towards the mean of the state of neighboring nodes. Parameter value: $\varepsilon = 0.3$.

As we will see later in this section, the eigenvalues and eigenvectors of the graph Laplacian are important characteristics when dealing with dynamical systems involving the graph Laplacian. To analyze them, one first notes that the graph Laplacian is self-adjoint with respect to the scalar product

$$\langle x, y \rangle = \sum_{l=1}^{M} x_l y_l \deg(l),$$

where $x, y \in \mathbb{R}^M$. Consequently, the eigenvectors $(u_j)_{j=1,\ldots,M}$ are orthogonal with respect to this scalar product and in particular, they form a basis of $\mathbb{R}^M$. Moreover, since L_G is diagonally dominant, it is positive semi-definite and its eigenvalues $\lambda_1, \ldots, \lambda_M$ can be ordered as

$$0 = \lambda_1 \leq \lambda_2 \leq \cdots \leq \lambda_M,$$

where $\lambda_1 = 0$ is always an eigenvalue to the corresponding eigenvector $u_1 = \mathbb{1} = (1, 1, \ldots, 1)^\top \in \mathbb{R}^M$. More specifically, the multiplicity of the eigenvalue 0 corresponds to the number of connected components of the graph G. If G has two connected components, then $\lambda_2 = 0$; if it has three connected components, then also $\lambda_3 = 0$, etc. If, however, G is connected, we always have $\lambda_2 > 0$.

In the following, we assume that the graph G is connected, since the full dynamics on an unconnected graph can be broken down into smaller dynamical systems on the connected components of G. In particular, we do not allow for isolated nodes, i.e., $\deg(k) \geq 1$ for all $k \in V$.

3.2.3   The Dynamics of our Coupled Map Lattice

Finally, the dynamics of the CML, that we consider and that has already been considered in [91], is given by alternately applying a step of (3.2.5) and then one of (3.2.6), such that the dynamics is given by

$$x^{n+1} = f_\mu(x^n) - \varepsilon L_G(f_\mu(x^n)), \tag{3.2.7}$$

where again $x^n = (x_1^n, \ldots, x_M^n) \in \mathbb{R}^M$ is the vector containing the states at the vertices $k = 1, \ldots, M$. This CML has an important invariant manifold, which is the (complete) synchronization manifold $\mathcal{M} := \{x_1 = x_2 = \cdots = x_M\}$. This manifold is invariant under the dynamics of (3.2.7), due to the invariance under both steps (3.2.5) and (3.2.6). A solution of (3.2.7) is called synchronized if it eventually ends up in $\mathcal{M}$, i.e., when $x_k^n = x_l^n$ for all k, l and all times $n \geq n_0$ for some $n_0 \in \mathbb{N}$. Since the states of all nodes agree, such a solution is also referred to as a synchronized solution. Importantly, a synchronized solution in $\mathcal{M}$ does not need to be constant in n, but could, for instance, show itself chaotic behavior. In such a case, one speaks of the (complete) synchronization of chaos [95].

However, since the CML (3.2.7) consists of a part (3.2.5) that defies synchronization and a part (3.2.6) that promotes synchronization, the transverse stability of $\mathcal{M}$ is nontrivial. Due to the importance of synchronized solutions, the stability analysis of $\mathcal{M}$ has attracted a lot of attention [95, 91, 68]. Since the two competing parts can be controlled using the main bifurcation parameter μ and the coupling parameter ε, one expects transverse stability of $\mathcal{M}$ to be dependent on μ and ε. The next subsection recalls an analytical approach to study the stability of $\mathcal{M}$ from [91].

3.2.4   Stability Analysis of the Homogeneous Solution

To analyze the transverse stability, we consider an orbit y^n of (3.2.1), i.e., such that $y^{n+1} = f_\mu(y^n)$. Caused by the invariance of $\mathcal{M}$, the homogeneous sequence $x^n = y^n \mathbb{1}$, where $\mathbb{1} = (1, 1, \ldots, 1)^\top$ is the vector in $\mathbb{R}^M$ containing only ones, is indeed a solution of (3.2.7) and thus $\mathcal{M}$ is invariant. To analyze its transverse stability, we can proceed as in [91]. In particular, we perturb the homogeneous solution $x^n = y^n \mathbb{1}$ in the direction of an eigenvector u_j of the graph Laplacian L_G. Doing that for all eigenvectors $j = 1, \ldots, M$, provides a complete picture about the local

dynamics around $\mathcal{M}$, since they form a basis of $\mathbb{R}^M$. However, we cannot expect every perturbation to decay, because perturbing with the constant eigenvector u_1, that corresponds to the eigenvalue $\lambda_1 = 0$, leaves $\mathcal{M}$ invariant. Thus, a decay of perturbations in the direction of all other eigenvectors $j = 2, \ldots, M$ entails transverse stability of $\mathcal{M}$. To analyze such a perturbation we proceed as in [91] and start with the ansatz

$$x^n = y^n \mathbb{1} + \delta \alpha_j^n u_j, \tag{3.2.8}$$

for some $j \geq 2$, $\alpha_j^n \in \mathbb{R}$ and small enough δ. A sufficient condition for the decay of these perturbations is

$$0 > \lim_{N \to \infty} \frac{1}{N} \log \left| \frac{\alpha_j^N}{\alpha_j^0} \right| = \lim_{N \to \infty} \frac{1}{N} \log \prod_{n=0}^{N-1} \left| \frac{\alpha_j^{n+1}}{\alpha_j^n} \right|, \tag{3.2.9}$$

since this entails $\alpha_j^N \to 0$ as $N \to \infty$. To get a formula for $\alpha_j^{n+1}/\alpha_j^n$, we insert the ansatz (3.2.8) into the left- and right-hand side evolution law of the CML (3.2.7) to obtain

$$y^{n+1} \mathbb{1} + \delta \alpha_j^{n+1} u_j = f_\mu(y^n \mathbb{1} + \delta \alpha_j^n u_j)$$
$$- \varepsilon L_G \Big(f_\mu(y^n \mathbb{1} + \delta \alpha_j^n u_j) \Big).$$

Next, we linearize $f_\mu(y^n \mathbb{1} + \delta \alpha_j^n u_j) \approx f_\mu(y^n) \mathbb{1} + f'_\mu(y^n) \delta \alpha_j^n u_j$, use the linearity of L_G and $L_G \mathbb{1} = 0$. This leads us to

$$y^{n+1} \mathbb{1} + \delta \alpha_j^{n+1} u_j \approx f_\mu(y^n) \mathbb{1} + f'_\mu(y^n) \delta \alpha_j^n u_j - \varepsilon f'_\mu(y^n) \delta \alpha_j^n L_G u_j.$$

Finally, noting that $f_\mu(y^n) = y^{n+1}$ and $L_G u_j = \lambda_j u_j$ this leads us to the linearized stability condition

$$\frac{\alpha_j^{n+1}}{\alpha_j^n} = f'_\mu(y^n)(1 - \varepsilon \lambda_j).$$

Inserting this into (3.2.9) yields

$$0 > \lim_{N \to \infty} \frac{1}{N} \log \prod_{n=0}^{N-1} \left| f'_\mu(y^n)(1 - \varepsilon \lambda_j) \right|$$
$$= \lim_{N \to \infty} \frac{1}{N} \sum_{n=0}^{N-1} \Big(\log(|f'_\mu(y^n)|) + \log(|1 - \varepsilon \lambda_j|) \Big)$$
$$= \mu_0 + \log(|1 - \varepsilon \lambda_j|),$$

where μ_0 is given by (3.2.4). Finally, after applying the exponential function to both sides, we are left with a sufficient linear stability condition

$$e^{\mu_0} |1 - \varepsilon\lambda_j| < 1 \tag{3.2.10}$$

for the decay of perturbations in the direction of the eigenfunction u_j and

$$e^{\mu_0} |1 - \varepsilon\lambda_j| < 1 \quad \text{for all } j = 2, \dots, M \tag{3.2.11}$$

for the transverse stability of $\mathcal{M}$.

3.2.5 Numerical Simulations

In order to get an intuition of how far the sufficient stability condition (3.2.11) is from being necessary and to get an intuition of the dynamics of (3.2.7) when (3.2.11) is not satisfied, we choose the logistic map (3.2.2) and numerically simulate the dynamics of (3.2.7) on a 3-nearest neighbor graph with 10 nodes, see Section 2.1. To determine, if the full 10-dimensional system is chaotic or not, we compute its Lyapunov coefficients. The largest of them, which we denote by $\mu_{\max}$, can be computed by

$$\mu_{\max} = \lim_{N \to \infty} \frac{1}{N} \log \left\| \prod_{n=0}^{N-1} D\mathcal{F}(x^n) \right\|,$$

where $\mathcal{F}$ is the right-hand side of (3.2.7), $\|\cdot\|$ is an arbitrary matrix norm and the product $\prod_{n=0}^{N-1} D\mathcal{F}(x^n)$ has to be understood as a product of matrices in the order $D\mathcal{F}(x^{N-1}) \cdots D\mathcal{F}(x^0)$. If $\mu_{\max} > 0$ we can conclude that the system is chaotic. If on the other hand $\mu_{\max} < 0$, the system does not show chaotic behavior. Furthermore, to measure the synchronization among the nodes, we use the standard deviation. For each time step n, it is given by

$$\zeta_n = \left(\frac{1}{M} \sum_{l=1}^{M} \left(x_l^n - \frac{1}{M} \sum_{j=1}^{M} x_j^n \right)^2 \right)^{\frac{1}{2}}. \tag{3.2.12}$$

A state $x^n = (x_1^n, \dots, x_M^n)$ is in the synchronized manifold $\mathcal{M}$ if and only if $\zeta_n = 0$. Figures 3.3(a)-(b) show a mean of ζ_n over many time steps and $\mu_{\max}$, respectively, for different values of μ and ε. Moreover, the area dashed by red lines in Figure 3.3(a) depict the area in which the stability condition (3.2.11) is valid. As one can see this agrees closely with the parameter region where the mean of the standard deviation is zero. Figures 3.3(c)-(e) show the dynamics for three different parameter value pairs (μ, ε). The parameter pairs for parts (c) and (d)
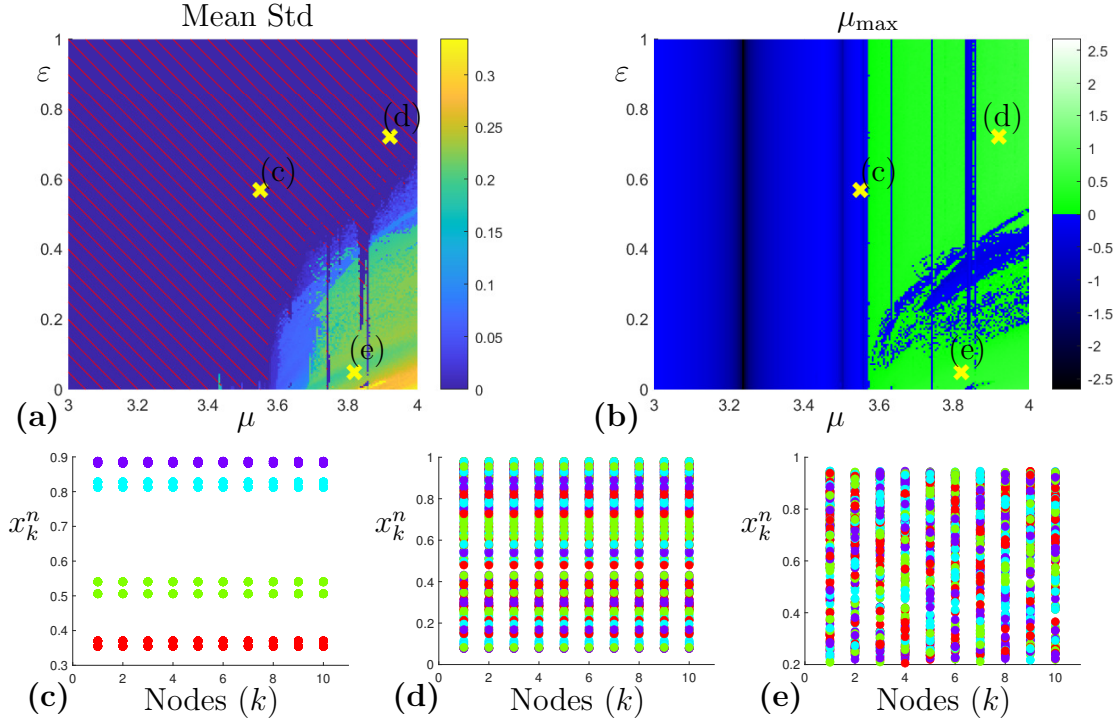
Figure 3.3: Simulation of a coupled map lattice (3.2.7) with the logistic map (3.2.2) on a 3-nearest neighbor graph with 10 nodes, starting from an initial condition that is close to the synchronized manifold $\mathcal{M}$. Part (a) shows the mean $\frac{1}{200} \sum_{n=5001}^{5200} \zeta_n$ of the standard deviations for different time steps. The parameter region dashed by the red lines indicates where the stability condition (3.2.11) is valid. The maximal Lyapunov coefficient is depicted in part (b). The system is chaotic whenever it is positive (green regions) and not chaotic when it is negative (blue regions). Each of the yellow crosses in (a) and (b) represents a pair (μ, ε) for which the dynamics is shown more detailedly in (c), (d) and (e). In particular, the values are $(\mu, \varepsilon) = (3.55, 0.57)$ for (c), $(\mu, \varepsilon) = (3.92, 0.72)$ for (d) and $(\mu, \varepsilon) = (3.82, 0.05)$ for (e). The plotted iterations in these three subfigures are $5000 < n \leq 5200$. The values of x_k^n are alternately plotted in red, cyan, green and purple upon increasing n.

are in a region, where the stability condition (3.2.11) is satisfied, and thus the synchronized manifold $\mathcal{M}$ is locally stable. Thus, when starting the simulation close to this manifold, the dynamics remains near it, as seen in parts (c) and (d) of the figure. While for part (c) the parameters (μ, ε) are in a region where $\mu_{\max} < 0$, for part (d) we have $\mu_{\max} > 0$. Therefore, the dynamics at parameter values in part (d) is chaotic but not chaotic in part (c). In particular, as seen in Figure 3.3(c), the dynamics settles to an eight-periodic orbit. Upon further increasing μ, the dynamics would undergo more period doubling bifurcations before

becoming chaotic. Finally, the parameter values of part (e) are in a region, where the stability condition (3.2.11) is not valid and $\mu_{\max} > 0$. Here, the dynamics is not synchronized and each node shows chaotic behavior, that is in no direct relation to the behavior of other nodes.

3.3   Defining Coupled Hypergraph Maps

Next, we want to extend the pairwise coupling property of CMLs to higher-order coupling. Since the coupling structure of CMLs is based on graphs and graphs can only encode pairwise coupling, we need to replace the graph by a hypergraph to allow for higher-order coupling. The resulting discrete-time dynamical system, that is then based on the hypergraph, is called a coupled hypergraph map (CHM).

However, in order to generalize CMLs to hypergraphs, we need to define a Laplacian on hypergraphs. In general, there are many generalizations of graph Laplacians to hypergraph Laplacians. To obtain them, one selects one or a few properties of the Laplacian on a graph and then derives an operator with similar properties, that is based on a hypergraph. The next two subsections present two possible ways of defining Laplacians on hypergraphs. We then choose one of these ways to define CHMs in Section 3.3.3.

3.3.1   Random Walk Hypergraph Laplacians

One such property of a graph Laplacian is its relation to a random walk on the underlying graph. In fact, given a graph $G = (V, E)$ with $V = \{v_1, \ldots, v_M\}$ and graph Laplacian L, one can define a random walk on the node set of the graph by imposing transition probabilities

$$\mathbb{P}(v_k \rightarrow v_l) := \begin{cases} 0 & \text{if } k = l, \\ -L_{kl} & \text{if } k \neq l, \end{cases} \tag{3.3.1}$$

i.e., the random walker has to move in each time step. Using this definition, it follows that this indeed defines a random walk, because $\mathbb{P}(v_k \rightarrow v_l) \geq 0$ for all k, l and $\sum_l \mathbb{P}(v_k \rightarrow v_l) = 1$.

If one now wants to define random walks on a hypergraph $H = (V, E)$, with node set V and hyperedge set E, one notices that there are many possibilities. In the simplest case, a random walker, that starts at a node $v \in V$ has two options for choosing its next position:

1. Go to a vertex w that is connected to v with a probability that is proportional to the number of hyperedges that v and w have in common, but does not depend on the sizes of such hyperedges.

2. First choose among the hyperedges containing v with equal probability, and when one such hyperedge is selected, go to any of its vertices other than v with equal probability. See for instance [184, 112, 51].

Given the transition probabilities that arise from these random walks, one can then define a hypergraph Laplacian $\mathcal{L}$ by reversing the definition order in (3.3.1), i.e., defining the random walk in terms of the transition probabilities as

$$\mathcal{L}_{kl} := \begin{cases} 1 & \text{if } k = l, \\ -\mathbb{P}(v_k \rightarrow v_l) & \text{if } k \neq l. \end{cases}$$

Importantly, a random walk on a hypergraph, as conceived here is defined in terms of transition probabilities for going from one vertex to another one. But this is a pairwise relation between vertices, and any pairwise relation between vertices can be encoded by an ordinary (possibly weighted) graph. Therefore, dynamical systems, that are based on a coupling by such a hypergraph Laplacian, can be reduced to dynamical systems with an underlying (weighted) graph. In particular, there is no benefit and there are no new effects when generalizing from weighted graphs to hypergraphs. Therefore, we do not take random walk hypergraph Laplacians to define dynamical systems on hypergraphs. Instead, to study effects, that are purely induced by higher-order (hypergraph) interactions, we need another generalization of graph Laplacians to hypergraphs.

3.3.2 Chemical Hypergraph Laplacians

Now, let us look at another possible definition of Laplacians on graphs that can easily be transferred to hypergraphs. Apart from the adjacency matrix, that is typically used to represent a graph $G = (V, E)$, one can also use an incidence matrix. Classically, if the node set is $V = \{v_1, \ldots, v_M\}$ and the edge set is $E = \{e_1, \ldots, e_L\}$, this incidence matrix $\mathcal{I} \in \{0, 1\}^{M \times L}$ is defined as

$$\mathcal{I}_{kl} := \begin{cases} 1 & \text{if } v_k \in e_l, \\ 0 & \text{else.} \end{cases}$$

Consequently, each column consists of exactly two ones and zeros otherwise. Next, we define a matrix $\mathcal{I}_o \in \{-1, 0, 1\}^{M \times L}$ by taking $\mathcal{I}$ and reversing the sign of exactly one of the non-zero entries in each column. As a remark, one can see this as introducing an orientation of the edges. Changing the orientation of an edge corresponds to multiplying the respective column by -1. However, even though there is a choice involved here, the following definitions and results are independent of this choice. Now, one can define a Laplace operator as

$$L = D^{-1}\mathcal{I}_o\mathcal{I}_o^\top, \tag{3.3.2}$$

where $D \in \mathbb{R}^{M \times M}$ is the degree matrix as introduced in Section 3.2.2. It can be shown that this definition of a graph Laplacian does not depend on the orientation of the edges and that it agrees with the definition from Section 3.2.2, see [92, 130]. Since hypergraphs can easily be represented by incidence matrices, the definition (3.3.2) of the graph Laplacian can be transferred to hypergraphs. First, however, we need to have an orientation of hyperedges. Hypergraphs with this property are called chemical hypergraphs [92] as they were introduced to model chemical reactions. In fact, each node of a chemical hypergraph corresponds to a chemical element, a hyperedge represents a chemical reaction and each node in a hyperedge is classified as input, output or both, depending on whether the corresponding element is an educt, product or catalyst of the reaction. The precise definition is given as:

Definition 3.3.1 (cf. [92]). A chemical hypergraph is a pair $\mathcal{H} = (V, H)$ such that V is a non-empty finite set and H is a set such that every $h \in H$ is a pair of elements $h = (V_h, W_h)$ with $V_h, W_h \subset V$. The sets V_h and W_h do not necessarily need to be disjoint and they are called inputs and outputs of the hyperedge, respectively. The order of the tuple (V_h, W_h) is called the orientation of the hyperedge. Changing the orientation of a hyperedge means replacing (V_h, W_h) by (W_h, V_h). Moreover, we still denote $|h| = |V_h \cup W_h|$ for the number of nodes in a hyperedge h.

Even though this definition allows for catalysts, i.e., nodes v with $v \in V_h$ and $v \in W_h$ for some h, we assume in the remainder of this chapter that there are no such nodes. For a chemical hypergraph neither of the two orientations of a hyperedge is preferred over the other. This is also what distinguishes oriented hypergraphs from directed hypergraphs [92].

Such a chemical hypergraph $\mathcal{H} = (V, H)$ with $V = \{v_1, \ldots, v_M\}$ and $H = \{h_1, \ldots, h_L\}$ can be represented by its incidence matrix $\mathcal{I}_o \in \{-1, 0, 1\}^{M \times L}$, given by

$$(\mathcal{I}_o)_{kl} := \begin{cases} -1 & \text{if } v_k \in V_{h_l}, \\ 1 & \text{if } v_k \in W_{h_l}, \\ 0 & \text{else.} \end{cases}$$

Now, the chemical Laplacian $\Delta_{\mathcal{H}}$, which was introduced along with the chemical hypergraphs in [92], is given by

$$\Delta_{\mathcal{H}} := D^{-1} \mathcal{I}_o \mathcal{I}_o^{\top}, \tag{3.3.3}$$

where D is the hyperdegree matrix defined by $D_{kl} = 0$ if $k \neq l$ and $D_{kk} =$

hypdeg(k), with

$$\text{hypdeg}(k) := \sum_{h:v_k \in h} (|h| - 1). \tag{3.3.4}$$

Again, changing the orientation of a hyperedge does not influence the definition (3.3.3) of the chemical Laplacian [92, 130]. Moreover, this definition can be reformulated to

$$(\Delta_{\mathcal{H}} x)_k = \frac{\sum_{h_{\text{in}}:k \text{ input}} \left(\sum_{k' \text{ input of } h_{\text{in}}} x_{k'} - \sum_{l' \text{ output of } h_{\text{in}}} x_{l'} \right)}{\text{hypdeg}(k)}$$
$$- \frac{\sum_{h_{\text{out}}:k \text{ output}} \left(\sum_{\hat{k} \text{ input of } h_{\text{out}}} x_{\hat{k}} - \sum_{\hat{l} \text{ output of } h_{\text{out}}} x_{\hat{l}} \right)}{\text{hypdeg}(k)}, \tag{3.3.5}$$

where $x \in \mathbb{R}^M$ and $k = 1, \ldots, M$. Here, the first sum runs over $\{h_{\text{in}} : k \text{ input}\}$, which is the set of all hyperedges h_{in}, in which the k-th node is classified as an input node. For a given h_{in}, the set $\{k' \text{ input of } h_{\text{in}}\} = V_{h_{\text{in}}}$ consists of all nodes which are an input of h_{in} and the other summations can be explained analogously. The chemical hypergraph Laplacian $\Delta_{\mathcal{H}}$ is a natural generalization of the classical normalized Laplacian for graphs as introduced in Section 3.2.2. Observe that the graph Laplacian from Section 3.2.2 gives the difference between the value x_k and the average of the values x_l, where the l's are the neighbors of the node k. The hypergraph Laplacian has a similar, but more complex, interpretation. In fact, the contribution of x_l in $(\Delta_{\mathcal{H}} x)_k$ depends on how many hyperedges the nodes k and l have in common, as well as on the orientations that k and l have on these hyperedges. For example, if two nodes k and l are contained in exactly two common hyperedges h_1 and h_2, and they have the same orientation in h_1 while they have opposite orientations in h_2, then x_l does not appear in $(\Delta_{\mathcal{H}} x)_k$, because the terms that correspond to h_1 and h_2 cancel each other. In order to give a more practical interpretation, we state a third equivalent definition of the chemical hypergraph Laplacian as follows. Given a node k and an hyperedge h, let

$$o(k, h) := \begin{cases} 1 & \text{if } k \in h \text{ is an input,} \\ -1 & \text{if } k \in h \text{ is an output,} \\ 0 & \text{otherwise.} \end{cases}$$

Then,

$$(\Delta_{\mathcal{H}} x)_k = \frac{1}{\text{hypdeg}(k)} \left(\sum_{h:k \in h} \mathcal{F}(k, h) \right), \tag{3.3.6}$$

where

$$\mathcal{F}(k,h) := \sum_{\substack{k' \in h: \\ \mathrm{o}(k',h)=\mathrm{o}(k,h)}} x_{k'} - \sum_{\substack{l' \in h: \\ \mathrm{o}(l',h)=-\mathrm{o}(k,h)}} x_{l'}. \tag{3.3.7}$$

Hence, if we see x_k as the amount of a given quantity at node k, then $\mathcal{F}(k,h)$ is the difference between the total amount of that quantity at all nodes with the same orientation as k in h, and the total amount of that quantity at all nodes with a different orientation as k in h. As it only matters if the orientation is the same or different than the one of node k, the reformulation (3.3.6), (3.3.7) is best to see that changing the orientation of an edge does not influence the value of $\Delta_{\mathcal{H}}$. The closer $\mathcal{F}(k,h)$ is to zero, the more does the total amount of input balance the total amount of output of h. But the individual input nodes can contribute quite differently, as only their sum enters into the balance, and the same is true for the individual output nodes. This is the source of new phenomena for dynamics on hypergraphs governed by the chemical Laplacian compared to what we can see on ordinary graphs. Therefore, we take this Laplacian to generalize CMLs to hypergraphs.

Finally, let us remark that there is no unique trivial extension of the degree of a vertex from graphs to hypergraphs. In particular, instead of defining the hyperdegree as in (3.3.4), one can also define the hyperdegree of a vertex as the amount of hyperedges, the vertex is contained in. Another possibility is to define it as the amount of nodes that v is directly connected to. However, we choose to work with the definition (3.3.4), as it correctly normalizes the chemical Laplacian (3.3.5). In particular, the hyperdegree (3.3.4) of vertex k corresponds to the amount of summands (except x_k) that appear in the numerator of (3.3.5).

3.3.3   The Definition of a Coupled Hypergraph Map

Analogously to (3.2.7), we now want to couple the dynamics on a hypergraph via $\Delta_{\mathcal{H}}$ for a given map $f_\mu\colon [0,1] \to [0,1]$ at each node. However, the hypergraph Laplacian may fail to satisfy the maximum principle. While it is easy to see that the CML (3.2.7) on graphs leaves the unit cube $[0,1]^M$ invariant if $\varepsilon \in [0,1]$, the nonexistence of a maximum principle for the hypergraph Laplacian causes the unit cube $[0,1]^M$ not to be invariant anymore when directly replacing L_G in (3.2.7) by $\Delta_{\mathcal{H}}$, even if $\varepsilon \in [0,1]$. In particular, due to the normalization with the hyperdegree in (3.3.5) and (3.3.6), values in a process that is analogous to (3.2.7) with L_G replaced by $\Delta_{\mathcal{H}}$, do not directly leave the unit cube $[0,1]^M$ through the upper boundary, but they first become negative before potentially diverging to

infinity. To overcome this problem, we define a periodic triangular function

$$\sigma[x] := \begin{cases} x - 2i & \text{if } x \in [2i, 2i + 1] \\ 2(i + 1) - x & \text{if } x \in [2i + 1, 2i + 2] \end{cases}$$

for $i \in \mathbb{Z}$ and put

$$x^{n+1} = \sigma\left[f_\mu(x^n) - \varepsilon \Delta_\mathcal{H}(f_\mu(x^n))\right], \tag{3.3.8}$$

where the action of σ on a vector has to be understood as the application of σ to each of the elements of the vector. This makes the unit cube $[0, 1]^M$ invariant under the dynamics and does not influence important properties of the dynamics, such as synchronization and chaotic behavior, that we will consider below. The process (3.3.8) is what we call a coupled hypergraph map (CHM).

3.4 Dynamics of Coupled Hypergraph Maps

As for CMLs, the dynamical behavior of CHMs depends on the spectral properties of the coupling operator $\Delta_\mathcal{H}$. The spectrum of chemical Laplacians has similar properties as the spectrum of Laplacians on graphs. In particular, the chemical Laplacian is self-adjoint with respect to the scalar product

$$\langle x, y \rangle = \sum_{l=1}^M x_l y_l \text{ hypdeg}(l).$$

Thus, the eigenfunctions are orthogonal with respect to this scalar product and they form a basis of $\mathbb{R}^M$. Moreover, it can be shown that the eigenvalues are always non-negative [130]. However, the eigenvalue 0 might occur multiple times even when the hypergraph is connected. Further, the constant function is not necessarily an eigenfunction for the eigenvalue 0.

3.4.1 Dynamics on Hyperflowers

An example is the hyperflower $\mathcal{H}_{c,t,\ell}$ defined via three parameters c, t and ℓ, see [6]. It is a generalization of the star graph. There is a set of c central vertices and ℓ sets each consisting of t peripheral vertices. Each set containing peripheral vertices is called a leaf. Central vertices are contained in all hyperedges, but each hyperedge additionally includes only peripheral nodes from one leaf, so in total there are ℓ hyperedges. By convention we classify central vertices as inputs and peripheral nodes as outputs, see Figure 3.4(a). An example for the dynamics of (3.3.8) in Figure 3.4(b) shows chaotic cluster synchronization. In particular, we speak of

chaotic cluster synchronization if x_k^n is constant within each component of the hyperflower, when n is large, but x_k^n and x_l^n are different when k and l are from different components. As seen in Figure 3.4(b), chaotic cluster synchronization emerges from an initial condition that is globally synchronized with a small generic perturbation.

(a)   **(b)**
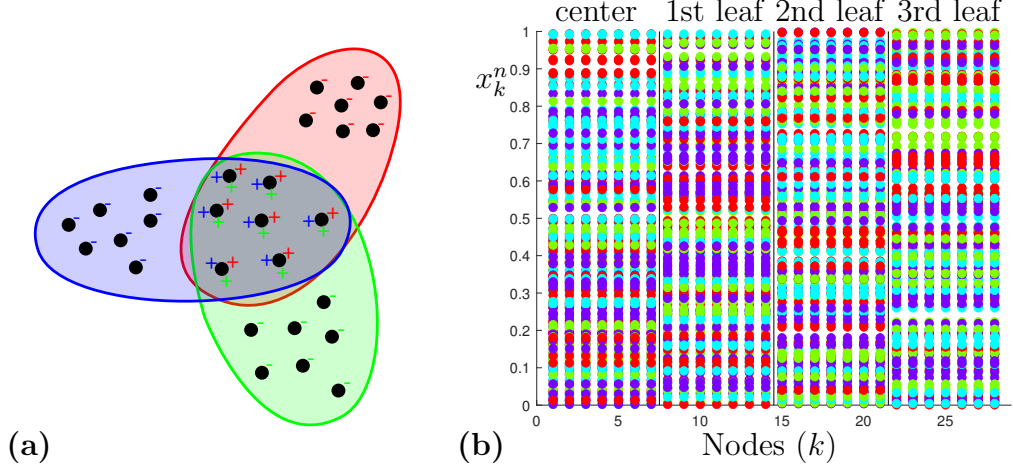
Figure 3.4: Part (a) shows an example of a hyperflower $\mathcal{H}_{c,t,\ell}$ with $c = t = 7$ and $\ell = 3$. Inputs of a hyperedge are represented by a plus sign and outputs by a minus sign. Part (b) shows a numerical integration of (3.3.8) for $f_\mu(x) = \mu x(1-x)$ on the hyperflower depicted in (a) for $\mu = 1.4$ and $\varepsilon = 8$. The initial condition x_k^0 was chosen synchronized over all components with a small generic perturbation. Plotted iterations are $5000 < n \leq 5200$. The values of x_k^n are alternately plotted in red, cyan, green and purple upon increasing n.

To understand how and when such chaotic cluster synchronization can emerge from a globally synchronized solution, we analyze the synchronized solution by studying the eigenvalue/eigenfunction structure of $\Delta_\mathcal{H}$ on a hyperflower. The function which equals -1 on central nodes and $+1$ on peripheral nodes is an eigenfunction for the eigenvalue $(c+t)/(c+t-1)$. Next, we have functions that are $+1$ on one leaf, -1 one on another and 0 elsewhere, corresponding to the second largest eigenvalue $t/(c+t-1)$. There are $\ell - 1$ such linearly independent eigenfunctions. The remaining eigenfunctions have eigenvalue 0. There is one eigenfunction, which attains the value $1/c$ on central nodes and $1/t$ on peripheral nodes. Furthermore, every function that is $+1$ on one node, -1 on another of the same component (the center or a leaf) and 0 elsewhere is an eigenfunction; there are $c - 1 + \ell(t - 1)$ such linearly independent functions. Altogether, we have generated $c + t\ell$ linearly independent eigenfunctions, which is the required number. Note that the synchronized solution only exists if the constant function is

an eigenfunction for the eigenvalue 0. Since this corresponds to $c = t$, we therefore need to require $c = t$. Then, deriving a transverse stability condition for the synchronized solution follows a similar pattern as the analysis in Section 3.2.4, as one just has to replace L_G by $\Delta_{\mathcal{H}}$. In particular, perturbations in the direction of an eigenfunction u_j of $\Delta_{\mathcal{H}}$ decay if the condition (3.2.10) is satisfied, where λ_j is the corresponding eigenvalue.

A necessary condition to retain at least partial synchronization ($x_k = x_l$ for some $k \neq l$) is stability in the direction of eigenfunctions, which are $+1$ on one vertex -1 on another vertex in the same component and 0 everywhere else. As this is an eigenfunction corresponding to the zero eigenvalue, (3.2.10) is equivalent to

$$\mu_0 < 0. \tag{3.4.1}$$

This is in clear contrast to the assumption $\mu_0 > 0$ for CMLs on graphs. In fact, on graphs the instability in direction of a spatially constant perturbation, which was caused by $\mu_0 > 0$, was necessary to have non-stationary dynamics of a synchronized solution. Given the condition $\mu_0 < 0$ on hyperflowers, the constant eigenfunction can no longer generate non-stationary dynamics. However, in contrast to L_G, the hypergraph Laplacian on the hyperflower has further eigenfunctions, which are constant on certain components of the hyperflower. By requiring instability of the synchronized solution with respect to perturbations in direction of these eigenfunctions, we may still hope to retain non-stationary dynamics of partially synchronized solutions. In other words, the eigenfunctions that are constant on each of the components and thus corresponding to positive eigenvalues are taking over the job of the constant eigenfunction corresponding to the eigenvalue 0 on graphs. Instability in direction of the positive eigenvalue $\tilde{\lambda} = (c + t)/(c + t - 1)$, which is responsible for differences between central and peripheral nodes, and $\hat{\lambda} = t/(c + t - 1)$, that governs differences across the leaves, directly translates into the conditions

$$\left| e^{\mu_0}(1 - \varepsilon\tilde{\lambda}) \right| > 1, \tag{3.4.2}$$

$$\left| e^{\mu_0}(1 - \varepsilon\hat{\lambda}) \right| > 1. \tag{3.4.3}$$

Even though one actually needs to find additional stability conditions around a partially synchronized solution, our numerical simulations reveal that the instability conditions around the completely synchronized solution do already provide great insight about the existence of non-stationary partially synchronized solutions. Especially, if f_μ is given by the tent map (3.2.3) this makes sense, as f_μ is piecewise linear and thus stability conditions derived from a linearization of $f_\mu(x)$ are to some extent independent of the particular state x. For the tent map (3.2.3), the Lyapunov coefficient can explicitly be given by $\mu_0 = \ln(\mu/2)$. This allows us to further investigate which pairs (μ, ε) fulfill the (in)stability conditions (3.4.1), (3.4.2)

and (3.4.3). In particular, we marked areas in which these conditions are satis-
fied by diagonal lines seen in Figure 3.5. Further, a numerical integration of the
CHM (3.3.8), starting from a slight perturbation of a completely synchronized
state, yields areas in which one has non-stationary partial synchronization with
different dynamics in each of the components of the underlying hyperflower, see
green regions in Figure 3.5.
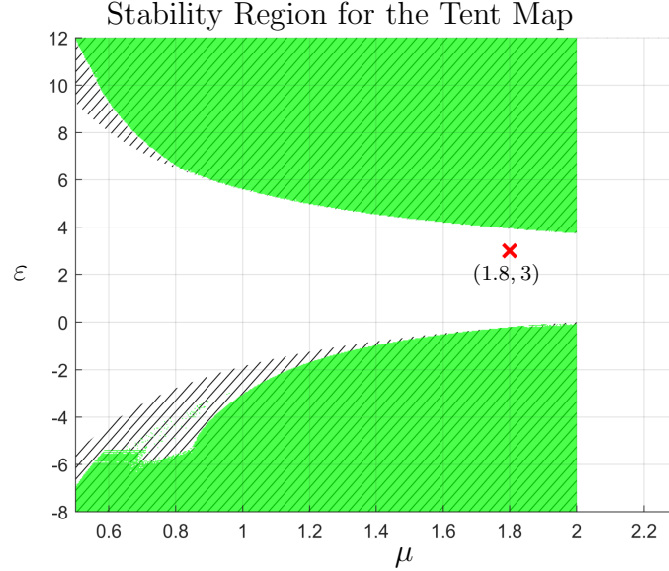
Figure 3.5: Stability region for the tent map. The diagonal lines represent areas
in the (μ, ε) parameter plane for which the (in)stability conditions (3.4.1), (3.4.2)
and (3.4.3) around a completely synchronized solution are satisfied for the tent
map (3.2.3). The green region depicts (μ, ε) values for which numerical simulations
revealed non-stationary partial synchronization with different dynamics on each
component. The parameter pair $(\mu, \varepsilon) = (1.8, 3)$ satisfies (3.4.1) and (3.4.2) but
not (3.4.3), see Figure 3.6.

As can be seen in Figure 3.5, our (in)stability conditions (3.4.1), (3.4.2), (3.4.3)
match the green region pretty closely even though they represent theoretical con-
ditions for stability of the completely synchronized solution and the green region
indicates when a solution is partially synchronized with different dynamics on each
component. In particular, condition (3.4.1), which says $\mu < 2$, applies for both the
green region and the diagonal lines. Overall the green region is contained in the re-
gion depicted by the diagonal lines, which tells us that our conditions (3.4.1),(3.4.2)
and (3.4.3) are here necessary for non-stationary partial synchronization with dif-
ferent dynamics on each component. A closer look at the dynamics for parameter
values in the green region shows chaotic dynamics on each component of the hy-

perflower, as also observed in Figure 3.4(b). In particular, chaotic dynamics can appear for values of $\mu < 2$ for which the one-dimensional iteration (3.2.1) of the tent map (3.2.3) alone exhibits no chaotic dynamics, but here a sufficiently positive or negative coupling induces chaos.

By neglecting the requirement of stability condition (3.4.3), i.e., allowing perturbations that are -1 on one leaf, $+1$ on another leaf and 0 elsewhere to decay, we additionally observe parameter regions, in which all peripheral nodes synchronize among themselves and so do the central nodes but the two groups show different dynamics. For instance $(\mu, \varepsilon) = (1.8, 3)$ satisfies (3.4.1) and (3.4.2) but not (3.4.3). The resulting dynamics can be seen in Figure 3.6.
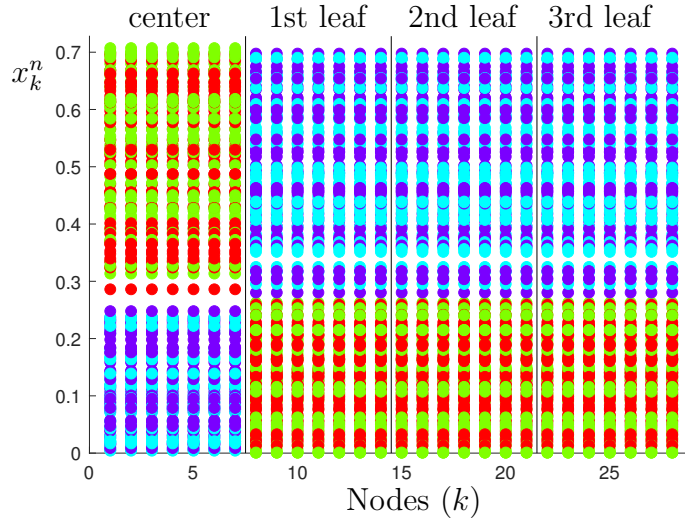
Figure 3.6: Numerical integration of (3.3.8) for $f_\mu(x)$ given by the tent map (3.2.3) on a hyperflower with $c = t = 7$ and $\ell = 3$ for $\mu = 1.8$ and $\varepsilon = 3$. Plotted iterations are $5000 < n \leq 5200$. The values of x_k^n are alternately plotted in red, cyan, green and purple upon increasing n. The parameters μ, ε satisfy the conditions (3.4.1) and (3.4.2) but not (3.4.3).

Even though our analytical derivations of stability conditions require assumptions about the hyperflower, numerical simulations can of course be performed for the cases not covered by our analytical derivations. Specifically, we consider simulations on a hyperflower with $c = 10$, $\ell = 5$ and $t = 3$, which are parameters for which a globally synchronized solution does not exist. For a given parameter pair (μ, ε), we numerically infer synchronization of the central nodes if the standard deviation ζ_n over $k = 1, \ldots, c$ of x_k^n, see (3.2.12), drops below a certain threshold $(\approx 10^{-5})$ as $n \to \infty$. Similarly, we infer chaos in the center of the hyperflower if the leading Lyapunov coefficient is positive on the central nodes. In the same way we deduce synchronization and chaotic behavior of nodes in the first leaf of the

hyperflower. Based on those four criteria this allows us to classify the dynamical behavior for given parameter values and initial conditions. In particular, we say that the dynamics shows doubly synchronized chaos if both of the leading Lyapunov coefficients for the two clusters are positive and the values of x^n synchronize within the two clusters (but not necessarily across the clusters). Now, we conduct numerical simulations for different parameter values of μ and ε but with the same initial condition for each simulation and investigate for each parameter pair (μ, ε) the occurrence of doubly synchronized chaos. The yellow regions in Figure 3.7 depict such areas, whereas there is no doubly synchronized chaos in the blue region. On hyperflowers, we have detected a variety of other patterns, including steady and periodic synchronization patters, as well as chaotic cluster patterns, where a single cluster chaotically forces other clusters.
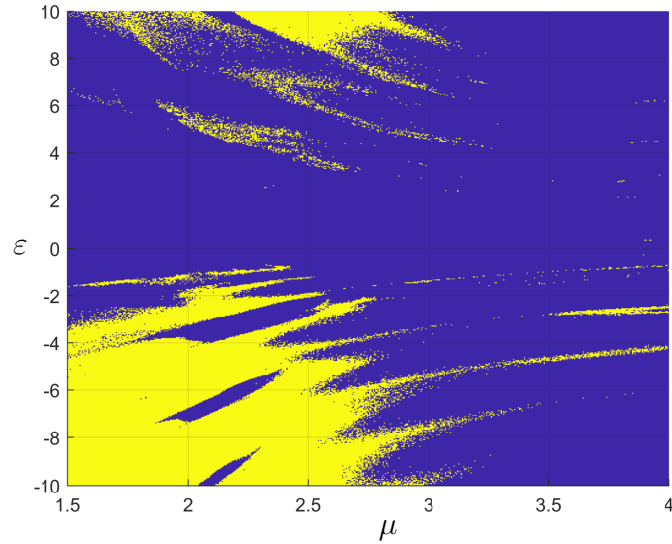
Figure 3.7: Numerical simulations of (3.3.8) for $f_\mu(x) = \mu x(1-x)$ on a hyperflower with $c = 10$, $\ell = 5$ and $t = 3$ reveal cluster synchronization of chaos in yellow regions. Doubly synchronized chaos occurs for all parameter values (μ, ε) in the yellow regions. This is a case that is not covered by our analytical derivations. The yellow regions, do not seem to be regular shapes as the regions shown in Figure 3.5. They rather seem to resemble irregular and somewhat fractal shapes, that are difficult to analyze analytically. This shows that the assumption $c = t$ and taking f_μ to be the tent map (3.2.3) was indeed helpful to derive analytical conditions.

3.4.2 Dynamics on Other Types of Hypergraphs

The analysis of the dynamics of hyperflowers that was conducted in the last section, can, of course, also be performed on other types of hypergraphs. Since this exactly follows the lines of Section 3.4.1, we will not present it here. Instead, we present a few examples of simulations on other types of hypergraphs.

First, we consider a CHM on hyperferns, which is a class of hypergraphs defined in [7], see Figure 3.8(a). They consist of c central nodes, which are connected by a hyperedge, in which all nodes are classified as inputs. Moreover, each central node is connected to two sets (leaves) of peripheral nodes by one hyperedge each and all of these leaves consist of t nodes. By convention, nodes of these leaves are outputs and the central node that they are connected to is an input of the connecting hyperedge. In total, there are $n = c(2t+1)$ nodes and $2c+1$ hyperedges. On these hypergraphs, we have detected parameter regions in which another interesting phenomenon occurs, see Figure 3.8(b). Here, we consider a hyperfern with $c = 3$ and $t = 2$, where the nodes are labeled such that the first three nodes are the central nodes. Nodes with the numbers 4 and 5 form one leaf that is connected to the first node in the center. Then, the next two nodes form another leaf, that is connected to the first central node, too. The next four nodes form two leaves, both connected to the second central node. Finally, the last four nodes create two leaves, which are both connected to the last central node. Interestingly, when choosing parameter values as in Figure 3.8(b), starting from a synchronized initial condition with slight perturbation, the dynamics ends up in a region where all nodes are chaotic, the central nodes are desynchronized, the leaves are synchronized within itself but not among each other. In particular, there seem to exist two trapping intervals in which x_k^n can end up in, when k is a peripheral node. In particular, $0 \leq x_k^n \lesssim 0.25$ for some peripheral nodes k and $0.2 \lesssim x_k^n \lesssim 0.65$ for other peripheral nodes k. While the synchronization of leaves always causes two peripheral nodes that are in a same leaf to end up in the same trapping interval, the situation is reversed if they are not in the leaf but still connected to the same central node. In fact, then they always end up in different trapping intervals. Consequently, by their indirect connection via a central node, two peripheral nodes seem to repel each other. Thus, this phenomenon combines the concept of chaotic cluster synchronization with desynchronization or repulsion across clusters.

Next, we consider lattice hypergraphs [7], which do not consist of central and peripheral nodes. Rather, each node is contained in two hyperedges and the number of nodes of a lattice hypergraph is determined by two parameters $a, b \in \mathbb{N}$. In fact, one can imagine a lattice hypergraph by arranging $n = ab$ nodes in a grid of a rows and b columns. Then, there are two more parameters $\alpha \in \mathbb{N}$ and $\beta \in \mathbb{N}$ with $1 \leq \alpha \leq a$ and $1 \leq \beta \leq b$, that determine the hyperedges of a lattice hypergraph. In fact, each row is connected by a hyperedge such that the first α nodes are inputs
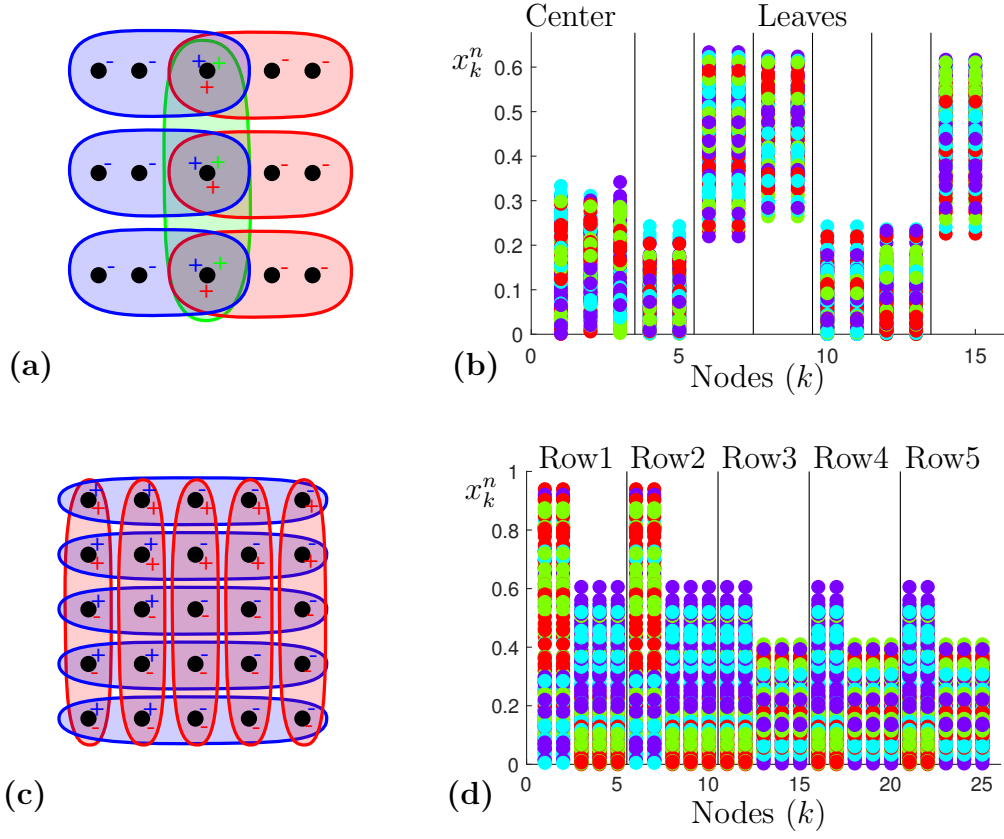
Figure 3.8: Simulation on other types of hypergraphs. Part (a) depicts a hyperfern with $c = 3$ and $t = 2$. Part (b) shows a simulation result on the hyperfern from part (a). Here, f_μ is given by the tent map (3.2.3) and the parameter values are $\mu = 0.82$ and $\varepsilon = 4.4$. Part (c) illustrates a lattice hypergraph with $a = b = 5$ and $\alpha = \beta = 2$. Finally, part (d) shows a simulation on this lattice hypergraph when $\mu = 1.4$, $\varepsilon = 3.8$ and f_μ is given by the tent map (3.2.3). The values of x_k^n in parts (b) and (d) are alternately plotted in red, cyan, green and purple upon increasing n and the plotted iterations are $5000 < n \leq 5200$.

and the remaining $a - \alpha$ nodes are outputs. Similarly, each column is grouped by a hyperedge, in which the first β nodes are inputs and the last $b - \beta$ nodes are outputs, see Figure 3.8(c). In total there are $a + b$ hyperedges. For particular parameter choices we observed the emergence of node clusters that synchronize even though the node cluster might not be connected via an edge. In particular, when $a = b = 5$ and $\alpha = \beta = 2$, as in Figure 3.8(c), the nodes of the hypergraph can be split into four main groups. The first group consists of nodes which are inputs in each hyperedge, i.e., $k = 1, 2, 6, 7$. We call this group a symmetric group.

Then, there is a group of nodes, which are inputs in the hyperedges connecting the rows but outputs in hyperedges encompassing one row. The node labels of this group are $k = 3, 4, 5, 8, 9, 10$ and we call this an anti-symmetric group. There is another symmetric and another anti-symmetric group, in which the roles of inputs and outputs are reversed. As one can see in Figure 3.8(c), the two anti-symmetric groups are not connected via any hyperedge. Yet, as seen in Figure 3.8(d), their nodes can still synchronize. Moreover, the two symmetric groups are synchronized within themselves but not among them.

Furthermore, we have considered less symmetric hypergraphs, e.g., the cyclic hypergraphs $\mathcal{Z}_{e,\ell,m,s}$, which is a class defined by four parameters e, ℓ, m, s. One can view $\mathcal{Z}_{e,\ell,m,s}$ as a set of $M = es$ nodes, which are arranged in a circle, see Figure 3.9(a). There are e edges each encompassing ℓ neighbors. These edges are distributed uniformly around the circle such that if one edge starts at a node k on the circle, the next edge starts at node that is s nodes away from k. If one goes around the circle, the first m nodes of each edge are specified as input nodes, whereas the remaining ones are output nodes. While for some parameters, this class of hypergraphs has symmetries under permutation of nodes, it does not for others. If we consider, for example, the cyclic hypergraph with $e = 10$ edges, $\ell = 6$, $m = 1$ and $s = 2$, there is no symmetric subgroup that leaves the hypergraph Laplace operator $\Delta_{\mathcal{H}}$ invariant. Permuting two nodes would either cause edges to be spanned over non-neighboring nodes or edges not to start with nodes specified as input, both contradicting with a possible invariance of the hypergraph Laplacian. However, a numerical simulation starting from a completely synchronized initial condition with small perturbation, see Figure 3.9(b), shows that both even and odd nodes form a cluster within which the dynamics synchronizes and shows chaotic behavior but there is no synchronization across the two clusters.

3.5 Summary

Although CMLs have been a prototypical dynamical system studied on usual graphs for quite some time, so far no natural generalization to hypergraphs has been available. Here, we provided this extension, which has been triggered by the requirement to model physical processes beyond pairwise coupling. Classical CMLs show highly complex patterns due to the intertwining of Laplacian coupling and nonlinear iterated maps. Replacing the regular Laplacian by a hypergraph Laplacian led to new challenges. We used linearized stability analysis for synchronized states in combination with hypergraph spectral theory, and numerical methods, to detect robust regions of chaotic cluster synchronization for CHMs. Chaotic cluster synchronization occurs large regions in the parameter space, which is made up of the coupling strength and the main bifurcation parameter in the unimodal map
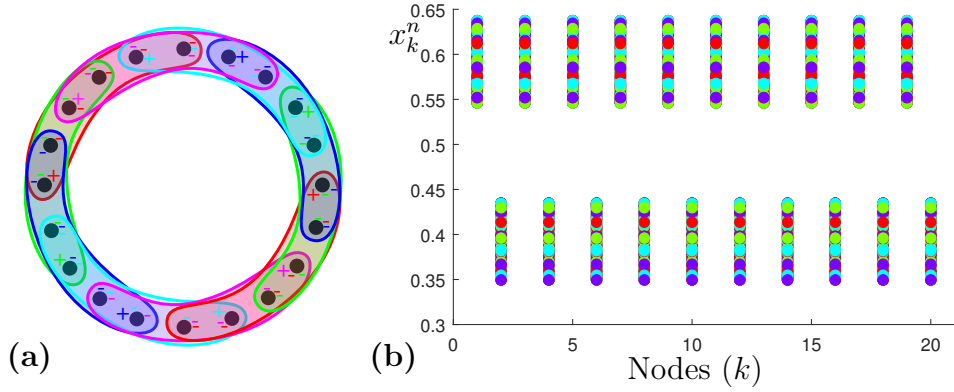
Figure 3.9: A cyclic hypergraph and a numerical integration of a CHM on this hypergraph. Part (a) depicts a cyclic hypergraph with $e = 10$, $\ell = 6$, $m = 1$ and $s = 2$. Part (b) shows the numerical integration of (3.3.8) with f_μ being the logistic map (3.2.2) and parameter values $\mu = 2.868$ and $\varepsilon = 6.03$ on the cyclic hypergraph depicted in part (a). Plotted iterations are $5000 < n \leq 5200$. The values of x_k^n are alternately plotted in red, cyan, green and purple upon increasing n. This is an example of chaotic cluster synchronization on a hypergraph for which the nodes in a cluster (here, even nodes and odd nodes), within which we observe synchronization, cannot be permuted such that the permutation of the nodes represents a hypergraph automorphism.

at each node. We found key differences between Laplacian and hypergraph Laplacian coupling and also detected various other classes of periodic and quasi-periodic patterns. The results show the high complexity of CHMs.

Chapter 4

Higher-Order Phase Reductions for Oscillators with Non-circular Limit Cycles

Phase reductions are a technique to derive phase oscillator models, i.e., systems of ODEs with $\mathbb{T}^M$ as the phase space, from coupled oscillator systems that are posed in a higher-dimensional phase space. These phase oscillator models include, but are not limited to, the Kuramoto model (1.1.1), a pairwise phase oscillator model (2.2.2) and higher-order variants such as (2.4.1). The next section introduces phase reductions and the organization of this chapter.

This chapter is based on the publication [20], which is joint work with Christian Bick and Christian Kuehn. In particular, the technical parts are taken from this publication of which I am the main author.

Data Availability This chapter is accompanied by software. In particular, the MATLAB code that generates the figures and the MATHEMATICA code that computes the phase reductions is publicly available on a GitHub repository [33] that can be accessed via
https://github.com/tobiasboehle/HigherOrderPhaseReductions.

4.1 An Introduction to Phase Reductions

Phase reductions are a powerful tool from nonlinear analysis that allow to study coupled limit-cycle oscillators just in terms of their phases [142, 128, 133]. Consider

for example the continuous-time coupled particle system

$$\dot{x}_k = f(x_k) + \frac{K}{M} \sum_{j=1}^{M} a_{kj} \, g(x_j, x_k), \quad k = 1, \ldots, M, \qquad (4.1.1)$$

where $x_k \in \mathbb{R}^d$ is the state of particle $k = 1, \ldots, M$ in a d-dimensional state space. Further, $K \in \mathbb{R}$ is the coupling strength, $(a_{kj})_{k,j=1,\ldots,M}$ are the coefficients of an adjacency matrix of a graph, that describes the coupling structure, $g \colon \mathbb{R}^d \times \mathbb{R}^d \to \mathbb{R}^d$ is a smooth coupling function and $f \colon \mathbb{R}^d \to \mathbb{R}^d$ is a smooth vector field that describes the intrinsic dynamics of each particle. Moreover, assume that the system $\dot{x} = f(x)$, i.e., a single uncoupled particle, has a stable hyperbolic limit cycle $\gamma \colon [0, T] \to \mathbb{R}^d$ with period T such that $\gamma(0) = \gamma(T)$. This assumption is satisfied by many real-world dynamical systems. Examples range from biological systems such as pacemaking cells in a healthy human heart, regularly spiking neurons or flashing fireflies to large scale technological systems, such as power grids, or the periodic motion of planets [144, 44, 75]. Each of these systems consists of coupled particles that have stable periodic orbits. In any case, as this limit cycle is a closed one-dimensional curve in $\mathbb{R}^d$, which is homeomorphic to $\mathbb{T} := \mathbb{R}/(2\pi\mathbb{Z})$, one can represent the position of the particle on the limit cycle by just one element (or phase) $\phi \in \mathbb{T}$. In particular, one can describe $x \in \gamma([0, T])$ by $\phi = \frac{2\pi}{T}\gamma^{-1}(x)$. In this case, the evolution of a particle on the limit cycle can be described by $\dot{\phi} = \frac{2\pi}{T} =: \omega$. Thus, the limiting dynamics of a single limit-cycle oscillator takes place on $\mathbb{T}$. As a consequence, the dynamics of the particle system (4.1.1) without coupling, i.e., $K = 0$, settles to an invariant torus $\mathbb{T}^M$. If one uses the same representation $\phi_k = \frac{2\pi}{T}\gamma^{-1}(x_k)$ for each particle on the limit cycle in terms of a phase ϕ_k, the dynamics on this invariant torus is just given by $\dot{\phi}_k = \omega$ for $k = 1, \ldots, M$. As the limit cycle γ is hyperbolic, the invariant torus persists for small coupling strengths $K \neq 0$. In this case, the dynamics on the torus can be described by a phase oscillator model of the form

$$\dot{\phi}_k = \omega + \mathcal{G}_k(K, \phi), \quad k = 1, \ldots, M, \qquad (4.1.2)$$

with $\phi = (\phi_1, \ldots, \phi_M)^\top \in \mathbb{T}^M$ and interaction functions $\mathcal{G}_k \colon (-\varepsilon_0, \varepsilon_0) \times \mathbb{T}^M \to \mathbb{R}$ for small enough $\varepsilon_0 > 0$. Note that these interaction functions satisfy $\mathcal{G}_k(0, \phi) = 0$. The process of transitioning from (4.1.1) to (4.1.2) is called phase reduction. Since the explicit derivation of the functions $\mathcal{G}_k$ is hard, one typically approximates them as expansions in K. Approximations of (4.1.2) that rely on first-order expansions of $\mathcal{G}_k$ in K are called first-order phase reductions. Similarly, if one includes terms of second order in K, the resulting system is called a second-order phase reduction. Because one usually only considers a first-order phase reduction, everything beyond first order is also referred to as a higher-order phase reduction. For example, (2.2.2)

might be a first-order phase reduction while (2.4.1) with $K_2 := K$ and $K_3 := K^2$ might be a higher-order phase reduction.

If the coupling is weak, i.e., $|K|$ is small enough, and the first-order phase reduction is non-degenerate, these first-order phase reductions provide a good approximation of the full/unreduced system and they have found application to elucidate collective dynamics, such as synchronization, for example in neuroscience [9]. However, only considering first-order phase reductions, can be insufficient to describe the dynamics of the full/unreduced system when the first-order truncation undergoes a bifurcation or when the coupling is stronger.

To accurately describe the dynamics of the full system in these cases, one has to consider higher-order phase reductions. Recently, progress has been made to compute such phase reductions: Explicit computations show how nonpairwise phase interactions enter the phase-reduced equations once one goes to second or higher orders [114, 70]. However, in general, computing higher-order phase reductions is not straightforward and the focus has been on simple systems. This includes, for example, the system (4.1.1), when f denotes the right-hand side of simple oscillator model, such as a Stuart–Landau oscillator. In particular, the authors of [114] consider coupled Stuart–Landau oscillators, which is special in the sense that these oscillators have a rotational symmetry such that the limit cycle is the unit circle. Their computations make explicit use of this symmetry and the resulting phase equations reflect the symmetry properties. However, such an assumption of rotational symmetry is rarely satisfied for general oscillator systems.

In this chapter, we derive higher-order phase reductions for systems in which the limit cycle of the individual oscillators is non-circular. In particular, we consider networks of coupled Stuart–Landau oscillators on a graph that are subject to a small perturbation. This perturbation deforms the circular limit cycle of regular (unperturbed) Stuart–Landau oscillators into one that has a phase-dependent amplitude. Consequently, our perturbation also breaks the rotational symmetry of the system. We derive phase reductions as expansion in terms of both the coupling strength between oscillators as well as in the parameter that controls the size of the limit cycle deformation. We then analyze how these higher-order interaction terms affect the stability of full synchrony—all oscillators are at the same state— and the splay configuration, in which the phases of the oscillators are uniformly spread out.

Our approach not only allows to compute phase reductions for all-to-all coupled networks, but also for coupled oscillators on arbitrary graphs. It turns out that the resulting second-order terms in these phase reductions resemble the non-pairwise terms in (2.4.1) that include interactions which depend on three oscillator phases. In particular, we can explicitly compute corresponding coefficients $(b_{kli})_{k,l,i=1,\dots,M}$ and interaction functions such that these two terms match. By interpreting these

coefficients as entries of a 3-tensor that define a hypergraph, this yields a tool to construct phase dynamics on a family of hypergraphs, which is a meaningful approximation of nonlinearly coupled oscillators. This family is parameterized in terms of the underlying coupling graph as well as the system parameters. The result is especially useful as so far, many phase oscillator networks with higher-order interactions that have been considered were ad-hoc, for example, by generalizing the Kuramoto model to hypergraphs (see, e.g., [160, 22]). By contrast, our results provide a natural family of hypergraphs together with phase interaction functions that describe the dynamics of an (unreduced) nonlinear oscillator network.

The rest of this chapter is organized as follows: In Section 4.2 we recall the main points of a previous work [114] considering higher-order phase reductions for globally coupled Stuart–Landau oscillators. Then, in Section 4.3 we study a system whose limit cycle can be obtained from perturbing the circular limit cycle from a Stuart–Landau oscillator. We derive phase reductions as an expansion up to second order in the coupling strength and the parameter that controls the deformation of the limit cycle. Next, in Section 4.4 we numerically analyze how the deformation of the limit cycle affects the stability of synchronized and splay states. We investigate how accurately first- and second-order phase reductions reproduce these stability properties. Finally, Section 4.6 contains a short summary.

4.2   Phase Reductions for Stuart–Landau Oscillators

In this section, we recall the main aspects of how to derive higher-order phase reductions for coupled Stuart–Landau oscillators from [114]. We highlight the main assumptions that are made to derive these reductions.

First, let us consider a single complex Stuart–Landau oscillator with state $A = A(t) \in \mathbb{C}$, that evolves according to

$$\dot{A} = A - (1 + \mathrm{i}c_2) \left| A \right|^2 A, \tag{4.2.1}$$

where $c_2 \in \mathbb{R}$ is a parameter. The right-hand side of (4.2.1) is equivariant with respect to the continuous group $\mathbb{T}$, which acts on $\mathbb{C}$ by shifting an oscillator by a given phase. Due to this symmetry, it makes sense to introduce polar coordinates $A = re^{\mathrm{i}\phi}$ with $r \geq 0$ and $\phi \in \mathbb{T}$. In these new coordinates, the evolution of a Stuart–Landau oscillator (4.2.1) is given by

$$\dot{r} = r - r^3,$$
$$\dot{\phi} = -c_2 r^2$$

and one can see that the system has a stable limit cycle at $r = 1$. Moreover, on this limit cycle, the dynamics can be described by just the phase ϕ. In fact, on the limit cycle, the phase ϕ increases with constant speed $-c_2$, such that $\phi(t) = \phi(0) - c_2 t$. To understand the dynamics off the limit cycle, we note that every point in the basin of attraction of this attractive limit cycle has an asymptotic phase, which is the phase of an initial condition of a trajectory on the limit cycle that the point converges to. The set of points with the same asymptotic phase are called isochrons [82, 111]. To define them, we introduce the notation $\Phi^t A_0$ for the solution of (4.2.1) with $A(0) = A_0$ at time t. If A_0 is on the limit cycle, i.e., $|A_0| = 1$, and $\phi(t) = \theta - c_2 t$ then

$$\mathcal{I}(\theta) := \{\hat{A}_0 \in \mathbb{C} : \lim_{t \to \infty} \Phi^t \hat{A}_0 - e^{i(\theta - c_2 t)} = 0\}$$

is the isochron with asymptotic phase θ. Upon variation of θ, the isochrons foliate the basin of attraction of the limit cycle. For (4.2.1), they can explicitly be calculated [114] to be

$$\mathcal{I}(\theta) = \{A = re^{i\phi} : \theta = \phi - c_2 \ln r\}.$$

As one can see from this formula these isochrons are symmetric in the sense that one isochron can be obtained from another by shifting it by a constant phase, see Figure 4.1. This property also follows directly from the $\mathbb{T}$ symmetry of (4.2.1). An important observation about this isochrons is that $\dot{\theta} = \dot{\phi} - c_2 \dot{r}/r = -c_2$. Consequently, in new coordinates (r, θ), a Stuart–Landau oscillator can be described by

$$\dot{r} = r - r^3,$$
$$\dot{\theta} = -c_2,$$

which makes r and θ independent. This will later be helpful when deriving phase equations.

Having studied a single Stuart–Landau oscillator, we now consider $M \in \mathbb{N}$ coupled Stuart–Landau oscillators described by complex variables A_k, $k = 1, \ldots, M$. When the coupling is as in [114], they satisfy

$$\dot{A}_k = A_k - (1 + ic_2)|A_k|^2 A_k + \varepsilon(1 + ic_1)(\bar{A} - A_k), \quad k = 1, \ldots, M. \qquad (4.2.2)$$

Here, c_1, c_2 are two real parameters, $\varepsilon \geq 0$ relates to the coupling strength and $\bar{A} = \frac{1}{M}\sum_{j=1}^{M} A_j$. Now, one changes to polar coordinates $A_k = r_k e^{i\phi_k}$, with $r_k \geq 0$ and $\phi_k \in \mathbb{T}$. After conducting the additional nonlinear transformation $\theta = \phi - c_2 \ln(r)$ to straighten the isochrons, the authors of [114] arrive at the system

$$\dot{r}_k = f(r_k) + \varepsilon g_k(r, \theta), \qquad (4.2.3a)$$
$$\dot{\theta}_k = \omega + \varepsilon h_k(r, \theta), \qquad (4.2.3b)$$
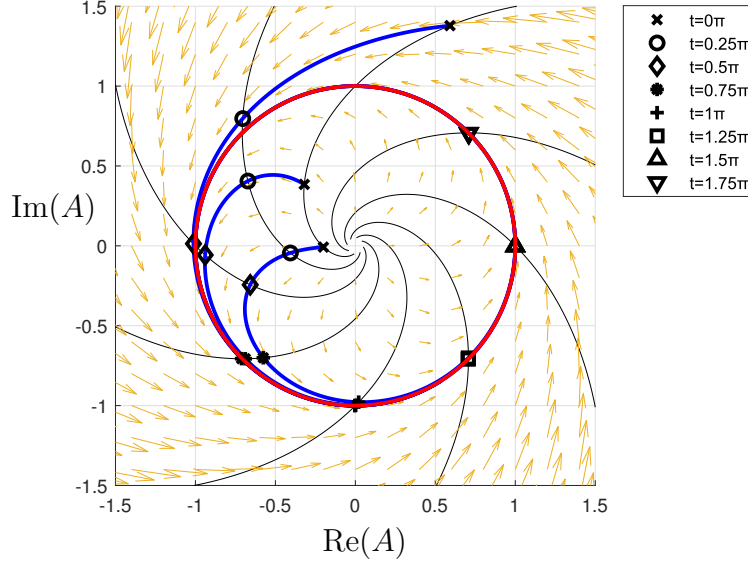
Figure 4.1: Isochrons of a Stuart–Landau oscillator (4.2.1). The limit cylcle of the Stuart–Landau oscillator is shown by the thick red line and the black lines depict eight different isochrons $\mathcal{I}(i\pi/4)$ for $i = 1, \ldots, 8$, respectively. Moreover, the blue lines represent the orbits of three initial conditions. Note, that at $t = 0$, these trajectories are on the same isochron. Thus, the trajectories are also on the same isochron if they are evaluated at a later time. In particular, the evaluation of these three trajectories at times $t = i\pi/4$ for $i = 1, \ldots, 8$ is depicted by different symbols. Observe that symbols of the same type are on the same isochron. Parameter values: $c_2 = -1$.

where $\omega \in \mathbb{R}$ is a parameter that depends on c_2, $f(r) = r(1 - r^2)$ and the functions g_k and h_k are given by

$$
g_k(r, \theta) = -r_k + \frac{1}{M} \sum_{j=1}^{M} \left\{ r_j \left[\cos\left(\theta_j - \theta_k + c_2 \ln \frac{r_j}{r_k} \right) \right.\right.
$$

$$
\left.\left. - c_1 \sin\left(\theta_j - \theta_k + c_2 \ln \frac{r_j}{r_k} \right) \right] \right\},
$$

$$
h_k(r, \theta) = c_2 - c_1 + \frac{1}{Mr_k} \sum_{j=1}^{M} \left\{ r_j \left[(c_1 - c_2) \cos\left(\theta_j - \theta_k + c_2 \ln \frac{r_j}{r_k} \right) \right.\right.
$$

$$
\left.\left. + (1 + c_1 c_2) \sin\left(\theta_j - \theta_k + c_2 \ln \frac{r_j}{r_k} \right) \right] \right\}.
$$

Changing the coordinate system from (r, ϕ) to (r, θ) is necessary to make (4.2.3b) independent of r when $\varepsilon = 0$, as we see later. The coupling in (4.2.2) respects the $\mathbb{T}$ symmetry of a Stuart–Landau oscillator such that (4.2.2) again possesses a $\mathbb{T}$ symmetry group that acts on $\mathbb{C}^M$ by shifting all oscillators $A_1, \ldots, A_M$ by the same phase. Since the transformation that straightens the isochrons does not break this symmetry, the system (4.2.3) inherits the same symmetry group. This fact can also be observed by directly looking at the structure of the functions g_k, h_k and f. Since they only depend on phase differences, they are invariant when all oscillators are shifted by the same phase. Therefore, we can change into a co-rotating coordinate frame

$$\theta \mapsto \theta + \omega t, \tag{4.2.4}$$

and thereby set $\omega = 0$ without loss of generality.

Next, we derive first- and second-order phase reductions for the system (4.2.3). In absence of the coupling, i.e., $\varepsilon = 0$, each oscillator in (4.2.2) and (4.2.3) has a stable limit cycle at $|A_k| = 1$ or $r_k = 1$, respectively. Therefore, the limiting dynamics of the whole system takes place on the M-dimensional torus that is described by $r_k \equiv 1$ for all $k = 1, \ldots, M$. When slightly varying ε this torus persists but it gets perturbed. The radii of this invariant torus are then functions of the phases. In fact, they can be expanded in terms of ε such that

$$r_k(\theta) = r_k^{(0)}(\theta) + \varepsilon r_k^{(1)}(\theta) + \varepsilon^2 r^{(2)}(\theta) + \mathcal{O}(\varepsilon^3), \tag{4.2.5}$$

with $r_k^{(0)} \equiv 1$, see [114]. Inserting the ansatz (4.2.5) into (4.2.3b) as done in [114] yields

$$\begin{aligned}
\dot{\theta}_k &= \varepsilon h_k(r(\theta), \theta) \\
&= \varepsilon h_k(r^{(0)}(\theta) + \varepsilon r^{(1)}(\theta) + \mathcal{O}(\varepsilon^2), \theta) \\
&= \varepsilon h_k(r^{(0)}(\theta), \theta) + \varepsilon^2 \nabla_r h_k(r^{(0)}(\theta), \theta) \cdot r^{(1)}(\theta) + \mathcal{O}(\varepsilon^3), \tag{4.2.6}
\end{aligned}$$

since $\omega = 0$. By truncating terms of order $\mathcal{O}(\varepsilon^2)$, one can obtain a first-order phase reduction. In particular, a first-order phase reduction is given by

$$\dot{\theta}_k = \varepsilon h_k(r^{(0)}(\theta), \theta) = \varepsilon h_k(\mathbb{1}, \theta)$$

$$= \varepsilon(c_2 - c_1) + \varepsilon \frac{1}{M} \sum_{j=1}^{M} \Big((c_1 - c_2) \cos(\theta_j - \theta_k) + (1 + c_1 c_2) \sin(\theta_j - \theta_k) \Big),$$

where $\mathbb{1} = (1, \ldots, 1)^\top \in \mathbb{R}^M$. This shows the importance of using isochrons for conducting phase reductions. As explained, if one did not change into the coordinates (r, θ), (4.2.3b) would depend on r in absence of the coupling, i.e.,

when $\varepsilon = 0$. Such a dependence would then cause the existence of ε^0 terms in (4.2.6) that depend on r. Even after truncating $\mathcal{O}(\varepsilon^2)$ terms, the right-hand side of (4.2.6) would still be dependent on r. Consequently, one cannot obtain a closed system for just the phases in this way.

To derive a second-order phase reduction one keeps the ε^2 terms in (4.2.6) and truncates only the $\mathcal{O}(\varepsilon^3)$ terms. These second-order terms are made up of $\nabla_r h_k(\mathbb{1}, \theta)$ and $r^{(1)}(\theta)$. An expression for $\nabla_r h_k$ can be derived by direct differentiation of h_k. An expression for $r^{(1)}(\theta)$ can be obtained by inserting (4.2.5) into (4.2.3a) and collecting terms of order ε, see [114]. One then ends up with

$$\dot{r}_k^{(1)} = f'(r_k^{(0)})r_k^{(1)} + g_k(r^{(0)}, \theta). \tag{4.2.7}$$

Moreover, by the chain rule, one has

$$\begin{aligned}\dot{r}_k = (\nabla_\theta r_k) \cdot \dot{\theta} &= (\nabla_\theta r_k) \cdot (\omega \mathbb{1} + \varepsilon h(r, \theta)) \\ &= \left(\nabla_\theta r_k^{(0)} + \varepsilon \nabla_\theta r_k^{(1)} + \mathcal{O}(\varepsilon^2)\right) \cdot \left(\omega \mathbb{1} + \varepsilon h(r^{(0)} + \mathcal{O}(\varepsilon), \theta)\right),\end{aligned}$$

for the dynamics on the invariant torus. Now, it is crucial that ω can be set to 0, because then collecting terms of order ε in this equation yields

$$\dot{r}_k^{(1)} = (\nabla_\theta r_k^{(0)}) \cdot h(r^{(0)}, \theta). \tag{4.2.8}$$

Because $\nabla_\theta r_k^{(0)} = \nabla_\theta \mathbb{1} = 0$, combining (4.2.7) and (4.2.8), the authors of [114] arrive at

$$r_k^{(1)} = -\frac{g_k(r^{(0)}, \theta)}{f'(r^{(0)})} = \frac{1}{2}g_k(r^{(0)}, \theta).$$

Substituting that into (4.2.6) and truncating $\mathcal{O}(\varepsilon^3)$ terms yields the second-order phase reduction

$$\dot{\theta}_k = \varepsilon h_k(\mathbb{1}, \theta) + \frac{1}{2}\varepsilon^2 \nabla_r h_k(\mathbb{1}, \theta) \cdot g(\mathbb{1}, \theta).$$

An explicit calculation of the second-order terms yields

$$\begin{aligned}&\nabla_r h_k(\mathbb{1}, \theta) \cdot g(\mathbb{1}, \theta) \\ &= \frac{1 + c_2^2}{2M^2} \sum_{l=1}^{M} \sum_{j=1}^{M} \Big(-(1 + c_1^2)\sin(\theta_j + \theta_k - 2\theta_l) + (c_1^2 - 1)\sin(\theta_j - 2\theta_k + \theta_l) \\ &\qquad\qquad + 2c_1\cos(\theta_j - \theta_k) - 2c_1\cos(\theta_j - 2\theta_k + \theta_l) - (c_1^2 - 1)\sin(\theta_j - \theta_k)\Big).\end{aligned}$$

Observe, that these second-order terms contain both pairwise and triplet interactions. In the special case[1] $c_2 = 0$, this second-order phase reduction can also be rewritten using trigonometric identities as

$$
\begin{aligned}
\dot{\theta}_k = {}& \varepsilon\,|1 + \mathrm{i}c_1|\,S\sin(\Xi - \theta_k + \alpha) - \varepsilon\,|1 + \mathrm{i}c_1|\sin(\alpha) \\
&+ \frac{\varepsilon^2\,|1 + \mathrm{i}c_1|^2}{4}\Big(SQ\sin(\Upsilon - \Xi - \theta_k) + S\sin(\Xi - \theta_k + 2\alpha) \\
&\qquad\qquad - S^2\sin(2\Xi - 2\theta_k + 2\alpha)\Big),
\end{aligned}
\tag{4.2.9}
$$

where $\alpha = \arg(1 + \mathrm{i}c_1)$, $Qe^{\mathrm{i}\Upsilon} = \frac{1}{M}\sum_{j=1}^{M} e^{2\mathrm{i}\phi_j}$ and $Se^{\mathrm{i}\Xi} = \frac{1}{M}\sum_{j=1}^{M} e^{\mathrm{i}\phi_j}$, to match the notation of [114, Equation (15)].

4.3 Phase Reductions for Limit Cycles with Phase Dependent Amplitude

In this section, we introduce a variation of Stuart–Landau oscillators where the limit cycle is not circular but has a phase dependent amplitude. We then derive first- and second-order phase reductions for this class of oscillators subject to coupling as in the previous section. Finally, we investigate how these phase reductions are affected by the parameter that determines the deviation of the shape of the limit cycle from a circle.

Similarly to the work [114], the starting point of this section is a Stuart–Landau oscillator. However, instead of considering the case when the isochrons are bent, i.e., $c_2 \neq 0$, we want to generalize a Stuart–Landau oscillator in another way, which allows for non-circular limit cycles. If $\delta \in (-1, 1)$ with $|\delta| \ll 1$ is the parameter that determines deviation from a circular limit cycle and $g\colon \mathbb{T} \to \mathbb{R}$ is a smooth function that determines the shape of the deviation, consider an oscillator $A = re^{\mathrm{i}\phi} \in \mathbb{C}$ whose state evolves according to

$$
\dot{r} = \delta g'(\phi)\omega\frac{r}{1 + \delta g(\phi)} + mr^2(r - 1 - \delta g(\phi)),
\tag{4.3.1a}
$$

$$
\dot{\phi} = \omega,
\tag{4.3.1b}
$$

where $\omega > 0$ is the angular velocity of the oscillator and $m < 0$. If $\delta = 0$ the limit cycle is circular and (4.3.1) agrees with (4.2.1), when $c_2 = 0$. Upon varying δ, the oscillator's limit cycle deforms into one that is parameterized by $r = 1 + \delta g(\phi)$ and m determines the rate of attraction to this limit cycle. When g is a constant this would keep the shape of the limit cycle but only alter its radius.

---

[1]An equivalent representation is also available if $c_2 \neq 0$, see [114].

Since this is only a rescaled version of a regular Stuart–Landau oscillator, we assume $\int_{\mathbb{T}} g(\phi) \mathrm{d}\phi = 0$.

Now, given an ensemble of M oscillators $(A_k = r_k e^{\mathrm{i}\phi_k})_{k=1,\dots,M}$, we assume a mean-field coupling, of the form

$$\dot{A}_k = \mathcal{F}(A_k) + K e^{\mathrm{i}\alpha}(\bar{A} - A_k), \tag{4.3.2}$$

where $\mathcal{F}(A_k)$ denotes the intrinsic dynamics of oscillator k as described in (4.3.1), $K \in \mathbb{R}$ is the coupling strength, $\alpha \in \mathbb{T}$ is a parameter and $\bar{A} = \frac{1}{M} \sum_{j=1}^{M} A_j$ is the average position as before. Rewritten in polar coordinates, this results in the system

$$\dot{r}_k = \delta g'(\phi_k) \omega \frac{r_k}{1 + \delta g(\phi_k)} + m r_k^2 (r_k - 1 - \delta g(\phi))$$

$$+ \frac{K}{M} \sum_{l=1}^{M} [r_l \cos(\phi_l - \phi_k + \alpha) - r_k \cos(\alpha)],$$

$$\dot{\phi}_k = \omega + \frac{K}{M r_k} \sum_{l=1}^{M} [r_l \sin(\phi_l - \phi_k + \alpha) - r_k \sin(\alpha)].$$

After the transformation

$$R_k = \frac{r_k}{1 + \delta g(\phi_k)},$$

to transform the phase-dependent limit cycle to a circle, we arrive by a direct, but slightly lengthy, calculation at the system

$$\dot{R}_k = F(R_k, \phi_k) + K G_k(R, \phi), \tag{4.3.3a}$$

$$\dot{\phi}_k = \omega + K H_k(R, \phi), \tag{4.3.3b}$$

with functions F, G_k and H_k defined by

$$F(R_k, \phi_k) = m R_k^2 (R_k - 1)(1 + \delta g(\phi_k))^2,$$

$$G_k(R, \phi) = \frac{1}{M} \sum_{l=1}^{M} \left[R_l \frac{1 + \delta g(\phi_l)}{1 + \delta g(\phi_k)} \cos(\phi_l - \phi_k + \alpha) - R_k \cos(\alpha) \right.$$

$$\left. - \delta g'(\phi_k) \left(R_l \frac{1 + \delta g(\phi_l)}{(1 + \delta g(\phi_k))^2} \sin(\phi_l - \phi_k + \alpha) - R_k \frac{\sin(\alpha)}{1 + \delta g(\phi_k)} \right) \right],$$

$$H_k(R, \phi) = \frac{1}{M} \sum_{l=1}^{M} \left[\frac{R_l(1 + \delta g(\phi_l))}{R_k(1 + \delta g(\phi_k))} \sin(\phi_l - \phi_k + \alpha) - \sin(\alpha) \right].$$

It is important to note, that F, G and H depend explicitly on the phase. Therefore, the system (4.3.3) does not have a $\mathbb{T}$ symmetry. Hence, we cannot change into a co-rotating coordinate system. That means, unlike in the system (4.2.3), we cannot assume $\omega = 0$ without loss of generality. However, $\omega = 0$ was a crucial assumption to derive formula (4.2.8) in Section 4.2. Next, we show how to generalize the methods of [114] to derive higher-order phase reductions anyway.

4.3.1 Phase Reductions of First-Order

Because there is an additional parameter δ in our system, we expand in both K and δ, i.e., we study asymptotics in two parameters [103]. Regarding notation, if W is a function or a scalar, we write $W^{(n,j)}$ for the contribution of order $K^n \delta^j$ to W, i.e.,

$$W = \sum_{n,j=0}^{\infty} K^n \delta^j W^{(n,j)}.$$

Moreover, we write $W^{(n,\star)}$ for all contributions of order K^n, which includes all orders in δ. Similarly, $W^{(\star,j)}$ includes all terms of order δ^j. Consequently,

$$W = \sum_{j=0}^{\infty} \delta^j W^{(\star,j)} = \sum_{n=0}^{\infty} K^n W^{(n,\star)}.$$

In particular, if the quantity W is independent of K, we have $W = W^{(0,\star)}$, but we use the notation $W = W^{(-,\star)}$ to highlight the independence of K. We use this notation to derive phase reductions of different approximation order in K and δ. To distinguish these phase reductions, we speak of an (a, b)-phase reduction when a is the highest approximation order in K and b is the highest order in δ. In particular, an (a, b)-phase reduction is given by

$$\phi_k = \sum_{n=0}^{a} \sum_{j=0}^{b} K^n \delta^j P_k^{(n,j)}(\phi),$$

where $P_k^{(n,j)}(\phi)$ denotes the contribution on the order $K^n \delta^j$. Explicit expressions for $P_k^{(n,j)}(\phi)$ will be derived below.

By the same reasons as illustrated in Section 4.2, the limiting dynamics of the system (4.3.3) takes place on an attractive invariant M-dimensional torus. If $K = 0$ this torus is described by $R_k \equiv 1$ for all $k = 1, \ldots, M$. If $|K|$ is small, the torus persists and the radii of this torus can be expanded in terms of K as

$$R_k(\phi) = R_k^{(0,\star)}(\phi) + K R_k^{(1,\star)}(\phi) + K^2 R_k^{(2,\star)}(\phi) + \mathcal{O}(K^3), \tag{4.3.4}$$

where $R_k^{(0,\star)}(\phi) \equiv 1$. When inserting the expansion (4.3.4) into the system (4.3.3b) we obtain

$$
\begin{aligned}
\dot{\phi}_k &= \omega + KH_k\Big(R^{(0,\star)}(\phi) + KR^{(1,\star)}(\phi) + K^2 R^{(2,\star)}(\phi) + \mathcal{O}(K^3), \phi\Big) \\
&= \omega + KH_k(R_k^{(0,\star)}(\phi), \phi) + K^2 \nabla_R H_k(R^{(0,\star)}(\phi), \phi) \cdot R^{(1,\star)}(\phi) + \mathcal{O}(K^3) \\
&= \omega + KH_k(\mathbb{1}, \phi) + K^2 \nabla_R H_k(\mathbb{1}, \phi) \cdot R^{(1,\star)}(\phi) + \mathcal{O}(K^3), \quad\quad (4.3.5)
\end{aligned}
$$

which is the base equation for phase reductions of any order. A phase reduction of first-order can be obtained by truncating terms of order $\mathcal{O}(K^2)$, a second-order phase reduction is derived from (4.3.5) by ignoring all terms of order $\mathcal{O}(K^3)$, etc. In particular, the $(1, \infty)$-phase reduction is given by

$$
\begin{aligned}
\dot{\phi}_k &= \omega + KH_k(\mathbb{1}, \phi) \\
&= \omega + K\frac{1}{M}\sum_{l=1}^{M}\left[\frac{1 + \delta g(\phi_l)}{1 + \delta g(\phi_k)}\sin(\phi_l - \phi_k + \alpha) - \sin(\alpha)\right]. \quad\quad (4.3.6)
\end{aligned}
$$

Up to now, this contains all orders of δ, but by writing

$$
H_k(R, \phi) = H_k^{(-,0)}(R, \phi) + \delta H_k^{(-,1)}(R, \phi) + \delta^2 H_k^{(-,2)}(R, \phi) + \mathcal{O}(\delta^3),
$$

the $(1, \infty)$-phase reduction can also be written as

$$
\dot{\phi}_k \approx \sum_{n=0}^{1}\sum_{j=0}^{\infty} K^n \delta^j P_k^{(n,j)}(\phi),
$$

where $P_k^{(0,0)}(\phi) \equiv \omega$, $P_k^{(0,j)}(\phi) \equiv 0$ for all $j \in \mathbb{N}$ and

$$
P_k^{(1,j)}(\phi) = H_k^{(-,j)}(\mathbb{1}, \phi), \quad j \in \mathbb{N}_0.
$$

For example, we find

$$
P_k^{(1,0)}(\phi) = \frac{1}{M}\sum_{l=1}^{M}\left[\sin(\phi_l - \phi_k + \alpha) - \sin(\alpha)\right],
$$

$$
P_k^{(1,1)}(\phi) = \frac{1}{M}\sum_{l=1}^{M}(g(\phi_l) - g(\phi_k))\sin(\phi_l - \phi_k + \alpha),
$$

$$
P_k^{(1,2)}(\phi) = \frac{1}{M}\sum_{l=1}^{M} g(\phi_k)(g(\phi_k) - g(\phi_l))\sin(\phi_l - \phi_k + \alpha).
$$

Consequently, the $(1, 0)$-phase reduction is

$$\dot{\phi}_k = \sum_{n=0}^{1} \sum_{j=0}^{0} K^n \delta^j P_k^{(n,j)}(\phi)$$

$$= \omega + \frac{K}{M} \sum_{l=1}^{M} \left[\sin(\phi_l - \phi_k + \alpha) - \sin(\alpha) \right],$$

which is the Kuramoto–Sakaguchi model [155] for identical oscillators.

4.3.2 Higher-Order Phase Reductions

Having explicitly stated the first-order phase reductions, we move on by considering the terms of order K^2 in (4.3.5), thereby deriving a second-order phase reduction. As in Section 4.2, this requires knowledge of $R^{(1,\star)}(\phi)$. To get a formula describing it, we follow the lines of [114] and insert the expansion (4.3.4) into (4.3.3a). Using $R^{(0,\star)} \equiv \mathbb{1}$ and applying the chain rule, we find that the left-hand side of (4.3.3a) turns into

$$\dot{R}_k = \frac{\mathrm{d}}{\mathrm{d}t} R_k(t)$$

$$= \frac{\mathrm{d}}{\mathrm{d}t} \left(R_k^{(0,\star)}(\phi(t)) + K R_k^{(1,\star)}(\phi(t)) + \mathcal{O}(K^2) \right)$$

$$= K \nabla_\phi R_k^{(1,\star)}(\phi(t)) \cdot \dot{\phi}(t) + \mathcal{O}(K^2)$$

$$= K \nabla_\phi R_k^{(1,\star)}(\phi(t)) \cdot \left(\omega \mathbb{1} + K H(R, \phi) \right) + \mathcal{O}(K^2)$$

$$= K \omega \nabla_\phi R_k^{(1,\star)}(\phi(t)) \cdot \mathbb{1} + \mathcal{O}(K^2), \tag{4.3.7}$$

whenever the dynamics is constrained to the limiting torus. Using, $\mathbb{1} = (1, 1, \ldots, 1)^\top \in \mathbb{R}^M$ it follows that

$$\omega \nabla_\phi R_k^{(1,\star)}(\phi) \cdot \mathbb{1} = \omega \sum_{l=1}^{M} \frac{\partial}{\partial \phi_l} R_k^{(1,\star)}(\phi).$$

Similarly, the right-hand of (4.3.3a) side turns into

$$F \left(R_k^{(0)}(\phi(t)) + K R_k^{(1)}(\phi(t)) + \mathcal{O}(K^2)), \phi_k \right)$$

$$+ K G_k \left(R^{(0)}(\phi(t)) + K R^{(1)}(\phi(t)) + \mathcal{O}(K^2), \phi \right)$$

$$= F(R_k^{(0)}(\phi), \phi_k) + K F_R(R_k^{(0)}(\phi), \phi_k) R_k^{(1)}(\phi) + K G_k(R^{(0)}(\phi), \phi) + \mathcal{O}(K^2)$$

$$= F(R_k^{(0)}(\phi), \phi_k) + K \left(F_R(R_k^{(0)}(\phi), \phi_k) R_k^{(1)}(\phi) + G_k(R^{(0)}(\phi), \phi) \right) + \mathcal{O}(K^2), \tag{4.3.8}$$

where $F_R(R, \phi) = \frac{\partial}{\partial R} F(R, \phi)$. Now, equating (4.3.7) and (4.3.8) and collecting terms of order K yields

$$F_R(1, \phi_k) R_k^{(1,\star)}(\phi) + G_k(\mathbb{1}, \phi) = \omega \nabla_\phi R_k^{(1,\star)}(\phi) \cdot \mathbb{1}, \qquad (4.3.9)$$

or equivalently, when using the definitions of F and G,

$$m(1 + \delta g(\phi_k))^2 R_k^{(1,\star)}(\phi) + \frac{1}{M} \sum_{l=1}^{M} \left[\frac{1 + \delta g(\phi_l)}{1 + \delta g(\phi_k)} \cos(\phi_l - \phi_k + \alpha) - \cos(\alpha) \right.$$

$$\left. - \delta g'(\phi_k) \left(\frac{1 + \delta g(\phi_l)}{(1 + \delta g(\phi_k))^2} \sin(\phi_l - \phi_k + \alpha) - \frac{\sin(\alpha)}{1 + \delta g(\phi_k)} \right) \right] = \omega \nabla_\phi R_k^{(1,\star)}(\phi) \cdot \mathbb{1},$$

which is a linear first-order partial differential equation describing $R_k^{(1,\star)}(\phi)$.

Ideally, we would like to set $\omega = 0$, because then (4.3.9) turns into an algebraic equation that we can easily solve for $R_k^{(1,\star)}(\phi)$. However, at this point, we can no longer proceed as in Section 4.2, because we cannot set $\omega = 0$, since our system is not rotationally invariant. Thus, we generalize the methods of [114] by solving the PDE (4.3.9), as proposed in [70]. Assuming an expansion

$$R_k^{(1,\star)}(\phi) = R_k^{(1,0)}(\phi) + \delta R_k^{(1,1)}(\phi) + \delta^2 R_k^{(1,2)}(\phi) + \mathcal{O}(\delta^3), \qquad (4.3.10)$$

we solve the PDE (4.3.9) order by order [67, 59, 96]. When $\delta = 0$, the PDE describing $R_k^{(1,0)}$ is

$$m R_k^{(1,0)}(\phi) + \frac{1}{M} \sum_{l=1}^{M} [\cos(\phi_l - \phi_k + \alpha) - \cos(\alpha)] = \omega \nabla_\phi R_k^{(1,0)}(\phi) \cdot \mathbb{1}.$$

The solution to this PDE, which can, for example, be found with the method of characteristics [67] or a computer algebra software[2], is given by

$$R_k^{(1,0)}(\phi) = \frac{1}{Mm} \sum_{l=1}^{M} s_0(\phi_k, \phi_l), \qquad s_0(\phi_k, \phi_l) = -\cos(\phi_l - \phi_k + \alpha) + \cos(\alpha).$$
$$(4.3.11)$$

On first-order in δ, the resulting PDE is

$$m R_k^{(1,1)}(\phi) + 2mg(\phi_k) R_k^{(1,0)}(\phi) - \omega \nabla_\phi R_k^{(1,1)}(\phi) \cdot \mathbb{1}$$

$$= -\frac{1}{M} \sum_{l=1}^{M} \left[(g(\phi_l) - g(\phi_k)) \cos(\phi_l - \phi_k + \alpha) \right. \qquad (4.3.12)$$

$$\left. - g'(\phi_k) (\sin(\phi_l - \phi_k + \alpha) - \sin(\alpha)) \right].$$

---

[2]This PDE can be solved with the MATHEMATICA code, which is available on GitHub, see [33].

The solution of this PDE now depends on the specific choice of g. However, as one can infer from the structure of (4.3.12), its solutions are linear in g in the sense that if $\hat{R}_k^{(1,1)}(\phi)$ is a solution to (4.3.12) when $g = \hat{g}$ and $\tilde{R}_k^{(1,1)}(\phi)$ is one if $g = \tilde{g}$, then $\gamma \hat{R}_k^{(1,1)}(\phi)$ is a solution when $g = \gamma \hat{g}$ for all $\gamma \in \mathbb{R}$. Moreover, $\hat{R}_k^{(1,1)}(\phi) + \tilde{R}_k^{(1,1)}(\phi)$ is the solution to (4.3.12) when $g = \hat{g} + \tilde{g}$. If $g(\phi) = \sin(\phi)$, the solution of (4.3.12) is given by

$$R_k^{(1,1)}(\phi) = \frac{1}{2M(m^2 + \omega^2)} \sum_{l=1}^{M} s_1(\phi_k, \phi_l), \tag{4.3.13}$$

where $s_1(\phi_k, \phi_l)$ is a trigonometric polynomial that is defined by

$$s_1(\phi_k, \phi_l) = \omega \Big(4\cos(\phi_l + \alpha) - \cos(\phi_k - 2\phi_l - \alpha) + 2\cos(2\phi_k - \phi_l - \alpha)$$
$$- 2\cos(\phi_k - \alpha) - 3\cos(\phi_k + \alpha) \Big)$$
$$+ m \Big(4\sin(\phi_l + \alpha) + \sin(\phi_k - 2\phi_l - \alpha) + 2\sin(2\phi_k - \phi_l - \alpha)$$
$$- 2\sin(\phi_k - \alpha) - 3\sin(\phi_k + \alpha) \Big). \tag{4.3.14}$$

A solution for (4.3.12) for general functions g is stated in Appendix A. Equivalently, if $\alpha = 0$, this condenses into

$$s_1(\phi_k, \phi_l) = -2 \Big(1 - \cos(\phi_k - \phi_l) \Big)$$
$$\cdot \Big(2\omega \cos(\phi_k) - \omega \cos(\phi_l) + 2m \sin(\phi_k) - m \sin(\phi_l) \Big)$$

Finally, the PDE on order $\mathcal{O}(\delta^2)$ is

$$mR^{(1,2)}(\phi) + 2mg(\phi_k)R_k^{(1,1)}(\phi) + mg(\phi_k)^2 R_k^{(0,1)}(\phi) - \omega \nabla_\phi R_k^{(1,2)}(\phi) \cdot \mathbb{1}$$
$$= -\frac{1}{M} \sum_{l=1}^{M} \bigg[g'(\phi_k) \Big((g(\phi_k) - g(\phi_l)) \sin(\phi_l - \phi_k + \alpha)$$
$$+ g(\phi_k)(\sin(\phi_l - \phi_k + \alpha) - \sin(\alpha)) \Big)$$
$$+ g(\phi_k)(g(\phi_k) - g(\phi_l)) \cos(\phi_l - \phi_k + \alpha) \bigg].$$

This PDE, however, is not linear in g. In particular, if $\hat{R}_k^{(1,2)}(\phi)$ is a solution for $g = \hat{g}$ then $\gamma^2 \hat{R}_k^{(1,2)}(\phi)$ solves the PDE whenever $g = \gamma \hat{g}$, for $\gamma \in \mathbb{R}$. If $g(\phi) = \sin(\phi)$

a solution is of the form

$$R_k^{(1,2)}(\phi) = \frac{1}{-4mM\left(m^4 + 5m^2\omega^2 + 4\omega^4\right)} \sum_{l=1}^{M} s_2(\phi_k, \phi_l),$$

where $s_2(\phi_k, \phi_l)$ is a trigonometric polynomial of the same form as $s_1(\phi_k, \phi_l)$ but with more summands[3].

To determine the second-order interactions in (4.3.5), we also need to expand $\nabla_R H_k(R^{(0)}(\phi), \phi)$ in terms of delta. Denoting $H_k(R, \phi) = H_k^{(-,0)}(R, \phi) + \delta H_k^{(-,1)}(R, \phi) + \delta^2 H_k^{(-,2)}(R, \phi) + \mathcal{O}(\delta^3)$, we find

$$\nabla_R H_k^{(-,0)}(\mathbb{1}, \phi) = \frac{1}{M}\begin{pmatrix} \sin(\phi_1 - \phi_k + \alpha) \\ \vdots \\ \sin(\phi_M - \phi_k + \alpha) \end{pmatrix} - \frac{1}{M}e_k \sum_{l=1}^{M} \sin(\phi_l - \phi_k + \alpha),$$

$$\nabla_R H_k^{(-,1)}(\mathbb{1}, \phi) = \frac{1}{M}\begin{pmatrix} (g(\phi_1) - g(\phi_k))\sin(\phi_1 - \phi_k + \alpha) \\ \vdots \\ (g(\phi_M) - g(\phi_k))\sin(\phi_M - \phi_k + \alpha) \end{pmatrix}$$
$$- \frac{1}{M}e_k \sum_{l=1}^{M} (g(\phi_l) - g(\phi_k))\sin(\phi_l - \phi_k + \alpha),$$

$$\nabla_R H_k^{(-,2)}(\mathbb{1}, \phi) = \frac{1}{M}\begin{pmatrix} g(\phi_k)(g(\phi_k) - g(\phi_1))\sin(\phi_1 - \phi_k + \alpha) \\ \vdots \\ g(\phi_k)(g(\phi_k) - g(\phi_M))\sin(\phi_M - \phi_k + \alpha) \end{pmatrix}$$
$$- \frac{1}{M}e_k \sum_{l=1}^{M} g(\phi_k)(g(\phi_k) - g(\phi_l))\sin(\phi_l - \phi_k + \alpha),$$

where e_k is the k-th unit vector in $\mathbb{R}^M$. Finally, we can put everything together and calculate the second-order terms in (4.3.5):

$$\nabla_R H_k(\mathbb{1}, \phi) \cdot R_k^{(1,\star)}(\phi) = P_k^{(2,0)}(\phi) + \delta P_k^{(2,1)}(\phi) + \delta^2 P_k^{(2,2)}(\phi) + \mathcal{O}(\delta^3),$$

with

$$P_k^{(2,0)}(\phi) = \nabla_R H_k^{(-,0)}(\mathbb{1}, \phi) \cdot R^{(1,0)}(\phi), \tag{4.3.15a}$$

$$P_k^{(2,1)}(\phi) = \nabla_R H_k^{(-,0)}(\mathbb{1}, \phi) \cdot R^{(1,1)}(\phi) + \nabla_R H_k^{(-,1)}(\mathbb{1}, \phi) \cdot R^{(1,0)}(\phi), \tag{4.3.15b}$$

$$P_k^{(2,2)}(\phi) = \nabla_R H_k^{(-,0)}(\mathbb{1}, \phi) \cdot R^{(1,2)}(\phi) + \nabla_R H_k^{(-,1)}(\mathbb{1}, \phi) \cdot R^{(1,1)}(\phi)$$
$$+ \nabla_R H_k^{(-,2)}(\mathbb{1}, \phi) \cdot R^{(1,0)}(\phi). \tag{4.3.15c}$$

---

[3]The full expression of $s_2(\phi_k, \phi_l)$ can be generated with the MATHEMATICA code, which is available on GitHub, see [33].

Evaluating these expressions yields, for example,

$$P_k^{(2,0)}(\phi) = \frac{1}{2M^2m} \sum_{l=1}^{M} \sum_{i=1}^{M} \Big(\sin(\phi_i + \phi_k - 2\phi_l) - \sin(\phi_i - \phi_k + 2\alpha)$$
$$+ \sin(\phi_i - 2\phi_k + \phi_l + 2\alpha) \Big)$$

for the second-order terms in K when $\delta = 0$. We emphasize that it is here clearly visible that three phases interact with each other, which is different from the pairwise terms that appear in a $(1,0)$-phase reduction. In other words, higher-order interactions appear in higher-order phase reductions.

In conclusion, the $(2,2)$-phase reduction is given by

$$\dot{\phi}_k = \omega + K \Big(P_k^{(1,0)}(\phi) + \delta P_k^{(1,1)}(\phi) + \delta^2 P_k^{(1,2)}(\phi) \Big)$$
$$+ K^2 \Big(P_k^{(2,0)}(\phi) + \delta P_k^{(2,1)}(\phi) + \delta^2 P_k^{(2,2)}(\phi) \Big),$$

where $P_k^{(1,0)}(\phi)$, $P_k^{(1,1)}(\phi)$ and $P_k^{(1,2)}(\phi)$ are as in Section 4.3.1 and $P_k^{(2,0)}(\phi)$, $P_k^{(2,1)}(\phi)$ and $P_k^{(2,2)}(\phi)$ are defined in (4.3.15).

4.3.3 Comparison of Phase Reductions With and Without Symmetry

As we have highlighted in this section, the full system (4.3.3) has a $\mathbb{T}$ symmetry, when $\delta = 0$, that it does not have when $\delta \neq 0$. When existent, this symmetry acts on the phase space by shifting all oscillators by a common phase. Now, we compare the full system to its phase reductions and see if the symmetry of the full system gets passed on to the phase reductions, when $\delta = 0$. Moreover, when $\delta = 0$, the phase reductions should agree with the phase reductions derived in [114], as outlined in Section 4.2.

The $(2,0)$-phase reduction, i.e., the second-order phase reduction when $\delta = 0$, is given by

$$\dot{\phi}_k = \omega + K P_k^{(1,0)}(\phi) + K^2 P_k^{(2,0)}(\phi)$$
$$= \omega + K \frac{1}{M} \sum_{l=1}^{M} [\sin(\phi_l - \phi_k + \alpha) - \sin(\alpha)]$$
$$+ K^2 \frac{1}{2M^2m} \sum_{l=1}^{M} \sum_{i=1}^{M} \Big(\sin(\phi_i + \phi_k - 2\phi_l) - \sin(\phi_i - \phi_k + 2\alpha)$$
$$+ \sin(\phi_i - 2\phi_k + \phi_l + 2\alpha) \Big).$$

As one can see, the right-hand side of this equation only depends on phase differences. Therefore, its value remains invariant when shifting all oscillators by a common phase. Consequently, the $(2,0)$-phase reduction inherits the $\mathbb{T}$ symmetry of the full system. This $(2,0)$-phase reduction can also be written as

$$\dot{\phi}_k = \omega + KS\sin(\Xi - \phi_k + \alpha) - K\sin(\alpha) + K^2\frac{1}{2m}\Big(SQ\sin(\Xi + \phi_k - \Upsilon)$$
$$- S\sin(\Xi - \phi_k + 2\alpha) + S^2\sin(2\Xi - 2\phi_k + 2\alpha)\Big),$$

which agrees with (4.2.9), if one switches into a suitable rotating coordinate system and chooses $K = \varepsilon|1 + ic_1|$, $m = -2$ and $c_2 = 0$. Note also, that $\phi_k = \theta_k$, when comparing this equation with (4.2.9), since $c_2 = 0$. The plausibility of $K = \varepsilon|1 + ic_1|$ is immediate, when comparing the coupling strength in (4.2.2) with those in (4.3.2). Moreover, $m = -2$ can be explained as follows: When $\delta = 0$, the parameter m is the rate of attraction towards the limit cycle of a single oscillator (4.3.1). In particular, this rate can be obtained by linearizing (4.3.1a) with respect to r and evaluating at the limit cycle $r = 1$. Doing the same for the Stuart–Landau oscillator (4.2.1), yields that the rate of attraction to this limit cycle is -2.

Now, let us consider phase reductions when $\delta \neq 0$. In particular, a $(1,1)$-phase reduction is given by the system

$$\dot{\phi}_k = \omega + KP_k^{(1,0)}(\phi) + K\delta P_k^{(1,1)}(\phi)$$
$$= \omega + K\frac{1}{M}\sum_{l=1}^{M}[\sin(\phi_l - \phi_k + \alpha) - \sin(\alpha)]$$
$$+ K\delta\frac{1}{M}\sum_{l=1}^{M}(\sin(\phi_l) - \sin(\phi_k))\sin(\phi_l - \phi_k + \alpha)$$

which does not have a $\mathbb{T}$ symmetry, because the right-hand side does not remain invariant when one shifts all oscillators by a common phase. Specifically, this is the case for the terms of order δ^1. Since, higher-order phase reductions also consist of these terms, any phase reduction of higher-order than 1 in δ is also not $\mathbb{T}$ symmetric. To conclude, phase reductions of the full system (4.3.3) possess a $\mathbb{T}$ symmetry if and only if the full system itself possesses this symmetry.

As a remark, when $\alpha = 0$, the $(1,1)$-phase reduction can also be written as

$$\dot{\phi}_k = \omega + K\frac{1}{M}\sum_{l=1}^{M}\sin(\phi_l - \phi_k)\Big[1 + \delta(\sin(\phi_l) - \sin(\phi_k))\Big].$$

This formula shows that the effect of δ on the $(1,1)$-phase reduction can also be seen as a perturbation of the $(1,0)$-phase reduction. Similarly, when $\alpha = 0$, the $(2,1)$-phase reduction can be written as

$$\dot{\phi}_k = \omega + K \frac{1}{M} \sum_{l=1}^{M} \sin(\phi_l - \phi_k) \Big[1 + \delta(\sin(\phi_l) - \sin(\phi_k)) \Big]$$

$$+ K^2 \frac{1}{M^2 m} \sum_{l=1}^{M} \sum_{i=1}^{M} \bigg\{ \sin(\phi_l - \phi_k)(1 - \cos(\phi_i - \phi_l))$$

$$\cdot \Big[1 + \delta\big(u(\phi_l, \phi_i) + \sin(\phi_l) - \sin(\phi_k)\big) \Big]$$

$$- \sin(\phi_l - \phi_k)(1 - \cos(\phi_i - \phi_k))$$

$$\cdot \Big[1 + \delta\big(u(\phi_k, \phi_i) + \sin(\phi_l) - \sin(\phi_k)\big) \Big] \bigg\},$$

where

$$u(\phi_k, \phi_i) = \frac{-m}{m^2 + \omega^2} (2\omega \cos(\phi_k) - \omega \cos(\phi_i) + 2m \sin(\phi_k) - m \sin(\phi_i)).$$

Again, the effect of δ on the $(2,1)$-phase reduction can be seen as a correction of the $(2,0)$-phase reduction.

4.4 Dynamics in Phase-Reduced Systems

In this section we consider two different orbits, specifically, the synchronized orbit and the splay orbit, and compare their stability in a few different systems, including the full system (4.3.3) and various phase reductions of different order.

4.4.1 The Synchronized Orbit

First, we consider synchronized states in the full system. A state in the phase space is called synchronized if all the oscillators are at the same position. In the full system (4.3.3) this state is defined by $\{A_1 = \cdots = A_M\}$ or in polar coordinates

$$\{R_1 = \cdots = R_M\} \quad \text{and} \quad \{\phi_1 = \cdots = \phi_M\}. \tag{4.4.1}$$

Consequently, if a state is synchronized, it is uniquely given by its amplitude $R^\star := R_k$ and its phase $\phi^\star := \phi_k$ for any $k = 1, \ldots, M$. Due to the S_M symmetry of (4.3.3) the set of synchronized states (4.4.1) is dynamically invariant. Thus, we

can insert the ansatz (4.4.1) into the system (4.3.3) to obtain ODEs for $R^\star$ and $\phi^\star$ as

$$\dot{R}^\star = m(R^\star)^2(R^\star - 1)(1 + \delta g(\phi^\star))^2,$$
$$\dot{\phi}^\star = \omega.$$

Based on these equations one can see that always $R^\star = 1$ on the invariant torus and that the rate of attraction to $R^\star = 1$ is given by $m(1 + \delta g(\phi^\star))^2$. Since $|\delta|$ is small, this rate is mostly governed by $m < 0$. Moreover, the phase $\phi^\star$ evolves with constant speed ω. Consequently, the synchronized orbit on the invariant torus is given by $\gamma^{\mathrm{f}}(t) = (\mathbb{1}, (\phi_0 + \omega t)\mathbb{1})$, which is periodic with period $T = 2\pi/\omega$.

Now, we look at synchronized states in phase-reduced systems. In a phase-reduced system, there are no amplitudes and thus, a synchronized state is present when the single condition $\phi_1 = \cdots = \phi_M$ is fulfilled. Here, a synchronized state is only determined by its phase $\phi^\star := \phi_k$ for any $k = 1, \ldots, M$. Similarly to the full system, phase-reduced systems retain the S_M symmetry and therefore the set of synchronized states is dynamically invariant. Inserting $\phi \equiv \phi^\star$ into any of the phase reductions derived in Section 4.3 yields

$$\dot{\phi}^\star = \omega.$$

Therefore, the synchronized orbit in phase-reduced systems is $\gamma^{\mathrm{pr}}(t) = (\phi_0 + \omega t)\mathbb{1}$ with period $T = 2\pi/\omega$.

Having established representations for the synchronized orbits, we now investigate their stability. Usually, when one wants to check the stability of a synchronized orbit, one changes into a co-rotating coordinate system, in which each synchronized state is an equilibrium. Then, one linearizes the vector field around this equilibrium and calculates the eigenvalues of this linearization. If they are all negative, apart from a single 0 eigenvalue that corresponds to perturbations along the continuum of synchronized states, the synchronized orbit is linearly stable and linearly (neutrally) unstable otherwise. However, when $\delta \neq 0$, we cannot change into a co-rotating coordinate system, since the full system as well as phase-reduced systems are not $\mathbb{T}$ symmetric. In particular, the rate of attraction to the limit cycle depends on the position on the limit cycle. Consequently, one needs to take averages over all rates of attraction of one period of the limit cycle. These averages are called Floquet exponents. The concept of Floquet exponents and Poincaré return maps is often helpful when analyzing the stability of periodic orbits [50, 170]. To understand it, let us consider the general differential equation

$$\dot{x} = \mathcal{H}(x), \qquad \mathcal{H}\colon \mathcal{X} \to \mathrm{T}\mathcal{X},$$

where $\mathcal{H}$ is a smooth vector field on the phase space $\mathcal{X}$ and $\mathrm{T}\mathcal{X}$ is its tangent bundle. Suppose there is a periodic orbit $\gamma\colon [0, T] \to \mathcal{X}$ with period T. Later

we want to apply this to the full system, in which $x = (R, \phi)^\top \in \mathbb{R}^M_{\geq 0} \times \mathbb{T}^M$, and phase-reduced systems with $x = \phi \in \mathbb{T}^M$. To analyze the stability of the orbit γ, one assumes a perturbation of the starting point of the periodic orbit $x(0) = \gamma(0) + \varepsilon\eta(0)$ and continues this perturbation along the periodic orbit such that $x(t) = \gamma(t) + \varepsilon\eta(t)$. One the one hand, if all possible perturbations $\eta(0)$ decay after one period T, we expect the periodic orbit γ to be stable. On the other hand, if some perturbations $\eta(0)$ grow in amplitude, the orbit γ is unstable. Therefore, we solve for $\eta(t)$. However, since that is difficult to do in general, we first linearize in ε to obtain on first order

$$\dot{\eta}(t) = A(t)\eta(t), \quad A(t) = D\mathcal{H}(\gamma(t)), \tag{4.4.2}$$

which is a system of linear ODEs with a time-dependent coefficient matrix $A(t)$. Now, let $\Phi(t) \in \mathbb{R}^{M \times M}$ be a fundamental solution of this ODE such that $\eta(t) = \Phi(t)\eta(0)$. To determine the linear stability of the periodic orbit $\gamma(t)$ one propagates all possible perturbations $\eta(0)$ over one period T of the orbit and then looks at the eigenvalues of the map $\Phi(T)$. Of course, this map has an eigenvalue 1, that corresponds to the eigenvector that represents a perturbation along the periodic orbit. All other eigenvalues λ_k, $k = 1, \ldots, M - 1$ are the multipliers of a Poincaré return map. They are related to the Floquet exponents q_k of the orbit as $\lambda_k = e^{Tq_k}$, for $k = 1, \ldots, M - 1$. If the largest absolute value of all Poincaré return map multipliers (PRMMs) is less than 1, the periodic orbit is linearly stable. If one PRMM has an absolute value greater than 1, the orbit is linearly unstable.

Next, we apply this concept to the synchronized orbit in phase-reduced systems. We start by calculating the PRMMs for the $(1, \infty)$-phase-reduced system (4.3.6). When putting this system into the framework of (4.4.2), we see that the matrix $A(t)$ is given by

$$A(t) = f(\gamma(t))\frac{K}{M}(J_M - M\mathrm{Id}_M),$$

where $J_M := \{1\}^{M \times M}$ is the $M \times M$ matrix where all entries are ones, Id_M is the $M \times M$ dimensional identity matrix and

$$f(\gamma) = \frac{1}{1 + \delta g(\gamma)}\Big(\delta g'(\gamma)\sin(\alpha) + (1 + \delta g(\gamma))\cos(\alpha)\Big).$$

Due to the S_M symmetry of the synchronized state in the phase-reduced systems, the matrix $A(t)$ has the special property that it is just a multiple of $J_M - M\mathrm{Id}_M$. Since matrices of this form commute with each other, a fundamental solution $\Phi(t)$ of (4.4.2) can explicitly be calculated using the matrix exponential:

$$\Phi(t) = \exp\left(\int_0^t A(\hat{t})\mathrm{d}\hat{t}\right)$$

$$= \exp\left(\int_0^t f(\gamma(\hat{t}))\mathrm{d}\hat{t}\left(\frac{K}{M}(J_M - M\mathrm{Id}_M)\right)\right).$$

Integrating $f(\gamma(t))$ over one period of the orbit $\gamma(t) = \phi_0 + \omega t$ yields

$$\int_0^T f(\gamma(\hat{t}))\,\mathrm{d}\hat{t} = \left[\sin(\alpha)\ln(1 + \delta g(\gamma(\hat{t}))) + \hat{t}\cos(\alpha)\right]_{\hat{t}=0}^{\hat{t}=T}$$

$$= T\cos(\alpha) = \frac{2\pi}{\omega}\cos(\alpha).$$

Combining this with the fact that the eigenvalues of $\exp(\frac{a}{M}(J_M - M\mathrm{Id}_M))$ are e^{-a} with multiplicity $M-1$ and 1 with multiplicity 1, we infer that the critical PRMM is

$$\lambda^{\mathrm{crit}} = \exp\left(\frac{-2\pi K}{\omega}\cos(\alpha)\right). \tag{4.4.3}$$

Interestingly, this is independent of δ even though the system $(1, \infty)$-phase reduction includes all orders in δ. Consequently, the stability of a synchronized orbit is unaffected by δ in any phase reduction without higher-order interactions. A similar calculation[4] yields that the critical PRMM of the synchronized orbit in a $(2, 0)$-phase reduction is

$$\lambda^{\mathrm{crit}} = \exp\left(\frac{-2\pi K}{m\omega}(m\cos(\alpha) - K\sin(\alpha)^2)\right). \tag{4.4.4}$$

The critical PRMM in a $(2, 1)$-phase reduction agrees with (4.4.4), which can be shown using the formulas (4.3.13) and (4.3.15b) if $g(\phi) = \sin(\phi)$. When g is a general function, the formulas to show that can be found in Appendix A. Finally, when $g(\phi) = \sin(\phi)$, the critical PRMM in a $(2, 2)$-phase reduction it is given by

$$\lambda^{\mathrm{crit}} = \exp\left(\frac{-2\pi K}{m\omega(m^2 + \omega^2)}\Big(m^3\cos(\alpha) + m\omega^2\cos(\alpha) - Km^2\sin(\alpha)^2\right.$$

$$\left. - 2Km^2\delta^2\sin(\alpha)^2 - K\omega^2\sin(\alpha)^2\Big)\right), \tag{4.4.5}$$

which finally shows the dependence on δ.

Having derived stability conditions for synchronized orbits in phase-reduced system, we now analyze the stability of the synchronized orbit in the full system. Unfortunately, when applying the concept (4.4.2) to the full system, the matrices $A(t)$ and $A(s)$ do not commute with each other. Therefore, it is not possible to

---

[4]The MATHEMATICA code, that calculates these PRMMs, is available on GitHub, see [33].

use the matrix exponential to analytically compute PRMMs and Floquet exponents, but we have to resort to numerical methods to determine them. Yet, in the special case $\delta = 0$, the stability analysis of these periodic orbits simplifies quite significantly. In fact, in this case, the full system has a $\mathbb{T}$ symmetry, which acts by shifting all oscillators by a constant phase. Then, one can also change to a co-rotating coordinate frame, in which $\omega = 0$. In these new coordinates all synchronized states are then equilibria. The spectrum of the right-hand side of the system at the synchronized state then contains information about the stability. There will be one zero eigenvalue, since there is a one-dimensional continuum of synchronized states. If all the other eigenvalues have negative real part, the synchronized state as an equilibrium in the co-rotating frame is linearly stable and thus the synchronized orbit in the original system inherits this stability. Conversely, if one eigenvalue has positive real part, the synchronized orbit in the original system is unstable. Conducting this analysis for the full system (4.3.3) yields that the linearization of the right-hand side is given by a matrix

$$\begin{pmatrix} m\mathrm{Id}_M + \frac{K}{M}\cos(\alpha)(J_M - M\mathrm{Id}_M) & -\frac{K}{M}\sin(\alpha)(J_M - M\mathrm{Id}_M) \\ \frac{K}{M}\sin(\alpha)(J_M - M\mathrm{Id}_M) & \frac{K}{M}\cos(\alpha)(J_M - M\mathrm{Id}_M) \end{pmatrix}. \qquad (4.4.6)$$

The eigenvalues of this matrix can explicitly be calculated and are given by

$$q_1 = 0,$$
$$q_{2,\dots,M} = \frac{1}{2}\left(m - 2K\cos(\alpha) + \sqrt{-2K^2 + m^2 + 2K^2\cos(2\alpha)}\right),$$
$$q_{M+1} = m,$$
$$q_{M+2,\dots,2M} = \frac{1}{2}\left(m - 2K\cos(\alpha) - \sqrt{-2K^2 + m^2 + 2K^2\cos(2\alpha)}\right),$$

where we denote them by q_k for $k = 1,\dots,2M$ because they describe the instantaneous rate of attraction to the periodic orbit and thus relate to the Floquet exponents. In fact, since this instantaneous rate of attraction is constant over the whole orbit, these eigenvalues agree with the Floquet exponents. Note that $m < 0$ and thus, when $K = 0$, we have $q_{2,\dots,M} = 0$ and $q_{M+1,\dots,2M} = m$, which is the rate of attraction to the limit cycle. Consequently, the first M eigenvalues correspond to perturbations of the phases ϕ and the last M eigenvalues originate from perturbations in the radial directions. To compare this model with phase-reduced models, we assume that $|m|$ is big enough such that the last M eigenvalues can be neglected and the critical Floquet exponent q^{crit} is given by $q_2,\dots,q_M$. Of course there is also the zero eigenvalue q_1. However, that does not contribute to the stability as it corresponds to a perturbation along the continuum of synchronized states. Given the critical Floquet exponent, one can then obtain the critical PRMM by simply calculating $\lambda^{\mathrm{crit}} = \exp(q^{\mathrm{crit}}T) = \exp(\frac{2\pi}{\omega}q^{\mathrm{crit}})$. When $\delta \neq 0$ in

the full system, PRMMs can only numerically be calculated, as shown in Figure 4.2(a). Figures 4.2(b-d) compare PRMMs from the full system with PRMMs from phase-reduced systems.
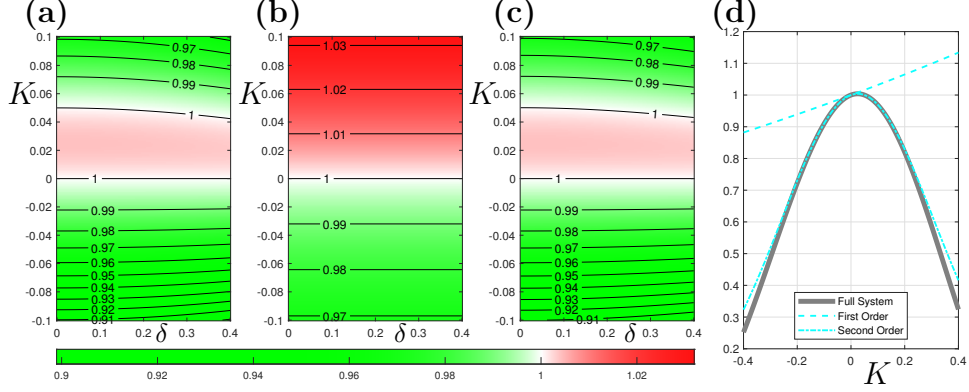
Figure 4.2: Comparison of the critical multipliers of the Poincaré return map of the synchronized orbit in the full system and phase-reduced systems. Part (a) shows the critical PRMM of the synchronized orbit in the full system in dependence of δ and the coupling strength K. Part (b) depicts the critical PRMM (4.4.3) of the synchronized orbit in a $(1, \infty)$-phase reduction and part (c) illustrates the critical PRMM (4.4.5) of the same orbit in a $(2, 2)$-phase reduction. Finally, part (d) depicts the critical PRMM in the full system, the $(1, \infty)$-phase reduction and the $(2, 2)$-phase reduction when $\delta = 0$. Note that the range of K in part (d) is wider than in parts (a)-(c). As one can see in part (d), the critical PRMM in the full system agrees with the critical PRMM of a $(2, 2)$-phase reduction for a wide range of K. Parameter values: $\omega = 1, m = -1, \alpha = \pi/2 + 1/20, g(\phi) = \sin(\phi)$.

4.4.2   The Splay Orbit

While all oscillators gather at one point on the circle if they are synchronized, one can say that the splay state is the opposite of that. A splay state is given when the oscillators phases are equidistantly distributed on the circle. More specifically, a state $\phi \in \mathbb{T}^M$ is a splay state if there is a permutation $\sigma \colon [M] \to [M]$ such that

$$\phi_{\sigma(k+1)} = \phi_{\sigma(k)} + \frac{2\pi}{M},$$

for $k = 1, \ldots, M - 1$. By relabeling the nodes, we might also assume that σ is the identity map. Thus, the set of splay states is given by

$$D := \{\phi \in \mathbb{T}^M : \phi_{k+1} = \phi_k + \frac{2\pi}{M} \text{ for } k = 1, \ldots, M - 1\}. \qquad (4.4.7)$$

A splay state in this set can be characterized by just the first phase ϕ_1. This set has a $Z_M := \mathbb{Z}/(M\mathbb{Z})$ symmetry group that acts on a state by shifting the indices, which have to be understood modulo M, of each oscillator by a constant integer. Now, let us consider the set of splay states in phase-reduced systems with $\delta = 0$. Since the right-hand sides of $(1,0)$- and $(2,0)$-phase-reduced systems are equivariant with respect to this group action, the set of splay states is dynamically invariant. In particular, when inserting a splay state into the right-hand side of a $(1,0)$-phase reduction and a $(2,0)$-phase reduction, it follows that $\dot{\phi}_k = \omega - K \sin(\alpha) =: \hat{\omega}$. Therefore, if $\hat{\omega} \neq 0$, there exists a periodic orbit $\gamma^{\mathrm{pr}}(t) \in \mathbb{T}^M$ with $\gamma_k^{\mathrm{pr}}(t) := \hat{\omega}t + \frac{2\pi k}{M}$, that has period $T = \frac{2\pi}{\hat{\omega}} = \frac{2\pi}{\omega - K \sin(\alpha)}$. We refer to this orbit as the splay orbit.

Next, we consider splay states in the full system (4.3.3) and still assume $\delta = 0$. Inserting the ansatz (4.4.7) into the full system (4.3.3) yields that the amplitudes on the invariant torus are given by

$$R_k \equiv \frac{1}{2} \left(1 + \sqrt{1 + \frac{4K \cos(\alpha)}{m}} \right) =: R^\star. \tag{4.4.8}$$

Therefore, we call a state $(R, \phi) \in \mathbb{R}_{\geq 0}^M \times \mathbb{T}^M$ a splay state if $\phi \in D$ and the amplitudes satisfy (4.4.8). Then, the splay state in the full system has the same symmetry group Z_M as splay states in phase-reduced systems. Moreover, since the right-hand side of the full system (4.3.3) is again equivariant with respect to this symmetry group, the splay state is dynamically invariant. Furthermore, the angular frequency of the phases is $\dot{\phi}_k = \omega - K \sin(\alpha) = \hat{\omega}$ as for phase-reduced systems. Therefore, there exists a periodic orbit $\gamma^{\mathrm{f}}(t) = (R^{\mathrm{f}}(t), \phi^{\mathrm{f}}(t))^\top$ with $R_k^{\mathrm{f}}(t) = R^\star$ and $\phi_k^{\mathrm{f}}(t) = \hat{\omega}t + \frac{2\pi k}{M}$, that has the same period as the one in phase-reduced systems.

When analyzing the stability of these splay orbits in both phase-reduced and the full system, it is important to note that splay orbits are just one single periodic orbit in a whole continuum of periodic orbits. In particular, in phase-reduced systems, all incoherent states, that are characterized by

$$Z := \frac{1}{M} \sum_{k=1}^M e^{\mathrm{i}\phi_k} = 0, \tag{4.4.9}$$

rotate around the circle with constant frequency $\hat{\omega}$. In the full system states $(R, \phi) \in \mathbb{R}_{\geq 0}^M \times \mathbb{T}^M$ with $R_k = R^\star$ for $k = 1, \ldots, M$ and $Z = 0$ rotate around the circle with the same constant frequency. Therefore, there exist further periodic orbits, which we refer to as incoherent orbits. Since a splay state is a special incoherent state, but in general the set of incoherent states is larger than the set of splay states, the splay orbit is only one orbit in a continuum of incoherent orbits.

Consequently, when analyzing the stability of the splay orbits with PRMMs or Floquet exponents, there is always one neutral multiplier or exponent, respectively. The only exception is present when the set of incoherent states coincides with the set of splay states, i.e., when $M = 3$. To overcome the problem of neutral stability, we restrict ourselves to $M = 3$.

If $\delta = 0$, we can change into a rotating frame coordinate system, in which splay states are equilibria. After having done that, we linearize the right-hand side at the splay state and thereby obtain Jacobians with eigenvalues

$$q_1 = 0, \quad q_{2,3} = \frac{K}{2} e^{\pm i\alpha}$$

in a $(1, 0)$-phase reduction and

$$q_1 = 0, \quad q_{2,3} = \frac{K}{2} e^{\pm i\alpha} \left(1 - \frac{1}{2m} K e^{\pm i\alpha} \right)$$

in a $(2, 0)$-phase reduction. An analytical derivation of the eigenvalues in the full system turned out to be too complicated. In both cases, the critical Floquet exponent is given by $q^{\mathrm{crit}} = q_{2,3}$ and thus the critical PRMM is $\lambda^{\mathrm{crit}} = e^{T q^{\mathrm{crit}}}$.

While all the previous theory was only valid for $\delta = 0$, we now investigate what happens if $\delta \neq 0$. In this case, the right-hand sides of both the phase-reduced systems and the full system are no longer equivariant with respect to Z_M. Therefore, splay states are in general not invariant anymore. However, when $M = 3$ and $\delta = 0$, there is a single periodic orbit, i.e., the splay orbit. For general parameter values, this orbit has no PRMMs whose absolute value equals 1. Thus, this splay orbit is hyperbolic. Slight changes in δ away from 0 preserve the existence of a periodic orbit in the neighborhood of the splay orbit. To illustrate the stability of these orbits, we numerically search for periodic orbits in a neighborhood of the splay orbit in the full system and phase-reduced systems. Then, we numerically calculate their critical PRMMs to determine the stability of these orbits, see Figure 4.3.

A numerical analysis revealed that there is a subcritical Neimark-Sacker bifurcation in Figure 4.3(f) when K is negative and the modulus of the critical PRMM passes through 1. In particular, there are two complex conjugated PRMMs that pass through the complex unit circle. This correctly represents the bifurcation behavior of the full system, as in Figure 4.3(d). A $(1, \infty)$-phase reduction does not even capture the bifurcation, see Figure 4.3(e). The bifurcation at $K = 0$ is degenerate. When $K = 0$ there is no coupling and so all eigenvalues and Floquet exponents are 0.
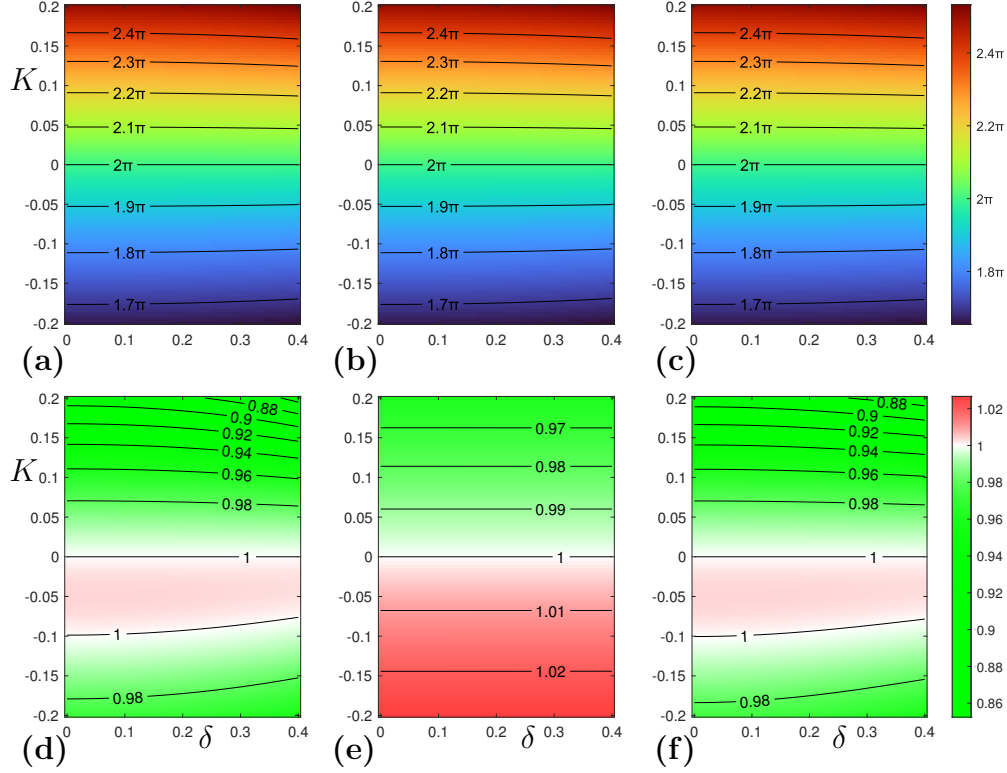
Figure 4.3: Numerical calculation of periods and critical multipliers of the Poincaré return map of periodic orbits in a neighborhood of the splay orbit. The first column represents the full system, the second column is the $(1, \infty)$-phase reduction and the third column displays the $(2, 2)$-phase reduction. The upper row is the period of the resulting periodic orbit, while the lower row depicts the critical PRMM of this orbit. Parameters: $\alpha = \pi/2 + 1/20, m = -1, \omega = 1, M = 3, g(\phi) = \sin(\phi)$

4.5 Phase Reduction Beyond All-To-All Coupled Networks

In Sections 4.3 and 4.4, we have started with a system of coupled oscillators, derived various phase reductions and compared the stability of synchronized and splay orbits. The system (4.3.2), that we started with, consists of M complex Stuart–Landau oscillators coupled with each other via a mean-field coupling, i.e., each oscillator influences every other oscillator in the same way. However, instead of such an all-to-all coupling, one could also assume that the coupling between oscillators is described by a graph. In Section 4.5.1 we adopt our calculations from the previous sections to a non all-to-all coupling and Section 4.5.2 then contains an interpretation of the higher-order interactions terms that we derive from

a phase reduction of nonlocally coupled Stuart–Landau oscillators. This provides additional evidence that it is important to study dynamical systems on hypergraphs which have recently been encountered in many different contexts; see for example [160, 35, 156, 78, 80, 69].

4.5.1   Derivation of the Phase-Reduced Dynamics

Now, let us assume that the coupling structure is not given by an all-to-all topology, but instead by a (possibly directed and weighted) graph $\Gamma = (V, E)$ that is described by its adjacency matrix $A \in \mathbb{R}^{M \times M}$ with entries a_{kl}. Then, the governing equation is

$$\dot{A}_k = \mathcal{F}(A_k) + K e^{i\alpha} \frac{1}{M} \sum_{l=1}^{M} a_{kl} \, (A_l - A_k), \qquad (4.5.1)$$

which contains (4.3.2) as a special case when $a_{kl} = 1$ for all $k, l = 1, \ldots, M$. Now, one can do the same analysis as in Section 4.3, but with (4.5.1) as a starting point. The procedure from Section 4.3 is directly applicable to (4.5.1), only the resulting formulas are slightly different. Therefore, will not explain the whole procedure again, but only state the results.

The system (4.5.1) can be written in polar coordinates $A_k = r_k e^{i\phi_k}$. Transforming the radii as $R_k = r_k / (1 + \delta g(\phi_k))$ yields the system

$$\dot{R}_k = F(R_k, \phi_k) + K G_k(R, \phi) \qquad (4.5.2a)$$

$$\dot{\phi}_k = \omega + K H_k(R, \phi), \qquad (4.5.2b)$$

with functions F, G_k and H_k defined by

$$F(R_k, \phi_k) = m R_k^2 (R_k - 1)(1 + \delta g(\phi_k))^2,$$

$$G_k(R, \phi) = \frac{1}{M} \sum_{l=1}^{M} a_{kl} \left[R_l \frac{1 + \delta g(\phi_l)}{1 + \delta g(\phi_k)} \cos(\phi_l - \phi_k + \alpha) - R_k \cos(\alpha) \right.$$

$$\left. - \delta g'(\phi_k) \left(R_l \frac{1 + \delta g(\phi_l)}{(1 + \delta g(\phi_k))^2} \sin(\phi_l - \phi_k + \alpha) - R_k \frac{\sin(\alpha)}{1 + \delta g(\phi_k)} \right) \right],$$

$$H_k(R, \phi) = \frac{1}{M} \sum_{l=1}^{M} a_{kl} \left[\frac{R_l(1 + \delta g(\phi_l))}{R_k(1 + \delta g(\phi_k))} \sin(\phi_l - \phi_k + \alpha) - \sin(\alpha) \right].$$

The existence of an invariant torus as in (4.3.4) is still guaranteed. Therefore, proceeding as in Section 4.3, we obtain the first-order phase reduction

$$\dot{\phi}_k = \omega + K P_k^{(1,\star)}(\phi) = \omega + K H_k(\mathbb{1}, \phi)$$

$$= \omega + K \frac{1}{M} \sum_{l=1}^{M} a_{kl} \left[\frac{1 + \delta g(\phi_l)}{1 + \delta g(\phi_k)} \sin(\phi_l - \phi_k + \alpha) - \sin(\alpha) \right]. \tag{4.5.3}$$

To obtain second-order phase reductions in K, we need to solve the PDE (4.3.9). When $\delta = 0$, this PDE has the solution

$$R_k^{(1,0)}(\phi) = \frac{1}{Mm} \sum_{l=1}^{M} a_{kl} s_0(\phi_k, \phi_l),$$

with $s_0(\phi_k, \phi_l)$ as in (4.3.11). Similarly, if $g(\phi) = \sin(\phi)$, on the first order in δ the solution is

$$R_k^{(1,1)}(\phi) = \frac{1}{2M(m^2 + \omega^2)} \sum_{l=1}^{M} a_{kl} s_1(\phi_k, \phi_l),$$

where $s_1(\phi_k, \phi_l)$ is as in (4.3.14). Finally, if $g(\phi) = \sin(\phi)$, the solution on second order in δ is

$$R_k^{(2,1)}(\phi) = \frac{1}{-4mM(m^4 + 5m^2\omega^2 + 4\omega^4)} \sum_{l=1}^{M} a_{kl} s_2(\phi_k, \phi_l).$$

To determine the second-order phase reduction in K, one also needs to calculate the gradient of H as illustrated in (4.3.15). It turns out that

$$\nabla_R H_k^{(-,0)}(\mathbb{1}, \phi) = \frac{1}{M} \begin{pmatrix} a_{k1} \sin(\phi_1 - \phi_k + \alpha) \\ \vdots \\ a_{kM} \sin(\phi_M - \phi_k + \alpha) \end{pmatrix} - \frac{1}{M} e_k \sum_{l=1}^{M} a_{kl} \sin(\phi_l - \phi_k + \alpha)$$

and that gradients on higher order in δ are generally of the form

$$\nabla_R H_k^{(-,\beta)}(\mathbb{1}, \phi) = \frac{1}{M} \begin{pmatrix} a_{k1} w_\beta(\phi_k, \phi_1) \\ \vdots \\ a_{kM} w_\beta(\phi_k, \phi_M) \end{pmatrix} - \frac{1}{M} e_k \sum_{l=1}^{M} a_{kl} w_\beta(\phi_k, \phi_l),$$

for $\beta = 0, 1, 2, \ldots$, where w_β are trigonometric polynomials. Now, calculating the second-order contributions $P_k^{(2,0)}(\phi)$ yields[5]

$$P_k^{(2,0)}(\phi) = -\frac{1}{2M^2m} \sum_{l=1}^{M} \sum_{i=1}^{M} a_{kl} a_{ki} \Big(\sin(\phi_i - \phi_l) - \sin(\phi_i - 2\phi_k + \phi_l + 2\alpha)$$

$$- \sin(\phi_k - \phi_l) - \sin(\phi_k - \phi_l - 2\alpha) \Big). \tag{4.5.4a}$$

---

[5]The expression for $P_k^{(2,1)}(\phi)$ and $P_k^{(2,2)}(\phi)$ can be generated with the MATHEMATICA code, which is available on GitHub, see [33].

$$+ \frac{1}{2M^2m} \sum_{l=1}^{M} \sum_{i=1}^{M} a_{kl} a_{li} \Big(\sin(\phi_i + \phi_k - 2\phi_l) - \sin(\phi_k - \phi_l)$$

$$- \sin(\phi_k - \phi_l - 2\alpha) - \sin(\phi_i - \phi_k + 2\alpha) \Big)$$

$$(4.5.4b)$$

The next subsection discusses these second-order contributions.

4.5.2   Second-Order Phase Reductions as Higher-Order Networks

We now discuss the individual coupling terms that constitute the $(2,0)$-phase reduction. The coupling includes nonpairwise terms and we discuss how the coupling can be interpreted as a higher-order phase oscillator network on hypergraphs that can be derived from the original graph $\Gamma = (V, E)$ that describes the coupling of the nonlinear oscillators. In summary, the $(2,0)$-phase reduction is given by

$$\dot{\phi}_k = \omega + K P_k^{(1,0)}(\phi) + K^2 P_k^{(2,0)}(\phi),$$

where

$$P_k^{(1,0)}(\phi) = H_k^{(-,0)}(\mathbb{1}, \phi) = \frac{1}{M} \sum_{l=1}^{M} a_{kl} \Big(\sin(\phi_l - \phi_k + \alpha) - \sin(\alpha) \Big) \qquad (4.5.5)$$

agrees with (4.5.3) for $\delta = 0$ and $P_k^{(2,0)}(\phi)$, as specified in (4.5.4), contains the second-order terms. First, note that the coupling of the first-order phase reduction (4.5.5) is posed on the graph $\Gamma^{(1)} := \Gamma$ that describes the interactions of the coupled nonlinear oscillator network.

The second-order phase interaction terms (4.5.4) not only contain pairwise interactions along network edges but also nonpairwise interactions between triplets of oscillators. On a broad level, these can be interpreted as phase interactions on two 3-uniform directed hypergraph, defined by the 3-tensors $\hat{h}, \bar{h} \in \mathbb{R}^{M \times M \times M}$ with coefficients

$$\hat{h}_{kli} := a_{kl} a_{ki}, \qquad \bar{h}_{kli} := a_{kl} a_{li},$$

where a triplet (k, l, i) describes the strength of the group interaction between three nodes k, l, i on node k. The coupling functions along these hyperedges are

$$\hat{g}(\phi_k, \phi_l, \phi_i) = 2\cos(\alpha)\sin(\phi_l - \phi_k + \alpha) + \sin(\phi_i - \phi_l) - \sin(\phi_i - 2\phi_k + \phi_l + 2\alpha),$$
$$\bar{g}(\phi_k, \phi_l, \phi_i) = 2\cos(\alpha)\sin(\phi_l - \phi_k + \alpha) - \sin(\phi_i - \phi_k + 2\alpha) + \sin(\phi_i + \phi_k - 2\phi_l).$$

$$(4.5.6)$$

$$\sin(\phi_l - \phi_k + \alpha) \qquad \sin(\phi_i - \phi_l) \qquad \sin(\phi_i - 2\phi_k + \phi_l + 2\alpha)$$

(a1) **(b1)** **(c1)**

$$\sin(\phi_l - \phi_k + \alpha) \qquad \sin(\phi_i - \phi_k + 2\alpha) \qquad \sin(\phi_i + \phi_k - 2\phi_l)$$

(a2) **(b2)** **(c2)**
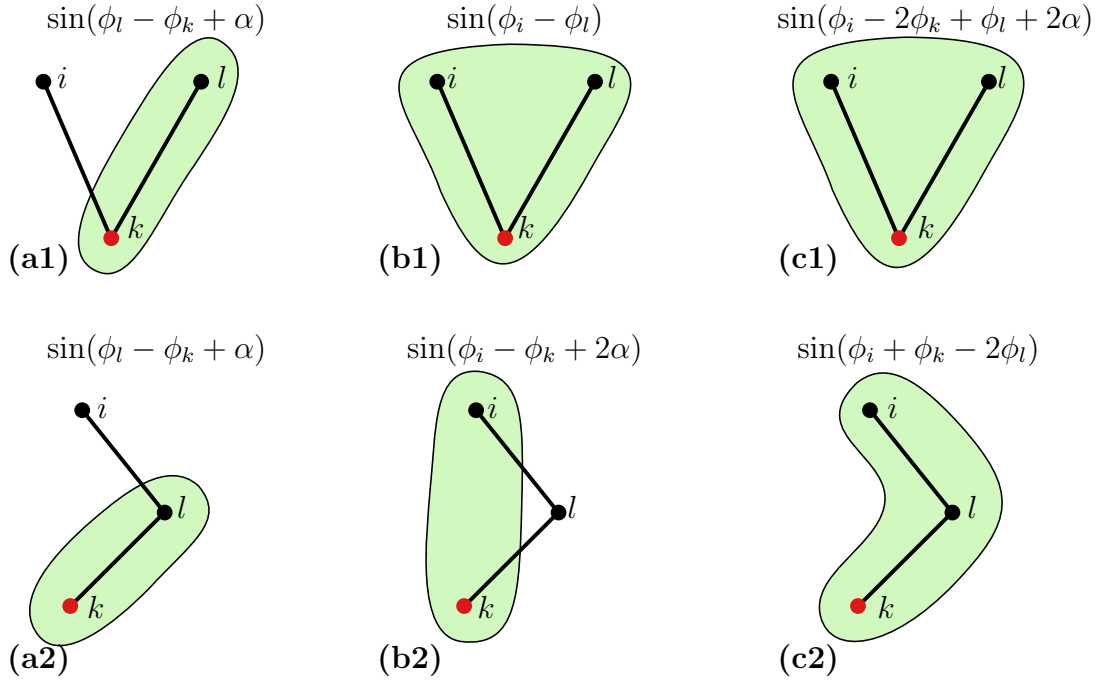
Figure 4.4: Illustration of second-order phase interactions in K that affect node k (indicated in red). The first row corresponds to terms appearing in $\hat{g}$, while the second row lists terms of $\bar{g}$. The black lines indicate edges in the graph Γ that describe the interaction of the unreduced nonlinear oscillator network. The (hyper)edges that describe the directed phase interactions are indicated by green blobs (with node k being the head). These include pairwise interactions (panels a1, a2), pairwise interactions that may be virtual (panel b2), and three types of nonpairwise interactions (panels b1, c1, c2).

These can be obtained from (4.5.4) using trigonometric identities and we have

$$P_k^{(2,0)}(\phi) = -\frac{1}{2M^2m}\sum_{l,i=1}^{M}\hat{h}_{kli}\hat{g}(\phi_k, \phi_l, \phi_i) + \frac{1}{2M^2m}\sum_{l,i=1}^{M}\bar{h}_{kli}\bar{g}(\phi_k, \phi_l, \phi_i).$$

Since the coupling functions (4.5.6) contain both pairwise and nonpairwise phase interactions, the interaction structure can be further broken down: Each of the three summands can be associated with a particular type of interaction, which results in six subclasses in total. These are illustrated in Figure 4.4.

First, there are pairwise correction terms to the first-order phase reduction, that correspond to the first summand in the definition of $\hat{g}$ and $\bar{g}$; see (4.5.6). The coupling of these pairwise correction terms is posed on the graph $\Gamma_a^{(2)} := \Gamma$ that is the same graph as the coupling of the full system and the coupling of the first-order phase reduction $\Gamma^{(1)}$; see Figure 4.4(a). One of these pairwise correction terms is weighted with the degree of the node k; see Figure 4.4(a1), while the other

term is weighted with the degree of node l (that is in the neighborhood of k), see Figure 4.4(a2). Moreover, the interaction function $\sin(\phi_l - \phi_k + \alpha)$ agrees with the interaction function of a first-order phase reduction (4.5.5) up to the shift $\sin(\alpha)$ and a constant factor. Since the two pairwise correction terms in Figure 4.4(a) share the same coupling structure $\Gamma_{\mathrm{a}}^{(2)}$ and the same interaction function, they can be combined into

$$\frac{-\cos(\alpha)}{M^2 m} \left(\sum_{l=1}^{M} a_{kl}(\deg(k) - \deg(l)) \sin(\phi_l - \phi_k + \alpha) \right).$$

Based on this formula, one can see that the sign of the pairwise correction terms is determined by comparing the degree of node k with the average degrees of all neighbors l of k.

Next, consider the second summand in $\bar{g}$ that describes a pairwise interaction between node k and node i that is in the neighborhood of a neighbor l of k. While this yields a pairwise interaction from node i to node k, there may not necessarily be and edge $(i,k) \in E(\Gamma)$ from i to k in the graph Γ that describes the original network of coupled nonlinear oscillators. If $(i,k) \in E(\Gamma)$ then this second-order term describes a second-order correction to the first-order interaction. If $(i,k) \notin E(\Gamma)$ then this interaction can be considered as a virtual edge, which is present in a weighted graph $\Gamma_{\mathrm{b2}}^{(2)}$ defined by the adjacency matrix $C = (c_{ki})_{k,i=1,\ldots,M}$ with coefficients $c_{ki} := \sum_l a_{kl} a_{li}$ but not in Γ. As one can see from the definition of the entries c_{ki} of the adjacency matrix of $\Gamma_{\mathrm{b2}}^{(2)}$, this interaction is weighted by the number of paths connecting k to i in the graph Γ.

Third, the second summand of $\hat{g}$ represents a part of the second-order interactions, in which two nodes i and l, that are both neighbors of k, influence the node k. Thus, there is a nonpairwise interaction as two nodes jointly influence a third node (even though the interaction is independent on the state of k); see Figure 4.4(b1). This interaction can be represented by a directed and possibly weighted hypergraph $\mathcal{H}_{\mathrm{b1}}^{(2)}$, which could be described by a 3-tensor indexed by k, l, i. Then, there would be a symmetry by swapping the indices l and i, but this hypergraph is in general still directed as one can not arbitrarily permute all indices k, l, i.

Finally, there are two further triplet interactions. The first triplet interaction, i.e., the last summand in the definition of $\hat{g}$ is an interaction between two neighbors i and l of the node k. The coupling structure of this interaction can be described by a directed and weighted hypergraph $\mathcal{H}_{\mathrm{c1}}^{(2)}$, whose 3-tensor agrees with $\hat{h}$. Note that there is a symmetry between i and l, but one cannot arbitrarily permute all indices which is why in general the hypergraph is directed. The second triplet interaction, which is governed by the last summand in the definition of $\bar{g}$, is one between the node k itself, a neighbor l of k and a neighbor i of l. Again,

the coupling structure can be described by a directed hypergraph $\mathcal{H}_{c2}^{(2)}$. This time, however, the 3-tensor, that describes this hypergraph and corresponds with $\bar{h}$, does not possess any symmetry with respect to a permutation of indices.

To summarize, the first-order phase reduction, that we have considered, consists of only one interaction term, whose coupling structure $\Gamma^{(1)}$ agrees with the coupling structure Γ of the full system (4.5.2). In a second-order phase reduction, quite a few new interaction terms appear. While the coupling of some of them is posed on a graph that agrees with Γ, the coupling of others is determined by a graph that consists of virtual edges that might not be present in Γ. Moreover, there are also three types of triplet interactions on directed hypergraphs, which can be derived from the adjacency matrix of Γ.

To conclude this section, we want to remark that a second-order phase reduction contains interaction terms on directed hypergraphs, even when the underlying graph Γ, that determined the coupling in the full system (4.5.2), is undirected and unweighted. The only exception is when Γ itself is an all-to-all graph. However, whenever Γ is connected, yet non all-to-all, there exists an open triangle as seen in Figure 4.4(c1), which causes the hypergraph, that governs the second-order phase reduction, to be directed.

4.6 Summary

Phase reductions provide a useful tool to analyze the dynamics of coupled oscillator networks. Here, we derived explicit expressions for nonlinear oscillations with phase-dependent amplitude subject to simple mean-field coupling. By using a suitable coordinate transformation, our results also apply to systems where the limit cycle is simple but the coupling is phase dependent or a combination thereof.

While the shape of the limit cycle affects the collective dynamics, a first-order phase reduction is insufficient to capture the dynamical effects of the amplitude dependence: The phase reduction needs to be at least of second order in both the coupling strength K and the parameter δ that describes the perturbation from a circular limit cycle. We showed that second-order phase reductions were able to accurately predict the stability properties of the synchronized and splay orbit when all terms of up to second order in K and δ are included. Importantly, the amplitude dependence breaks the rotational symmetry of phase equations that is typical, for example, of the Kuramoto equations. While such symmetry breaking has been analyzed from the perspective of the phase equations [42], it arises in our setup through a perturbation of the underlying nonlinear oscillator. This perspective allows to make direct comparisons between the nonlinear system and the phase-reduced dynamics in contrast to phase reductions via normal forms [10], where normal form symmetries—that may be absent in the full equations [56]—can

appear in the phase reduction.

As detailed in Section 4.5.2, the second-order phase interaction term for coupled oscillators on a given graph Γ can be interpreted as phase oscillator dynamics on (directed) hypergraphs. Specifically, the second-order phase interaction terms correspond to second-order corrections of interactions along edges of Γ, possible virtual pairwise connections between oscillator pairs that are not joined by an edge in Γ, and nonpairwise triplet interactions of different type.

Chapter 5

Bifurcation Analysis of Twisted States in Nonlocally Coupled Higher-Order Phase Oscillator Networks

The content of this chapter is based on the publication [22], which is joint work together with Christian Bick and Christian Kuehn. In particular, the technical parts are taken from this publication, of which I am the main author.

5.1   Introduction

While the classical Kuramoto model (1.1.1) assumes all-to-all coupling, in many real-world systems the coupling is actually not all-to-all but interactions are captured by a graph. As an example, each oscillator may have a spatial position and coupling between oscillators depends on their positions; such networks often arise in neural field modeling [5, 55, 66], where coupling strength typically relates to the distance of nodes. These coupling schemes can be realized by considering Kuramoto oscillators on a graph. Suppose there are M oscillators and this graph is given by its adjacency $A = (a_{ij})_{i,j=1,\dots,M}$. Then, there is a coupling between two oscillators i and j if $a_{ij} = 1$ and the oscillators are uncoupled if $a_{ij} = 0$. The phase $\phi_i \in \mathbb{T} := [0, 2\pi]/(0 \sim 2\pi)$ of oscillator i evolves according to

$$\dot{\phi}_i = \omega_i + \frac{1}{M} \sum_{j=1}^{M} a_{ij} \sin(\phi_j - \phi_i), \tag{5.1.1}$$

for $i = 1, \dots, M$. Graphs that do not describe all-to-all coupling allow for more interesting dynamics beyond full phase synchrony [149]. For example, one can

79

consider a $\Bbbk$-nearest neighbor graphs of M nodes: As illustrated in Section 2.1, the oscillators are arranged around a circle and each oscillator is coupled to all of its $\Bbbk$ predecessors and all of its $\Bbbk$ successors. In other words, $a_{ij} = 1$ if $\min(|i - j|, M - |i - j|) \leq \Bbbk$ and $a_{ij} = 0$ otherwise. Changing $\Bbbk$ changes the coupling range: For $\Bbbk = 1$ we have a ring with local nearest neighbor coupling, for $\Bbbk = M/2$ the network is globally all-to-all coupled, and for intermediate $\Bbbk$ the coupling is often called nonlocal. On such networks, the Kuramoto model with $\omega_i \equiv 0$ converges to many interesting patterns. For example regular twisted states [177] or irregular chimera states [136, 180] when we allow for phase lag parameters in the coupling function.

While the classical Kuramoto model assumes interactions between pairs of oscillators, higher-order interactions can have a profound impact on the dynamics; cf. [16, 23]. Such nonpairwise interactions arise naturally in phase oscillator networks that originate from (higher-order) phase reductions, see Chapter 4, and become important for the dynamics as the coupling strength is increased [10, 114]. Moreover, nonpairwise interactions also arise in ring-like networks of nonlocally coupled oscillators: In [121], the authors consider a network of eight nanoelectromechanical oscillators coupled via higher-order nearest neighbor interactions. They found that this system exhibits complex and exotic states even though the coupling functions are fairly simple.

It turns out, that instead of analyzing twisted states on large finite networks, it is easier to consider them in the continuum limit, as introduced in Section 2.3. In order for this continuum limit to be well defined, or specifically, in order for the network sequence to converge to a graphon, the parameter $\Bbbk$ has to scale with the system size M. Thus, we fix a coupling range $r = \Bbbk/M$ and send $M \to \infty$ to obtain a well defined continuum limit. Then, we consider the dynamics of this continuum limit. In particular, we analyze the stability and the bifurcation around twisted states. While twisted states have originally been studied in [177], a lot of research has been done to generalize these results [126, 125, 122, 137, 136, 48, 71].

In this chapter, we propose an extension of the pairwise coupling in the continuum limit to higher-order interactions. We study the stability of twisted states and show how this property is influenced by higher-order interactions. To this end, we analyze the bifurcation point where a twisted state loses or gains stability. We investigate which nontrivial equilibria bifurcate from the twisted states and how they depend on the parameters of the system, which are the coupling range r and the strengths of the higher-order interactions. We apply this theory to regular models without higher-order interactions and thereby extend the analysis from many previous works by a bifurcation analysis. Moreover, we show how higher-order interactions can make twisted states stable or unstable and how they affect the type of the bifurcation.

This chapter is organized as follows: In Section 5.2 we derive the continuum limit for the Kuramoto model on $\Bbbk$-nearest-neighbor networks, present the original stability analysis of twisted states [177] and mention related works on this topic. Section 5.3 introduces our system and clarifies general notation. Next, in Section 5.4, we first perform a Lyapunov–Schmidt reduction to convert the infinite-dimensional problem of finding equilibria in the continuum limit into a finite-dimensional problem. Then, we explain how to use the symmetry of the system to simplify the finite-dimensional problem into a two-dimensional one. Next, we tackle this two-dimensional problem to determine the type of the bifurcation. In the last part of this section, we derive equilibria approximations and analyze linear stability of bifurcating equilibria. Section 5.5 contains three interesting special cases, for which we conduct numerical simulations that illustrate and confirm the theory. In Section 5.6 we compare different ways of generalizing pairwise $\Bbbk$-nearest neighbor coupling to higher-order interactions and explain the advantages of our particular choice. Finally, Section 5.7 summarizes our findings.

5.2 Background

5.2.1 Continuum Limit Derivation

Even though we have already introduced a general continuum limit in Section 2.3, we repeat the derivation here for limits of nearest neighbor graphs. In fact, these graphs make the derivation special, as the coefficients a_{ij} of the adjacency matrix only depend on $i - j$. Thus, they can be represented as $a_{ij} = \hat{a}_{i-j}$ for some one-dimensional array of coefficients $\hat{a}$. By a slight abuse of notation, we drop the hat, and denote $a_i = 1$ if $\min(|i|, M - |i|) \leq \Bbbk$ and $a_i = 0$ otherwise. Then, the graph, whose adjacency matrix is given by $A = (a_{i-j})_{i,j=1,\dots,M}$, where the index $i - j \in [M]$ has to be understood modulo M, is a $\Bbbk$-nearest neighbor graph. On this graph we now consider M identical Kuramoto oscillators, i.e., $\omega_i \equiv \omega$ in (5.1.1), where without loss of generality $\omega = 0$. The phase ϕ_i of oscillator i then evolves according to

$$\dot{\phi}_i = \frac{1}{M} \sum_{j=1}^{M} a_{i-j} \sin(\phi_j - \phi_i), \quad \text{for } i = 1, \dots, M. \tag{5.2.1}$$

This ODE system is posed in the phase space $\mathbb{T}^M$ and the underlying coupling structure is illustrated in Figure 2.1(b). The system (5.2.1) has multiple symmetries. First, there is continuous symmetry that shifts all the oscillators by a common phase $\alpha \in \mathbb{T}$. Moreover, since a_{i-j} only depends on the difference $i - j$ and the network is symmetric, the system also has a finite symmetry group D_M,

which is the dihedral group consisting of $2M$ elements. For a full investigation of symmetry in this system see [11]. For $q \in \mathbb{Z}$, a q-twisted state is a phase configuration that satisfies

$$\phi_i^q = 2\pi q i / M + \alpha, \quad \text{for } i = 1, \dots, M, \tag{5.2.2}$$

where $\alpha \in \mathbb{T}$ is an arbitrary parameter, see Figure 5.1(a). The parameter q is also referred to as the winding number. By exploiting these symmetries and the odd symmetry of the coupling function sin, one can show that these q-twisted states are equilibria of (5.2.1). While showing the time invariance of a q-twisted state on (5.2.1) is relatively easy, investigating its stability turns out to be more complicated [71].
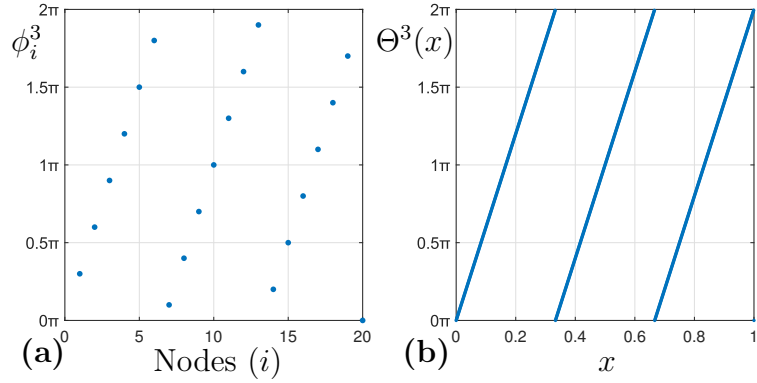
Figure 5.1: An illustration of the q-twisted state. Part (a) depicts the q-twisted state (5.2.2) for $q = 3$ in the finite dimensional. Part (b) shows its infinite-dimensional analog (5.2.9). In both cases the parameter α is set to 0. Even though it seems as if Θ^3 is discontinuous it is continuous when regarded as a function to $\mathbb{T}$.

To understand the stability of q-twisted states one often considers the continuum limit of the network dynamical system with infinitely many oscillators [177, 126]. Now, we repeat the derivation from Section 2.3 at the example of the model (5.2.1). Given a solution $\phi_i^M(t)$ of the system (5.2.1), one can derive the continuum limit by first defining a function $\Theta^M(t, x)$ as

$$\Theta^M(t, x) = \phi_i(t) \qquad \text{if } x \in \left[\frac{i-1}{M}, \frac{i}{M} \right). \tag{5.2.3}$$

Here, x represents the position of an oscillator in the infinite network limit. In order to distinguish the phase space $\mathbb{T}$ from the index set of the network nodes, we regard x as a variable on the unit circle $\mathbb{S} := [0, 1]/(0 \sim 1)$, that we parameterize from 0 to 1. This is slightly different from the convention in Section 2.3, where

$x \in I$, but here $x \in \mathbb{S}$ is more convenient for two reasons. First, $\mathbb{S}$ is more suitable to represent the ring-topology of a $\Bbbk$-nearest neighbor network, see Figure 2.1(b). Second, whenever $x, y \in \mathbb{S}$ we also have $x - y \in \mathbb{S}$, which would not be the case for I instead of $\mathbb{S}$. Since we often evaluate functions on $x - y \in \mathbb{S}$ we do not need to go through the hassle of periodically extending functions from I to $\mathbb{R}$ or evaluating them on $x - y \mod 1$. The function $\Theta^M(t, x)$ from (5.2.3) then satisfies

$$\frac{\partial}{\partial t}\Theta^M(t, x) = \int_{\mathbb{S}} W_r^M(x - y) \sin(\Theta^M(t, y) - \Theta^M(t, x)) \, \mathrm{d}y, \qquad (5.2.4)$$

where $W_r^M \colon \mathbb{S} \to \mathbb{R}$ is defined as

$$W_r^M(x) = a_i \qquad \text{if } x \in \left[\frac{i - 1}{M}, \frac{i}{M}\right),$$

for $x \in \mathbb{S}$. Keeping the coupling range $r := \Bbbk/M \in (0, \frac{1}{2}]$ fixed and letting $M \to \infty$, we formally obtain the limit $W_r^M \to W_r \in L^2(\mathbb{S})$, with

$$W_r(x) := \begin{cases} 1 & \text{if } \min(x, 1 - x) \leq r \\ 0 & \text{else} \end{cases}, \qquad (5.2.5)$$

where we consider the representation of $x \in \mathbb{S}$ in $[0, 1)$. This limiting process is illustrated in Figure 5.2. As W_r is an even function, the choice of W_r in (5.2.5)

(a)   **(b)**   **(c)**   **(d)**
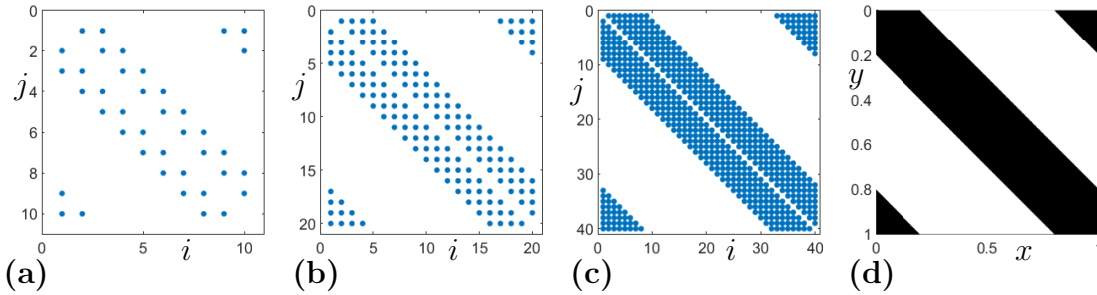
Figure 5.2: Limit of a sequence of nearest-neighbor networks. Here, the coupling range $r = \Bbbk/M$ is fixed to be 0.2. Parts (a)-(c) depict the adjacency matrix of $\Bbbk$-nearest neighbor graphs on $M = 10$, $M = 20$ and $M = 40$ nodes, respectively. There is a blue dot whenever $a_{i-j} = 1$ and no dot otherwise. Finally, part (d) shows the function $W_r(x - y)$. Its value is 1 in the black regions and 0 in the white regions.

yields a Fourier decomposition in which no sin-terms appear. In particular,

$$W_r(x) = \frac{1}{2}\hat{W}_r(0) + \sum_{k=1}^{\infty} \hat{W}_r(k) \cos(2\pi k x), \qquad (5.2.6)$$

with

$$\hat{W}_r(k) = \begin{cases} \frac{2\sin(2\pi kr)}{\pi k} & \text{if } k \neq 0, \\ 4r & \text{if } k = 0. \end{cases} \tag{5.2.7}$$

Now, suppose that $\lim_{M\to\infty} \Theta^M(t,x) = \Theta(t,x)$ for a function Θ. Then, formally taking the limit of (5.2.4) as $M \to \infty$, we obtain the continuum limit

$$\frac{\partial}{\partial t}\Theta(t,x) = \int_{\mathbb{S}} W_r(x-y)\sin(\Theta(t,y) - \Theta(t,x)) \, \mathrm{d}y. \tag{5.2.8}$$

In this continuum limit, a q-twisted state, see Figure 5.1(b), is given by a function $\Theta^q \colon \mathbb{S} \to \mathbb{T}$ with

$$\Theta^q(x) = 2\pi q x + \alpha. \tag{5.2.9}$$

Even though this derivation was formal, it can be rigorously shown that the continuum limit (5.2.8) approximates the dynamics of the finite system (5.2.1) for large M, see [124, 123, 105, 73].

5.2.2   The Original Analysis of Twisted States

In their analysis from 2006, the authors Wiley, Strogatz and Girvan numerically studied the global dynamics of the finite dimensional model (5.2.1), discovered twisted states as attractors and subsequently analyzed the their stability [177]. They began their study by numerically simulating this model for random initial conditions, i.e., ones for which $\phi_i(0)$ are independent and uniformly distributed on $\mathbb{T}$ for $i = 1, \ldots, M$. Simulating the system (5.2.1) for many sampled initial conditions of this kind gives numerical evidence that the only attractors of this model are q-twisted states (5.2.2). Moreover, they found that the probability to converge to the synchronized state ($q = 0$) increases with $\Bbbk$. In fact, on the one hand, if $\Bbbk \gtrsim 0.33M$ every initial condition converges to the synchronized state. On the other hand, the lower the value of $\Bbbk$ is, the more likely are q-twisted states to appear as attractors with higher values of $|q|$.

In particular, numerical simulations from [177] revealed that the probability that a random initial condition converges to a q-twisted state can be approximated with a Gaussian distribution, see Figure 5.3. The standard deviation of this Gaussian distribution decreases with $\Bbbk$, such that the synchronized state becomes a more likely attractor if $\Bbbk$ increases. Specifically, they found that the standard deviation σ of this Gaussian only depends on the coupling range $r = \Bbbk/M$ and can be approximated as $\sigma = a\sqrt{1/r} + b$ for some parameters $a > 0$ and $b \in \mathbb{R}$, see [177].
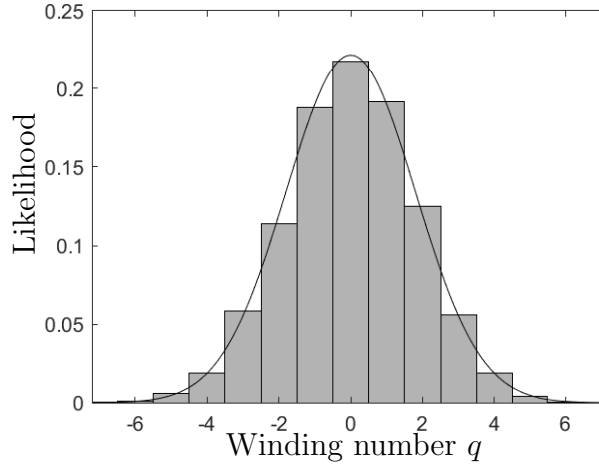
Figure 5.3: Twisted states as attractors for the system (5.2.1). A simulation for this system with parameters $M = 100$ and $\Bbbk = 1$ for 10^4 uniformly random initial conditions revealed only q-twisted states (5.2.2) as attractors. The histogram depicts the likelihood of converging to a twisted state with winding number q. Moreover, the bell curve is the probability density function of a Gaussian with zero mean and standard deviation $\sigma = 1.8$.

Note that the model (5.2.1) only admits finitely many q-twisted states, as a q-twisted state (5.2.2) agrees with a $q + M$-twisted state. However, the support of the Gaussian is unbounded and thus a Gaussian describes infinitely many twisted states as attractors. Consequently, the approximation of the probability of converging to a q-twisted state by a Gaussian cannot be very precise when M is small. If M gets larger and $r = \Bbbk/M$ is fixed, this approximation becomes better and better, as numerical simulations in [177] revealed.

Motivated by their numerical findings, the authors proceed to analytically analyze the stability of twisted states. Instead of conducting their analysis in the finite dimensional model (5.2.1), they switch to the continuum limit (5.2.8) since the analysis there is simpler and the dynamics of these two models is close if M is large, see Section 5.2.1. In this continuum limit, the q-twisted states (5.2.9) can be checked to be invariant, too. Inserting the ansatz

$$\Theta(t, x) = \Theta^q(x) + \eta(t, x),$$

for Θ^q as in (5.2.9) and a perturbation η with $|\eta| \ll 1$, into the continuum limit (5.2.8) yields

$$\frac{\partial}{\partial t}\eta(t, x) = \int_{\mathbb{S}} W_r(x - y) \sin(\Theta^q(y) - \Theta^q(x) + \eta(t, y) - \eta(t, x)) \, \mathrm{d}y$$

$$= \int_{\mathbb{S}} W_r(x-y) \Big[\sin(\Theta^q(y) - \Theta^q(x))$$

$$+ (\eta(t,y) - \eta(t,x)) \cos(\Theta^q(y) - \Theta^q(x)) + \mathcal{O}(\eta^2) \Big] \, \mathrm{d}y.$$

Now, keeping only linear terms in this equation and assuming an expansion $\eta(t,x) = \sum_{k \in \mathbb{Z}} \hat{\eta}_k(t) e^{2\pi \mathrm{i} k x}$ we obtain

$$\sum_{k \in \mathbb{Z}} \hat{\eta}'_k(t) e^{2\pi \mathrm{i} k x} = \sum_{k \in \mathbb{Z}} \hat{\eta}_k(t) \int_{\mathbb{S}} W_r(x-y)(e^{2\pi \mathrm{i} k y} - e^{2\pi \mathrm{i} k x}) \cos(2\pi q(y-x)) \, \mathrm{d}y.$$

Next, using the expansion (5.2.6) one can solve the integral on the right-hand side of the last equation (see Appendix B.1 for the details) and collect terms of order $e^{2\pi \mathrm{i} k x}$ resulting in

$$\hat{\eta}'_k(t) = \xi_k \eta_k(t), \quad \xi_k = \frac{1}{4}\Big(\hat{W}_r(q-k) + \hat{W}_r(q+k) - 2\hat{W}_r(q) \Big), \qquad (5.2.10)$$

for $k \in \mathbb{Z}$, where we use the convention $\hat{W}_r(-k) := \hat{W}_r(k)$ if $k \geq 0$. Note that $\xi_0 = 0$, so there always is a zero eigenvalue that corresponds to shifting the q-twisted state by a constant phase. As such a perturbation leaves the set of twisted states invariant, the authors argued that this zero eigenvalue can be neglected. Moreover, we have $\xi_k = \xi_{-k}$. As a consequence the authors of [177] came up with the stability condition $\xi_k < 0$ for all $k \in \mathbb{N}$ of a q-twisted state (5.2.9). Even though this stability analysis was very formal, it was later made rigorous and the linear stability was transferred to nonlinear stability [126].

5.2.3   Further Works about Twisted States

Since twisted states have been discovered as (stable) equilibria in (5.2.1) and (5.2.8) a lot of work has been conducted to analyze and generalize these equilibria in various different setting. A few selected works are presented below:

The authors of [71] analyzed the finite dimensional Kuramoto model (5.2.1) as well as the infinite dimensional continuum limit (5.2.8) on nearest neighbor graphs after a reversal of time $t \mapsto -t$. This is equivalent to multiplying the right-hand side of these two systems by the factor -1 or changing the interaction function from $\sin$ to $-\sin$. Since two oscillators in (5.2.1), that are close to each other, repel each other, this model and its continuum limit is also referred to as the repulsive Kuramoto model. For each winding number q, their analysis elucidates parameter regions for the coupling range r in which the q-twisted state is stable in the continuum limit of the repulsive Kuramoto model. Moreover, to compare the finite dimensional model to the continuum limit, they show that whenever a twisted state is asymptotically stable in the continuum limit, it is also asymptotically

stable in the finite dimensional system if the system size M is sufficiently large. Apart from focusing on the analysis of twisted states they also conduct numerical simulations with random initial conditions to explore the whole phase space of the repulsive Kuramoto model, which is in analogy with the simulation conducted in [177], see Section 5.2.2. It turns out that the global dynamics of the repulsive Kuramoto model on nearest neighbor graphs is fundamentally different than the dynamics of the model (5.2.1) with regular (attractive) coupling. In particular the repulsive Kuramoto model not only admits regular twisted states as attractive equilibria but also more complicated equilibria that the authors of [71] call multi-twisted states. While q-twisted states (5.2.2) have a constant phase difference $\phi_{i+1}^q - \phi_i^q = 2\pi q/M$, the phase differences of multi-twisted states are not constant. Specifically, they are roughly $2\pi q/M$ in one part and $-2\pi q/M$ in another part of the domain [71].

In [125] the authors consider twisted states (5.2.2) in a finite dimensional Kuramoto model with attractive and then with repulsive coupling. Instead of analyzing these twisted states on nearest neighbor graphs, they rather take more complicated graphs such as Paley graphs. Similarly to nearest neighbor graphs, the adjacency matrix of these Paley graphs is given by $(a_{i-j})_{i,j=1,\dots,M}$, such that their entries only depend on $i - j$. The type of this dependence is a bit more complicated and relies on a number theoretic relation, in particular, on the existence of square roots in the cyclic group $Z_M = \mathbb{Z}/(M\mathbb{Z})$. The authors of [125] found that the stability of q-twisted states then depends on the fact of whether q is a square in this cyclic group or not.

Instead of considering the Kuramoto model on a ring or $\Bbbk$-nearest neighbor graphs whose nodes can be parameterized by a one-dimensional variable one can extend the graph to two or even higher-dimensional lattices. In particular, the authors of [74] considered the Kuramoto model on a lattice of $M = M_1 M_2$ nodes where two nodes are connected if their distance in the grid with respect to a given norm is less than a certain threshold. Moreover, there are also edges connecting the nodes in the first row with corresponding nodes in the last row. Similarly, there are edges that warp around the lattice to connect the first column with the last column. In this scenario one can define generalized twisted states, that are characterized by a row-winding number $q_1 \in \mathbb{Z}$ and a column-winding number $q_2 \in \mathbb{Z}$. In analogy with (5.2.2), resulting (q_1, q_2)-twisted states are a linear function of the indices and are of the form

$$\phi_{ij}^{(q_1,q_2)} = 2\pi i q_1/M_1 + 2\pi j q_2/M_2 + \alpha,$$

where i is an index for the row of the oscillator and j describes the column of the oscillator. Moreover, $\alpha \in \mathbb{T}$ is a constant. The authors of [74] analyze these double twisted states and derive criteria for their stability.

A global numerical analysis for the same model shows that these doubly twisted states are not the only attracting equilibria [136]. Instead, one can also observe chimera-like patterns where the oscillators' phases seem to depend continuously on their indices in one part of the domain and irregularly behave in another part of the domain. Moreover, some of these patterns even show spiraling behavior [136].

Apart from the analysis of Kuramoto models on deterministic graphs, twisted states have also been analyzed on a variety of random graphs, such as Erdös–Rényi graphs [125] and small-world graphs, which can be regarded as an interpolation between $\Bbbk$-nearest neighbor networks and Erdös–Rényi graphs [122].

5.3   Our Model of Nonlocally Coupled Phase Oscillators with Higher-Order Interactions

5.3.1   Extension by Higher-Order Interactions

Motivated by the dynamical effects that higher-order interactions can generate and their ability to better approximate a coupled oscillator network, as seen in Chapter 4, we propose an extension of (5.2.8) that includes higher-order interactions. An example for triplet interactions between three oscillators at $x, y, z \in \mathbb{S}$ with phases $\Theta(t,x), \Theta(t,y), \Theta(t,z)$ at time t is given by $\sin(\Theta(t,z) + \Theta(t,y) - 2\Theta(t,x))$. To incorporate these nonpairwise higher-order interactions, we extend the continuum limit (5.2.8) in the natural way: For a network with pure triplet interactions the phases evolve according to

$$\frac{\partial}{\partial t}\Theta(t,x) = \int_{\mathbb{S}} \int_{\mathbb{S}} W(z,y,x) \sin(\Theta(t,z) + \Theta(t,y) - 2\Theta(t,x)) \, \mathrm{d}y \mathrm{d}z,$$

where $W \colon \mathbb{S}^3 \to \mathbb{R}$ is a general 3-tensor that describes in which triplets there is an interaction and thereby generalizes the weighted adjacency tensor for pairwise interactions.

As we are interested in q-twisted states, we consider a specific class of nonlocal higher-order interaction structure $W(z,y,x) = W_r(z + y - 2x)$ for the coupling function $\sin(\Theta(t,z) + \Theta(t,y) - 2\Theta(t,x))$. This higher-order network topology allows for long range connections: An oscillator x is not only influenced by triangles spanned by nodes neighboring x. Instead, if say $x = 0$, a triangle (x,y,z) exists when $|z + y| \leq r$ in $\mathbb{S}$, which is the case when for example $z = 1/4$ and $y = 3/4$. In particular, in this case $z + y - 2x = 0$ and thus this triangle exists for all coupling ranges $r > 0$, see Figure 5.4(a). In that sense, it is distinct from the "nearest neighbor" higher-order networks considered in [121].

We focus on this interaction structure and coupling function for several reasons. First, the coupling function $\sin(\Theta(t,z) + \Theta(t,y) - 2\Theta(t,x))$ arises in higher-order
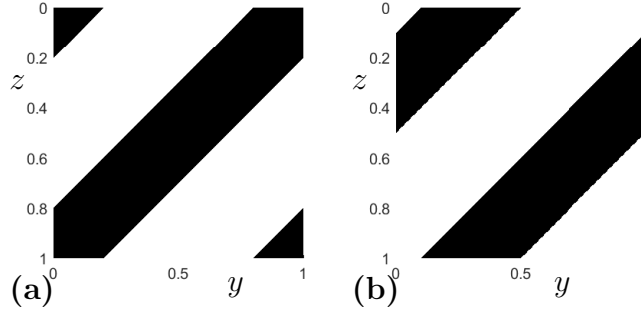
Figure 5.4: Network topology of the triplet interactions. Part (a) shows all pairs (y, z) for which a triangle between (x, y, z) for $x = 0$ exists, i.e., that satisfy $W_r(z + y - 2 \cdot 0) = 1$. There pairs are depicted by the black area. In part (b) we have $x = 0.15$ and the black region depicts pairs (y, z) such that $W_r(z + y - 2 \cdot 0.15) = 1$. For both parts, $r = 0.2$.

phase reduction of coupled oscillators; see for example (4.5.4) with $\alpha = 0$ or [114]. Second, this choice of network topology naturally extends nonlocal pairwise interactions and in the resulting network dynamical system q-twisted states are still relative equilibria—the resulting network topology can be seen in Figure 5.4. While we focus on this particular generalization, there are other nonlocal higher-order network topologies that preserve the invariance of q-twisted states. Some of them have even closer connections to higher-order topologies that arise in phase-reductions, as we discuss in Section 5.6. However, third, we found that our choice of generalization is best analytically tractable, among other tested higher-order network topologies and coupling functions. In this sense, our choice of generalization to triplet interactions is a first step in understanding the dynamics of all possible types of triplet interactions. Furthermore, using our generalization, we demonstrate which dynamical effects are in principle possible with higher-order interactions. Our nonlocal higher-order coupling also naturally extends beyond triplet coupling: In the following we will consider a combination of pairwise and higher-order (triplet and quadruplet) interactions. Specifically, we consider the continuum limit

$$\frac{\partial}{\partial t}\Theta(t, x) = \int_{\mathbb{S}} W_r(x - y) \sin(\Theta(t, y) - \Theta(t, x)) \, \mathrm{d}y$$

$$+ \lambda \int_{\mathbb{S}} \int_{\mathbb{S}} W_r(z + y - 2x) \sin(\Theta(t, z) + \Theta(t, y) - 2\Theta(t, x)) \, \mathrm{d}y\mathrm{d}z$$

$$+ \mu \int_{\mathbb{S}} \int_{\mathbb{S}} \int_{\mathbb{S}} W_r(z - y + w - x)$$

$$\cdot \sin(\Theta(t, z) - \Theta(t, y) + \Theta(t, w) - \Theta(t, x)) \, \mathrm{d}w\mathrm{d}y\mathrm{d}z,$$

$$(5.3.1)$$

where $r \in (0, \frac{1}{2}]$ describes the coupling range and $\lambda, \mu \in \mathbb{R}$ are the strengths of the higher-order interactions. These three parameters can be summarized into one parameter $p = (r, \lambda, \mu) \in \mathcal{P}$, where $\mathcal{P} = (0, \frac{1}{2}] \times \mathbb{R} \times \mathbb{R}$ denotes the parameter space. Here, the first line of (5.3.1) describes the continuum limit of a Kuramoto model with nonlocal coupling and the remaining lines are triplet and quadruplet higher-order interactions.

The system (5.3.1) has the same symmetries as the system (5.2.8). In particular, the system (5.3.1) has a continuous $\mathbb{T} \times \mathbb{S}$ symmetry and a discrete Z_2 symmetry, where Z_2 is the group of two elements defined by $\mathbb{Z}/(2\mathbb{Z})$. A symmetry element $\beta \in \mathbb{T}$ acts by a phase shift

$$\beta : \Theta(t, x) \mapsto \Theta(t, x) + \beta \qquad (5.3.2)$$

to all oscillators and an element $\phi \in \mathbb{S}$ acts by rotating the ring-like network, that is,

$$\phi : \Theta(t, x) \mapsto \Theta(t, x + \phi). \qquad (5.3.3)$$

Besides these two continuous symmetries, an element $\zeta \in Z_2$, acts by reflecting the spatial variable, i.e.,

$$\zeta : \Theta(t, x) \mapsto \Theta(t, (-1)^\zeta x). \qquad (5.3.4)$$

The combination of (5.3.3) and (5.3.4) can be seen as the limit of the D_M symmetry of the finite-dimensional system as $M \to \infty$; cf. [24]. The symmetry property (5.3.2) can directly be shown by inserting $\Theta(t, x) + \beta$ into (5.3.1). To see (5.3.3) and (5.3.4) one first inserts the right-hand sides of these symmetries in the system (5.3.1) and then performs linear substitutions $y \mapsto y + \phi$, $z \mapsto z + \phi$, $w \mapsto w + \phi$ and $y \mapsto -y$, $z \mapsto -z$, $w \mapsto -w$, as necessary. In the latter case one also uses the reflective symmetry $W_r(x) = W_r(-x)$. Since the discrete symmetry (5.3.4) maps q-twisted states to $-q$-twisted states, the stability properties of them agree. Therefore, from now on we consider $q \in \mathbb{N}$ and thus focus only on q-twisted states, where q is positive. In particular, we also exclude the synchronized state $q = 0$ from our analysis.

5.3.2   Mathematical Setting and Linearization

We want to analyze the stability and bifurcations of q-twisted states for (5.3.1) and determine the existence and stability of possible bifurcating branches that occur as system parameters are varied. To answer these kind of questions, eigenvalues of the linearization of the right-hand side of (5.3.1) are of importance. The continuous phase shift symmetry (5.3.2) of system (5.3.1) implies that if $\Theta(t, x)$ is a solution to

the PDE (5.3.1), then so is $\Theta(t,x) + \beta$ with a constant $\beta \in \mathbb{T}$, see [77]. Therefore, the system has a neutrally stable direction, which yields a zero eigenvalue in the linearization of the right-hand side of (5.3.1), see also Section 5.2.2. We can avoid the zero eigenvalue by considering the evolution of phase differences $\Psi(t,x) := \Theta(t,x) - \Theta(t,0)$ which reduces the continuous phase shift symmetry (5.3.2). The function $\Psi(t,x)$ satisfies

$$
\begin{aligned}
\frac{\partial}{\partial t}\Psi(t,x) = {}& \int_{\mathbb{S}} W_r(x-y)\sin(\Psi(t,y) - \Psi(t,x))\,\mathrm{d}y - \int_{\mathbb{S}} W_r(y)\sin(\Psi(y))\,\mathrm{d}y \\
& + \lambda\left[\int_{\mathbb{S}}\int_{\mathbb{S}} W_r(z+y-2x)\sin(\Psi(t,z) + \Psi(t,y) - 2\Psi(t,x))\,\mathrm{d}y\mathrm{d}z\right. \\
& \left. - \int_{\mathbb{S}}\int_{\mathbb{S}} W_r(z+y)\sin(\Psi(t,z) + \Psi(t,y))\,\mathrm{d}y\mathrm{d}z\right] \\
& + \mu\left[\int_{\mathbb{S}}\int_{\mathbb{S}}\int_{\mathbb{S}} W_r(z-y+w-x)\right. \\
& \qquad \cdot \sin(\Psi(t,z) - \Psi(t,y) + \Psi(t,w) - \Psi(t,x))\,\mathrm{d}w\mathrm{d}y\mathrm{d}z \\
& \left. - \int_{\mathbb{S}}\int_{\mathbb{S}}\int_{\mathbb{S}} W_r(z-y+w)\sin(\Psi(t,z) - \Psi(t,y) + \Psi(t,w))\,\mathrm{d}w\mathrm{d}y\mathrm{d}z\right]
\end{aligned}
\tag{5.3.5}
$$

and $\Psi(t,0) = 0$. We denote the right-hand side of this system by $F(\Psi, p)$. In this system, a q-twisted state is given by $\Psi^q(x) = 2\pi q x$ for $q \in \mathbb{N}$ and it cannot be perturbed along a constant function anymore, since the perturbed function would then violate $\Psi(t,0) = 0$. Moreover, since we are particularly interested in the behavior of F in a neighborhood of a q-twisted state, we define

$$
F^q(v,p) := F(\Psi^q + v, p), \qquad F^q\colon X \times \mathcal{P} \to X, \qquad \text{for } q \in \mathbb{N}.
$$

Here, v can be seen as a perturbation of the q-twisted state. We consider perturbations v in the space $X := H_0^1 := H_0^1(\mathbb{S}, \mathbb{R})$, which is the function space whose functions $f\colon \mathbb{S} \to \mathbb{R}$ and their weak derivatives are in $L^2(\mathbb{S}, \mathbb{R})$ and which satisfy the boundary condition $f(0) = 0$. Since $H^1(\mathbb{S}, \mathbb{R}) \subset C(\mathbb{S})$, these boundary conditions can be imposed in the classical sense. That F^q indeed maps into X is shown as a special case in Appendix B.3. Together with the scalar product

$$
f \cdot g := \int_{\mathbb{S}} f(x)g(x)\,\mathrm{d}x + \int_{\mathbb{S}} Df(x)Dg(x)\,\mathrm{d}x
$$

the space X forms a Hilbert space. Moreover, the induced norm is given by

$$
\|f\|_{H_0^1} = \sqrt{f \cdot f} = \sqrt{\|f\|_{L^2}^2 + \|Df\|_{L^2}^2}.
$$

Since every function $\eta \in H_0^1$ can be written as

$$\eta(x) = \sum_{k=1}^{\infty} a_k \sin(2\pi k x) + b_k(1 - \cos(2\pi k x)),$$

the functions $u_k(x) = \sin(2\pi k x)$ and $w_k(x) = 1 - \cos(2\pi k x)$ for $k \geq 1$ form a Schauder basis of H_0^1, see also Lemma B.2.1 for a justification. It can be shown, see Appendix B.3, that the Fréchet derivative of $F^q(v, p)$ with respect to v around 0 is given by a bounded linear operator $F_v^q(0, p) \colon X \to X$. An evaluation of $F_v^q(0, p)$ on these basis elements yields

$$\begin{aligned} F_v^q(0, p)[u_k] &= c_1(q, k, p) u_k, \\ F_v^q(0, p)[w_k] &= c_1(q, k, p) w_k, \end{aligned} \tag{5.3.6}$$

for $k \in \mathbb{N}$ and

$$c_1(q, k, p) := \frac{1}{4}\left(\hat{W}_r(q - k) + \hat{W}_r(q + k) - 2\hat{W}_r(q) - (4\lambda + 2\mu)\hat{W}_r(q) \right),$$

where we continue to use the convention $\hat{W}_r(-k) := \hat{W}_r(k)$. The eigenvalues are then given by $\xi_k = c_1(q, k, p)$, each with multiplicity 2. Note, that without higher-order interactions, i.e., $\lambda = \mu = 0$, this agrees with (5.2.10). Since $F_v^q(0, p)$ is a multiplication operator on this basis, the spectrum is the closure of the set of eigenvalues, i.e.,

$$\sigma(F_v^q(0, p)) = \mathrm{cl}(\{\xi_k, k \in \mathbb{N}\}).$$

When one of these spectral values passes through 0, we may expect a change of stability of the q-twisted state. This is what we investigate in the next section.

5.4   Bifurcation Theory

Now, we analyze the bifurcation of twisted states upon varying the parameters in $\mathcal{P}$. In particular, we vary the parameters along a general one-dimensional curve in the parameter space. For phase oscillator networks that arise as phase reductions from a physical system [10], we expect that a variation of a physical system parameter gives rise to such a curve. Specifically, we assume from now on that

1. there is a smooth curve through the interior of the parameter space $p \colon (-\delta, \delta) \to \mathrm{int}(\mathcal{P})$, $p(s) = (r(s), \lambda(s), \mu(s))$ with $p(0) = p_0 = (r_0, \lambda_0, \mu_0)$,

2. at $s = 0$ we have $c_1(q, \ell, p(s)) = 0$ for one $\ell \in \mathbb{N}$ and for all $s \in (-\delta, \delta)$ we have $c_1(q, k, p(s)) \notin (-\epsilon, \epsilon)$ for some $\epsilon > 0$ and all $k \neq \ell$,

3. $c_1(q, \ell, p(s))$ is an isolated eigenvalue, i.e., for all $s \in (-\delta, \delta)$, the sequence $(c_1(q, k, p(s)))_{k \in \mathbb{N}}$ does not have an accumulation point at ξ_ℓ,

4. the zero eigenvalue passes through 0 with nonvanishing speed as s passes through 0, i.e., $\frac{\mathrm{d}}{\mathrm{d}s} c_1(q, \ell, p(s)) \neq 0$ for $s = 0$.

Remark 5.4.1. Since $\lim_{k \to \infty} c_1(q, k, p) = \frac{1}{4} \hat{W}_r(q)(-2 - (4\lambda + 2\mu))$ exists, it is the only possible spectral value that is not an eigenvalue. Moreover, since it depends continuously on all parameters, Assumption 3 only has to be checked at $s = 0$. Furthermore, since $c_1(q, k, p)$ is uniformly (w.r.t. k) Lipschitz continuous in p, Assumption 2 only has to be checked at $s = 0$.

From now on we use the notation V for an open neighborhood of p_0 in $\mathcal{P}$. By a slight abuse of notation, this V might have to be shrunk from one statement to the other, but always represents a small enough open neighborhood of p_0. Similarly, $(-\delta, \delta)$, which represents an open neighborhood of 0 in $\mathbb{R}$, might have to be shrunk from statement to statement.

5.4.1 Lyapunov–Schmidt Reduction

At the bifurcation point $s = 0$, the nullspace of the linearization is given by

$$N := \mathcal{N}(F_v^q(0, p_0)) = \mathrm{span}\{u_\ell, w_\ell\}.$$

Further, we denote the range of the linearization by $R = \mathrm{span}\{u_k, w_k : k \neq \ell\}$. Following the notation from [97], we consider $F_v^q(0, p)$ as a map from $X \times \mathcal{P}$ to Z, where $X = Z = H_0^1$. Even though $X = Z$, we use different notation for the domain and target set to emphasize the distinction between them. These spaces can be decomposed into

$$X = N \oplus X_0 \qquad \text{and} \qquad Z = R \oplus Z_0,$$

where X_0 is a complement of N in X and Z_0 is a complement of R in Z. We choose $Z_0 = N$ and $X_0 = R$. Moreover, the projection onto Z_0 is defined by

$$Q \colon Z \to Z_0 \quad \text{along } R.$$

To determine equilibria of (5.3.5), we need to find solutions to $F^q(v, p) = 0$. By performing a Lyapunov-Schmidt reduction we can reduce this infinite-dimensional problem to a finite-dimensional problem, as the next theorem shows.

Theorem 5.4.2 ([97, Chapter I.2])**.** *There is a neighborhood $U_1 \times V_1 \subset X \times \mathcal{P}$ of $(0, p_0)$ such that the full infinite-dimensional problem of finding equilibria of (5.3.5), i.e., solving*

$$F^q(v, p) = 0$$

in $U_1 \times V_1$ is equivalent to solving

$$\Phi(v, p) = 0,$$

where $\Phi\colon U_2 \times V_2 \to Z_0$ for $(v, p) \in U_2 \times V_2 \subset N \times \mathcal{P}$. Here, $\Phi(0, p_0) = 0$ and Φ is defined by

$$\Phi(v, p) = QF^q(v + \psi(v, p), p), \tag{5.4.1}$$

where $\psi\colon U_2 \times V_2 \to X_0$ is a function satisfying $\psi(0, p_0) = 0$. It is implicitly defined to be the unique solution to the equation

$$(I - Q)F^q(v + \psi(v, p), p) = 0 \tag{5.4.2}$$

in a neighborhood of $(0, p_0)$.

The proof of this theorem relies on the implicit function theorem. For details see [97, Chapter I.2] and for an introduction see [102].

We introduce a coordinate representation of the function Φ by considering the basis of the dual space Z_0' of Z_0, which is given by two functionals z_1^*, z_2^* that are defined by

$$\langle z_1^*, u_\ell \rangle = 1, \qquad \langle z_1^*, w_\ell \rangle = 0,$$
$$\langle z_2^*, u_\ell \rangle = 0, \qquad \langle z_2^*, w_\ell \rangle = 1,$$

where $\langle \cdot, \cdot \rangle$ denotes the dual pairing. Since, $\{u_\ell, w_\ell\}$ is a basis of the finite-dimensional space Z_0, the functionals are uniquely defined by their actions on these basis functions. Moreover, one can see that these functionals can also be written as

$$\langle z_1^*, v \rangle = 2 \int_{\mathbb{S}} \sin(2\pi\ell x)v(x) \, \mathrm{d}x,$$

$$\langle z_2^*, v \rangle = -2 \int_{\mathbb{S}} \cos(2\pi\ell x)v(x) \, \mathrm{d}x.$$

Then, we define a function $\hat{\Phi}\colon U_3 \times (-\delta, \delta) \to \mathbb{R}^2$, where $U_3 \subset \mathbb{R}^2, (-\delta, \delta) \subset \mathbb{R}$ are sufficiently small neighborhoods around the origin, as

$$\hat{\Phi}\left(\begin{pmatrix} a \\ b \end{pmatrix}, s\right) := \begin{pmatrix} \langle z_1^*, \Phi(au_\ell + bw_\ell, p(s)) \rangle \\ \langle z_2^*, \Phi(au_\ell + bw_\ell, p(s)) \rangle \end{pmatrix}. \tag{5.4.3}$$

Given $(a_0, b_0)^\top$ in a neighborhood of $(0, 0)^\top$ and $s \in (-\delta, \delta)$ such that $\hat{\Phi}((a_0, b_0)^\top, s) = (0, 0)^\top$ we then know that $F(\Psi^q + a_0 u_\ell + b_0 w_\ell + \psi(a_0 u_\ell + b_0 w_\ell, p(s)), p(s)) = 0$. Therefore, this first argument of F represents an equilibrium. Conversely, due to the equivalence in Theorem 5.4.2, every equilibrium in a neighborhood of the bifurcation point can be found in that way.

5.4.2 Problem Reduction Using Symmetry

While reducing the system to phase differences (5.3.5) has reduced the phase-shift symmetry, the system still has the residual rotational symmetry (5.3.3). One can expect that this symmetry is reflected in the bifurcation behavior. Indeed, the Lyapunov–Schmidt reduction can be carried out such that it preserves symmetries; cf. [77]. Here, we show explicitly that the reduced equation (5.4.3) retains the rotational symmetry. This simplifies the system to a one-dimensional problem by eliminating the symmetry.

Specifically, in phase differences, the rotational symmetry (5.3.3) acts as an operator $B_\phi\colon X \to X$ for $\phi \in \mathbb{S}$ given by

$$(B_\phi f)(x) = f(x + \phi) - f(\phi).$$

and the right-hand side F^q is equivariant with respect to this operation. The nullspace N is spanned by u_ℓ and w_ℓ, which can be obtained from each other by shifting one function around the circle and adding a constant such that it satisfies the boundary conditions, i.e., by applying the operator B_ϕ. For the reduced equation determined by $\hat{\Phi}$, this corresponds to a rotation. Specifically, with

$$A_\phi = \begin{pmatrix} \cos(2\pi\ell\phi) & \sin(2\pi\ell\phi) \\ -\sin(2\pi\ell\phi) & \cos(2\pi\ell\phi) \end{pmatrix}$$

for a two-dimensional rotation matrix, we now show that $\hat{\Phi}$ is $\mathbb{S}$-equivariant with respect to the action given by A_ϕ.

Proposition 5.4.3. *In a neighborhood of the origin, $\hat{\Phi}$ satisfies*

$$\hat{\Phi}\left(A_\phi \begin{pmatrix} a \\ b \end{pmatrix}, s\right) = A_\phi \hat{\Phi}\left(\begin{pmatrix} a \\ b \end{pmatrix}, s\right), \tag{5.4.4}$$

for all ϕ.

Proof. A straight-forward calculation confirms that F^q satisfies

$$F^q(B_\phi \eta, p) = B_\phi F^q(\eta, p) \tag{5.4.5}$$

for all $\eta \in X$ and all $p \in \mathcal{P}$. Now, let us see how this property propagates to the function ψ. By definition, ψ solves

$$(I - Q)F^q(v + \psi(v, p), p) = 0$$

for all $v \in U_2 \subset N, p \in V_2 \subset \mathcal{P}$. Let us choose $v = B_\phi u \in U_2$ for some $u \in U_2$ and note that B_ϕ leaves N invariant and further commutes with Q. Then, on the one hand

$$(I - Q)F^q(B_\phi u + \psi(B_\phi u, p), p) = 0. \tag{5.4.6}$$

On the other hand

$$
\begin{aligned}
0 &= B_\phi 0 \\
&= B_\phi (I - Q) F^q(u + \psi(u, p), p) \\
&= (I - Q) B_\phi F^q(u + \psi(u, p), p) \\
&= (I - Q) F^q(B_\phi [u + \psi(u, p)], p) \\
&= (I - Q) F^q(B_\phi u + B_\phi \psi(u, p), p), \tag{5.4.7}
\end{aligned}
$$

by the symmetry property (5.4.5). By comparing (5.4.6) and (5.4.7) one sees that

$$
\psi(B_\phi u, p) = B_\phi \psi(u, p) \tag{5.4.8}
$$

for all $u \in U_2$ due to the uniqueness of ψ. Furthermore, the definition (5.4.1) of Φ implies that for all $v \in U_2 \subset N$

$$
\begin{aligned}
\Phi(B_\phi v, p) &= Q F^q(B_\phi v + \psi(B_\phi v, p), p) \\
&= Q F^q(B_\phi v + B_\phi \psi(v, p), p) \\
&= Q F^q(B_\phi [v + \psi(v, p)], p) \\
&= Q B_\phi F^q(v + \psi(v, p), p) \\
&= B_\phi Q F^q(v + \psi(v, p), p) \\
&= B_\phi \Phi(v, p), \tag{5.4.9}
\end{aligned}
$$

where we have used (5.4.8) and (5.4.5).

Since $\Phi \colon U_2 \times V_2 \to N$, where U_2 is a neighborhood of 0 in N and V_2 is neighborhood of p_0 in $\mathcal{P}$, for small enough $|a|, |b|$, we can write

$$
\Phi(a u_\ell + b w_\ell, p) = c u_\ell + d w_\ell
$$

for each fixed $p \in V$ and some $c, d \in \mathbb{R}$. Note that the coefficients a, b, c, d should be considered as fixed parameters. In particular, there is no linear dependence of c, d on a, b. Now, by applying B_ϕ to both sides of the equation and using the symmetry property (5.4.9), a straight-forward calculation confirms that

$$
\begin{aligned}
&\Phi([a \cos(2\pi\ell\phi) + b \sin(2\pi\ell\phi)] u_\ell + [-a \sin(2\pi\ell\phi) + b \cos(2\pi\ell\phi)] w_\ell, p) \\
&= [c \cos(2\pi\ell\phi) + d \sin(2\pi\ell\phi)] u_\ell + [-c \sin(2\pi\ell\phi) + d \cos(2\pi\ell\phi)] w_\ell.
\end{aligned}
$$

Using (5.4.3), this yields the result. $\qquad\square$

Next, we show that $\hat{\Phi}$ does not change the angle of a vector but only multiplies its length by a (possibly negative) factor.

To achieve this, we first define the space of odd functions O:

$$
O := \{f \in X : f(x) = -f(-x)\}.
$$

Lemma 5.4.4. *Let $p \in \mathcal{P}$ and $v \in O$. Then $F^q(v, p) \in O$.*

This lemma follows by a calculation using linear substitutions of the integrating variables that appear in the definition of F^q and F.

Given this lemma, we can consider the restriction of F^q to the space of odd functions O:

$$F^{q,\dagger} \colon X^\dagger \times \mathcal{P} \to Z^\dagger, \qquad F^{q,\dagger}(v, p) := F^q(v, p),$$

where both $X^\dagger = Z^\dagger = O$. We use the symbol $\dagger$ whenever we are referring to a function or a space that is reduced to O.

Under this restriction $F^{q,\dagger}$ inherits smoothness from F and F^q. Following the notation from Section 5.4.1 we denote $N^\dagger := \mathcal{N}(F_v^{q,\dagger}(0, p_0)) = \mathrm{span}\{u_\ell\}$. Moreover, there are decompositions

$$X^\dagger = N^\dagger \oplus X_0^\dagger \qquad \text{and} \qquad Z^\dagger = R^\dagger \oplus Z_0^\dagger,$$

where $R^\dagger$ is the range of $F_v^{q,\dagger}(0, p_0)$ and we choose $X_0^\dagger = R^\dagger$ and $Z_0^\dagger = N^\dagger$. Additionally, we denote $Q^\dagger$ for the restricted projection of Q from $X^\dagger$ onto $N^\dagger$. Now we can perform another Lyapunov-Schmidt reduction on the space of odd functions:

Lemma 5.4.5 ([97]). *Solving the infinite-dimensional problem*

$$F^{q,\dagger}(v, p) = 0$$

is equivalent to solving

$$\Phi^\dagger(v, p) = 0,$$

where $\Phi^\dagger \colon U^\dagger \times V \to Z_0^\dagger$ and $(v, p) \in U^\dagger \times V \subset N^\dagger \times \mathcal{P}$. Here, $\Phi^\dagger(0, p_0) = 0$ and $\Phi^\dagger$ is defined by

$$\Phi^\dagger(v, p) := Q^\dagger F^{q,\dagger}(v + \psi^\dagger(v, p), p), \tag{5.4.10}$$

where $\psi^\dagger \colon U^\dagger \times V \to X_0^\dagger$ is a unique function satisfying $\psi^\dagger(0, p_0) = 0$. It is implicitly defined to be the unique solution of the equation

$$(I - Q^\dagger)F^{q,\dagger}(v + \psi^\dagger(v, p), p) = 0 \tag{5.4.11}$$

in a neighborhood of $(0, p_0)$.

This Lemma follows from [97]. We can use it to show the next lemma:

Lemma 5.4.6. *The function $\hat{\Phi}$ does not change the angle of a vector but only multiplies its length by a (possibly negative) factor. To be precise, for all (a, b) in a small neighborhood U of $(0, 0)$ and $s \in (-\delta, \delta)$,*

$$\hat{\Phi}\left(\begin{pmatrix} a \\ b \end{pmatrix}, s\right) = \hat{h}((a, b)^\top, s) \begin{pmatrix} a \\ b \end{pmatrix}, \tag{5.4.12}$$

where $\hat{h} \colon U \times (-\delta, \delta) \to \mathbb{R}$ is a rotationally invariant function, i.e.

$$\hat{h}\left(A_\phi \begin{pmatrix} a \\ b \end{pmatrix}, s\right) = \hat{h}\left(\begin{pmatrix} a \\ b \end{pmatrix}, s\right)$$

for all ϕ.

Proof. First note, that due to Proposition 5.4.3, it suffices to show (5.4.12) for $b = 0$. Therefore, it is left to show that $\hat{\Phi}_2((a, 0)^\top, s) = 0$. Since both ψ and $\psi^\dagger$ are uniquely defined, $\psi^\dagger$ must be the restriction of ψ to the space O. In particular,

$$\psi(v, p) = \psi^\dagger(v, p) \in O,$$

whenever $v \in O$. This shows that $\psi(au_\ell, p)$ is an odd function. Now, we evaluate $\hat{\Phi}_2((a, 0)^\top, s)$:

$$\begin{aligned}
\hat{\Phi}_2((a, 0)^\top, s) &= \langle z_2^*, \Phi(au_\ell, p(s)) \rangle \\
&= \langle z_2^*, QF^q(au_\ell + \psi(au_\ell, p(s)), p(s)) \rangle \\
&= 0,
\end{aligned}$$

because $au_\ell + \psi(au_\ell, p(s))$ is odd and F^q maps odd functions to odd functions, see Lemma 5.4.4. Therefore, when $b = 0$ in (5.4.3) and a and s are in a small neighborhood of the bifurcation point, we find that $\hat{\Phi}_2 = 0$. Since $\hat{\Phi}((0, 0)^\top, s) = (0, 0)^\top$, we can choose $\hat{h}$ such that the claim of the lemma holds. Finally, by Proposition 5.4.3 it follows that $\hat{h}$ has to satisfy the rotational invariance condition. $\square$

Consequently, when looking for zeros of $\hat{\Phi}((a, b)^\top, s)$, we can restrict ourselves to $b = 0$, see Figure 5.5. Given a, s such that $\hat{\Phi}((a, 0)^\top, s) = 0$, all other zeros can then be obtained by applying A_ϕ to $(a, 0)^\top$. Therefore, we might as well study the problem of finding zeros of

$$h(a, s) := \hat{\Phi}((a, 0)^\top, s) = \hat{\Phi}^\dagger(a, s) := \langle z_1^*, \Phi^\dagger(au_\ell, p(s)) \rangle.$$

This statement can also be reformulated without using coordinates (a, b): If $\hat{v} \in \mathcal{O}$ is a solution of $\Phi^\dagger(\hat{v}, p(s)) = 0$ then all solutions $\tilde{v}$ of $\Phi(\tilde{v}, p(s)) = 0$ are of the form $\tilde{v} = B_\phi \hat{v}$ for some $\phi \in \mathbb{S}$. By Theorem 5.4.2, all solutions of $F^q(v, p(s)) = 0$ are then of the form $v = \tilde{v} + \psi(\tilde{v}, p(s)) = B_\phi \hat{v} + \psi(B_\phi \hat{v}, p(s)) = B_\phi(\hat{v} + \psi(\hat{v}, p(s)))$. Since $\hat{v} + \psi(\hat{v}, p(s))$ is an odd function, all solutions v of $F^q(v, p(s))$ can be obtained from an odd function via the transformation B_ϕ. In the next section, we Taylor-expand h to see which zeros it has in a neighborhood of the origin.
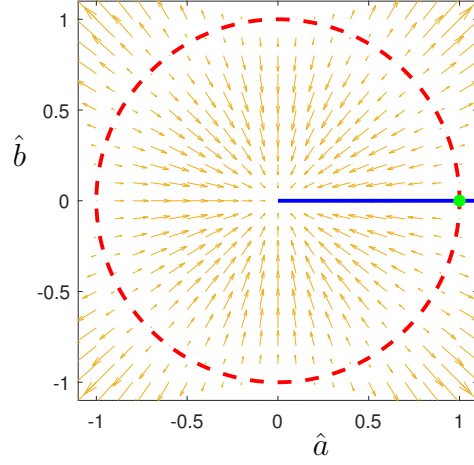
Figure 5.5: Illustration of Lemma 5.4.6. For given s with $|s|$ small enough, the vectorfield $\hat{\Phi}((a,b)^{\top}, s)$, depicted by yellow arrows, has a rotational symmetry. Thus, when searching for zeros of $\hat{\Phi}$, we can restrict ourselves to zeros with $b = 0$ and $a \geq 0$, as illustrated by the blue line. If, there is a zero, here indicated by a green dot, somewhere on this blue line, then all other zeros can be obtained by rotating the green dot around the origin. Here, $\hat{a}, \hat{b}$ are coordinates with $0 < \frac{a}{\hat{a}} = \frac{b}{\hat{b}} \ll 1$ such that (a, b) is in a small neighborhood of the origin.

5.4.3 Taylor Expansion around the Bifurcation Point

In order to determine the type of the bifurcation it is necessary to compute the derivatives of h. Since F is smooth, as proven in Appendix B.3, the function $\psi^{\dagger}$, $\Phi^{\dagger}$ and $\hat{\Phi}^{\dagger}$, which originate from the implicit function theorem or are concatenations of smooth functions, are smooth as well. In order to derive expressions for the derivative of h we first need to compute derivatives of $F^{q,\dagger}$. These derivatives are given in the next lemma:

Lemma 5.4.7. *The derivative of $F^{q,\dagger}$, evaluated on the basis functions satisfies*

$$F_v^{q,\dagger}(0, p)[u_k] = c_1(q, k, p)u_k. \tag{5.4.13}$$

An evaluation of second derivatives of $F^{q,\dagger}$ on the basis elements u_k yields

$$F_{vv}^{q,\dagger}(0, p)[u_k, u_k] = c_2(q, k, p)u_{2k}. \tag{5.4.14}$$

Further, second derivatives, evaluated on distinct basis functions, are given by

$$F_{vv}^{q,\dagger}(0, p)[u_m, u_k] = c_3(q, m, k, p)u_{m-k} + c_4(q, m, k, p)u_{m+k}, \tag{5.4.15}$$

for all $m, k \in \mathbb{N}$ with $m \neq k$. Here, we use the convention $u_{-n} = -u_n$ for $n \in \mathbb{N}$. Furthermore, we find

$$F_{vvv}^{q,\dagger}(0,p)[u_k, u_k, u_k] = 3c_5(q, k, p)u_k + c_6(q, k, p)u_{3k}, \qquad (5.4.16)$$

for $k \in \mathbb{N}$. Here, $c_1, \ldots, c_6$ are coefficients that depend on q, k, m, p and the Fourier coefficients $\hat{W}_r(k)$ of the coupling function. The full expressions for these coefficients can be found in Appendix B.1.

Proof. This lemma can be proven by inserting the basis functions into the representation of the derivative of F, derived in Appendix B.3. $\square$

Now, we can use Lemma 5.4.7 to calculate derivatives of $\psi^\dagger$ and $\Phi^\dagger$. This follows the lines of [97, Section I.6].

Lemma 5.4.8. *The derivatives of $\psi^\dagger$ satisfy*

$$\psi_v^\dagger(0, p_0)u_\ell = 0, \qquad (5.4.17)$$

$$\psi_{vv}^\dagger(0, p_0)[u_\ell, u_\ell] = -\frac{c_2(q, \ell, p_0)}{c_1(q, 2\ell, p_0)}u_{2\ell}. \qquad (5.4.18)$$

Proof. Taking the derivative of (5.4.11) with respect to v yields

$$(I - Q^\dagger)F_v^{q,\dagger}(v + \psi^\dagger(v, p), p)[v_1 + \psi_v^\dagger(v, p)v_1] = 0 \qquad (5.4.19)$$

for all $v_1 \in N^\dagger$. Now, we insert $v = 0$ and $p = p_0$ into (5.4.19). Noting that $F_v^{q,\dagger}(0, p_0)v_1 = 0$ and $Q^\dagger F_v^{q,\dagger}(0, p_0) = 0$, we are left with $F_v^{q,\dagger}(0, p)\psi_v^\dagger(0, p_0)v_1 = 0$. Since $\psi^\dagger$ maps $N^\dagger$ into $X_0^\dagger$ and $F_v^{q,\dagger}(0, p)$ regarded as a map from $X_0^\dagger$ to $R^\dagger$ is bijective, we obtain (5.4.17). Differentiating (5.4.19) once more with respect to v gives

$$(I - Q^\dagger)F_{vv}^{q,\dagger}(v + \psi^\dagger(v, p), p)[v_1 + \psi_v^\dagger(v, p)v_1, v_2 + \psi_v^\dagger(v, p)v_2]$$
$$+ (I - Q^\dagger)F_v^{q,\dagger}(v + \psi^\dagger(v, p), p)\psi_{vv}^\dagger(v, p)[v_1, v_2] = 0.$$

for all $v_1, v_2 \in N^\dagger$. Again, by inserting $v = 0$ and $p = p_0$ into the previous equation we obtain

$$(I - Q^\dagger)F_{vv}^{q,\dagger}(0, p_0)[v_1, v_2] + F_v^{q,\dagger}(0, p_0)\psi_{vv}^\dagger(0, p_0)[v_1, v_2] = 0 \qquad (5.4.20)$$

for all $v_1, v_2 \in N^\dagger$. Now, we compute $\psi_{vv}^\dagger(0, p_0)[u_\ell, u_\ell]$ by choosing $v_1 = v_2 = u_\ell$ in (5.4.20) and using (5.4.14). We obtain

$$F_v^{q,\dagger}(0, p_0)\psi_{vv}^\dagger(0, p_0)[u_\ell, u_\ell] = -c_2(q, \ell, p_0)u_{2\ell}.$$

Therefore, by noting that $\psi_{vv}^\dagger(0, p_0)[u_\ell, u_\ell] \in X_0^\dagger$, considering $F_v^{q,\dagger}(0, p_0)\colon X_0^\dagger \to R^\dagger$ as an invertible map and using (5.4.13), we are left with (5.4.18). $\square$

Now, we can use these derivatives to calculate the derivatives of $\hat{\Phi}^\dagger$:

Lemma 5.4.9. $\hat{\Phi}^\dagger$ *satisfies*

$$\hat{\Phi}^\dagger(0,0) = 0, \qquad\qquad \hat{\Phi}^\dagger_a(0,0) = 0,$$
$$\hat{\Phi}^\dagger_{aa}(0,0) = 0, \qquad\qquad \hat{\Phi}^\dagger_{aaa}(0,0) = 6\gamma_1,$$

where

$$\gamma_1 := \frac{1}{2}\left(c_5(q,\ell,p_0) - \frac{c_2(q,\ell,p_0)c_3(q,2\ell,\ell,p_0)}{c_1(q,2\ell,p_0)} \right). \tag{5.4.21}$$

Proof. By differentiating (5.4.10) with respect to v we get

$$\Phi^\dagger_v(v,p)v_1 = Q^\dagger F^{q,\dagger}_v(v + \psi^\dagger(v,p),p)[v_1 + \psi^\dagger_v(v,p)v_1], \tag{5.4.22}$$
$$\Phi^\dagger_{vv}(v,p)[v_1,v_2] = Q^\dagger F^{q,\dagger}_{vv}(v + \psi^\dagger(v,p)[v_1 + \psi^\dagger_v(v,p)v_1, v_2 + \psi^\dagger_v(v,p)v_2]$$
$$+ Q^\dagger F^{q,\dagger}_v(v + \psi^\dagger(v,p),p)\psi^\dagger_{vv}(v,p)[v_1,v_2],$$
$$\Phi^\dagger_{vvv}(v,p)[v_1,v_2,v_3] = Q^\dagger F^{q,\dagger}_{vvv}(v + \psi^\dagger(v,p),p)[v_1 + \psi^\dagger_v(v,p)v_1,$$
$$v_2 + \psi^\dagger_v(v,p)v_2, v_3 + \psi^\dagger_v(v,p)v_3]$$
$$+ Q^\dagger F^{q,\dagger}_{vv}(v + \psi^\dagger(v,p),p)[v_1 + \psi^\dagger_v(v,p)v_1, \psi^\dagger_{vv}(v,p)[v_2,v_3]]$$
$$+ Q^\dagger F^{q,\dagger}_{vv}(v + \psi^\dagger(v,p),p)[v_2 + \psi^\dagger_v(v,p)v_2, \psi^\dagger_{vv}(v,p)[v_1,v_3]]$$
$$+ Q^\dagger F^{q,\dagger}_{vv}(v + \psi^\dagger(v,p),p)[v_3 + \psi^\dagger_v(v,p)v_3, \psi^\dagger_{vv}(v,p)[v_1,v_2]]$$
$$+ Q^\dagger F^{q,\dagger}_v(v + \psi^\dagger(v,p),p)\psi^\dagger_{vvv}(v,p)[v_1,v_2,v_3]$$

for all $v_1, v_2, v_3 \in N^\dagger$. Evaluating these derivatives at $v = 0$ and $p = p_0$ and using (5.4.17) yields

$$\Phi^\dagger_v(0,p_0)v_1 = 0, \tag{5.4.23a}$$
$$\Phi^\dagger_{vv}(0,p_0)[v_1,v_2] = Q^\dagger F^{q,\dagger}_{vv}(0,p_0)[v_1,v_2], \tag{5.4.23b}$$
$$\Phi^\dagger_{vvv}(0,p_0)[v_1,v_2,v_3] = Q^\dagger F^{q,\dagger}_{vvv}(0,p_0)[v_1,v_2,v_3]$$
$$+ Q^\dagger F^{q,\dagger}_{vv}(0,p_0)[v_1, \psi^\dagger_{vv}(0,p_0)[v_2,v_3]]$$
$$+ Q^\dagger F^{q,\dagger}_{vv}(0,p_0)[v_2, \psi^\dagger_{vv}(0,p_0)[v_1,v_3]] \tag{5.4.23c}$$
$$+ Q^\dagger F^{q,\dagger}_{vv}(0,p_0)[v_3, \psi^\dagger_{vv}(0,p_0)[v_1,v_2]].$$

By the definition of $\Phi^\dagger$ we get

$$\hat{\Phi}^\dagger(0,0) = 0$$

By (5.4.23a) we get

$$\hat{\Phi}^\dagger_a(0,0) = \langle z_1^*, \Phi_v(0,p_0)u_\ell \rangle = 0.$$

Using (5.4.23b) and (5.4.14), we obtain

$$\hat{\Phi}^\dagger_{aa}(0,0) = \langle z_1^*, \Phi^\dagger_{vv}(0,p_0)[u_\ell, u_\ell] \rangle = \langle z_1^*, Q^\dagger F^{q,\dagger}_{vv}(0,p_0)[u_\ell, u_\ell] \rangle = \langle z_1^*, 0 \rangle = 0.$$

Using (5.4.23c), (5.4.16), (5.4.18) and (5.4.15) yields

$$\begin{aligned}
\Phi^\dagger_{vvv}(0,p_0)[u_\ell, u_\ell, u_\ell] &= Q^\dagger F^{q,\dagger}_{vvv}(0,p_0)[u_\ell, u_\ell, u_\ell] \\
&\quad + 3Q^\dagger F^{q,\dagger}_{vv}(0,p_0)[u_\ell, \psi^\dagger_{vv}(0,p_0)[u_\ell, u_\ell]] \\
&= Q^\dagger F^{q,\dagger}_{vvv}(0,p_0)[u_\ell, u_\ell, u_\ell] \\
&\quad - \frac{3c_2(q,\ell,p_0)}{c_1(q,2\ell,p_0)} Q^\dagger F^{q,\dagger}_{vv}(0,p_0)[u_\ell, u_{2\ell}] \\
&= 3c_5(q,\ell,p_0)u_\ell - \frac{3c_2(q,\ell,p_0)c_3(q,2\ell,\ell,p_0)}{c_1(q,2\ell,p_0)} u_\ell
\end{aligned}$$

Therefore, $\hat{\Phi}^\dagger_{aaa}(0,0) = 6\gamma_1$.

$\square$

Now, we compute derivatives involving s.

Lemma 5.4.10. $\hat{\Phi}^\dagger$ *satisfies*

$$\hat{\Phi}^\dagger_s(0,0) = 0, \qquad \hat{\Phi}^\dagger_{as}(0,0) = \gamma_2,$$

where

$$\gamma_2 := \left. \frac{\mathrm{d}}{\mathrm{d}s} c_1(q,\ell,p(s)) \right|_{s=0}. \tag{5.4.24}$$

Proof. Since $F^{q,\dagger}(0,p) = F(\Psi^q, p) = 0$ for all $p \in \mathcal{P}$, we have $\hat{\Phi}^\dagger(0,s) = 0$ for all $s \in (-\delta, \delta)$. In particular,

$$\hat{\Phi}_s(0,0) = 0.$$

To compute the mixed derivative, we first differentiate (5.4.11) with respect to p to obtain

$$(I - Q^\dagger)F^{q,\dagger}_v(v + \psi^\dagger(v,p), p)\psi_p(v,p) + (I - Q^\dagger)F^{q,\dagger}_p(v + \psi^\dagger(v,p), p) = 0. \tag{5.4.25}$$

Now, we insert $v = 0$, $p = p_0$ to get

$$(I - Q^\dagger)F^{q,\dagger}_v(0,p_0)\psi^\dagger_p(0,p_0) + (I - Q^\dagger)F^{q,\dagger}_p(0,p_0) = 0.$$

Again, because $F^{q,\dagger}(0,p) = 0$ for all p its derivative with respect to p, i.e., the second part of the previous equation, is 0. Moreover, for $v \in X_0^\dagger$, $(I-Q^\dagger)F_v^{q,\dagger}(0,p_0)v = 0$ is equivalent to $v = 0$ and therefore

$$\psi_p^\dagger(0,p_0) = 0. \tag{5.4.26}$$

Now, the mixed first derivatives can be computed by differentiating (5.4.22) with respect to p as follows:

$$\Phi_{vp}^\dagger(v,p)[v_1,p_1] = Q^\dagger F_{vv}^{q,\dagger}(v+\psi^\dagger(v,p),p)[v_1 + \psi_v^\dagger(v,p)v_1]\psi_p^\dagger(v,p)p_1$$
$$+ Q^\dagger F_{vp}^{q,\dagger}(v+\psi^\dagger(v,p),p)[v_1 + \psi_v^\dagger(v,p)v_1,p_1]$$
$$+ Q^\dagger F_v^{q,\dagger}(v+\psi^\dagger(v,p),p)\psi_{vp}^\dagger(v,p)[v_1,p_1]$$

for all $v_1 \in N^\dagger, p_1 \in \mathbb{R}^3$. Evaluating that at $v = 0$, $p = p_0$ yields

$$\Phi_{vp}^\dagger(0,p_0)[u_\ell,p_1] = Q^\dagger F_{vp}^{q,\dagger}(0,p_0)[u_\ell,p_1]$$
$$= D_p c_1(q,k,p)\Big|_{p=p_0} p_1 u_\ell.$$

Consequently,

$$\hat{\Phi}_{as}(0,0) = D_p c_1(q,k,p)\Big|_{p=p_0} p'(0)$$
$$= \frac{\mathrm{d}}{\mathrm{d}s} c_1(q,\ell,p(s))\Big|_{s=0}.$$

$\square$

Now, we can put these lemmas together and formulate the concluding theorem of this section:

Theorem 5.4.11. *The Taylor-expansion of $\hat{\Phi}^\dagger(a,s) = h(a,s)$ is*

$$\hat{\Phi}^\dagger(a,s) = \left[\gamma_1 a^3 + \mathcal{O}(a^4)\right] + s\left[\gamma_2 a + \mathcal{O}(a^2)\right] + \mathcal{O}(s^2)$$
$$= a(\gamma_1 a^2 + \gamma_2 s) + \mathcal{O}(a^4 + |s|\,a^2 + s^2) \tag{5.4.27}$$

Here, γ_1 and γ_2 are defined as in (5.4.21) and (5.4.24), respectively.

Proof. Since F is smooth, this follows from Lemmas 5.4.9 and 5.4.10. $\square$

Here, (5.4.27) is the Taylor expansion of a pitchfork bifurcation. In fact, by using the implicit function theorem, one can show that except for the trivial solution branch $a = 0$ there is another curve of equilibria in the neighborhood of the trivial solution. This nontrivial solution branch can be parameterized by a twice

continuously differentiable curve $\tau \mapsto (s(\tau), a(\tau))$ for $\tau \in (-\epsilon, \epsilon)$ and $0 < \epsilon$ small enough. In this case, $s(0) = a(0) = 0$ and the parameterization can be chosen such that $a'(0) = 1$. Then, $s'(0) = 0$ and $s''(0) = -2\gamma_1/\gamma_2$. Here, a prime denotes differentiation with respect to τ. Given these derivatives, the nontrivial solution curve exists for $s \leq 0$ when $\gamma_2/\gamma_1 > 0$ and for $s \geq 0$ when $\gamma_2/\gamma_1 < 0$. Moreover, in a neighborhood of the bifurcation point, we can approximate

$$a \approx a^{\mathrm{app}}(s) := \sqrt{\frac{-\gamma_2 s}{\gamma_1}}. \tag{5.4.28}$$

Given parameters a_0, s_0 with $h(a_0, s_0) = 0$ we infer that all $\tilde{a}_0, \tilde{b}_0, \tilde{s}_0$ with $\tilde{a}_0^2 + \tilde{b}_0^2 = a_0^2$ and $s_0 = \tilde{s}_0$ satisfy $\hat{\Phi}((\tilde{a}_0, \tilde{b}_0)^\top, \tilde{s}_0) = 0$, due to the symmetry (5.4.4) of $\hat{\Phi}$, see Figure 5.5.

5.4.4   Higher-Order Equilibria Approximations

In the last section, we clarified existence of solutions to $\Phi(v, p(s)) = 0$. In this section we explain how to use these solutions to derive formulas that can be used to approximate the zeros of F^q in H_0^1. Given $v \in N$ that solves $\Phi(v, p(s)) = 0$ we know that $F(\Psi^q + v + \psi(v, p(s)), p(s)) = F^q(v + \psi(v, p(s)), p(s)) = 0$. For a given $p(s)$, a zero of F is therefore given by $Z(v, s) := \Psi^q + v + \psi(v, p(s))$. A naive 0-th order approximation for this zero would be given by

$$Z(v, s) = \Psi^q + \mathcal{O}(\|(v, s)\|).$$

However, since after neglecting the higher-order terms this approximation coincides with the trivial zero of F, i.e., the q-twisted state, this approximation is not useful.

An approximation of first order can be derived by expanding $Z(v, s)$ in terms of v and s up to first derivatives. This yields

$$Z(v, s) = \Psi^q + v + \psi_v(0, p_0)v + s\psi_p(0, p_0)p'(0) + \mathcal{O}(\|(v, s)\|^2)$$
$$= \Psi^q + v + \mathcal{O}(\|(v, s)\|^2),$$

where we have used that $\psi_v(0, p_0) = 0$ and $\psi_p(0, p_0) = 0$. Neglecting the higher-order terms, we denote

$$Z^1(v, s) = \Psi^q + v \tag{5.4.29}$$

for the first order approximation.

To get a more precise approximation, we assume that $p \colon (-\delta, \delta) \to \mathcal{P}$ is a smooth curve. Then, we expand up to second order:

$$\Psi^q + v + \psi(v, p(s)) = \Psi^q + v + \frac{1}{2}(v, p(s) - p(0))H\begin{pmatrix} v \\ p(s) - p(0) \end{pmatrix} + O(\|(v, s)\|^3),$$

with

$$H = \begin{pmatrix} \psi_{vv}(0,p_0)[v,v] & \psi_{vp}(0,p_0)[v,p'(0)] \\ \psi_{vp}(0,p_0)[v,p'(0)] & \psi_{pp}(0,p_0)[p'(0),p'(0)] + \psi_p(0,p_0)p''(0) \end{pmatrix}$$

First, we take care of H_{22}, which is the lower right entry of H. Note that $\psi_p(0,p_0) = 0$, as shown in (5.4.26). Next, differentiating (5.4.25) with respect to p and evaluating at $p = p_0$ and $v = 0$ yields

$$0 = (I - Q)F_{vv}^q(0,p_0)[\psi_p(0,p_0)p'(0), \psi_p(0,p_0)p'(0)] \tag{5.4.30a}$$
$$+ (I - Q)F_{vp}^q(0,p_0)[\psi_p(0,p_0)p'(0), p'(0)] \tag{5.4.30b}$$
$$+ (I - Q)F_v^q(0,p_0)\psi_{pp}(0,p_0)[p'(0), p'(0)] \tag{5.4.30c}$$
$$+ (I - Q)F_{vp}^q(0,p_0)[\psi_p(0,p_0)p'(0), p'(0)] \tag{5.4.30d}$$
$$+ (I - Q)F_{pp}^q(0,p_0)[p'(0), p'(0)]. \tag{5.4.30e}$$

Again, due to $\psi_p(0,p_0) = 0$, we observe that the terms (5.4.30a), (5.4.30b) and (5.4.30d) equal 0. Moreover, $F^q(0,p) = 0$ for all $p \in \mathcal{P}$. Therefore, $F_{pp}^q(0,p_0) = 0$, and thus (5.4.30e) is 0 as well. As a consequence

$$0 = (I - Q)F_v^q(0,p_0)\psi_{pp}(0,p_0)[p'(0), p'(0)].$$

Since ψ maps into X_0 we conclude that $\psi_{pp}(0,p_0)[p'(0), p'(0)] = 0$ and thus $H_{22} = 0$. Next, we look at the off-diagonal entries $H_{21} = H_{12}$. To obtain an expression for $\psi_{vp}(0,p_0)$ we differentiate (5.4.19) with respect to p, insert $v = 0$, $p = p_0$ and thereby obtain

$$0 = (I - Q)F_{vv}^q(0,p_0)[v_1, \psi_p(0,p_0)p'(0)] \tag{5.4.31a}$$
$$+ (I - Q)F_{vp}^q(0,p_0)[v_1, p'(0)] \tag{5.4.31b}$$
$$+ (I - Q)F_v^q(0,p_0)\psi_{vp}(0,p_0)[v_1, p'(0)], \tag{5.4.31c}$$

for all $v_1 \in N$. Since $\psi_p(0,p_0) = 0$, as shown in (5.4.26), (5.4.31a) equals 0. Moreover, for all $p \in \mathcal{P}$, $F_v(0,p)v \in Z_0$ for all $v \in N$. Therefore, $F_{vp}^q(0,p)[v,p'(0)] \in Z_0$, too, and consequently (5.4.31b) is 0. Again, we conclude that $\psi_{vp}(0,p_0) = 0$. Therefore,

$$H = \begin{pmatrix} \psi_{vv}(0,p_0)[v,v] & 0 \\ 0 & 0 \end{pmatrix}$$

and thus

$$\Psi^q + v + \psi(v,p(s)) = \Psi^q + v + \frac{1}{2}\psi_{vv}(0,p_0)[v,v] + O(\|(v,s)\|^3)$$

for all $v \in N$ and $s \in (-\delta, \delta)$ in a neighborhood of $(0,0)$. We denote

$$Z^2(v, s) = \Psi^q + v + \frac{1}{2}\psi_{vv}(0, p_0)[v, v] \tag{5.4.32}$$

for the second order expansion.

However, until now we have assumed that v solves $\Phi(v, p(s)) = 0$. Since this solution v depends on s, we denote it by $v(s)$. Unfortunately, for given s these solutions $v(s)$ are not known exactly but they also have to be approximated by a function that we call v^{app}. We derive v^{app} by first computing $a^{\mathrm{app}}(s)$ according to (5.4.28). Then, $\hat{\Phi}^{\dagger}(a^{\mathrm{app}}(s), s) \approx 0$ and consequently $\hat{\Phi}(A_\phi(a^{\mathrm{app}}(s), 0)^\top, s) \approx 0$ for all ϕ, but for simplicity we keep $\phi = 0$. Now, we define $v^{\mathrm{app}}(s) := a^{\mathrm{app}}(s)u_\ell$ and because $\hat{\Phi}$ is the coordinate version of Φ, it follows that $\Phi(v^{\mathrm{app}}(s), s) \approx 0$. Given this function $v^{\mathrm{app}}(s)$, we use $Z^i(v^{\mathrm{app}}(s), s)$ for $i \in \{1, 2\}$ to approximate the real equilibrium $Z(v(s), s)$. Consequently, the total approximation error is given by

$$\left|Z^i(v^{\mathrm{app}}(s), s) - Z(v(s), s)\right| \leq \left|Z^i(v^{\mathrm{app}}(s), s) - Z^i(v(s), s)\right| \tag{5.4.33a}$$
$$+ \left|Z^i(v(s), s) - Z(v(s), s)\right|. \tag{5.4.33b}$$

In the remaining part of this subsection, we determine the magnitude of the approximation error of both parts (5.4.33a) and (5.4.33b) in dependence of the parameter s.

To obtain an estimate for the first part (5.4.33a), we reconsider the curve $(a(\tau), s(\tau))$ that describes the nontrivial equilibria. Because $a'(0) = 1$, we can reparameterize the curve such that locally $a(\tau) = \tau$. Then, we still have $s(0) = 0$, $s'(0) = 0$ and $s''(0) = -2\gamma_1/\gamma_2$. Due to $a'(\tau) = 1$ for all τ in a small neighborhood of the origin and the symmetry of $\hat{\Phi}$ discussed in Lemma 5.4.6, we can infer that $s(-\tau) = s(\tau)$. Consequently, $s(\tau)$ has vanishing third derivative at $\tau = 0$. Since the curve is smooth that results in $s(\tau) = -\gamma_1/\gamma_2\tau^2 + \mathcal{O}(\tau^4)$. Using this representation, one can show that

$$|a^{\mathrm{app}}(s(\tau)) - a(\tau)| = \left|\sqrt{\frac{-\gamma_2 s(\tau)}{\gamma_1}} - \tau\right| = \mathcal{O}(\tau^3) = \mathcal{O}(s^{\frac{3}{2}}).$$

Since $Z^i(v, s)$ is Lipschitz-continuous in v and has non-vanishing derivative with respect to v, that then results in

$$Z^i(v^{\mathrm{app}}(s), s) - Z^i(v(s), s) = \mathcal{O}(s^{\frac{3}{2}}).$$

To estimate the second part of the error (5.4.33b), it is important to note that $v(s)$ is dependent on s. In fact, due to the form of the pitchfork bifurcation, its

dependence can be expressed as $v(s) = \mathcal{O}(s^{\frac{1}{2}})$. Combining that with $Z^i(v,s) - Z(v,s) = \mathcal{O}(\|(v,s)\|^{i+1})$, as shown above, we find

$$Z^i(v(s), s) - Z(v(s), s) = \mathcal{O}(\|(v(s), s)\|^{i+1}) = \mathcal{O}(s^{\frac{i+1}{2}}).$$

Putting these two errors together, we conclude that the total approximation error is given by

$$Z^i(v^{\mathrm{app}}(s), s) - Z(v(s), s) = \mathcal{O}(s^{\min(\frac{3}{2}, \frac{i+1}{2})}). \tag{5.4.34}$$

In particular, deriving a third order approximation $Z^3(v, s)$ or even higher-order approximations is useless unless one can also improve the approximation in the first step (5.4.33a). This, however, would require a more detailed Taylor-expansion of $\hat{\Phi}^\dagger$ than the one given in Theorem 5.4.11 and thus more derivatives of F^q.

5.4.5   Linear Stability

Up to now, we have only determined the existence of equilibria of the PDE

$$\frac{\partial}{\partial t}\Psi(t, x) = F(\Psi, p)(x).$$

We have seen that apart from the trivial solution, there exists a solution curve of nontrivial solutions. In this section, we formally investigate the linear stability of q-twisted states and bifurcating branches. A rigorous proof of nonlinear stability is beyond the scope of this thesis.

Without loss of generality, we assume $\gamma_2 > 0$. If $\gamma_2 < 0$, reverse the parameterization of $p(s)$ by considering $p(-s)$ instead. Moreover, since the stability depends on the spectrum of the linearization, we denote

$$\kappa(s) := \sup_{\substack{k \in \mathbb{N} \\ k \neq \ell}} c_1(q, k, p(s))$$

and assume $\kappa(0) < 0$ since otherwise neither the twisted state nor the bifurcating equilibria can be stable. Note that $\kappa(s)$ is continuous in s and thus $\kappa(s) < 0$ for all s in a neighborhood of 0. Consequently, we only have to investigate how the critical zero eigenvalues at the bifurcation change, when perturbing (Ψ^q, p_0) to nearby equilibria.

Stability of the twisted state.   Since $\gamma_2 = \frac{\mathrm{d}}{\mathrm{d}s}c_1(q, \ell, p(s))\big|_{s=0}$ is assumed to be positive, $c_1(q, \ell, p(s)) < 0$ for all $s < 0$. Consequently, $\sup_{k \in \mathbb{N}} c_1(q, k, p(s)) < 0$ for all $s < 0$, which means that the spectrum of $F_v^q(0, p(s))$ is in the left half of the complex plane. Therefore, Ψ^q is linearly stable. If, on the other hand $s > 0$, $F_v^q(0, p(s))$ has positive eigenvalues, from which we can conclude linear instability.

Stability of the bifurcating branches in O. First, we study the stability of the bifurcating equilibria only in the space of odd functions O. Considering the bifurcation problem in this reduced space, there is only one critical eigenvalue with multiplicity one that passes through 0 and a one-dimensional curve of bifurcating equilibria. As explained at the end of Section 5.4.3, this curve corresponds to $\tau \mapsto (s(\tau), a(\tau))$ for $\tau \in (-\epsilon, \epsilon)$ with $s(0) = a(0) = 0$ and $a'(0) = 1$. Further, we denote $v(\tau) = a(\tau)u_\ell + \psi^\dagger(a(\tau)u_\ell, p(s(\tau)))$ for the equilibrium of $F^{q,\dagger}$ such that $F^{q,\dagger}(v(\tau), p(s(\tau))) = 0$. The principle of exchange of stability [97, Section I.7] can now be applied to study the linear stability of these bifurcating equilibria. First, the critical zero eigenvalue gets perturbed to an eigenvalue $\nu(\tau)$ of $F_v^{q,\dagger}(v(\tau), p(s(\tau)))$, see [97, Proposition I.7.2]. To be precise,

$$F_v^{q,\dagger}(v(\tau), p(s(\tau)))(u_\ell + \omega(\tau)) = \nu(\tau)(u_\ell + \omega(\tau)),$$

where $\omega(\tau) \in O$ is a continuously differentiable curve, $\nu(0) = 0$ and $s \in (-\delta, \delta)$. Moreover, $\nu(\tau)$ is continuously differentiable and represents the perturbation of the zero eigenvalue. Its derivative at $\tau = 0$ can be computed using the formula

$$\gamma_2 s'(0) = -\nu'(0),$$

see also formula ($I.7.41$) in [97]. However, due to $s'(0) = 0$ we obtain $\nu'(0) = 0$. The second derivative satisfies

$$2\gamma_2 s''(0) = -\nu''(0),$$

see formula ($I.7.45$) in [97]. Using $s''(0) = -2\gamma_1/\gamma_2$ we find $\nu''(0) = 4\gamma_1$. Since $\kappa(s) < 0$, the stability of the bifurcating branch in a neighborhood of the bifurcation point is then determined by the sign of the perturbed eigenvalue $\nu(\tau)$. To be precise, if $\gamma_1 < 0$ then $s''(0) > 0$ and thus bifurcating solutions exist whenever $s > 0$ is close to 0. Since $\gamma_2 < 0$, the q-twisted state has a positive eigenvalue and is thus linearly unstable in that parameter region. The leading eigenvalue of the bifurcating solution $v(\tau)$, however, is given by $\nu(\tau) < 0$. Therefore, the bifurcating solutions are stable. In this case, the bifurcation is supercritical. If $\gamma_1 > 0$, we have $s''(0) < 0$. Consequently, the bifurcating solutions exist for $s < 0$. Here, the q-twisted state is linearly stable and the leading eigenvalue of the bifurcating branch is $\nu(\tau) > 0$. Thus, these bifurcating equilibria are unstable. Such a bifurcation is called subcritical.

Stability of the bifurcating branches in H_0^1. Now, we consider the bifurcation problem in H_0^1. First note, that since $O \subset H_0^1$, the equilibrium $v(\tau)$ is still an equilibrium of F^q when considered in H_0^1. Furthermore, by applying the symmetry condition (5.4.5), one can retrieve every other equilibria in a neighborhood of

the bifurcation point. Specifically, for all $\phi \in \mathbb{R}$, the functions $B_\phi(v(\tau))$ are also equilibria. This symmetry results in a two-dimensional surface of equilibria, that is parameterized by ϕ and τ. Corresponding to this surface of equilibria, there are two critical zero spectral values, that we need to track when perturbing the trivial equilibria $(0, p_0)$ to bifurcating equilibria $(v(\tau), p(s(\tau)))$ that lies on the surface. Obviously, since $O \subset H_0^1$, $(v(\tau), p(s(\tau)))$ inherits the eigenvalue $\nu(\tau)$. Because $(v(\tau), p(s(\tau)))$ lies on a surface of equilibria, the other spectral value is given by 0. Even though this zero spectral value prevents us from directly concluding linear stability, our numerical simulations in the next section support the statement that bifurcating equilibria are stable in H_0^1 when they are stable in O for some specific parameter choices.

Remark 5.4.12. The bifurcation analysis, that has been presented in this section, is in principle also applicable to a much wider class of systems as just (5.3.5). In particular, one can also add $(d+1)$-way interactions (5.6.3) as those described in Section 5.6, i.e., quintuplet interactions, sextuplet interactions, ect. Then, one can perform a similar bifurcation analysis going along the lines of Sections 5.4.1-5.4.3. One expects to find a pitchfork bifurcation in the space of odd functions, since this bifurcation generically occurs in systems with a trivial zero, that is given by the twisted state, and symmetries (5.3.2), (5.3.3). Therefore, showing the presence of a pitchfork bifurcation should not be seen as the first priority of the bifurcation analysis. Instead, questions such as "When do bifurcating equilibria exist?", "Are they stable?", "Is the bifurcation sub- or supercritical?" are more interesting. To answer these kind of questions one needs to know the coefficients γ_1 and γ_2 that appear in Theorem 5.4.11. Obtaining them ultimately comes down to calculating the coefficients $c_1, \ldots, c_6$ in the representation of the derivative of the right-hand side, see Lemma 5.4.7. As illustrated in Appendix B.1, these calculations are already long for just pairwise interactions. Using symbolic differentiation software, we could still evaluate the derivatives for the triplet and quadruplet interactions in (5.3.5), but even that becomes a challenge for even higher-order interactions. Finally, as we will see in the next section, we can already (un)stabilize twisted states, influence the position (i.e., for which r it occurs) of the bifurcation and change the type of the bifurcation from sub- to supercritical and vice versa. Since all of that is already possible with just the pairwise, triplet and quadruplet interactions, that are included in (5.3.1), we believe that no new local dynamical effects appear when adding even higher-order interactions.

5.5   Applications

In this section, we take a few specific choices of the curve $p(s)$ and evaluate the bifurcation in more detail. We compute the ratio γ_2/γ_1 which determines if bi-

furcating solutions exist for $s > 0$ or $s < 0$. Moreover, we approximate these bifurcating solutions using the expansions in Section 5.4.4 and study their existence numerically as a cross-validation. In the first part of the section, we only look at graph coupling. The second subsection additionally includes triplet interactions and shows how they can influence the stability of twisted states. Finally, in the last part of this section, we let $\lambda \neq 0$ and $\mu \neq 0$ simultaneously, and explain how the triplet and quadruplet interactions can be used to change the type of the bifurcation from subcritial to supercritical or vice versa.

5.5.1   The Kuramoto Model on Nonlocal Graphs

The Attractive Kuramoto Model (Subcritical Bifurcation)

In this section we apply the bifurcation theory to the Kuramoto model on limits of $\Bbbk$-nearest neighbor graphs. Specifically, we consider no higher-order interactions, i.e., $\lambda = \mu = 0$ in (5.3.5). Instead, we only consider the coupling range r in the continuum limit as a parameter. When $r > 0$ is very small, the eigenvalues around a q-twisted state are all negative [177]. Then, upon increasing r, the eigenvalue corresponding to $k = 1$ is the first one that passes through 0. We denote this threshold by $r_0^{\mathrm{a}}(q)$ with a superscript a to indicate that we are working with the attractive Kuramoto model. It is called attractive, since two oscillators that are close attract each other. In our notation that means $c_1(q, k, (r, 0, 0)) < 0$ for all $k \in \mathbb{N}$ and $r \in (0, r_0^{\mathrm{a}}(q))$ and $c_1(q, 1, (r_0^{\mathrm{a}}(q), 0, 0)) = 0$, see Figure 5.6 and [177].

To analyze this bifurcation we choose a curve $p \colon (-\delta, \delta) \to \mathcal{P}$ with $p(s) = (r_0^{\mathrm{a}}(q) + s, 0, 0)$. As explained in Section 5.4.3, finding equilibria of the Kuramoto model on a graph around the q-twisted state in a neighborhood of the bifurcation at $r_0^{\mathrm{a}}(q)$ is equivalent to finding solutions to the equation $\hat{\Phi}^{\dagger}(a, s) = 0$ in a neighborhood of the origin. According to the results in the same section, for given $s_0 \in (-\delta, \delta)$, an approximate solution is given by a^{app} and it exists whenever the quantity under the root in (5.4.28) is positive. As seen in Figure 5.7 and shown in Appendix B.2.3, $\gamma_2/\gamma_1 > 0$. Moreover, since the first eigenvalue passes through 0 from below, we have $\gamma_2 > 0$, which then implies $\gamma_1 > 0$. Therefore, for $r \in (r_0^{\mathrm{a}}(q) - \delta, r_0^{\mathrm{a}}(q))$ there exist further equilibria of (5.3.1) and (5.3.5) when $\lambda = \mu = 0$ around the q-twisted states. However, according to the principles explained in Section 5.4.5, the q-twisted state is stable in that regime and the bifurcating solutions are unstable.

To confirm the existence of the bifurcating solutions, we consider the sequence of finite particle systems (5.2.1) whose continuum limit is given by (5.2.8), or equivalently (5.3.1) with $\lambda = \mu = 0$. In these systems, the coefficients a_i are defined by $a_i = 1$ if $\min(|i|, M - |i|) \leq \lfloor Mr \rfloor$ and $a_i = 0$ otherwise. The corresponding
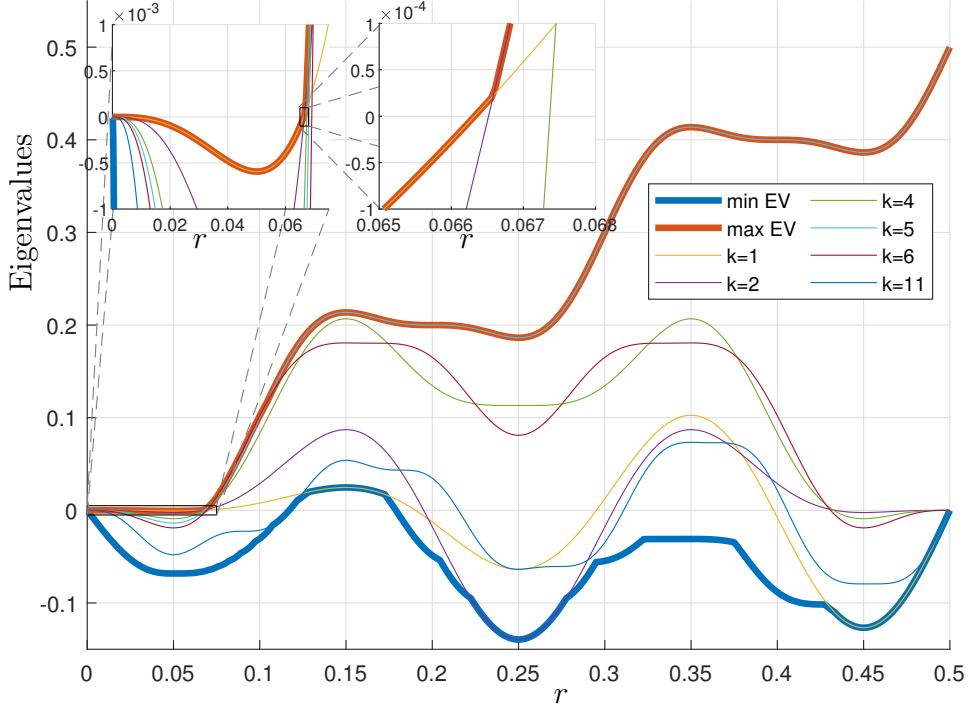
Figure 5.6: Eigenvalues $c_1(5, k, (r, 0, 0))$ of a 5-twisted state. Until $r_0^a(5) \approx 0.06632$ all eigenvalues are negative. At $r_0^a(5)$, the eigenvalue $c_1(5, k, (r, 0, 0))$ with $k = 1$ passes through 0. Shortly thereafter, the eigenvalue corresponding to $k = 2$ passes through 0 as well. For $0.1170 \lesssim r \lesssim 0.1789$ all eigenvalues are positive.

system of phase differences, defined by $\theta_i := \phi_i - \phi_1$, is given by

$$\dot{\theta}_i = \frac{1}{M} \sum_{j=1}^{M} a_{i-j} \sin(\theta_j - \theta_i) - \frac{1}{M} \sum_{j=1}^{M} a_{1-j} \sin(\theta_j). \qquad (5.5.1)$$

However, since the definition of a_i involves rounding, r cannot be regarded as a continuous bifurcation parameter. Therefore, we consider the system

$$\dot{\theta}_i = \frac{1}{M} \sum_{j=1}^{M} b_{i-j} \sin(\theta_j - \theta_i) - \frac{1}{M} \sum_{j=1}^{M} b_{1-j} \sin(\theta_j), \qquad (5.5.2)$$
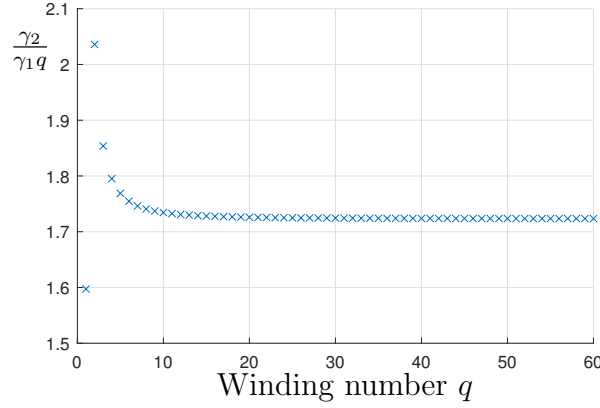
Figure 5.7: Bifurcation ratio $\frac{\gamma_2}{\gamma_1 q}$ for the attractive Kuramoto model at $r = r_0^{\mathrm{a}}(q)$ when the first ($k = 1$, independent of q) eigenvalue passes through 0. The value of $\frac{\gamma_2}{\gamma_1 q}$ seems to converge to ≈ 1.723.

in which the coefficients b_i are defined as follows: Let $\Bbbk_0 = \lfloor rM \rfloor$. Then,

$$b_i := \begin{cases} 1 & \text{if } \min(|i|, M - |i|) \leq \Bbbk_0, \\ rM - \Bbbk_0 & \text{if } \min(|i|, M - |i|) = \Bbbk_0 + 1, \\ 0 & \text{otherwise.} \end{cases}$$

Here, r can be considered as a continuous bifurcation parameter.

However, when simulating the finite particle system (5.5.2), it turns out that the bifurcation does not occur at $r_0^{\mathrm{a}}(q)$ but at another value $r_0^{\mathrm{a},M}(q)$ which is slightly different from $r_0^{\mathrm{a}}(q)$. In fact, numerical simulations show $r_0^{\mathrm{a}}(q) = r_0^{\mathrm{a},M}(q) + \mathcal{O}(1/M)$. For example, for $q = 5$ we get $r_0^{\mathrm{a}}(5) \approx 0.06632$ whereas $r_0^{\mathrm{a},1000}(5) \approx 0.06582$. Consequently, when looking for bifurcating solutions of q-twisted state in the finite particle system (5.5.2) one should search in a neighborhood of $r_0^{\mathrm{a},M}(q)$. In particular, we fix $s = s_0$ and look for bifurcating solutions for $r = r_0^{\mathrm{a},M}(q) + s_0$. In order to get an approximation for a solution of $\Phi(v, p(s)) = 0$, we calculate γ_1 and γ_2 according to (5.4.21) and (5.4.24) based on the value $r = r_0^{\mathrm{a}}(q)$. Then, we calculate $a^{\mathrm{app}}(s_0)$ according to (5.4.28) and proceed by along the steps explained in Section 5.4.4 to get v^{app}. Next, we use a discrete analog of the first order approximation $Z^1(v^{\mathrm{app}}, s_0)$ as the initial condition of a zero finding algorithm (e.g., a Newton-iteration), that we then apply to the right-hand side of (5.5.2). For one specific parameter choice, the solution $\hat{Z}$ of this zero-finding algorithm is depicted in Figure 5.8.

As a last numerical experiment, we study how good the first- and second-order approximations $Z^i(v^{\mathrm{app}}(s), s)$ with $i = 1, 2$ are as $s \to 0$. To this end, we let s be in a discrete set of values $\mathcal{S}$, for which bifurcating equilibria exist. Here, we
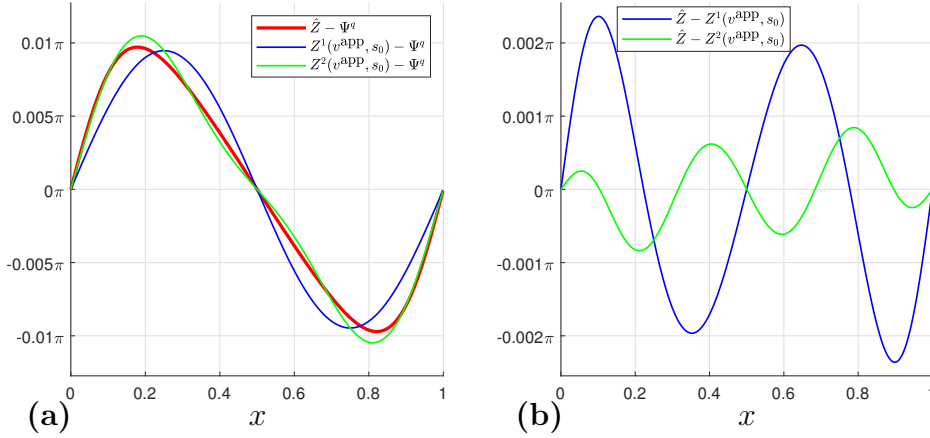
Figure 5.8: Bifurcating solution around a q-twisted state in the system (5.5.2). Part (a) shows $\hat{Z} - \Psi^q$ (red line), which when added to Ψ^q results in the nontrivial solution $\hat{Z}$, its first order approximation $Z^1(v^{\mathrm{app}}, s_0) - \Psi^q$ (blue) and its second order approximation $Z^2(v^{\mathrm{app}}, s_0) - \Psi^q$ (green). Here, $v^{\mathrm{app}} = a^{\mathrm{app}} u_1$ such that $\Phi(v^{\mathrm{app}}, p(s_0)) \approx 0$ up to higher-order terms. If this was exact, as explained in Section 5.4.4, we would have $F(Z(v, s_0), p(s_0)) = 0$. Here, we denote $\hat{Z}$ for an equilibrium of the system (5.5.2) for $r = r_0^{\mathrm{a}, M}(q) + s_0$. Moreover, part (b) depicts the first order error $\hat{Z} - Z^1(v^{\mathrm{app}}, s_0)$ (blue line) and the second order error $\hat{Z} - Z^2(v^{\mathrm{app}}, s_0)$ (green line). Parameter values: $M = 1000$, $s_0 = -10^{-4}$, $q = 5$. That results in $\gamma_1 \approx 9.494 \cdot 10^{-3}, \gamma_2 \approx 8.400 \cdot 10^{-2}, a^{\mathrm{app}} = 2.974 \cdot 10^{-2}$.

choose $\mathcal{S}$ as $\mathcal{S} = -10^{-5.5+j/12}$ with $j = 0, \ldots, 30$. Then, for each $s \in \mathcal{S}$, we calculate the bifurcating equilibria $\hat{Z}(s)$ of (5.5.2) for $r = r^{\mathrm{a}, M}(q) + s$ by a zero finding algorithm as before. Moreover, for each $s \in \mathcal{S}$, we calculate the first and second order approximations $Z^i(v^{\mathrm{app}}(s), s)$ with $i = 1, 2$ as before. Finally, to compare the approximations with the true bifurcating equilibria, we compute $\left\| \hat{Z}(s) - Z^i(v^{\mathrm{app}}(s), s) \right\|$ and analyze its dependence on s. As one can see in Figure 5.9, the set $\mathcal{S}$ is split into three main regions. For large $|s|$, specifically for $s \lessapprox -3 \cdot 10^{-4}$ nonlinear effects take place. Then, for intermediate values of $|s|$, specifically for $-3 \cdot 10^{-4} \lessapprox s \lessapprox -10^{-5}$, the approximation error seems to depend algebraically on s, such that $\left\| \hat{Z}(s) - Z^i(v^{\mathrm{app}}(s), s) \right\| = \mathcal{O}(s^{\alpha_i})$. An estimate from Figure 5.9 gives $\alpha_1 \approx 0.92$ and $\alpha_2 \approx 1.38$, which is only slightly worse than the analytical prediction $\alpha_i = \min(\frac{3}{2}, \frac{i+1}{2})$ from (5.4.34). Finally, we believe that for even smaller values of $|s|$, numerical inaccuracies terminate the algebraic convergence.

While the simulations depicted in Figure 5.8 and Figure 5.9 are based on the system (5.5.2), in which r is a continuous bifurcation parameter, similar results hold for the system (5.5.1). Here, however, we could not choose M arbitrarily.
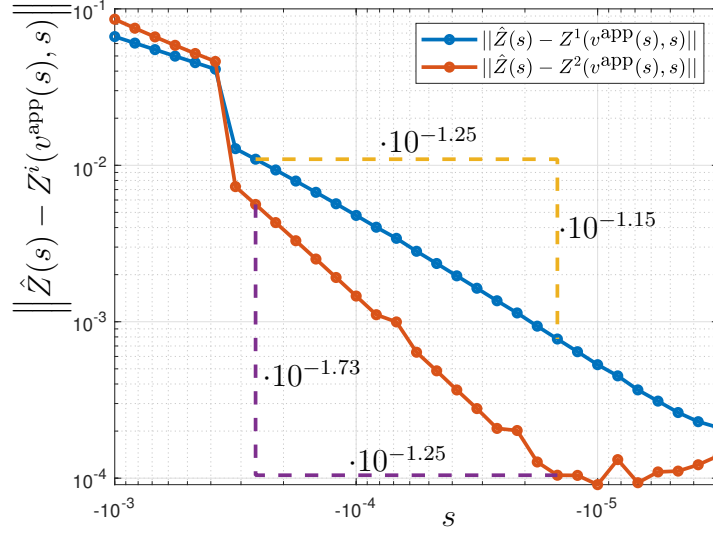
Figure 5.9: Approximation error $\left\|\hat{Z}(s) - Z^i(v^{\mathrm{app}}(s), s)\right\|$ for $i = 1, 2$ and $s \in \mathcal{S} = -10^{-5.5+j/12}$ with $j = 0, \ldots, 30$. Here, $\hat{Z}(s)$ is a bifurcating equilibria of (5.5.2) for $r = r^{\mathrm{a},M}(q) + s$. Moreover, the norm is given by $\|\cdot\| = \|\cdot\|_{\mathrm{L}^2}$. The rate of convergence depicted by the triangles is approximately $1.15/1.25 \approx 0.92$ for $i = 1$ and $1.73/1.25 \approx 1.38$ for $i = 2$. Parameter values: $q = 5$, $M = 5000$, $r_0^{\mathrm{a},M}(q) \approx 0.06622$, $\gamma_1 \approx 9.494 \cdot 10^{-3}$, $\gamma_2 \approx 8.400 \cdot 10^{-2}$.

Instead, we were particularly successful finding bifurcating solutions when $r_0^{\mathrm{a},M}(q)$ is close to an integer multiple of $1/M$.

The Repulsive Kuramoto Model (Supercritical Bifurcation)

Now we consider a variant of (5.3.5) with $\lambda = \mu = 0$, in which we reverse the sign of the right-hand side. In particular, we look at

$$\frac{\partial}{\partial t}\Psi(t, x) = -\int_{\mathbb{S}} W_r(x - y)\sin(\Psi(t, y) - \Psi(t, x))\, \mathrm{d}y + \int_{\mathbb{S}} W_r(y)\sin(\Psi(y))\, \mathrm{d}y. \tag{5.5.3}$$

Its finite-dimensional analog of (5.5.2) is then given by

$$\dot{\theta}_k = \frac{-1}{M}\sum_{j=1}^{M} b_{k-j}\sin(\theta_j - \theta_k) + \frac{1}{M}\sum_{j=1}^{M} b_{1-j}\sin(\theta_j). \tag{5.5.4}$$

Here, two oscillators that are close to each other, repel each other. Therefore, we call this model the repulsive Kuramoto model, see also [71].

Because the systems (5.5.3) and (5.3.5) with $\lambda = \mu = 0$ are only different by a factor of -1 on the right-hand side, they share the same equilibria. Yet, they are not identical, since the stability of these equilibria depends on the eigenvalues of the linearization of the right-hand side and they are nonidentical. In fact, the spectrum of the linearization of the right-hand side of (5.5.3) can be obtained from multiplying the spectrum of (5.3.5) by -1. Similarly, the eigenvalues of the system (5.5.4) can be obtained by multiplying the eigenvalues from (5.5.2) by -1. Therefore, the eigenvalues of the linearization of the right-hand side around a q-twisted state are $-c_1(q, k, (r, 0, 0))$. Consequently, the q-twisted state is linearly stable if $c_1(q, k, (r, 0, 0)) > 0$ for all $k \in \mathbb{N}$.

As seen in Figure 5.6, for $q = 5$ there is an interval $r \in (0.117, 0.1789)$ in which all these conditions are satisfied. Moreover, in a neighborhood of the lower boundary of this interval, $\max_k -c_1(5, k, (r, 0, 0)) = -\min_k c_1(5, k, (r, 0, 0))$ is attained for $k = 11$. In general, it was shown in [71] that for all $q \in \mathbb{N}$ with $q > 1$ there is an interval in which a q-twisted state is linearly stable in the repulsive Kuramoto model. In particular, the authors showed that stability holds if $1.1787 \lessapprox 2qr \lessapprox 1.7829$, which agrees with our observation in Figure 5.6. For $q = 1$ there is no bifurcation in the repulsive Kuramoto model.

To analyze the bifurcation, we denote $r_0^r(q)$ for the smallest value of r until which there is a positive eigenvalue of the q-twisted state in the repulsive Kuramoto model. For example $r_0^r(5) \approx 0.11787$. We then choose the parameter curve $p(s) = (r_0^r(q) + s, 0, 0)$ and select k for which $\min_k c_1(q, k, (r_0^r(q), 0, 0))$ is attained. For example, for $q = 5$, we have $k = 11$, but in general the critical eigenvalue depends on q, see Figure 5.10(a). A numerical evaluation of (5.4.21) and (5.4.24) for $q \leq 60$ shows $\gamma_1, \gamma_2 > 0$, see also Figure 5.10(b). Therefore, bifurcating solutions exist when $s < 0$, or equivalently $r < r_0^r(5)$. Since the 5-twisted state is unstable in that regime, these bifurcating solutions are linearly stable.

To validate that numerically, we first choose M large enough and then determine $r_0^{r,M}(5)$, which is the bifurcation point in the M-particle system with $\lim_{M \to \infty} r_0^{r,M}(5) \to r_0^r(5)$. Next, we choose $s < 0$ with small enough $|s|$. To numerically confirm that bifurcating equilibria in the repulsive Kuramoto model are stable and that trajectories with initial conditions, which are close to the 5-twisted state, converge to these bifurcating equilibria, we simulate the system (5.5.4). We choose three different random initial conditions, that are close to the 5-twisted state. In particular, these random initial conditions are obtained by adding centered random modulations with amplitude $3 \cdot 10^{-2}$ to the 5-twisted state. Each of these random modulations is depicted by a different color in Figure 5.11. We simulate the system (5.5.4) until the trajectories reach an equilibrium. We observe, see Figure 5.11, that all resulting equilibria lie in a neighborhood of the 5-twisted state. Therefore, we represent the equilibria by modulations of the 5-
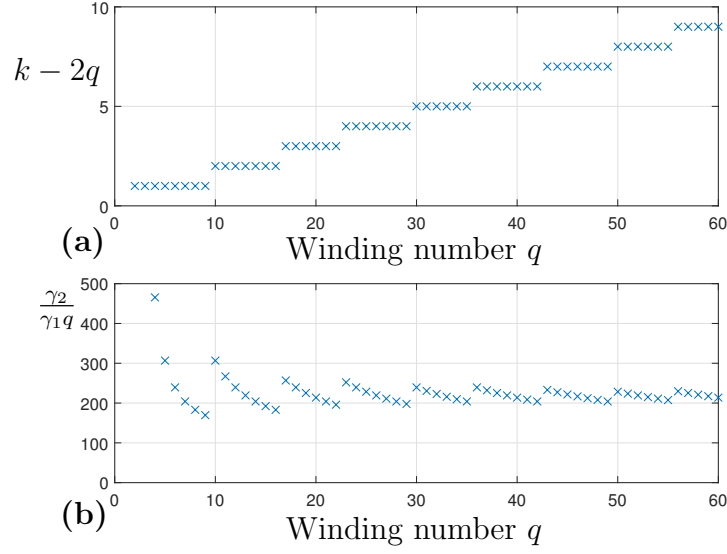
Figure 5.10: Bifurcation in the repulsive Kuramoto model at $r = r_0^{\mathrm{r}}(q)$. Part (a) shows how the critical eigenvalue, i.e., the value of k for which $\min_k c_1(q, k, (r, 0, 0))$ is attained, depends on q. For example, for $q = 5$ we have $k - 2q = 1$ so the minimum is attained for $k = 11$. Part (b) depicts the bifurcation ratio $\frac{\gamma_2}{\gamma_1 q}$ at $r = r_0^{\mathrm{r}}(q)$, which is the bifurcation when the q-twisted state first becomes stable upon increasing r. For $q = 1$, there is no bifurcation in the repulsive Kuramoto model and the data points that are approximately at $(2, 6248)$ and $(3, 1045)$ are omitted in this plot.

twisted state. These modulations $\mathcal{G}$ are depicted in the figure with the color that matches the color of the respective initial perturbation of the 5-twisted state. The modulations are sinusoidal functions with an amplitude of $0.12575 \approx 0.04\pi$, which is close to the prediction $a^{\mathrm{app}} = 0.0394\pi$ by (5.4.28), and 11 periods, caused by u_{11} and w_{11} spanning the unstable direction of the 5-twisted state. Furthermore, the modulations can be obtained from each other by applying the operator B_ϕ.

5.5.2   Stabilization via Higher-Order Interactions

In this section, we keep $r_0 \in (0, \frac{1}{2})$ and $\mu_0 = 0$ constant and vary λ. When considering the eigenvalues $c_1(q, k, (r_0, \lambda, 0))$ we note that $\frac{\mathrm{d}}{\mathrm{d}\lambda} c_1(q, k, (r_0, \lambda, 0))$ is independent of λ and k. We denote this quantity by $h(q, r_0)$. Note that it is given by

$$h(q, r_0) = -\hat{W}_{r_0}(q) = -\frac{2}{\pi q} \sin(2\pi q r_0).$$
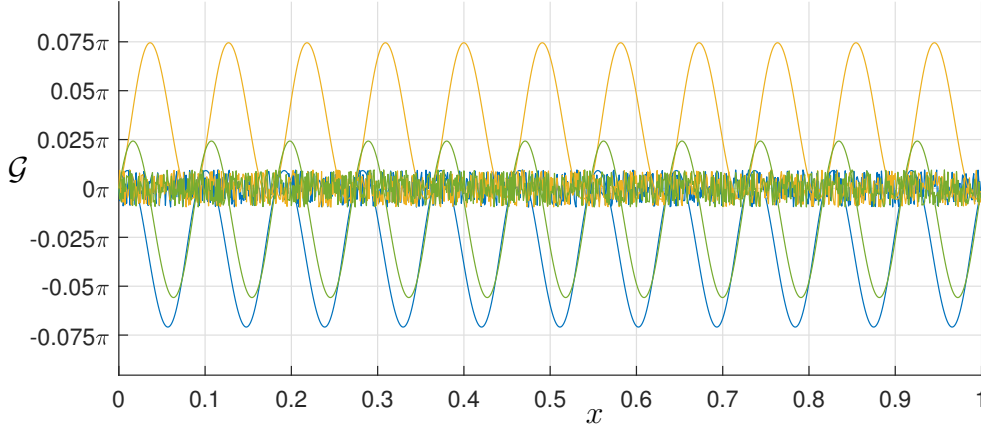
Figure 5.11: Simulation of the system (5.5.4) with three different initial conditions. The initial conditions are given by random modulations of the 5-twisted state. These modulations $\mathcal{G}$ are centered at 0 and all have an amplitude of $3 \cdot 10^{-2}$. They are displayed in the figure by different colors. For each of these three initial conditions, we simulate system (5.5.4) until each of the trajectories reaches an equilibrium. The resulting equilibria are represented in the figure as modulations of the 5-twisted state and their color matches the color of the respective initial condition. Parameter values: $M = 1000, s = -10^{-5}, r_0^{\mathrm{r},M}(5) \approx 0.11654, r_0^{\mathrm{r}}(5) = 0.11704, r = r_0^{\mathrm{r},M}(q) + s, \gamma_1 \approx 1.38 \cdot 10^{-3}, \gamma_2 \approx 2.12$.

Therefore, whenever this quantity is nonzero, one can use higher-order interactions to stabilize or destabilize q-twisted states on the continuum limit of $\Bbbk$-nearest neighbor graphs, as derived in Section 5.2.1, by adding them to the right-hand side of (5.2.8). To explain this, suppose for example, that $m := \max_k c_1(q, k, (r_0, 0, 0)) > 0$. In this case the q-twisted state is unstable in the model (5.3.5) with $\lambda = \mu = 0$. Due to the linearity of $c_1(q, k, (r_0, \lambda, 0))$ with respect to λ, we can then write

$$c_1(q, k, (r_0, \lambda, 0)) = c_1(q, k, (r_0, 0, 0)) + \lambda h(q, r_0).$$

Then, the maximal eigenvalue of the linearization around a q-twisted state for parameters r_0, λ is given by $m + \lambda h(q, r_0)$. Consequently, if a q-twisted state is unstable for $\lambda = 0$, i.e., $m > 0$, one can stabilize it by choosing $\lambda < \frac{-m}{h(q,r_0)}$ if $h(q, r_0) > 0$ and $\lambda > \frac{-m}{h(q,r_0)}$ if $h(q, r_0) < 0$. In the nongeneric case $h(q, r_0) = 0$, a (de)stabilization is not possible.

It can be shown (see Theorem B.2.3) that for all q and large enough r the largest eigenvalue $m = \max_k c_1(q, k, (r, 0, 0))$ is attained for $k = q$. In particular,
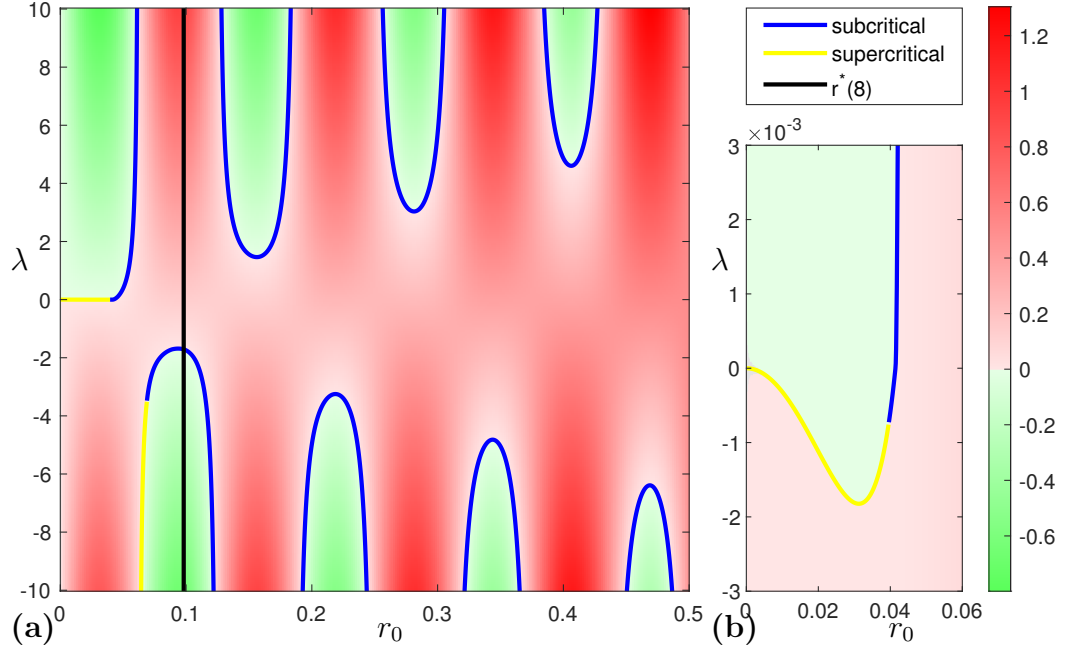
Figure 5.12: Maximal eigenvalue of a 8-twisted state for in the system (5.3.5) in dependence of r_0 and λ. Red colors represent an unstable 8-twisted state, whereas the 8-twisted state is stable in regions where the color is green. The bigger the magnitude of the maximal eigenvalue, the darker the color. The black line depicts the value of $r^\star(8)$. For all $r_0 > r^\star(8)$ the bifurcation boundary can be calculated from (5.5.6). The blue curve indicates a subcritical bifurcation whereas supercritical bifurcations are yellow. Part (b) is a more detailed view of one region in part (a). Note also that the bifurcation at $\lambda = 0$ and $r_0 \approx 0.0414$ is subcritical, as shown in Section 5.5.1.

a sufficient condition that the largest eigenvalue m is attained for $k = q$ is

$$\frac{2}{\pi q} \leq 2r - \frac{1}{\pi}\sin(2\pi r), \tag{5.5.5}$$

which is proven in Appendix B.2. Since the right-hand side of (5.5.5) is monotonically increasing in r, there is a threshold $\tilde{r}(q)$ such that (5.5.5) holds for all $r > \tilde{r}(q)$. Moreover, due to the continuity of the right-hand side and the convergence of the left-hand side to 0 as $q \to \infty$, this threshold converges to 0 as $q \to \infty$. However, since (5.5.5) is only a sufficient condition, the largest eigenvalue might already be attained by $k = q$ for $r < \tilde{r}(q)$. We denote $r^\star(q)$ for the smallest value of $r \in (0, \frac{1}{2})$ such that for all $r \geq r^\star(q)$, the largest eigenvalue is attained for $q = k$. We then have the inequality $0 \leq r^\star(q) \leq \tilde{r}(q) \leq \frac{1}{2}$. Consequently, when

$r_0 \in (r^\star(q), \frac{1}{2}]$ and $\hat{W}_{r_0}(q) \neq 0$ there is a bifurcation when $\lambda = \lambda_0$, with

$$\lambda_0 = -\frac{m}{h(q, r_0)} = \frac{\hat{W}_{r_0}(2q) + \hat{W}_{r_0}(0) - 2\hat{W}_{r_0}(q)}{4\hat{W}_{r_0}(q)}. \tag{5.5.6}$$

Remark 5.5.1. Note that we need $\lim_{k \to \infty} c_1(q, k, (r_0, \lambda_0, 0)) = -(\frac{1}{2} + \lambda_0)\hat{W}_{r_0}(q) \neq 0$ in order to ensure that an isolated eigenvalue is passing through 0 at the bifurcation point. When $r_0 > r^\star(q)$ this is equivalent to $\lambda_0 \neq -\frac{1}{2}$, since we assumed $\hat{W}_{r_0}(q) \neq 0$. However, since $\hat{W}_{r_0}(2q) + \hat{W}_{r_0}(0) > 0$, it is guaranteed by (5.5.6) that $\lambda_0 \neq -\frac{1}{2}$.

To determine whether a bifurcation is subcritical or supercritical, we note that bifurcating equilibria in subcritical bifurcations are unstable, whereas they are stable in supercritical bifurcations. As explained in Section 5.4.5, bifurcating equilibria are linearly stable if and only if q-twisted states are linearly unstable in the parameter region. Thus, by analyzing if bifurcating equilibria exist for $s < 0$ or $s > 0$ and combining this information with the stability of the twisted state in the same parameter region, we can determine if the bifurcation is sub- or supercritical. Due to the approximation (5.4.28) and the explanations in the paragraph above it, bifurcating equilibria exist when the sign of s and γ_2/γ_1 is opposite. For these s, we then determine the linear stability of the q-twisted states by looking at the eigenvalues. Finally, the stability of the bifurcating equilibria can be obtained by inverting the stability of the twisted states. The resulting type of the bifurcation is depicted in Figure 5.12.

5.5.3 Changing the Type of the Bifurcation

Here, we fix r and consider $4\lambda + 2\mu$ as the bifurcation parameter. Then, we vary λ and see how this variation affects the type of the bifurcation. Assuming (5.5.5), the largest eigenvalue is attained for $k = q$ and the bifurcation takes place at

$$4\lambda + 2\mu = \frac{\hat{W}_r(0) + \hat{W}_r(2q) - 2\hat{W}_r(q)}{\hat{W}_r(q)} =: H(q, r).$$

It is easy to see that (5.5.5) is satisfied if $2 \leq 2\pi qr - \sin(2\pi qr)$, which is equivalent to $qr \geq v_0 \approx 0.4065$, where v_0 solves $2 = 2\pi v_0 - \sin(2\pi v_0)$. Assuming that, we consider the curve

$$p^{\mathfrak{t}}(s) = (r^{\mathfrak{t}}(s), \lambda^{\mathfrak{t}}(s), \mu^{\mathfrak{t}}(s))^\top = (r_0, 4s - 2\mathfrak{t} + H(q, r_0)/4, 2s + 4\mathfrak{t})^\top,$$

which is parameterized by s and $\mathfrak{t} \in \mathbb{R}$ is an additional parameter. Note that $4\lambda^{\mathfrak{t}}(0) + 2\mu^{\mathfrak{t}}(0) = H(q, r)$ for all $\mathfrak{t} \in \mathbb{R}$. Therefore, there is a bifurcation at $s = 0$ for all $\mathfrak{t} \in \mathbb{R}$. We calculate

$$\gamma_2^{\mathfrak{t}} = \frac{\mathrm{d}}{\mathrm{d}s} c_1(q, q, p)\Big|_{s=0} = -5\hat{W}_r(q),$$

which is independent of $\mathfrak{t}$. Moreover,

$$c_5(q, q, p^{\mathfrak{t}}(0)) = c_5(q, q, p^0(0)) - \frac{1}{2}\mathfrak{t}\hat{W}_r(q),$$

$$c_2(q, q, p^{\mathfrak{t}}(0)) = c_2(q, q, p^0(0)) - \frac{1}{2}\mathfrak{t}(-\hat{W}_r(0) + \hat{W}_r(2q)),$$

$$c_3(q, 2q, q, p^{\mathfrak{t}}(0)) = c_3(q, 2q, q, p^0(0)),$$

$$c_1(q, 2q, p^{\mathfrak{t}}(0)) = c_1(q, 2q, p^0(0)),$$

which leads to

$$\gamma_1^{\mathfrak{t}} = \frac{1}{2}\left(c_5(q, q, p^{\mathfrak{t}}(0)) - \frac{c_2(q, q, p^{\mathfrak{t}}(0))c_3(q, 2q, q, p^{\mathfrak{t}}(0))}{c_1(q, 2q, p^{\mathfrak{t}}(0))}\right)$$

$$= \gamma_1^0 - \frac{1}{4}\mathfrak{t}\hat{W}_r(q) + \frac{c_3(q, 2q, q, p^0(0))}{4c_1(q, 2q, p^0(0))}\mathfrak{t}(-\hat{W}_r(0) + \hat{W}_r(2q))$$

$$= \gamma_1^0 + \mathfrak{t}X(q, r),$$

with

$$X(q, r) = -\frac{1}{4}\hat{W}_r(q) + \frac{c_3(q, 2q, q, p^0(0))}{4c_1(q, 2q, p^0(0))}(-\hat{W}_r(0) + \hat{W}_r(2q)).$$

It can be shown (see Appendix B.1) that

$$X(q, r) = \frac{1}{q}\iota(qr), \tag{5.5.7}$$

for a function $\iota: \mathbb{R}_{\geq 0} \to \mathbb{R}$, see Figure 5.13. Moreover, based on the explicit expression of ι that is given in the appendix, we infer $\iota(\upsilon) = \upsilon + \mathcal{O}(1)$ as $\upsilon \to \infty$.

To conclude, $\gamma_2^{\mathfrak{t}}$ is independent of $\mathfrak{t}$ and whenever $\gamma_2^{\mathfrak{t}} \neq 0$ there is a bifurcation at $s = 0$. Furthermore, if additionally $X(q, r) \neq 0$, $\gamma_1^{\mathfrak{t}}$ can take any value in $\mathbb{R}$ by suitably choosing $\mathfrak{t}$. Consequently, the ratio $\gamma_2^{\mathfrak{t}}/\gamma_1^{\mathfrak{t}}$ can also take arbitrary values in $\mathbb{R} \setminus \{0\}$. Since the sign of that ratio determines the type (sub- or supercritical) of the bifurcation, the parameter $\mathfrak{t}$ can be used to influence the type of the bifurcation. As can be rigorously shown, $\iota(\upsilon) > 0$ for all $\upsilon \geq \upsilon_0$, see Figure 5.13. Therefore, a sufficient condition to have $X(q, r) > 0$ is given by $qr \geq \upsilon_0$.

The possibility of changing the bifurcation type by adjusting the strengths of various higher-order interactions to the continuum limit of $\Bbbk$-nearest neighbor graphs extends previous results [160, 104]. In particular, [160] contains a global bifurcation analysis for a coupling composed of a pairwise and two higher-order interaction terms. The authors found that by suitably choosing the strengths of the higher-order interactions one can influence the type of the pitchfork bifurcation, in which a certain state changes its stability. Moreover, in [104] it is shown in the
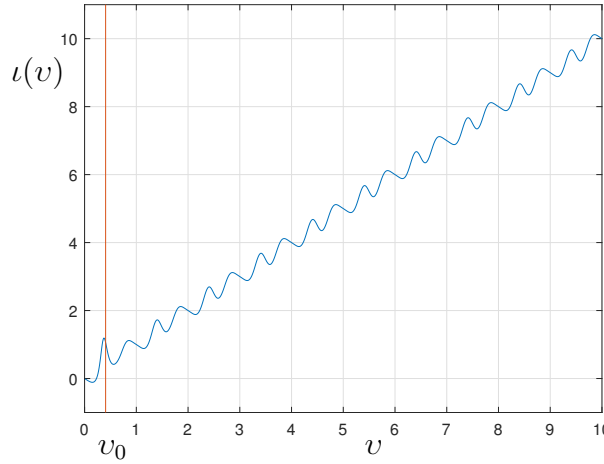
Figure 5.13: The function $\iota(v)$ and the value of $v_0 \approx 0.4065$.

context of bifurcations from trivial branches in network dynamics, that modifications of the original network model can generically induce changes between sub- and super-critical bifurcations. The main idea in [104] is to first formally study normal forms for suitable macroscopic observables and then monitor the effect of network model changes in the concrete bifurcation coefficients in the normal form. Hence, the results presented here concretely and rigorously prove that higher-order interactions can trigger the effect between sub- and supercritical bifurcations, even for nontrivial branches of twisted states.

5.6 Other Higher-Order Nonlocal Couplings

In this section, we discuss other possible generalizations of the pairwise interactions (5.2.8) to higher-order interactions. Instead of focusing on the system of phase differences, we consider the original system that describes the absolute position $\Theta(t, x)$ of the oscillators. The name "nearest neighbor" coupling for the graph interactions (5.2.1) originates from supposing that the individual oscillators $i = 1, \ldots, M$ are equidistantly placed on the unit circle in ascending order. In a $\Bbbk$-nearest neighbor graph, each oscillator is connected to all of its $\Bbbk$-predecessors and $\Bbbk$-successors on the circle. If one fixes $r = \Bbbk/M$ and sends $M \to \infty$, a nonlocal coupling in the continuum limit emerges. One can imagine two oscillators $x, y \in \mathbb{S}$ in the continuum limit to be coupled if $W_r(x - y) = 1$. The parameter r specifies how far the two oscillators can be spaced apart such that they are still considered neighbors.

Now, let us consider the higher-order coupling

$$\frac{\partial}{\partial t}\Theta(t,x) = \int_{\mathbb{S}}\int_{\mathbb{S}} W_r(z+y-2x)\sin(\Theta(t,z)+\Theta(t,y)-2\Theta(t,x))\ \mathrm{d}y\mathrm{d}z, \quad (5.6.1)$$

which is characterized by the coupling kernel $W_r(z+y-2x)$. While this is a straight-forward generalization of the pairwise continuum limit of $\Bbbk$-nearest neighbor coupling (5.2.8) to higher-order interactions, the terminology "nearest neighbor" has to be used more carefully. Strictly speaking, three oscillators $z,y,x \in \mathbb{S}$ do not need to neighbor each other for them to be coupled, which is the case when $W_r(z+y-2x) = 1$. For example, when $z = y = \frac{1}{2}$ and $x = 0$, we have $z+y-2x = 0 \in \mathbb{S}$. Therefore, these three oscillators are coupled for every $r > 0$, even though z and x are relatively far apart. Similar arguments also hold for the 4-way interaction in (5.3.1). One can further generalize (5.6.1) by replacing the coupling function and the interaction function to

$$\frac{\partial}{\partial t}\Theta(t,x) = \int_{\mathbb{S}}\int_{\mathbb{S}} W_r(m_1 z + m_2 y + m_3 x) \\ \cdot \sin(n_1\Theta(t,z)+n_2\Theta(t,y)+n_3\Theta(t,x))\ \mathrm{d}y\mathrm{d}z, \quad (5.6.2)$$

or even to the $(d+1)$-way coupling

$$\frac{\partial}{\partial t}\Theta(t,x) = \int_{\mathbb{S}^d} W_r\left(\sum_{i=1}^{d} m_i y_i + m_{d+1} x\right) \\ \cdot \sin\left(\sum_{i=1}^{d} n_i\Theta(t,y_i) + n_{d+1}\Theta(t,x)\right)\ \mathrm{d}y \quad (5.6.3)$$

for coefficients $m_i, n_i \in \mathbb{Z}\setminus\{0\}$. Note, however, that q-twisted states are in general not invariant under the evolution of (5.6.3). They are guaranteed to be invariant if $n_i = m_i$ for $i = 1,\ldots,d+1$. To see that one first inserts $\Theta^q(x)$ into (5.6.3) and then conducts a linear transformation $y_1 \mapsto \hat{y}_1 = \frac{1}{m_1}(\sum_{i=1}^{d} m_i y_i + m_{d+1} x)$ in the integral. After this transformation the integrand is independent of x, which confirms the invariance of twisted states. However, when for example $d = 1$ and $m_1 = m_2 = n_1 = -n_2 = 1$, twisted states are no longer invariant, as one can see by the same transformation. For special cases—as those considered above—the system is symmetric: If $\sum_{i=1}^{d+1} n_i = 0$ then we have a phase shift symmetry (5.3.2) and if $\sum_{i=1}^{d+1} m_i = 0$ then we have a rotational symmetry of the ring (5.3.3)

If one wants to derive higher-order continuum limits that overcome the issue of the nearest neighbor terminology in higher-order networks, one can consider other generalizations of (5.2.8). For example, three oscillators $z,y,x \in \mathbb{S}$ in the 3-way

coupling

$$\frac{\partial}{\partial t}\Theta(t,x) = \int_{\mathbb{S}}\int_{\mathbb{S}} W_r(z-x)W_r(y-x) \\ \cdot \sin(\Theta(t,z) + \Theta(t,y) - 2\Theta(t,x)) \, \mathrm{d}y\mathrm{d}z \tag{5.6.4}$$

are coupled if z is close to x and additionally y is close to x. As a result, all three oscillators z, y and x need to be close enough to each other for them to be coupled. Such a coupling topology is more reminiscent of higher-order network topologies derived in phase reduction. In particular, if one applies (4.5.4a) to $\Bbbk$-nearest neighbor graphs, sets $\alpha = 0$ and derives a continuum limit as $M \to \infty$ with $\Bbbk = \lfloor rM \rfloor$ for fixed r, then one part, i.e., one summand, of this continuum limit agrees with (5.6.4). Another possible higher-order generalization of (5.2.8) is given by

$$\frac{\partial}{\partial t}\Theta(t,x) = \int_{\mathbb{S}}\int_{\mathbb{S}} W_r(z-x)W_r(y-x)W_r(z-y) \\ \cdot \sin(\Theta(t,z) + \Theta(t,y) - 2\Theta(t,x)) \, \mathrm{d}y\mathrm{d}z. \tag{5.6.5}$$

This coupling additionally introduces a symmetry between x, y and z. In fact, if x, y, z are coupled, then any permutation of them is also coupled. Note that the prefactors $1, 1, -2$ of $\Theta(t,z), \Theta(t,y)$ and $\Theta(t,x)$ in (5.6.4) and (5.6.5) can also be generalized to arbitrary coefficients $n_1, n_2, n_3 \in \mathbb{Z} \setminus \{0\}$. However, they must add up to zero, i.e., $n_1 + n_2 + n_3 = 0$. Such "diffusive" coupling terms guarantees the invariance of q-twisted states and can correspond, for example, to a normal form symmetry in a phase reductions [10].

Of course, we can also study the stability of q-twisted states in the models (5.6.3), (5.6.4) and (5.6.5). Calculating the eigenvalues of the linearization of the right-hand sides of those systems around a q-twisted state yields the following:

Whenever $d > 1$, the eigenvalues of the linearization of the right-hand side of (5.6.3) with $n_i = m_i$, $i = 1, \ldots, d+1$ are given by $\lambda_0 = 0$ with multiplicity 1 and $\lambda_k = \frac{1}{2}m_{d+1}\hat{W}_r(q)$ if $k \neq 0$. This eigenvalue has multiplicity ∞. In the system (5.6.4), the eigenvalues are $\lambda_0 = 0$, again with multiplicity 1 and

$$\lambda_k = \frac{1}{4}\hat{W}_r(q)\left[\hat{W}_r(q+k) + \hat{W}_r(q-k) - 2\hat{W}_r(q)\right] \tag{5.6.6}$$

if $k \neq 0$, each with multiplicity 2. Finally, for the system (5.6.5), the eigenvalues around a q-twisted state are given by $\lambda_0 = 0$ (multiplicity 1) and

$$\lambda_k = \frac{1}{16}\sum_{\ell \in \mathbb{Z}} \hat{W}_r(\ell)\left[\hat{W}_r(-k+\ell-q)\hat{W}_r(\ell+q) + \hat{W}_r(-k+\ell+q)\hat{W}_r(\ell-q)\right.$$

$$+ \hat{W}_r(\ell - q)\hat{W}_r(k + q + \ell) + \hat{W}_r(\ell + q)\hat{W}_r(k - q + \ell)$$
$$- 4\hat{W}_r(\ell - q)\hat{W}_r(\ell + q)\Big]$$

if $k \neq 0$. Again, the multiplicity of these eigenvalues is 2. For all these systems, the eigenfunctions are given by $\sin(2\pi kx)$ and $\cos(2\pi kx)$.

In Section 5.5.2 we showed that adding higher-order interactions of the form (5.6.1) to the pairwise coupling (5.2.8) can stabilize q-twisted states, when the strength of the higher-order interactions is adjusted suitably. A numerical analysis shows that the systems (5.6.3), (5.6.4) and (5.6.5) can also stabilize q-twisted states when added to the pairwise coupling (5.2.8). However, we chose two different instances of higher-order interactions of the form (5.6.3) for a couple of reasons. First, the formulas for 3-way and 4-way coupling are simple, since they only include the evaluation of W_r once. In contrast, the 3-way coupling (5.6.5) involves three evaluations of W_r and a generalization to 4-way coupling would involve even more evaluations. Second, it is easier to compute eigenvalues of the linearization of the right-hand side of (5.6.3) around a twisted state than it is to compute them for (5.6.4) and (5.6.5). Third and most importantly, the eigenvalues of the linearization of (5.6.3) around a twisted state are independent of k. Therefore, when adding higher-order interactions of the form (5.6.3) to the pairwise system (5.2.8), the maximal eigenvalue is still attained for the same k when varying the strength of the higher-order coupling.

One possible way to make the triplet interactions (5.6.4) analytically tractable is to replace the function $W_r(x)$ from (5.2.5) by a function $G(x)$ everywhere, which consists only of finitely many Fourier modes, e.g.,

$$G_A(x) = 1 + A\cos(2\pi x),$$

where $A \in \mathbb{R}$ is a parameter. Then, the eigenvalues of the linearization of (5.6.4) around a 1-twisted state would be given by

$$\lambda_k = \begin{cases} 0 & \text{if } k = 0, \\ \frac{1}{4}A(2 - 2A) & \text{if } k = 1, \\ -\frac{1}{4}A^2 & \text{if } k = 2, \\ -\frac{1}{2}A^2 & \text{if } k \geq 3. \end{cases}$$

While strictly speaking these eigenvalues are dependent on k, they are a lot easier to handle as there are only finitely many — in this case three or four if one includes $k = 0$ — distinct eigenvalues. Consequently, when adding (5.6.4) with $W_r(x)$ replaced by $G_A(x)$ to a pairwise coupling, one can determine the maximal eigenvalue by a case distinction between $k = 0, 1, 2$ and $k \geq 3$, that depends on the parameters A and the higher-order coupling strength. Even though this approach would

lead to analytical results about the stability of the 1-twisted state, it also comes with a few drawbacks. First, the analysis by a case distinction can become very tedious. Second, when replacing $W_r(x)$ by $G_A(x)$, the continuum limit (5.2.8) does not originate from a $\Bbbk$-nearest neighbor topology anymore and thus does not agree with the continuum limit originally analyzed in [177]. Third, the function $G_A(x)$ can only be used to study the 1-twisted state. For other winding numbers $q \geq 2$, the eigenvalues (5.6.6) of the triplet interaction (5.6.4) would all be zero. In this regard, the dynamics induced by the coupling function $W_r(x)$ is a lot richer, which ultimately breaks down to the fact that it has infinitely many nonzero Fourier modes. All in all, this is another reason why we focused on triplet and quadruplet interactions of the form (5.6.3).

5.7 Summary

In this chapter, we considered the continuum limit of a Kuramoto model on $\Bbbk$-nearest neighbor graphs and extended it to include higher-order interactions. We analyzed the stability of q-twisted states and performed a rigorous Lyapunov–Schmidt reduction to find bifurcating equilibria. We saw that the bifurcation at which the twisted states lose their stability is a pitchfork bifurcation. Moreover, we determined leading coefficients in the Taylor expansion to classify the bifurcation as sub- or supercritical. This considers and extends previous works from two perspectives. Firstly, we added a bifurcation analysis to previous works [177, 71], which have analyzed stability of twisted state in the attractive and repulsive Kuramoto model on $\Bbbk$-nearest neighbor graphs. In particular, the problem of finding and classifying bifurcating solutions was left open in [177]. Secondly, the authors of [160] considered a higher-order all-to-all Kuramoto model whose right-hand side consists of a pairwise part and two higher-order interaction parts, thus resembling our model (5.3.5). In this model they analyzed the stability of the splay state and the bifurcation at which it loses its stability. While there is always a pitchfork bifurcation, they found that when varying the strengths of the higher-order couplings, as we did in Section 5.5.3, one can influence if the bifurcation is sub- or supercritical. In that regard, we have extended their results to the continuum limit of $\Bbbk$-nearest neighbor networks and thereby shown that the phenomenon that one can change the type of a bifurcation with suitable higher-order interactions generically occurs in a wider class of higher-order networks.

Chapter 6

Community Integration Algorithms (CIAs) for the Simulation of Large Network Dynamical Systems

This chapter is based on two publications [37, 36] which are both joint work with Mechthild Thalhammer and Christian Kuehn. In particular, the technical parts are taken from the publication [37] of which I am the main author.

Data Availability   This chapter is accompanied by software. In particular, the code that we use for our numerical simulations is publicly available on a GitHub repository [32] that can be accessed via
https://github.com/tobiasboehle/Community-Integration-Algorithms-CIAs.

6.1   Introduction and Background

Caused by the ability of network dynamical systems to model many real-world processes, the level of research activity in this field has lately seen a dramatic increase [176, 13, 146]. Since many real-world systems are complicated processes, so must be the network dynamical system, to describe them accurately. In particular, network dynamical systems can show complicated dynamical behavior, even if their governing equations are relatively simple. This makes intuitive predictions hard and as a result numerical simulations are of increasing importance. In many network dynamical systems, each node adjusts its own behavior according to an average of the inputs it receives from its neighbors. From a computational viewpoint, this can efficiently be evaluated if the interactions are very sparse because

then there are just a few function evaluations and the complexity scales linearly with the number of nodes. However, for all-to-all coupled networks, the averaging step consists of the evaluation of large sums and is therefore very costly. In fact, a direct approach yields that the computational complexity scales at least quadratically with the number of nodes. This situation gets much worse for temporal networks [87], adaptive networks [81], multilayer networks [30], and higher-order interactions beyond graphs [15]. To overcome this problem, one might hope that there is a low-dimensional number of averaged order parameters (or observables), which are similar or even identical inputs for each node at each time step.

In this chapter, we develop general community integration algorithms (CIAs) for the efficient simulation of a wide range of network dynamical systems. We show that these CIAs work for very general networks with community structure, that they are robust with regard to real data sets, that the general method yields linear computational complexity with respect to the dimensions of the systems in each time step, and that the steps naturally extend to higher-order dynamics.

The concept of computing global observables, that can be used as a common input for all—or at least many—nodes, has already appeared in the context of Fast Multipole Methods (FMMs), see [151, 79]. These FMMs can be used to accelerate simulations of particles coupled by a Coulomb (or gravitational) force. Given some charged (or weighted) particles contained in a specified region, one first computes global observables and then uses them to derive an approximation of the joint Coulomb (or gravitational) potential. This approximation can then efficiently be evaluated at many test positions at the same time. Similarly to our methods, this procedure is faster than computing the individual contributions of each particle to every test position. However, due to the singularity of the Coulomb (and gravitational) force at the origin, the approximation only converges for points that have some minimum distance to the specified region. We will develop similar methods, but in contrast to FMMs, the approximation used in our method converges inside the specified region.

Moreover, the concept of Random Batch Methods (RBM) [90] accelerates the time integration of dynamical systems on networks by choosing communities. In contrast to our CIAs, the network structure in RBM is assumed to be all-to-all. Furthermore, the time efficiency benefits from choosing communities as small as possible, whereas CIAs profit from large communities.

The remaining parts are organized as follows. In Section 6.2, we illustrate the main idea of our CIAs and introduce the considered classes of network dynamical systems. In Section 6.3, we detail and exemplify the key steps of community integration algorithms (CIAs) at a general example from our model class. Then, in Section 6.4 we list possible extensions of several CIA steps. Combining these extensions further enlarges the model class, to which our CIAs can be applied. In

Section 6.5, we present the advantages of our approach and confirm the substantial gain in efficiency by a series of numerical experiments for widely-used models and real-world networks. This includes Kuramoto systems arising in the description of synchronization, extended Kuramoto-type models involving higher-order interactions and Cucker–Smale systems modeling collective motion in real-world animal networks. Moreover, we illustrate that the approximation of the coupling function does not impede the accuracy solutions obtained by CIAs. Finally, Section 6.6 contains a brief summary. Supplementary calculations and illustrations are collected in Appendix C, which contains a detailed mathematical setup for all the examples and more numerical experiments confirming the accuracy of our methods.

6.2   Main Idea of CIAs and Model Class

Most real-world networks are neither extremely sparse nor extremely dense but rather contain many heterogeneous structures [134]. Therefore, using brute-force network simulations quickly encounters computational barriers. In this chapter, we are going to combine several mathematical ideas to simulate many large-scale network dynamics models efficiently. Here, we start with a non-technical presentation of our approach, which is split into two pre-simulation steps (P1),(P2), that only have to be done once, and two evaluation steps (E1),(E2), that have to be performed in each time step. The first step (P1) is to find communities, i.e., densely connected sub-networks, in the heterogeneous network, that describes all present interactions. The second step (P2) is to approximate the coupling function between nodes in a suitable function system, e.g., by using Fourier methods. This step helps us to identify possible observables, that later become relevant. The order of (P1) and (P2) can be reversed or parallelized. For each community, we utilize the similarity of nodes to calculate local observables that can then act as a common input for each node. This significantly reduces the information processing in step (E1) and reduces quadratic or worse polynomial scaling complexity to just linear cost with respect to the number of nodes. Since our networks are assumed to be heterogeneous, we must also account in step (E2) for the very sparsely connected nodes, which is possible by direct computation. Our approach yields significant reductions of the required memory capacities and the overall costs measured by the total numbers of function evaluations.

Simulations utilizing these four steps can be of importance in many sciences ranging from physics, chemistry, biology and medicine to social sciences [14, 146]. Illustrative examples for continuous-time dynamical systems on networks include Desai–Zwanzig systems [61] describing the motion of interactive particles under the influence of external confining potentials, Kuramoto models [107], tracking the evolution of phase oscillators, Cucker–Smale systems [57] describing the movements

and flocking behavior of birds, coupled van-der-Pol/FitzHugh–Nagumo models frequently used in neuroscience [38], and Hegselmann-Krause models for opinion formation [86]. Instead of studying classical versions of these models using all-to-all coupling, we study several of these models on general networks that possess community structure. Even though the network models originate from different disciplines, most of them can be described by one single general network model, which we focus on here. The model class is given by

$$\dot{x}_k = f_k(x_k) + \frac{1}{M} \sum_{l=1}^{M} a_{kl}\, g(x_l, x_k), \qquad , \ x_k(0) \text{ given}, \qquad (6.2.1)$$

where $k \in \{1, \ldots, M\}$, $t \in [0, T]$ and g is a smooth interaction function. This system is based on an underlying network that has M nodes and is represented by an $M \times M$-dimensional adjacency matrix A with entries a_{kl}. For the sake of simplicity, we first restrict ourselves to an undirected and unweighted graph such that A is additionally symmetric and $a_{kl} \in \{0, 1\}$. Later, in Section 6.4 we loosen this restriction. Further, $x_k(t)$ denotes the state of node k at time t, the functions f_k describe the intrinsic dynamics of the k-th node and $g(x_l, x_k)$ is a general coupling function that describes the interaction that node l has on node k, if they are coupled. Finally, $T > 0$ denotes a final time until which we want to integrate the system (6.2.1). While the range of x_k and thus also the domain of f_k and g is generally part of an abstract space $\mathcal{X}$, we typically have $\mathcal{X} \in \{\mathbb{R}, \mathbb{R}^d, \mathbb{R}/(2\pi\mathbb{Z}), \ldots\}$. By grouping the states of the nodes into one common vector $x = (x_1, \ldots, x_M)$ and introducing an M-dimensional function H with components

$$H_k(x) = f_k(x_k) + \frac{1}{M} \sum_{l=1}^{M} a_{kl}\, g(x_l, x_k), \quad k \in \{1, \ldots, M\}, \qquad (6.2.2a)$$

the initial value problem from (6.2.1) can also be written as

$$\dot{x} = H(x). \qquad (6.2.2b)$$

Even though this is a very general formulation, many typical network models have special structure. For example, in many models, the coupling function g is of the form $g(\tilde{x}, \hat{x}) = h(\tilde{x} - \hat{x})$. Table C.1, that can be found in the appendix, shows that many real-world systems fit into this framework. We remark that this includes all-to-all coupling in the case of a complete graph. This special case will be an automatically included sub-problem in our implementation of CIAs since the coupling within each community closely resembles an all-to-all coupling. Although the network systems that we have mentioned above are described by continuous-time dynamical systems and specifically by nonlinear ordinary differential equations, completely analogous considerations for CIAs hold for discrete-time network

dynamical systems. In fact, when numerically integrating a continuous-time dynamical system that is given by a system of ODEs, one first time-discretizes this ODE system. Our CIAs efficiently evaluate large sums that appear in the resulting discrete-time system. But one can also apply our CIAs to network models that are naturally posed in discrete time. We also cover the Bornholdt–Rohlf discrete-time network model for self-organized criticality [39] to illustrate this point.

6.3   Community Integration Algorithms

To numerically integrate the system (6.2.2) one first discretizes the time interval $[0, T]$ into many small steps $0 = t_0 < t_1 < \cdots < t_\Omega = T$ and then employs an iterative time stepping scheme [28], e.g., a Runge–Kutta or multistep method. Independent of the method, each time iteration step needs at least one evaluation of the right-hand side H. Therefore, it is of key importance for a fast numerical integration to implement the evaluation of H efficiently. However, when one looks at the specific structure of H, one notices that each of its components consist of a large sum. In total there are $\mathcal{O}(M^2)$ operations (summations and evaluations of the coupling function g) necessary to evaluate $H(x)$ for a given x only a single time. This quadratic dependence on M severely restricts the number of nodes that a network can possess such that numerical simulations are tractable. For higher-order systems, see Appendix C.1.7, the situation even worsens.

Our new community integration algorithms are applicable to a wide range of dynamical systems on networks that consist of densely connected subnetworks or communities with sparse connections across the communities. These CIAs achieve to evaluate the right-hand side H in (6.2.2) and require only $\mathcal{O}(M)$ operations in each time step. It consists of four main steps. The first two are done before the simulation and only need to be done once, whereas the other two have to be processed for each time step, see Figure 6.1. These steps are:

(P1) Application of an effective community detection algorithm and transformation of the adjacency matrix to block form by a permutation of nodes.

(P2) Identification of a suitable representation or high-order approximation, respectively, of the coupling function g.

(E1) Exploiting community structure by computing local observables for each community to avoid summations common among similar nodes.

(E2) Treatment of the remaining sparse parts of the network as well as small remaining heterogeneity within communities based on direct summations.
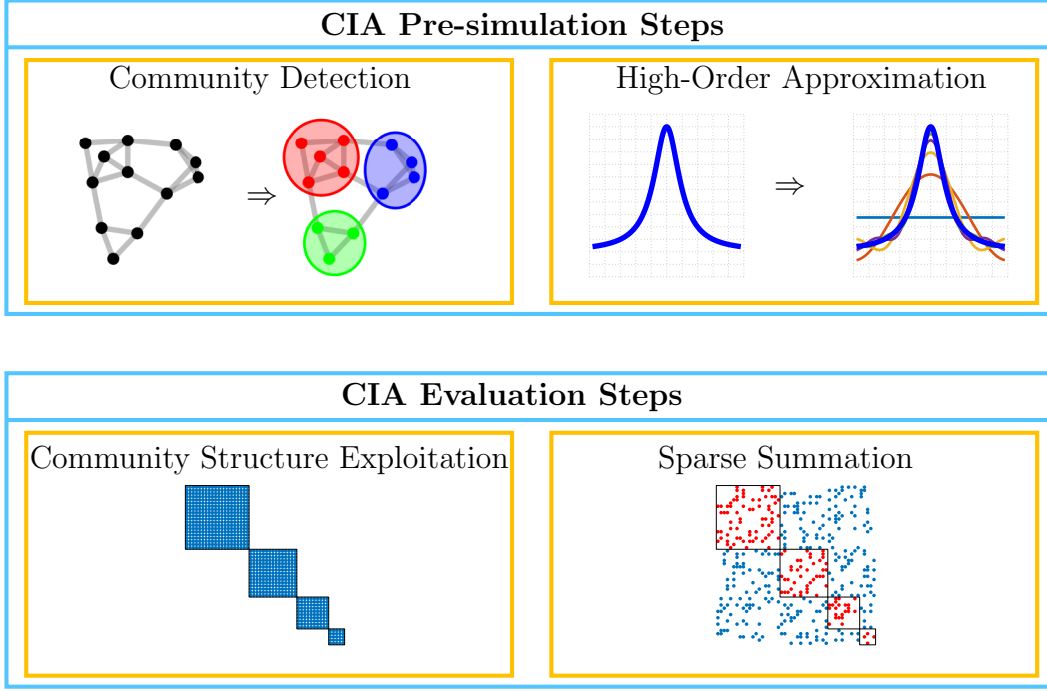
Figure 6.1: Flowchart that illustrates the steps of our community integration algorithm.

In the following we illustrate these steps via the example of phase oscillator systems

$$\dot{\phi}_k = f_k(\phi_k) + \frac{1}{M} \sum_{l=1}^{M} a_{kl} \; h(\phi_l - \phi_k). \tag{6.3.1}$$

Here, $\phi_k \in \mathbb{T} := \mathbb{R}/(2\pi\mathbb{Z})$ and the network is given by the adjacency matrix $A = (a_{kl})_{k,l=1,\dots,M}$ that can seen in Figure 6.2. To follow the steps below, one can also think of a more concrete example such as the Kuramoto model. In the classical Kuramoto model (1.1.1), we have $f_k(\phi_k) = \omega_k \in \mathbb{R}$, $a_{kl} \equiv 1$ and $h(\psi) = \sin(\psi)$, cf. [107]. We discuss the Kuramoto model in more detail in Appendix C.1.4.

6.3.1 CIA Pre-simulation Steps

Community Detection (P1): A key feature of our CIA is that it exploits the community structure of the underlying network. A community structure is present if the associated adjacency matrix is in block structure. However, when looking at the adjacency matrix that is depicted in Figure 6.2, there is at first no block structure evident. The community structure only becomes evident after
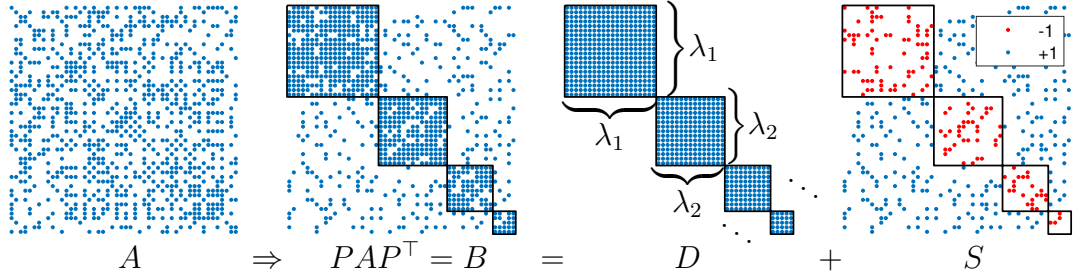
Figure 6.2: Community detection step (P1). Rearranging the rows and columns of the adjacency matrix A yields a matrix B that has apparent block structure. Moreover, B can be split into a part D that has exact block structure and a sparsity S that absorbs the deviation of B from exact block structure. A blue dot depicts a $+1$ entry in the matrix whereas a red dot represents a -1 entry.

permuting the nodes such that each community consists of nodes whose labels are consecutive integers. This permutation results in a matrix $B = PAP^\top$, where P is a permutation matrix that is induced by a permutation $\kappa : \{1, \ldots, M\} \rightarrow \{1, \ldots, M\}$.

In many real-world scenarios the matrix B does not have exact block structure but there may still be missing links inside a community and additional links across two communities. In any case, we assume, that the matrix B has an evident block structure and can thus be split into a dense matrix D, that has the exact block structure, and a sparse matrix S, such that $B = D + S$. Here, D only consists of entries in $\{0, 1\}$ whereas S is a sparse matrix with entries in $\{-1, 0, 1\}$. A $+1$ entry in S denotes that there is an additional edge connecting two communities whereas a -1 entry represents a missing edge in a community.

The aim of step (P1) is to detect communities such that the permuted adjacency matrix B has approximate block structure and can be decomposed into a dense matrix D and a sparse matrix S, as seen in Figure 6.2. This can be achieved as follows: First, one employs an algorithm to detect communities in the underlying network. In general, such an algorithm takes the adjacency matrix A as an input and outputs a partition of the node set into communities. There are many effective algorithms that can detect communities in the underlying graph, of which we particularly recommend one that is based on the optimization of a Hamiltonian [147, 148], see also Appendix C.1.1. For a general network, the major part of these algorithms have the computational complexity $\mathcal{O}(M^2)$. For a comparison of different algorithms see [36]. Second, one defines a permutation κ that permutes the nodes of the network such that nodes that are in the same community have consecutive labels. Then the resulting adjacency matrix $B = PAP^\top$, where P is the permutation matrix induced by the permutation κ, has an apparent block

structure as seen in Figure 6.2. Finally, one defines a matrix D that has blocks of ones on the diagonal whose sizes correspond to the sizes of the communities. The remaining sparse part can be obtained by calculating $S = B - D$.

It is not necessary to store the full matrix D but only the sizes of the communities that we denote by $\lambda_1, \lambda_2, \ldots, \lambda_\Lambda$ if there are a total of Λ communities. For numerical reasons it is sometimes better to allow nodes to belong to no community instead of letting them be part of a community that consists of very few or even only one node. Further, S can be stored in a sparse format, so the total memory requirement is $\mathcal{O}(M)$.

By using $PAP^\top = B = D + S$, where P is the permutation matrix induced by the permutation κ, and $\theta_k(t) := \phi_{\kappa(k)}(t)$, we can write (6.3.1) as

$$\dot{\phi}_{\kappa(k)} = f_{\kappa(k)}(\phi_{\kappa(k)}) + \frac{1}{M} \sum_{l=1}^{M} a_{\kappa(k)\kappa(l)} \, h(\phi_{\kappa(l)} - \theta_{\kappa(k)})$$

and so

$$\dot{\theta}_k = f_{\kappa(k)}(\theta_k) + \frac{1}{M} \sum_{l=1}^{M} b_{kl} \, h(\theta_l - \theta_k)$$

$$= \underbrace{f_{\kappa(k)}(\theta_k) + \frac{1}{M} \sum_{l=1}^{M} s_{kl} \, h(\theta_l - \theta_k)}_{=:H_k^{\text{sparse}}(\theta)} + \underbrace{\frac{1}{M} \sum_{l=1}^{M} d_{kl} \, h(\theta_l - \theta_k)}_{=:H_k^{\text{dense}}(\theta)}.$$

Thus, when evaluating the right-hand side, we only need to compute

$$\dot{\theta}_k = H_k^{\text{sparse}}(\theta) + H_k^{\text{dense}}(\theta). \tag{6.3.2}$$

Since $d_{kl} = 1$ if $1 \le k, l \le \lambda_1$ and $d_{kl} = 0$ if $1 \le k \le \lambda_1$ and $l > \lambda_1$ we obtain

$$H_k^{\text{dense}}(\theta) = \frac{1}{M} \sum_{l=1}^{\lambda_1} h(\theta_l - \theta_k)$$

for $1 \le k \le \lambda_1$, making it effectively an all-to-all coupling within that community. Similar representations of $H_k^{\text{dense}}(\theta)$ apply when $k > \lambda_1$.

High-Order Approximation (P2): This pre-simulation step is about the expansion of the coupling function h. Since the domain is 2π-periodic it makes sense to identify Fourier coefficients a_m, b_m, for $m \in \mathbb{N}$ with

$$h(\theta) = \sum_{m=0}^{\infty} \Big(a_m \cos(m\theta) + b_m \sin(m\theta) \Big).$$

Equivalently, one can also consider a Fourier expansion based on a complex Fourier series, see Appendices C.1.2 and C.1.4. Alternatively, yet not suitable here, an expansion in terms of polynomials is possible, see Appendix C.1.3. In any case for numerical reasons we terminate the series at a finite m and only deal with the approximation

$$h(\theta) \approx \sum_{m=0}^{p} \Big(a_m \cos(m\theta) + b_m \sin(m\theta) \Big), \qquad (6.3.3)$$

for some $p \in \mathbb{N}$. The magnitude of accuracy of this approximation is determined by the smoothness of h. If h is $\xi \geq 2$ times continuously differentiable the decay of the Fourier coefficients is $|a_m| = \mathcal{O}(m^{-\xi})$ and $|b_m| = \mathcal{O}(m^{-\xi})$. Thus, the approximation satisfies the error bound

$$\left| h(\theta) - \sum_{m=0}^{p} \Big(a_m \cos(m\theta) + b_m \sin(m\theta) \Big) \right| \leq c \frac{1}{p^{\xi-1}},$$

for a constant c. We will see in Section 6.5.2 and Appendix C.2 that this error in the approximation of the right-hand side also implies an error of the solution to the differential equation (6.3.1). Next, we show that approximating the coupling function makes it easier to identify good local observables.

6.3.2   CIA Evaluation Steps

Based on the preparation done in the CIA pre-simulation steps, the right-hand side of the initial value problem (6.3.1) or equivalently (6.3.2) can now be evaluated using just $\mathcal{O}(M)$ operations. This evaluation is structured into two main steps:

Community Structure Exploitation (E1):   This step aims to compute $H^{\mathrm{dense}}(\theta)$, which, as shown previously, can be written as

$$H_k^{\mathrm{dense}}(\theta) = \frac{1}{M} \sum_{l=1}^{\lambda_1} h(\theta_l - \theta_k),$$

if k is a node belonging to the first community, i.e., $1 \leq k \leq \lambda_1$ and similar representation are possible when k is not in the first community. Combining this with the Fourier approximation (6.3.3) from step (P2) and by using addition theorems for sin and cos, we obtain

$$H_k^{\mathrm{dense}}(\theta) \approx \frac{1}{M} \sum_{l=1}^{\lambda_1} \sum_{m=0}^{p} \Big(a_m \cos(m(\theta_l - \theta_k)) + b_m \sin(m(\theta_l - \theta_k)) \Big)$$

$$= \sum_{m=0}^{p} \frac{1}{M} \sum_{l=1}^{\lambda_1} \Big(a_m \sin(m\theta_l)\sin(m\theta_k) + a_m \cos(m\theta_l)\cos(m\theta_k)$$

$$+ b_m \sin(m\theta_l)\cos(m\theta_k) - b_m \cos(m\theta_l)\sin(m\theta_k) \Big), \qquad (6.3.4)$$

for $1 \le k \le \lambda_1$. Even though it first seems a lot messier, we have separated terms involving θ_l and terms with θ_k. Since we sum over l and the terms involving θ_l remain the same for each k, we can precompute quantities

$$q_m^{\cos} := \frac{1}{M} \sum_{l=1}^{\lambda_1} \cos(m\theta_l) \quad \text{and} \quad q_m^{\sin} := \frac{1}{M} \sum_{l=1}^{\lambda_1} \sin(m\theta_l), \qquad (6.3.5)$$

for $m = 0, \ldots, p$. In particular, (6.3.5) are precisely the local observables, which are felt as an input by all nodes within one community. They allow us to conclude

$$H_k^{\text{dense}}(\theta) \approx \sum_{m=0}^{p} \Big(a_m q_m^{\sin} \sin(m\theta_k) + a_m q_m^{\cos} \cos(m\theta_k)$$

$$+ b_m q_m^{\sin} \cos(m\theta_k) - b_m q_m^{\cos} \sin(m\theta_k) \Big) \qquad (6.3.6)$$

for $1 \le k \le \lambda_1$. It is important to note that the computational complexity in this representation of $H_k^{\text{dense}}(\theta)$ in independent of the total number of oscillators M. In summary, the procedure in this step is as follows:

1. Precompute the quantities (6.3.5) for each $m = 0, \ldots, p$ and similar quantities for other communities.

2. Use the precomputed quantities to obtain a high-order approximation of $H^{\text{dense}}(\theta)$ according to formula (6.3.6) and equivalent formulas for other communities.

The computational complexity of Step 1 is $\mathcal{O}(\lambda_1 p)$ for the first community and consequently $\sum_{\sigma=1}^{\Lambda} \mathcal{O}(\lambda_\sigma p) = \mathcal{O}(Mp)$ for the whole step. The same applies to Step 2. In particular, the computational complexity does not depend on the number of communities.

Sparse Summation (E2): In this step, first $H^{\text{sparse}}(\theta)$ is evaluated and then combined with the results from the previous step to obtain the final right-hand side of (6.3.2). Recall that $H_k^{\text{sparse}}(\theta)$ is given by

$$H_k^{\text{sparse}}(\theta) = f_{\kappa(k)}(\theta_k) + \frac{1}{M} \sum_{l=1}^{M} s_{kl} \, h(\theta_l - \theta_k). \qquad (6.3.7)$$

Since the matrix S with entries s_{kl} is sparse with at most $\mathcal{O}(M)$ non-zero entries, it is evident that even a straightforward summation of $H^{\text{sparse}}(\theta)$ requires only $\mathcal{O}(M)$ operations. This is exactly what this step is supposed to do. Finally, in this step we compute $H^{\text{dense}}(\theta) + H^{\text{sparse}}(\theta)$, which gives the right-hand side of (6.3.2). All of these computations can be done with a complexity of $\mathcal{O}(M)$.

Finally, we mention that the high-order approximation step (P2) is the only step that introduces small inaccuracies in our algorithm. There are no inaccuracies induced by the community detection step (P1). In fact, if one also replaces h by its high-order approximation (6.3.3) to evaluate the sparse part (6.3.7), the community detection step (P1) does not introduce any inaccuracies. Instead, results of the community detection step (P1) only affect the computation time of the CIA evaluation steps. The sparser the matrix S, the faster these steps will be.

6.4   Extendability to Other Network Models

6.4.1   Extending the High-Order Approximation Step (P2)

While the previous subsection only illustrate the CIA steps for one particular model (6.3.1), it is straightforward to see that it is applicable to many more network models. Our main argument to support this claim is that by using a Fourier or polynomial expansion of the coupling function g or h, the parts containing θ_l and those comprising θ_k or x_l and x_k, when dealing with a model that does not have a circular domain, respectively, can always be separated, as done in (6.3.4). This allows the precomputation of quantities that do not depend on k but still appear in each component of the right-hand side. These quantities consist of large sums whose single precomputation prevents unnecessary sums in the evaluation of each component of the right-hand side. Even when the coupling function g is not of the form $g(\tilde{x}, \hat{x}) = h(\tilde{x} - \hat{x})$, a two dimensional Fourier or polynomial expansion of g in terms of $\tilde{x}$ and $\hat{x}$ is possible. For example, one can expand g as

$$g(\tilde{x}, \hat{x}) = \sum_{\alpha \in \mathbb{Z}} \sum_{\beta \in \mathbb{Z}} c_{\alpha, \beta} e^{\frac{\pi \mathrm{i}}{L} \alpha \tilde{x}} e^{\frac{\pi \mathrm{i}}{L} \beta \hat{x}}$$

$$\approx \sum_{\alpha = -p}^{p} \sum_{\beta = -p}^{p} c_{\alpha, \beta} e^{\frac{\pi \mathrm{i}}{L} \alpha \tilde{x}} e^{\frac{\pi \mathrm{i}}{L} \beta \hat{x}},$$

where $c_{\alpha, \beta}$ are complex Fourier coefficients. Then, if the right-hand side of the network model consists of a sum of the form $\frac{1}{M} \sum_{l=1}^{M} g(x_l, x_k)$, one can apply a CIA evaluation step which approximates this sum as

$$\frac{1}{M} \sum_{l=1}^{M} g(x_l, x_k) \approx \frac{1}{M} \sum_{l=1}^{M} \sum_{\alpha = -p}^{p} \sum_{\beta = -p}^{p} c_{\alpha, \beta} e^{\frac{\pi \mathrm{i}}{L} \alpha x_l} e^{\frac{\pi \mathrm{i}}{L} \beta x_k}$$

$$= \sum_{\alpha=-p}^{p} \sum_{\beta=-p}^{p} c_{\alpha,\beta} e^{\frac{\pi \mathrm{i}}{L} \beta x_k} \underbrace{\left(\frac{1}{M} \sum_{l=1}^{M} e^{\frac{\pi \mathrm{i}}{L} \alpha x_l} \right)}_{=:r_\alpha}.$$

Now, if one precomputes the quantities r_α for $\alpha = -p, \ldots, p$, this formulation allows a fast evaluation. Instead of considering a complex Fourier expansion one can also work with real expansions, see Appendix C.1.2, or polynomial expansions, see Appendix C.1.3. While a Fourier expansion is suitable for any kind of periodic domain, the choice between a Fourier and a polynomial expansion relies on the structure of the coupling function. If the coupling function is already an ordinary or trigonometric polynomial the choice is simple, see for example Appendix C.1.5. If that is not the case both methods generally make sense. An approximation of the coupling function g then has to be chosen in a way that the approximation accurately resembles g at the points where it is evaluated. If, for example, all the particles x_k stay in a subset of the domain, it is only necessary to approximate the coupling function there. Furthermore, the coupling function does not always need to be approximated by either a Fourier series or a polynomial. Rather, parts or components of g that resemble a polynomial structure can be treated with a polynomial expansion while other parts and components might be better approximated by a Fourier series, see for example Appendix C.1.6. This further enlarges the class of network systems that can be integrated using out CIA method. Moreover, we want to highlight that our method is also applicable to higher-order interactions in which the coupling function g depends on more than two arguments, see Appendix C.1.7.

6.4.2 Extending the Community Structure Exploitation Step (E1)

The Community Structure Exploitation step (E1) as we have described it in Section 6.3 assumes that the nodes in each community are all-to-all coupled. However, there are cases for which the right-hand side of

$$\dot{x}_k = \frac{1}{M} \sum_{l=1}^{M} a_{kl} \ g(x_l, x_k) \tag{6.4.1}$$

can be efficiently evaluated in step (E1) even though the graph represented by the adjacency matrix $A = (a_{kl})_{k,l=1,\ldots,M}$ does not represent an all-to-all coupling or a very dense coupling. Examples include rank one matrices and nearest neighbor networks. Below, we briefly explain how an efficient evaluation on these networks is possible. For the sake of simplicity we assume that g is of the form $g(x, y) =$

$h(x - y)$ and h consists of only one complex harmonic, i.e., $h(x) = e^{ix}$. The general case can then be obtained by approximating g with more Fourier modes treating each harmonic individually and then recombining them by summation, as explained in Section 6.4.1.

Rank One Coupling

Here, we consider the case that the adjacency matrix is given by an outer product $a_{kl} = \alpha_k \beta_l$ for two vectors $\alpha, \beta \in \mathbb{R}^M$, i.e., we focus on the system

$$\dot{x}_k = \frac{1}{M} \sum_{l=1}^{M} \alpha_k \beta_l \; e^{i(x_l - x_k)}. \tag{6.4.2}$$

This is the only case in which we do not require $a_{kl} \in \{0, 1\}$. Since the CIA evaluation step (E1) as described in Section 6.3 is a special case of a rank one coupling, i.e., when $\alpha_k = \beta_l = 1$ for all k, l, this presents a generalization of (E1). Based on (6.4.2), we immediately see that it makes sense to precompute

$$r = \frac{1}{M} \sum_{l=1}^{M} \beta_l \; e^{ix_l}. \tag{6.4.3}$$

Then, (6.4.2) simplifies to

$$\dot{x}_k = \alpha_k r e^{-ix_k}. \tag{6.4.4}$$

Note that one can evaluate (6.4.3) and (6.4.4) for all $k = 1, \ldots, M$ with a complexity of $\mathcal{O}(M)$.

Nearest Neighbor Coupling

For a given $M \in \mathbb{N}$ and $\Bbbk \in \mathbb{N}$ with $\Bbbk \leq M/2$ one can define a $\Bbbk$-nearest neighbor graph on M nodes in terms of the adjacency matrix $A = (a_{kl})$ by setting $a_{kl} = 1$ if $\min(|k - l|, \; M - |k - l|) \leq \Bbbk$ and $a_{kl} = 0$ otherwise, see Section 2.1. That means, the system (6.4.1) can be written as

$$\dot{x}_k = \frac{1}{M} \sum_{l=1}^{M} a_{kl} e^{i(x_l - x_k)}$$
$$= \frac{1}{M} \sum_{l=k-\Bbbk}^{k+\Bbbk} e^{i(x_l - x_k)}, \tag{6.4.5}$$

where the particle index $l \in \{1, \ldots, M\}$ in (6.4.5) has to be understood modulo M. Note that this system agrees with the Kuramoto model with identical oscillators

on nearest neighbor graphs (5.2.1), which we analyzed in Chapter 5 if one adds the complex conjugate to the right-hand side. Since in general, this is not an all-to-all coupling, the nearest neighbor coupling is again a generalization of (E1) as described in Section 6.3. However, the procedure to efficiently evaluate (6.4.5) will be different and especially not based on precomputations but on an iterative method. In particular, given the representation (6.4.5) one obtains

$$\dot{x}_k e^{\mathrm{i}x_k} = \frac{1}{M} \sum_{l=k-\Bbbk}^{k+\Bbbk} e^{\mathrm{i}x_l} =: F_k(x).$$

With this notation,

$$F_{k+1}(x) = F_k(x) - \frac{1}{M}(e^{\mathrm{i}x_{k-\Bbbk}} - e^{\mathrm{i}x_{k+\Bbbk+1}}), \tag{6.4.6}$$

which gives an iterative procedure to compute F. The steps to compute $\dot{x}_k$ efficiently are therefore given by

1. Compute $F_1(x)$ by the definition

$$F_1(x) = \frac{1}{M} \sum_{l=1-\Bbbk}^{1+\Bbbk} e^{\mathrm{i}x_l}.$$

2. Use formula (6.4.6) to iteratively compute $F_2(x), F_3(x), \ldots, F_M(x)$.

3. Finally, compute $\dot{x}_k = F_k(x)e^{-\mathrm{i}x_k}$.

Note that the first step has a complexity of at most $\mathcal{O}(M)$. Further, each iteration in the second step consists only of a finite number of operations $\mathcal{O}(1)$. Since $M-1$ iterations are necessary, the second step is of total complexity $\mathcal{O}(M)$. Finally, the third step is obviously of complexity $\mathcal{O}(M)$ as well. Therefore, (6.4.5) can be computed for all $k = 1, \ldots, M$ requiring a complexity of only $\mathcal{O}(M)$. Importantly, this is independent of $\Bbbk$ and still holds when for example $\Bbbk = rM$, where $r \in (0, 1/2)$ is a factor that describes the coupling range. In this case the adjacency matrix A has approximately $2rM^2$ non-zero entries, yet an efficient computation in $\mathcal{O}(M)$ is possible. This procedure helps to simulate the system (5.2.1), that we considered in Chapter 5, and can also be transferred to the systems (5.5.1) and (5.5.2).

While the above calculations only consider pairwise coupling, one can also derive similar procedures to efficiently evaluate higher-order coupling structure, which is not all-to-all. In particular, one can consider a finite dimensional analog of (5.6.1) with M oscillators, by replacing the integrals with sums. Then, a naive

algorithm that evaluates the right-hand side of this system has a complexity of $\mathcal{O}(M^3)$. Using a generalized iterative procedure, this complexity can be reduced to just $\mathcal{O}(M^2)$, which is still worse than linear complexity, but much better than the complexity of a naive algorithm.

6.4.3   Extending the Community Detection Step (P1)

Until now, we have assumed that the nodes of the graph, which is represented by its adjacency matrix A, can be split into multiple communities. Grouping the nodes according to the communities and permuting the labels of the nodes then results in a matrix B, that has apparent blocks on the diagonal, see Figure 6.2. Moreover, this matrix B can be split into $B = D + S$, where D is a matrix that has exact blocks on the diagonal and S absorbs the deviation of B from the exact block structure. There are many algorithms that can detect such communities and thus transform the adjacency matrix A into a matrix B, that has apparent block diagonal structure, and yield a matrix D with exact block diagonal structure. However, this is not the only possible form of matrices D that allow an efficient evaluation step (E1). In particular, the blocks in D can also be away from the diagonal and they can also be rectangular instead of just quadratic, see for example matrix B_1 in Figure 6.3.

Furthermore, these blocks need not be filled entirely with ones. The only requirement is that the part of the right-hand side which is associated with each block can be computed with a complexity of $\mathcal{O}(M)$ as M becomes large. As we have seen in Section 6.4.2, this is also the case if each block represents a rank-one coupling or a nearest neighbor coupling, see for example matrices B_2 and B_3 in Figure 6.3.

Finally, it is also possible that the adjacency matrix A is given by the sum of a few matrices, say for example $A = A_1 + A_2 + A_3$. Now, one can ask for permutation matrices P_i, with $i = 1, 2, 3$ such that $B_i = P_i A_i P_i^\top$ have apparent general block structure. Here, general block structure includes off-diagonal and non-quadratic blocks as well as blocks, where the coupling structure is rank one or $\Bbbk$-nearest neighbor. If these permutation matrices exist, one can apply a CIA to each summand of A individually and sum the results. Thus, CIAs can also cope with adjacency matrices A that are as in Figure 6.3 or of similar type. For synthetically generated adjacency matrices A in which this structure is already evident, as in the example from Figure 6.3, our CIA steps work as well, but in real-world networks this structure first needs to be detected. However, there exist very few, if any, suitable algorithms, that can decompose A into its summands A_i and find permutation matrices P_i such $P_i A_i P_i^\top$ has general block structure.
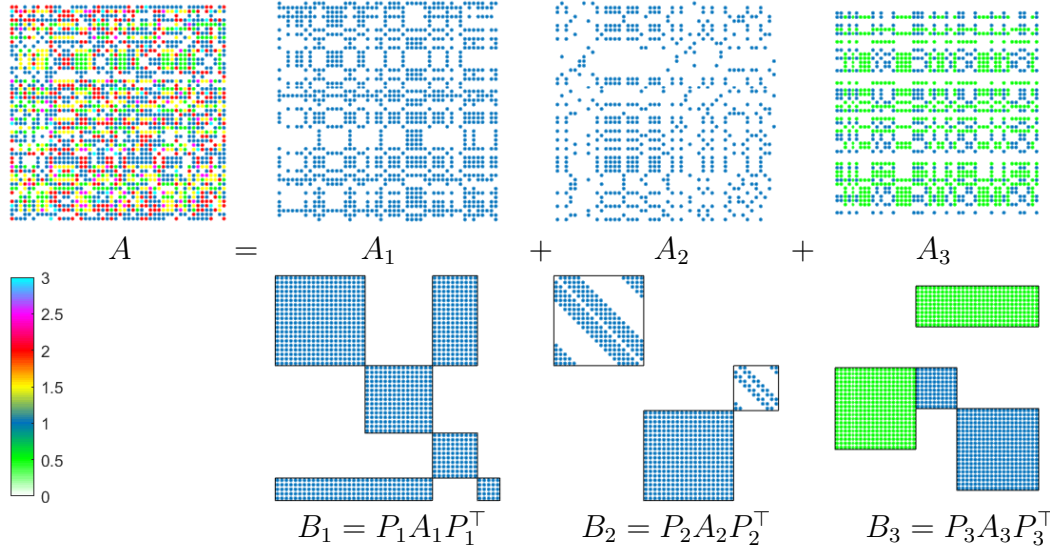
Figure 6.3: Illustration of the complicated structure that A can have, such that CIAs are applicable. Blue dots in the representation of matrices A_i, B_i for $i = 1, 2, 3$ represent $+1$ entries and there is no dot if the matrix has a zero entry at the respective position. Green dots in A_3 and B_3 illustrate a rank-one block matrix, for which symbolically the value is 0.5 everywhere. Finally, the entries in the matrix A can take many different values, as illustrated by different colors. Note, that there are no sparse parts here, i.e., $B_i = D_i + S_i$ with $S_i \equiv 0$.

6.4.4 Simulation of Coupled Map Lattices

Lastly, we want to remark that the matrix A, that we use to denote the adjacency matrix of a graph, can also be replaced by another matrix. For example one can take a matrix representation of the graph Laplacian $L = \mathrm{Id} - D^{-1}A$, as introduced in Section 3.2.2, instead of A. If the graph is regular, such that the degree matrix D is given by a multiple of the identity matrix, one can regard $-D^{-1}A$ (up to a constant) as the dense part and Id as the sparse part that are evaluated in the CIA steps (E1) and (E2), respectively. For example, this is the case for all-to-all graphs or $\Bbbk$-nearest neighbor graphs but the concept can also be applied to graphs that have general block structure. This allows for the efficient simulation of CMLs on large networks.

6.5 Numerical Results

Based on numerical simulations for a variety of widely-used large-scale network models we demonstrate that our CIAs are indeed efficient numerical algorithms.

Moreover, our numerical simulations show that this efficiency does not come with a significant expense of accuracy.

6.5.1   Efficiency of CIAs

In this section, we present the efficiency advantages of using a CIA in comparison to a naive approach. Including synthetic and real-world networks and for pairwise and higher-order coupling we provide numerical evidence for the robustness and efficiency of our approach. The network models that we consider in this section are

- a Cucker–Smale model [57] describing animal movement,

- a Kuramoto model [107] for phases of oscillators on the unit circle,

- a Desai–Zwanzig model [61] for interacting particles,

- and a Bornhold–Rholf model [39] for self-organized criticality.

We compare the models on a fixed computational architecture using a sequence of synthetically generated networks that consist of four known communities as seen in Figure 6.2. To integrate these systems, we used an explicit Euler scheme on an equidistant discretization of $[0, T]$ with $T = 20$ and $\Delta t = 1/10$. On the one hand, as seen in Figure 6.4, the computation time for the naive approach depends quadratically on M for all network models. Importantly, on the other hand, when using a CIA, the computation time depends only linearly on M. Furthermore, the memory requirements of a CIA are much lower as we can take advantage of sparsity outside of communities, while just calculating and storing a few observable values within each community, so simulations on much larger networks are possible. In particular, for $M \gtrsim 10^{4.5}$ storing the full matrix $A \in \mathbb{R}^{M \times M}$ exceeds memory capacities on current standard desktops. In this case, naive algorithms are not applicable; cf. Figure 6.4.

Next, we simulate the Cucker–Smale model on a real-world network that contains data from real bird interactions [2, 153], see Figure 6.5(a)-(b). Based on this network, we construct a sequence of networks with growing sizes such that each network in the sequence still reflects the community structure of the original network and the amount of edges deviating from this community structure grows linearly in M. This helps us to study the effect of the network size on the computation time. Again, to integrate the Cucker–Smale model on these networks, we use an explicit Euler scheme on an equidistant discretization of $[0, T]$ with $T = 20$ and $\Delta t = 0.1$. As seen in Figure 6.5(c), the computation time of a naive approach of evaluating the right-hand side scales with M^2. The computational complexity
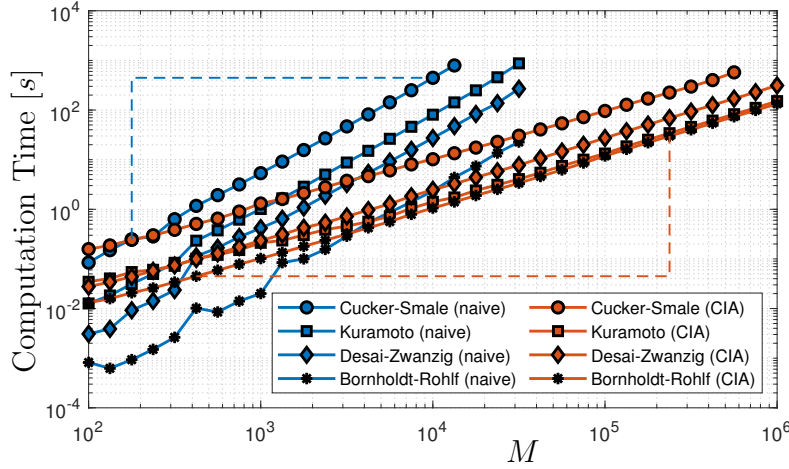
Figure 6.4: Integration times for Cucker–Smale, Kuramoto, Desai–Zwanzig and Bornholdt–Rholf systems on a sequence of synthetically generated graphs of the form as shown in Figure 6.2. The computation of the Cucker–Smale model takes the longest, since it has a two-dimensional phase space for each node. The computational complexities, derived from the slopes of the dashed triangles, correspond to $\mathcal{O}(M^{1.86})$ for the naive Cucker–Smale model and $\mathcal{O}(M^{1.03})$ for the integration of the Bornholdt–Rohlf using a CIA approach.

of a CIA approach is only $\mathcal{O}(M)$. This clearly shows that a CIA can be used to simulate dynamics on real-world networks.

Finally, we want to demonstrate that the idea of a CIA can also be applied to models that are beyond the general formulation (6.2.1). When considering higher-order models, such as a higher-order Kuramoto model, the computational complexity of a naive approach can be much worse than just $\mathcal{O}(M^2)$. In particular, for our tests, we consider the model

$$\dot{\phi}_k = \frac{1}{M^3} \sum_{l,i,j=1}^{M} \sin(\phi_l - \phi_i + \phi_j - \phi_k), \qquad k = 1, \dots, M.$$

Here, a naive evaluation of the triple sum requires $\mathcal{O}(M^3)$ evaluations of the sin function. Computing this triple sum for every $k = 1, \dots, M$ yields a total computational complexity for the evaluation of the right-hand side of $\mathcal{O}(M^4)$. As this quartic dependence on M for a naive approach severely limits the maximum system size for which simulations can be conducted, an approach via CIAs is desired. In fact, one can still pre-compute the observables (6.3.5) and then evaluate the right-hand side based on these. This reduces the computational complexity to just $\mathcal{O}(M)$, see Figure 6.6. For the details, see Appendix C.1.7.

(a)   **(b)**

(c)
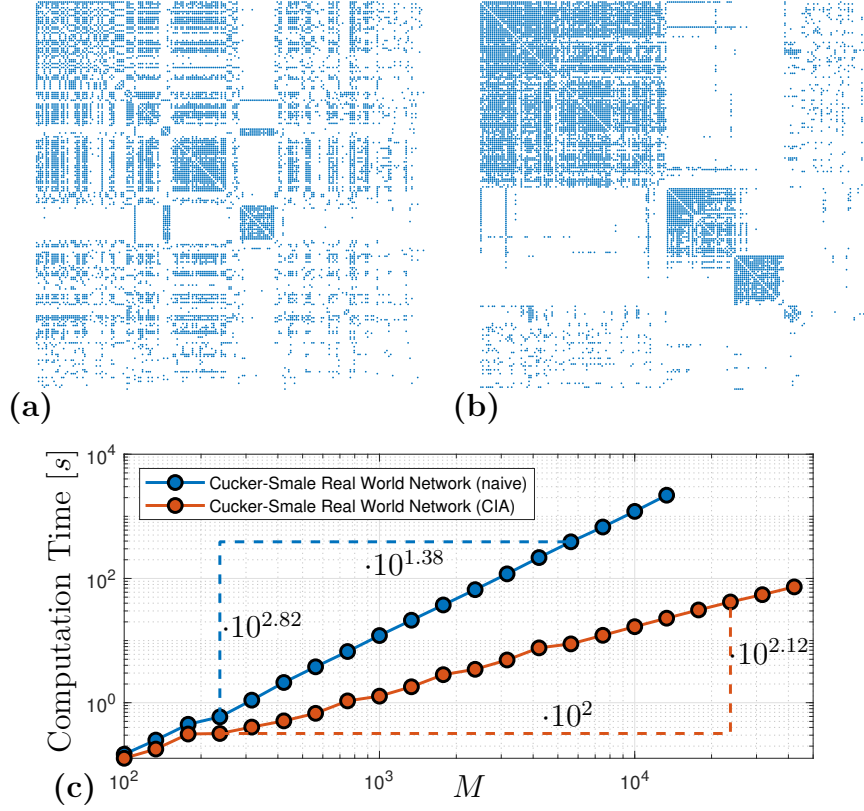
Figure 6.5: Simulation of the Cucker–Smale model on a real-world network from bird interactions [2, 153]. Part (a) shows the adjacency matrix A of the network in its original form. Part (b) shows the adjacency after permuting the nodes such that a block structure is apparent. Part (c) shows the computation time of a naive algorithm in comparison with our CIA approach. The dashed triangles yield computational complexities of $\mathcal{O}(M^\alpha)$ where $\alpha \approx 2.05$ for the naive algorithm and $\alpha \approx 1.06$ for the CIA approach.

6.5.2   Accuracy of CIAs

Note that in general our CIAs approximate the right-hand side of a network dynamical system rather then evaluating it exactly as naive approaches. Therefore, when integrating a dynamical system on a network a small error is introduced in each time step of the integration. Since these errors can add up, one expects that the resulting numerical solution obtained from a CIA differs from the solution obtained by using a naive algorithm. In this section we numerically analyze the difference between these two numerical solutions, to study the accuracy of CIAs. As explained at the end of Section 6.3, the only step that introduces an error is the high-order approximation step (P2) or more specifically, the approximation (6.3.3).
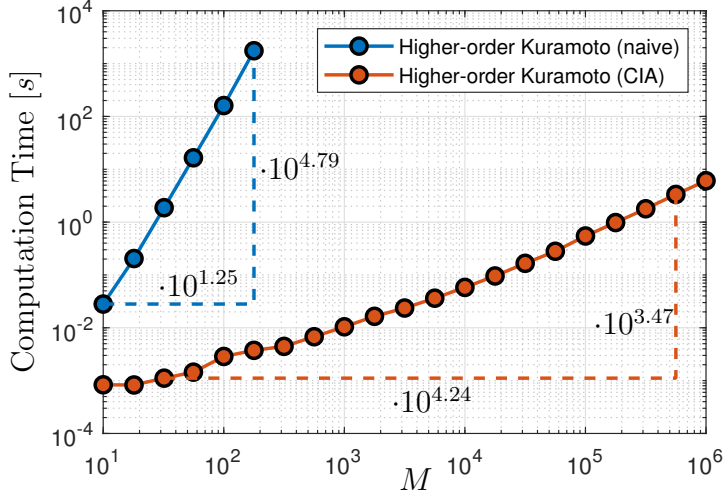
Figure 6.6: Numerical integration of a higher-order Kuramoto system. A naive implementation leads to quartic complexity $\mathcal{O}(M^4)$ (blue), whereas the application of a CIA based on a suitable reformulation and precomputations permits the reduction to linear complexity $\mathcal{O}(M)$ (red). To be precise, out numerical experiments revealed that the slope of the two graphs, which is calculated at the dashed triangles and corresponds to a complexity of $\mathcal{O}(M^\alpha)$, is given by $\alpha = 3.83$ for the naive algorithm and $\alpha = 0.82$ for the CIA approach.

The higher the approximation order p in (6.3.3), the more accurate are the results of this approximation. Thus, we compare two numerical solutions, one obtained using a naive approach and the other one by employing a CIA. Specifically, we study how their difference depends on the approximation order p. Here, we restrict our analysis to the phase oscillator model (6.3.1). An accuracy analysis for the Cucker–Smale model can be found in Appendix C.2.

In our test scenario, we consider the model (6.3.1) on a synthetically created network of $M = 500$ nodes. This network consists of four communities as seen in Figure 6.2. Moreover, we omit intrinsic dynamics, i.e., $f_k \equiv 0$. As we have explained in Section 6.3.1, the rate of convergence when approximating the coupling function h by a Fourier series, depends on the smoothness of h. Since the smoothness of h is related to the rate of decay of its Fourier coefficients, we choose a coupling function h as

$$h(\theta) = \sum_{m=1}^{\infty} b_m \sin(m\theta), \qquad b_m = m^{-\xi}$$

and let $\xi \in \mathbb{N}$ be a variable. Next, we randomly choose the initial conditions for all oscillators and simulate the system (6.3.1) using an explicit Euler scheme

until $T = 20$ with a time step size of $\Delta t = 1/10$. We use a naive approach to create a reference solution that we denote by $\theta^{\mathrm{ref}}_{k,t}$ with $k = 1, \dots, M$ and $t = 0, \Delta t, 2\Delta t, \dots, T$.

Then, we use our CIA, that relies on an approximation of the coupling function in step (P2) and simulate the same system. Again, we use an explicit Euler scheme and the same time discretization until $T = 20$. This produces a second solution that we denote by $\theta^{\mathrm{CIA}}_{k,t}$. Finally, we determine the error z by computing

$$z = \max_{k=1,\dots,M} \max_{t=0,\Delta t, 2\Delta t, \dots, T} |\theta^{\mathrm{ref}}_{k,t} - \theta^{\mathrm{CIA}}_{k,t}|.$$

The dependence of this error z on the approximation order p and the rate of decay ξ of the coupling function can be seen in Figure 6.7. As expected, we observe that the error z decreases upon increasing the approximation orders p. Moreover, the rate of decay of the Fourier coefficients of the coupling function crucially influences the integration error z. This does not come as a surprise, as for coupling functions that only consist of finitely many nonzero Fourier modes, i.e., when the rate of decay is the fastest, or CIAs, with p large enough, do not introduce an error at all.
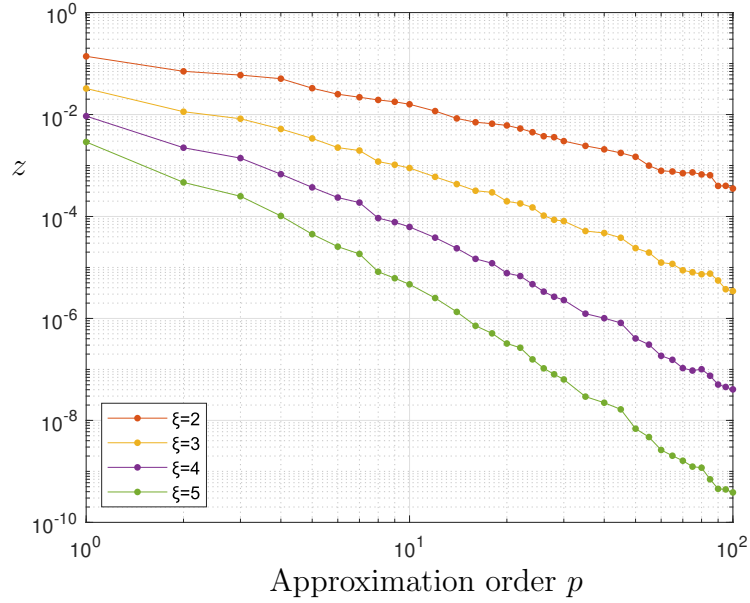
Figure 6.7: Integration error z independence of the approximation order p and the smoothness of h.

6.6 Summary

To summarize, we have developed a new method to integrate large-scale network models with community structure. Unlike a naive approach, the computational complexity of CIAs is always linear in the number of involved nodes M. We achieve this reduction to linear complexity by organizing our CIAs into two pre-simulation and two evaluation steps. The pre-simulation steps only need to be performed once during an entire simulation and their results can even be reused when simulating another network model on the same graph with the same coupling function. These pre-simulation steps consist of the detection of a community structure in the underlying network and an expansion of the coupling function to identify local observables. Then, in each time step, one evaluates the right-hand side of the network model using the two evaluation steps. In the first of which one uses the expansion of the coupling function and exploits the community structure by computing suitable observables. This helps to efficiently calculate the dense interactions within all communities. Then, one takes care of a possibly not ideal community structure by sparse summations. Importantly, both of these evaluation steps can be performed with linear complexity $\mathcal{O}(M)$. This linear dependence on M is much better than in a naive algorithm, where the complexity scales at least quadratically in M.

As we have shown this approach is applicable to a wide variety of networks. In particular, the underlying network does not need to have a community structure, but its adjacency matrix can also have dense blocks off the diagonal, or it can consist of parts where the coupling is nearest neighbor or rank one. Moreover, the adjacency matrix of the network does not have to define the coupling in the network model, but other graph related operators such as the graph Laplacian can also determine the coupling between the nodes. Further, the approach works independent of whether the coupling is pairwise or higher-order, and whether the underlying network is synthetic or a real-world network, which leads to many applications across all areas of science.

Chapter 7

Conclusion and Outlook

In this dissertation we have seen that network dynamical systems can exhibit a variety of different dynamical effects with high complexity, even though the evolution of the states of the nodes is governed by relatively simple equations. Apart from pairwise interactions in networks, higher-order interactions arise naturally, e.g., through phase reductions, and can crucially influence the behavior of a network dynamical system. For example, they can affect the stability of twisted states and those of equilibria that bifurcate from these twisted states, see Chapter 5. In fact, equilibria that are unstable with just pairwise interactions can become stable when including higher-order interactions in the model. Moreover, higher-order interactions are helpful when analyzing coupled oscillator networks through phase reductions, as we saw in Chapter 4. In particular, by including them in the phase reduction one can better approximate the stability of collective dynamics, such as synchrony or splay states, in the full/unreduced system.

However, one has to be careful when incorporating higher-order interactions to a pairwise coupled system, since they can also break the time invariance of certain equilibria. For example, the synchronized manifold, that we considered in Chapter 3 is always invariant with just pairwise coupling, but its invariance is lost when considering general hypergraph coupling. Similarly, twisted states do not remain invariant when adding general higher-order interactions to the right-hand side of the governing equations, see Section 5.6.

From an engineering perspective, one might use higher-order interactions to design a network dynamical system where given equilibria have desired properties. Even when considering only higher-order interactions that retain the invariance of these equilibria, they provide a lot more possibilities of designing such a system. This allows to design systems with equilibria whose required properties are more specific. For example, as we have seen in Section 5.5, one can suitably combine a few different higher-order interactions to shape the stability of twisted states and those of bifurcating equilibria. Realizing these higher-order interactions experi-

mentally remains a challenge for future work.

Apart from answering a lot of questions, this dissertation has also raised many questions and paved the way for future generalizations. For example, a topic that we did not consider across all chapters is randomness in network dynamical systems. Randomness can be included in a lot of different ways in these systems. If, for example, one considers the phase oscillator system (2.2.2), one can make the intrinsic frequencies random by sampling them from a probability distribution, as in the classical Kuramoto model (1.1.1). Moreover, one can consider the model on random graphs, e.g., on Erdös–Rényi or Barabási–Albert graphs, as introduced in Chapter 2. Further, one can consider a system of stochastic ODEs by adding random white noise to the right-hand side of any network dynamical system. When considering other network models, which include more parameters, one can also make them random.

Throughout this entire dissertation, we have assumed that the network is constant in time. However, one can let the network itself evolve over time and thereby make it adaptive. There are multiple ways of making a network adaptive. If, for example, the network is given by a graph, one can choose the entries of the adjacency matrix of this graph as functions of time. This basically makes the network dynamical system nonautonomous. As a more specific example, one can consider the Kuramoto model on nearest neighbor graphs as in Chapter 5 and choose the coupling range dependent on time. Another way to make the network adaptive is to impose an evolution law for the network that can potentially depend on the current state of the network dynamical system [73, 81, 17, 88]. Further generalizations and outlooks for future work that are specific to the models of each chapter are listed below:

In Chapter 3 we considered CMLs and CHMs that are given by the combination of an iterated unimodel map at each node and a graph or hypergraph Laplacian. We expect that the generic nature of using a unimodal map at each node and a generalization of the Laplacian should turn CHMs into an excellent universal model class for many concrete physical phenomena. However, finding such a concrete physical example, which is naturally modeled by a CHM, has to be done in future work. Moreover, in this chapter we have only considered models on finite graphs or hypergraphs. Since physical systems, that we want to model with CHMs, can consist of thousands of nodes, it makes sense to study CHMs on large hypergraphs or even on hypergraph limits.

In Chapter 4 we have derived second-order phase reduction for identical Stuart–Landau oscillators with a deformed limit cycle. In principle, the analysis presented in Section 4.3 can be extended to derive higher-order phase reductions beyond second order in both the coupling strength and the parameter that describes the deviation from the circular limit cycle. Such higher-order phase reductions would

include interactions between quadruplets of phases and allow to describe the approximate phase dynamics beyond second order. The main obstacle that has to be overcome is the algebraic complexity of these phase reductions. Already at second order, the terms for triplet interactions become quite long and bring symbolic computer algebra software, such as MATHEMATICA, to their limits. While we considered identical oscillators, real-world oscillators are rarely perfectly identical, motivating the question how heterogeneity affects the phase reduction. Here, we assumed that the oscillators are identical and, in particular, that their intrinsic frequencies are the same. If they were dependent on the oscillator, the first-order phase reduction would not change at all and one could just replace the general intrinsic frequency by an oscillator specific one everywhere. A second-order phase reduction could theoretically also be derived by adapting the methods from Section 4.3. Practically, however, the terms of second order start to depend nonlinearly on the intrinsic frequencies. Thus, already for circular limit cycles and just a few oscillators, finding a general analytic solution for the PDEs from Section 4.3 is challenging. Moreover, due to the higher complexity of the second-order phase reduction, it is practically intractable. Extending this to oscillators with non-circular limit cycles only worsens the problem. A possible approach to overcome this problem is to assume that the intrinsic frequencies are sampled from a probability distribution and consider a mean-field limit. We leave this for future work.

In Chapter 5 we have conducted a bifurcation analysis for twisted states on nearest neighbor graphs and higher-order extensions. While we have only considered the case where the coupling function $W_r(x)$ is taken to model nearest neighbor coupling, the analysis is also valid for other coupling functions. Thus, our work poses a framework within which one can study the effect of the Fourier coefficients of $W_r(x)$ on the bifurcation. Another example to which our theory could be applied is generalized twisted states on a two-dimensional lattice whose stability has been analyzed in [74]. Moreover, apart from the pairwise coupling we have only considered 3-way and 4-way higher-order interactions, however one can certainly add 5-way coupling, 6-way coupling, etc. and investigate how these interactions influence the bifurcation. Then, one might expect to control even higher-order derivatives at the bifurcation point.

Finally, in Chapter 6 we developed CIAs for the efficient numerical simulation of network dynamical systems. Even though the CIAs presented in this chapter are applicable to a wide range of network dynamical systems, there are a few approaches to further generalize them. For example, we have only considered polynomial and Fourier approximation methods (and a combination thereof) for the coupling function. However, it is possible that there might be even more functional approximation systems such that a separation of terms and thus a fast

evaluation is possible. Moreover, our CIAs rely on many parameters, such as the choice of the community detection algorithm which yields a decomposition of the adjacency matrix into a dense matrix and a sparse matrix, the approximation order and domain of the coupling function, and many more depending on the specific network model. All of these parameters influence both computation time and accuracy of our algorithms and have to be optimized under possible time/memory constraints and accuracy requirements. For example, spending more time on the community detection step might reveal a community structure that is more suitable by saving more time in the subsequent evaluation of the right-hand side. However, estimating the computation time of a community detection algorithm is difficult and can also depend on the number of communities, which is sometimes only known after they have been detected. To conclude, finding a good balance of computation time allocation for different steps and finding a good estimation of parameter values is nontrivial and developing a good estimation has to be done in future research.

Putting everything together, dynamical systems on networks are extremely diverse and their induced dynamical effects can depend on the smallest subtleties in the specific model. In this dissertation, we have thoroughly analyzed both local and global dynamics of special network dynamical systems by combining theoretical methods with numerical simulations. Thereby, we have contributed to the extensive challenge of understanding network dynamical systems.

Chapter 8

Lists of Symbols and Abbreviations

List of Symbols

$\mathbb{N}$	set of natural numbers $\{1, 2, 3, \dots\}$
$\mathbb{N}_0$	$\mathbb{N}_0 := \mathbb{N} \cup \{0\}$
$\mathbb{Z}$	set of integers
$\mathbb{R}$	set of real numbers
$\mathbb{C}$	set of complex numbers
M	number of nodes or particles in a finite graph
$[M]$	set of positive integers until M, i.e., $\{1, \dots, M\}$
$\mathbb{S}$	$\mathbb{S} := \mathbb{R}/\mathbb{Z}$ or $\mathbb{S} := [0, 1]/(0 \sim 1)$
	Usually used as the index space for oscillators in the continuum limit
$\mathbb{T}$	unit circle, defined by $\mathbb{T} := \mathbb{R}/(2\pi\mathbb{Z})$
	Usually used as the phase space of an oscillator
$\mathbb{T}^M$	$\mathbb{T} \times \cdots \times \mathbb{T}$ (M-times)
I	unit interval $[0, 1]$
Θ	phase of an oscillator in the network limit $M \to \infty$
Ψ	phase difference of two oscillators in the network limit $M \to \infty$
S_M	symmetric group of M elements,
	i.e., set of all permutations of $[M]$ (group order $M!$)
Z_M	cyclic group of M elements, defined by $\mathbb{Z}/(M\mathbb{Z})$ (group order M)
D_M	dihedral group of M elements (group order $2M$, for $M \geq 3$)
e_k	k-th unit vector in $\mathbb{R}^M$
$\mathbb{1}$	$(1, 1, \dots, 1)^\top \in \mathbb{R}^M$
Id_M	identity matrix in $\mathbb{R}^{M \times M}$
J_M	$J_M := \{1\}^{M \times M}$, the matrix in $\mathbb{R}^{M \times M}$ where all entries are ones
$\Bbbk$	coupling range in $\Bbbk$-nearest neighbor graphs

List of Abbreviations

CIA	Community Integration Algorithm
CHM	Coupled Hypergraph Map
CML	Coupled Map Lattice
NDS	Network Dynamical Systems
ODE	Ordinary Differential Equation
PDE	Partial Differential Equation
PRMM	Poincaré Return Map Multiplier

Bibliography

[1] Peter A Abrams. "Arguments in Favor of Higher Order Interactions". In: *The American Naturalist* 121.6 (June 1983), pp. 887–891.

[2] James S. Adelman, Sahnzi C. Moyers, Damien R. Farine, and Dana M. Hawley. "Feeder use predicts both acquisition and transmission of a contagious pathogen in a North American songbird". In: *Proceedings of the Royal Society B: Biological Sciences* 282.1815 (Sept. 2015).

[3] Kathleen T. Alligood, Tim D. Sauer, and James A. Yorke. *Chaos: An Introduction to Dynamical Systems*. Vol. 5. Springer, 1996.

[4] Unai Alvarez-Rodriguez, Federico Battiston, Guilherme Ferraz de Arruda, Yamir Moreno, Matjaž Perc, and Vito Latora. "Evolutionary dynamics of higher-order interactions in social networks". In: *Nature Human Behaviour* 5.5 (2021), pp. 586–595.

[5] Shun-ichi Amari. "Dynamics of pattern formation in lateral-inhibition type neural fields". In: *Biological Cybernetics* 27.2 (1977), pp. 77–87.

[6] Eleonora Andreotti and Raffaella Mulas. "Signless normalized Laplacian for hypergraphs". In: *Electronic Journal of Graph Theory and Applications* 10.2 (Sept. 2022), p. 485.

[7] Eleonora Andreotti and Raffaella Mulas. "Signless normalized Laplacian for hypergraphs". In: *Electronic Journal of Graph Theory and Applications* 10.2 (Sept. 2022), p. 485.

[8] Alex Arenas, Albert Díaz-Guilera, Jürgen Kurths, Yamir Moreno, and Changsong Zhou. "Synchronization in complex networks". In: *Physics Reports* 469.3 (Dec. 2008), pp. 93–153.

[9] Peter Ashwin, Stephen Coombes, and Rachel Nicks. "Mathematical Frameworks for Oscillatory Network Dynamics in Neuroscience". In: *Journal of Mathematical Neuroscience* 6.1 (2016), pp. 1–92.

[10] Peter Ashwin and Ana Rodrigues. "Hopf normal form with SN symmetry and reduction to systems of nonlinearly coupled phase oscillators". In: *Physica D: Nonlinear Phenomena* 325 (2016), pp. 14–24.

[11] Peter Ashwin and James W. Swift. "The dynamics of n weakly coupled identical oscillators". In: *Journal of Nonlinear Science* 2.1 (1992), pp. 69–108.

[12] Ágnes Backhausz and Balázs Szegedy. "Action convergence of operators and graphs". In: *Canadian Journal of Mathematics* 74.1 (Feb. 2022), pp. 72–121.

[13] Albert-László Barabási and Réka Albert. "Emergence of Scaling in Random Networks". In: *Science* 286.5439 (Oct. 1999), pp. 509–512.

[14] Alain Barrat, Marc Barthélemy, and Alessandro Vespignani. *Dynamical Processes on Complex Networks*. Cambridge University Press, 2008.

[15] Federico Battiston, Giulia Cencetti, Iacopo Iacopini, Vito Latora, Maxime Lucas, Alice Patania, Jean-Gabriel Young, and Giovanni Petri. "Networks beyond pairwise interactions: Structure and dynamics". In: *Physics Reports* 874 (Aug. 2020), pp. 1–92.

[16] Federico Battiston et al. "The physics of higher-order interactions in complex systems". In: *Nature Physics* 17.10 (Oct. 2021), pp. 1093–1098.

[17] Rico Berner, Eckehard Schöll, and Serhiy Yanchuk. "Multiclusters in Networks of Adaptively Coupled Phase Oscillators". In: *SIAM Journal on Applied Dynamical Systems* 18.4 (Jan. 2019), pp. 2227–2266.

[18] Christian Bick. "Heteroclinic Dynamics of Localized Frequency Synchrony: Heteroclinic Cycles for Small Populations". In: *Journal of Nonlinear Science* 29.6 (2019), pp. 2547–2570.

[19] Christian Bick. "Heteroclinic switching between chimeras". In: *Physical Review E* 97.5 (2018), pp. 1–5.

[20] Christian Bick, Tobias Böhle, and Christian Kuehn. "Higher-Order Interactions in Phase Oscillator Networks through Phase Reductions of Oscillators with Phase Dependent Amplitude". May 2023. arXiv: 2305.04277.

[21] Christian Bick, Tobias Böhle, and Christian Kuehn. "Multi-population phase oscillator networks with higher-order interactions". In: *Nonlinear Differential Equations and Applications NoDEA* 29.6 (Nov. 2022), p. 64.

[22] Christian Bick, Tobias Böhle, and Christian Kuehn. "Phase Oscillator Networks with Nonlocal Higher-Order Interactions: Twisted States, Stability and Bifurcations". June 2022. arXiv: 2206.01951.

[23] Christian Bick, Elizabeth Gross, Heather A. Harrington, and Michael T. Schaub. "What are higher-order networks?" Apr. 2021. arXiv: 2104.11329.

[24] Christian Bick and Davide Sclosa. "Mean-field limits of phase oscillator networks and their symmetries". 2021. arXiv: 2110.13686.

[25] Christian Bick, Marc Timme, Danilo Paulikat, Dirk Rathlev, and Peter Ashwin. "Chaos in symmetric phase oscillator networks". In: *Physical Review Letters* 107.24 (2011), pp. 1–4.

[26] Ian Billick and Ted J. Case. "Higher Order Interactions in Ecological Communities: What Are They and How Can They be Detected?" In: *Ecology* 75.6 (Sept. 1994), pp. 1529–1543.

[27] Frede Blaabjerg, Remus Teodorescu, Marco Liserre, and A.V. Timbus. "Overview of Control and Grid Synchronization for Distributed Power Generation Systems". In: *IEEE Transactions on Industrial Electronics* 53.5 (Oct. 2006), pp. 1398–1409.

[28] Sergio Blanes and Fernando Casas. *A Concise Introduction to Geometric Numerical Integration*. Vol. 4. Chapman and Hall/CRC, Nov. 2017, pp. 88–100.

[29] Vincent D. Blondel, Jean-Loup Guillaume, Renaud Lambiotte, and Etienne Lefebvre. "Fast unfolding of communities in large networks". In: *Journal of Statistical Mechanics: Theory and Experiment* 2008.10 (Oct. 2008), P10008.

[30] S. Boccaletti, G. Bianconi, R. Criado, C.I. del Genio, J. Gómez-Gardeñes, M. Romance, I. Sendiña-Nadal, Z. Wang, and M. Zanin. "The structure and dynamics of multilayer networks". In: *Physics Reports* 544.1 (Nov. 2014), pp. 1–122.

[31] Ágnes Bodó, Gyula Y. Katona, and Péter L. Simon. "SIS Epidemic Propagation on Hypergraphs". In: *Bulletin of Mathematical Biology* 78.4 (2016), pp. 713–735.

[32] Tobias Böhle. *Community-Integration-Algorithms-CIAs*. `https://github.com/tobiasboehle/Community-Integration-Algorithms-CIAs`. 2022.

[33] Tobias Böhle. *HigherOrderPhaseReductions*. `https://github.com/tobiasboehle/HigherOrderPhaseReductions`. 2023.

[34] Tobias Böhle and Christian Kuehn. "Mathematical analysis of nonlocal PDEs for network generation". In: *Mathematical Modelling of Natural Phenomena* 14.5 (Dec. 2019). Ed. by V. Vougalter and V. Volpert, p. 506.

[35] Tobias Böhle, Christian Kuehn, Raffaella Mulas, and Jürgen Jost. "Coupled hypergraph maps and chaotic cluster synchronization". In: *Europhysics Letters* 136.4 (Nov. 2021), p. 40005.

[36] Tobias Böhle, Christian Kuehn, and Mechthild Thalhammer. "On the reliable and efficient numerical integration of the Kuramoto model and related dynamical systems on graphs". In: *International Journal of Computer Mathematics* 99.1 (Jan. 2021), pp. 31–57.

[37] Tobias Böhle, Mechthild Thalhammer, and Christian Kuehn. "Community integration algorithms (CIAs) for dynamical systems on networks". In: *Journal of Computational Physics* 469 (Nov. 2022), p. 111524.

[38] Christoph Börgers and Nancy Kopell. "Synchronization in Networks of Excitatory and Inhibitory Neurons with Sparse, Random Connectivity". In: *Neural Computation* 15.3 (Mar. 2003), pp. 509–538.

[39] Stefan Bornholdt and Thimo Rohlf. "Topological Evolution of Dynamical Networks: Global Criticality from Local Dynamics". In: *Physical Review Letters* 84.26 (June 2000), pp. 6114–6117.

[40] Haim Brezis. *Functional Analysis, Sobolev Spaces and Partial Differential Equations.* New York, NY: Springer New York, 2011.

[41] Jared C. Bronski, Lee DeVille, and Moon Jip Park. "Fully synchronous solutions and the synchronization phase transition for the finite-N Kuramoto model". In: *Chaos* 22.3 (2012).

[42] Eric Brown, Philip Holmes, and Jeff Moehlis. "Globally Coupled Oscillator Networks". In: *Perspectives and Problems in Nolinear Science.* New York, NY: Springer New York, 2003, pp. 183–215.

[43] John Buck. "Synchronous Rhythmic Flashing of Fireflies II". In: *The Quarterly Review of Biology* 63.3 (1988), pp. 265–289.

[44] John Buck and Elisabeth Buck. "Mechanism of rhythmic synchronous flashing of fireflies". In: *Science* 159.3821 (1968), pp. 1319–1327.

[45] John Buck and Elisabeth Buck. "Synchronous Fireflies". In: *Scientific American* 234.5 (1976), pp. 74–85.

[46] John Buck, Elisabeth Buck, James F. Case, and Frank E. Hanson. "Control of flashing in fireflies - V. Pacemaker synchronization in Pteroptyx cribellata". In: *Journal of Comparative Physiology A* 144.3 (1981), pp. 287–298.

[47] Dumitru Călugăru, Jan Frederik Totz, Erik A. Martens, and Harald Engel. "First-order synchronization transition in a large population of strongly coupled relaxation oscillators." In: *Science Advances* 6.39 (Sept. 2020), pp. 1–8.

[48] Hayato Chiba, Georgi S. Medvedev, and Matthew S. Mizuhara. "Bifurcations in the Kuramoto model on graphs". In: *Chaos* 28.7 (2018), pp. 1–18.

[49] Hayato Chiba and Georgi S. Medvedev. "The mean field analysis of the Kuramoto model on graphs I. The mean field equation and transition point formulas". In: *Discrete & Continuous Dynamical Systems - A* 39.1 (2019), pp. 131–155.

[50] Carmen Chicone. *Ordinary Differential Equations with Applications*. Vol. 34. Texts in Applied Mathematics. Springer New York, 2006.

[51] Uthsav Chitra and Benjamin J. Raphael. "Random Walks on Hypergraphs with Edge-Dependent Vertex Weights". In: *36th International Conference on Machine Learning, ICML 2019*. May 2019, pp. 2002–2011.

[52] Young Pil Choi, Seung Yeal Ha, and Seok Bae Yun. "Complete synchronization of Kuramoto oscillators with finite inertia". In: *Physica D: Nonlinear Phenomena* 240.1 (2011), pp. 32–44.

[53] Sandeep Chowdhary, Aanjaneya Kumar, Giulia Cencetti, Iacopo Iacopini, and Federico Battiston. "Simplicial contagion in temporal higher-order networks". In: *Journal of Physics: Complexity* 2.3 (Sept. 2021), p. 035019.

[54] Aaron Clauset, M. E. J. Newman, and Cristopher Moore. "Finding community structure in very large networks". In: *Physical Review E* 70.6 (Dec. 2004), p. 066111.

[55] Stephen Coombes. "Waves, bumps, and patterns in neural field theories". In: *Biological Cybernetics* 93.2 (Aug. 2005), pp. 91–108.

[56] John David Crawford. "Introduction to bifurcation theory". In: *Reviews of Modern Physics* 63.4 (Oct. 1991), pp. 991–1037.

[57] Felipe Cucker and Steve Smale. "Emergent Behavior in Flocks". In: *IEEE Transactions on Automatic Control* 52.5 (May 2007), pp. 852–862.

[58] Felipe Cucker and Steve Smale. "On the mathematics of emergence". In: *Japanese Journal of Mathematics* 2.1 (Mar. 2007), pp. 197–227.

[59] E.M. De Jager and Jiang Furu. *The Theory of Singular Perturbations*. Elsevier, 1996.

[60] Fabiano Berardo De Sousa and Liang Zhao. "Evaluating and comparing the IGraph community detection algorithms". In: *Proceedings - 2014 Brazilian Conference on Intelligent Systems, BRACIS 2014* (2014), pp. 408–413.

[61] Rashmi C. Desai and Robert Zwanzig. "Statistical mechanics of a nonlinear stochastic model". In: *Journal of Statistical Physics* 19.1 (July 1978), pp. 1–24.

[62] Lee DeVille and Bard Ermentrout. "Phase-locked patterns of the Kuramoto model on 3-regular graphs". In: *Chaos: An Interdisciplinary Journal of Nonlinear Science* 26.9 (Sept. 2016), p. 094820.

[63] Helge Dietert and Bastien Fernandez. "The mathematics of asymptotic stability in the Kuramoto model". In: *Proceedings of the Royal Society A: Mathematical, Physical and Engineering Sciences* 474.2220 (2018).

[64] J. T. Enright. "Temporal Precision in Circadian Systems: A Reliable Neuronal Clock from Unreliable Components?" In: *Science* 209.4464 (Sept. 1980), pp. 1542–1545.

[65] P. Erdős and Alfréd Rényi. "On random graphs. I." In: *Publicationes Mathematicae Debrecen* 6.3-4 (July 1959), pp. 290–297.

[66] Bard Ermentrout. "Neural networks as spatio-temporal pattern-forming systems". In: *Reports on Progress in Physics* 61.4 (Apr. 1998), pp. 353–430.

[67] Lawrence C. Evans. *Partial Differential Equations.* 2nd ed. American Mathematical Soc., 2010.

[68] H. Fujisaka and T. Yamada. "Stability Theory of Synchronized Motion in Coupled-Oscillator Systems". In: *Progress of Theoretical Physics* 69.1 (Jan. 1983), pp. 32–47.

[69] L. V. Gambuzza, F. Di Patti, L. Gallo, S. Lepri, M. Romance, R. Criado, M. Frasca, V. Latora, and S. Boccaletti. "Stability of synchronization in simplicial complexes". In: *Nature Communications* 12.1 (Feb. 2021), p. 1255.

[70] Erik Gengel, Erik Teichmann, Michael Rosenblum, and Arkady S. Pikovsky. "High-order phase reduction for coupled oscillators". In: *Journal of Physics: Complexity* 2.1 (2021).

[71] Taras Girnyk, Martin Hasler, and Yuriy Maistrenko. "Multistability of twisted states in non-locally coupled Kuramoto-type models". In: *Chaos* 22.1 (2012).

[72] Marios Antonios Gkogkas and Christian Kuehn. "Graphop Mean-Field Limits for Kuramoto-Type Models". In: *SIAM Journal on Applied Dynamical Systems* 21.1 (Mar. 2022), pp. 248–283.

[73] Marios Antonios Gkogkas, Christian Kuehn, and Chuang Xu. "Continuum limits for adaptive network dynamics". In: *Communications in Mathematical Sciences* 21.1 (2023), pp. 83–106.

[74] Monica Goebel, Matthew S. Mizuhara, and Sofia Stepanoff. "Stability of twisted states on lattices of Kuramoto oscillators". In: *Chaos* 31.10 (June 2021), pp. 1–14.

[75] D Golomb, D Hansel, and G Mato. "Mechanisms of synchrony of neural activity in large networks, in: Handbook of Biological Physics". In: *Handbook of biological physics* 4 (2001), pp. 887–968.

[76] François Golse. "Mean Field Kinetic Equations". In: *Course of Polytechnique* (2013).

[77]   Martin Golubitsky and Ian Stewart. *The Symmetry Perspective*. Basel: Birkhäuser Basel, 2002.

[78]   Chen Chris Gong and Arkady Pikovsky. "Low-dimensional dynamics for higher-order harmonic, globally coupled phase-oscillator ensembles". In: *Physical Review E* 100.6 (Dec. 2019), p. 062210.

[79]   L. Greengard and V. Rokhlin. "A Fast Algorithm for Particle Simulations". In: *Journal of Computational Physics* 73 (Aug. 1987), pp. 325–348.

[80]   Jacopo Grilli, György Barabás, Matthew J. Michalska-Smith, and Stefano Allesina. "Higher-order interactions stabilize dynamics in competitive network models". In: *Nature* 548.7666 (Aug. 2017), pp. 210–213.

[81]   Thilo Gross and Hiroki Sayama, eds. *Adaptive Networks*. Understanding Complex Systems. Berlin, Heidelberg: Springer Berlin Heidelberg, 2009.

[82]   J. Guckenheimer. "Isochrons and phaseless sets". In: *Journal of Mathematical Biology* 1.3 (Sept. 1975), pp. 259–273.

[83]   Seung Yeal Ha, Taeyoung Ha, and Jong Ho Kim. "On the complete synchronization of the Kuramoto phase model". In: *Physica D: Nonlinear Phenomena* 239.17 (2010), pp. 1692–1700.

[84]   A A Hagberg, D A Schult, and P J Swart. "Exploring network structure, dynamics, and function using NetworkX". In: *7th Python in Science Conference (SciPy 2008)*. 2008.

[85]   Hamed Hatami, László Lovász, and Balázs Szegedy. "Limits of locally–globally convergent graph sequences". In: *Geometric and Functional Analysis* 24.1 (Feb. 2014), pp. 269–296.

[86]   Rainer Hegselmann and Ulrich Krause. "Opinion dynamics and bounded confidence: Models, analysis and simulation". In: *Jasss* 5.3 (2002).

[87]   Petter Holme and Jari Saramäki. "Temporal networks". In: *Physics Reports* 519.3 (Oct. 2012), pp. 97–125.

[88]   Leonhard Horstmeyer and Christian Kuehn. "Adaptive voter model on simplicial complexes". In: *Physical Review E* 101.2 (Feb. 2020), p. 022305.

[89]   Bukyoung Jhun, Minjae Jo, and B Kahng. "Simplicial SIS model in scale-free uniform hypergraph". In: *Journal of Statistical Mechanics: Theory and Experiment* 2019.12 (Dec. 2019), p. 123207.

[90]   Shi Jin, Lei Li, and Jian-Guo Liu. "Random Batch Methods (RBM) for interacting particle systems". In: *Journal of Computational Physics* 400 (Jan. 2020), p. 108877.

[91] Jürgen Jost and Maliackal Poulo Joy. "Spectral properties and synchronization in coupled map lattices". In: *Physical Review E - Statistical Physics, Plasmas, Fluids, and Related Interdisciplinary Topics* 65.1 (2002), pp. 1–9.

[92] Jürgen Jost and Raffaella Mulas. "Hypergraph Laplace operators for chemical reaction networks". In: *Advances in Mathematics* 351 (July 2019), pp. 870–896.

[93] Wolfram Just. "Globally coupled maps: phase transitions and synchronization". In: *Physica D: Nonlinear Phenomena* 81.4 (Mar. 1995), pp. 317–340.

[94] Dmitry Kaliuzhnyi-Verbovetskyi and Georgi S. Medvedev. "The Mean Field Equation for the Kuramoto Model on Graph Sequences with Non-Lipschitz Limit". In: *SIAM Journal on Mathematical Analysis* 50.3 (Jan. 2018), pp. 2441–2465.

[95] Kunihiko Kaneko. "Period-Doubling of Kink-Antikink Patterns, Quasiperiodicity in Antiferro-Like Structures and Spatial Intermittency in Coupled Logistic Lattice: Towards a Prelude of a "Field Theory of Chaos"". In: *Progress of Theoretical Physics* 72.3 (Sept. 1984), pp. 480–486.

[96] J. Kevorkian and J. D. Cole. *Multiple Scale and Singular Perturbation Methods*. Vol. 114. Applied Mathematical Sciences. New York, NY: Springer New York, 1996.

[97] Hansjörg Kielhöfer. *Bifurcation Theory*. Vol. 156. Applied Mathematical Sciences. New York, NY: Springer New York, 2012, pp. i–398.

[98] István Z. Kiss, Joel C. Miller, and Péter L. Simon. *Mathematics of Epidemics on Networks*. Springer, 2017.

[99] Steffen Klamt, Utz-Uwe Haus, and Fabian Theis. "Hypergraphs and Cellular Networks". In: *PLoS Computational Biology* 5.5 (May 2009). Ed. by Jörg Stelling, e1000385.

[100] M. Komarov and Arkady S. Pikovsky. "The Kuramoto model of coupled oscillators with a bi-harmonic coupling function". In: *Physica D: Nonlinear Phenomena* 289 (2014), pp. 18–31.

[101] Christian Kuehn. "Moment Closure—A Brief Review". In: *Control of Self-Organizing Nonlinear Systems*. Ed. by Eckehard Schöll, Sabine H. L. Klapp, and Philipp Hövel. Cham: Springer, 2016, pp. 253–271.

[102] Christian Kuehn. *PDE Dynamics: An Introduction*. SIAM, 2019.

[103] Christian Kuehn, Nils Berglund, Christian Bick, Maximilian Engel, Tobias Hurth, Annalisa Iuorio, and Cinzia Soresina. "A general view on double limits in differential equations". In: *Physica D: Nonlinear Phenomena* 431 (Mar. 2022), p. 133105.

[104]   Christian Kuehn and Christian Bick. "A universal route to explosive phenomena". In: *Science Advances* 7.16 (2021), pp. 1–7.

[105]   Christian Kuehn and Sebastian Throm. "Power network dynamics on graphons". In: *SIAM Journal on Applied Mathematics* 79.4 (2019), pp. 1271–1292.

[106]   Christian Kuehn and Chuang Xu. "Vlasov equations on digraph measures". 2021. arXiv: `2107.08419`.

[107]   Yoshiki Kuramoto. *Chemical Oscillations, Waves, and Turbulence*. Vol. 19. Springer Series in Synergetics. Berlin, Heidelberg: Springer Berlin Heidelberg, 1984.

[108]   Yoshiki Kuramoto. "Self-entrainment of a population of coupled non-linear oscillators". In: *Group* (1975), pp. 420–422.

[109]   Carlo R. Laing. "The dynamics of chimera states in heterogeneous Kuramoto networks". In: *Physica D: Nonlinear Phenomena* 238.16 (Aug. 2009), pp. 1569–1588.

[110]   M Lakshmanan and K Murali. *Chaos in Nonlinear Oscillators: Controlling and Synchronization*. Vol. 13. World Scientific Series on Nonlinear Science Series A. WORLD SCIENTIFIC, June 1996.

[111]   Peter Langfield, Bernd Krauskopf, and Hinke M. Osinga. "Solving Winfree's puzzle: The isochrons in the FitzHugh-Nagumo model". In: *Chaos: An Interdisciplinary Journal of Nonlinear Science* 24.1 (Mar. 2014), p. 013131.

[112]   Jungmin Lee, Minsu Cho, and Kyoung Mu Lee. "Hyper-graph matching via reweighted random walks". In: *CVPR 2011*. IEEE, June 2011, pp. 1633–1640.

[113]   E. A. Leicht and M. E. J. Newman. "Community Structure in Directed Networks". In: *Physical Review Letters* 100.11 (Mar. 2008), p. 118703.

[114]   Iván León and Diego Pazó. "Phase reduction beyond the first order: The case of the mean-field complex Ginzburg-Landau equation". In: *Physical Review E* 100.1 (July 2019), p. 012211.

[115]   Thomas M. Liggett. *Stochastic Interacting Systems: Contact, Voter and Exclusion Processes*. Vol. 324. Grundlehren der mathematischen Wissenschaften. Berlin, Heidelberg: Springer Berlin Heidelberg, 1999.

[116]   Pedro G. Lind, Jason A. C. Gallas, and Hans J. Herrmann. "Coherence in scale-free networks of chaotic maps". In: *Physical Review E* 70.5 (Nov. 2004), p. 056207.

[117]   M. A. Lohe. "Higher-dimensional generalizations of the Watanabe-Strogatz transform for vector models of synchronization". In: *Journal of Physics A: Mathematical and Theoretical* 51.22 (2018).

[118] Robert Macarthur and Richard Levins. "The Limiting Similarity, Convergence, and Divergence of Coexisting Species". In: *The American Naturalist* 101.921 (1967), pp. 377–385.

[119] Y.L. Maistrenko, O.V. Popovych, and P.A. Tass. "Desynchronization and Chaos in the Kuramoto Model". In: *Dynamics of Coupled Map Lattices and of Related Spatially Extended Systems*. Vol. 306. Berlin/Heidelberg: Springer-Verlag, 2005, pp. 285–306.

[120] Joan T. Matamalas, Sergio Gómez, and Alex Arenas. "Abrupt phase transition of epidemic spreading in simplicial complexes". In: *Physical Review Research* 2.1 (2020).

[121] Matthew H Matheny et al. "Exotic states in a simple network of nanoelectromechanical oscillators". In: *Science* 363.6431 (Mar. 2019).

[122] Georgi S. Medvedev. "Small-world networks of Kuramoto oscillators". In: *Physica D: Nonlinear Phenomena* 266 (2014), pp. 13–22.

[123] Georgi S. Medvedev. "The continuum limit of the Kuramoto model on sparse random graphs". In: *Communications in Mathematical Sciences* 17.4 (2019), pp. 883–898.

[124] Georgi S. Medvedev. "The nonlinear heat equation on dense graphs and graph limits". In: *SIAM Journal on Mathematical Analysis* 46.4 (2014), pp. 2743–2766.

[125] Georgi S. Medvedev and Xuezhi Tang. "Stability of Twisted States in the Kuramoto Model on Cayley and Random Graphs". In: *Journal of Nonlinear Science* 25.6 (2015), pp. 1169–1208.

[126] Georgi S. Medvedev and J. Douglas Wright. "Stability of twisted states in the continuum kuramoto model". In: *SIAM Journal on Applied Dynamical Systems* 16.1 (2017), pp. 188–203.

[127] Renato E. Mirollo and Steven H. Strogatz. "The spectrum of the partially locked state for the Kuramoto model". In: *Journal of Nonlinear Science* 17.4 (2007), pp. 309–347.

[128] Bharat Monga, Dan Wilson, Tim Matchen, and Jeff Moehlis. "Phase reduction and phase-based optimal control for biological systems: a tutorial". In: *Biological Cybernetics* 113.1-2 (Apr. 2019), pp. 11–46.

[129] Subhayan Mukerjee. "A systematic comparison of community detection algorithms for measuring selective exposure in co-exposure networks". In: *Scientific Reports* 11.1 (2021), pp. 1–11.

[130] Raffaella Mulas, Danijela Horak, and Jürgen Jost. "Graphs, Simplicial Complexes and Hypergraphs: Spectral Theory and Topology". In: *Understanding Complex Systems*. Springer International Publishing, 2022, pp. 1–58.

[131] Raffaella Mulas, Christian Kuehn, Tobias Böhle, and Jürgen Jost. "Random walks and Laplacians on hypergraphs: When do they match?" In: *Discrete Applied Mathematics* 317 (Aug. 2022), pp. 26–41.

[132] Raffaella Mulas, Christian Kuehn, and Jürgen Jost. "Coupled dynamics on hypergraphs: Master stability of steady states and synchronization". In: *Physical Review E* 101.6 (June 2020), p. 062313.

[133] Hiroya Nakao. "Phase reduction approach to synchronisation of nonlinear oscillators". In: *Contemporary Physics* 57.2 (Apr. 2016), pp. 188–214.

[134] M. E. J. Newman. "The Structure and Function of Complex Networks". In: *SIAM Review* 45.2 (Jan. 2003), pp. 167–256.

[135] O. E. Omel'chenko. "Mathematical Framework for Breathing Chimera States". In: *Journal of Nonlinear Science* 32.2 (Apr. 2022), p. 22.

[136] Oleh E. Omel'chenko. "The mathematics behind chimera states". In: *Nonlinearity* 31.5 (2018), R121–R164.

[137] Oleh E. Omel'chenko, Matthias Wolfrum, and Carlo R. Laing. "Partially coherent twisted states in arrays of coupled phase oscillators". In: *Chaos* 24.2 (June 2014).

[138] Motohisa Osaka. "Modified Kuramoto Phase Model for Simulating Cardiac Pacemaker Cell Synchronization". In: *Applied Mathematics* 08.09 (2017), pp. 1227–1238.

[139] James Pantaleone. "Synchronization of metronomes". In: *American Journal of Physics* 70.10 (Oct. 2002), pp. 992–1000.

[140] Theodosios Pavlidis. *Biological Oscillators: Their Mathematical Analysis*. New York [u.a.]: Acad. Press, 1973, p. 207.

[141] Louis M. Pecora and Thomas L. Carroll. "Synchronization in chaotic systems". In: *Physical Review Letters* 64.8 (Feb. 1990), pp. 821–824.

[142] Bastian Pietras and Andreas Daffertshofer. "Network dynamics of coupled oscillators and phase reduction techniques". In: *Physics Reports* 819 (July 2019), pp. 1–105.

[143] Arkady S. Pikovsky and Jürgen Kurths. "Do globally coupled maps really violate the law of large numbers?" In: *Physical Review Letters* 72.11 (Mar. 1994), pp. 1644–1646.

[144] Arkady S. Pikovsky, Michael Rosenblum, and Jürgen Kurths. *Synchronization*. Cambridge University Press, Oct. 2001.

[145] Pascal Pons and Matthieu Latapy. "Computing Communities in Large Networks Using Random Walks". In: *Computer and Information Sciences - ISCIS 2005*. Ed. by PInar Yolum, Tunga Güngör, Fikret Gürgen, and Can Özturan. Berlin, Heidelberg: Springer Berlin Heidelberg, 2005, pp. 284–293.

[146] Mason Porter and James Gleeson. *Dynamical Systems on Networks*. Vol. 4. Frontiers in Applied Dynamical Systems: Reviews and Tutorials. Cham: Springer International Publishing, 2016, p. 80.

[147] Jörg Reichardt and Stefan Bornholdt. "Detecting fuzzy community structures in complex networks with a potts model". In: *Physical Review Letters* 93.21 (2004), pp. 19–22.

[148] Jörg Reichardt and Stefan Bornholdt. "Statistical mechanics of community detection". In: *Physical Review E* 74.1 (July 2006), p. 016110.

[149] Francisco A. Rodrigues, Thomas K.D.M. Peron, Peng Ji, and Jürgen Kurths. "The Kuramoto model in complex networks". In: *Physics Reports* 610 (2016), pp. 1–98.

[150] Martin Rohden, Andreas Sorge, Marc Timme, and Dirk Witthaut. "Self-Organized Synchronization in Decentralized Power Grids". In: *Physical Review Letters* 109.6 (Aug. 2012), p. 064101.

[151] V. Rokhlin. "Rapid solution of integral equations of classical potential theory". In: *Journal of Computational Physics* 60.2 (Sept. 1985), pp. 187–207.

[152] Giulio Rossetti, Letizia Milli, and Rémy Cazabet. "CDLIB: a python library to extract, compare and evaluate communities from complex networks". In: *Applied Network Science* 4.1 (2019).

[153] Ryan A. Rossi and Nesreen K. Ahmed. "The Network Data Repository with Interactive Graph Analytics and Visualization". In: *AAAI*. 2015.

[154] Martin Rosvall, Jean-Charles Delvenne, Michael T. Schaub, and Renaud Lambiotte. "Different Approaches to Community Detection". In: *Advances in Network Clustering and Blockmodeling*. Ed. by Patrick Doreian, Vladimir Batagelj, and Anuška Ferligoj. Wiley, Nov. 2019, pp. 105–119.

[155] Hidetsugu Sakaguchi and Yoshiki Kuramoto. "A Soluble Active Rotater Model Showing Phase Transitions via Mutual Entertainment". In: *Progress of Theoretical Physics* 76.3 (Sept. 1986), pp. 576–581.

[156] Anastasiya Salova and Raissa M. D'Souza. "Cluster synchronization on hypergraphs". Jan. 2021. arXiv: 2101.05464.

[157] Alicia Sanchez-Gorostiaga, Djordje Bajić, Melisa L. Osborne, Juan F. Poyatos, and Alvaro Sanchez. "High-order interactions distort the functional landscape of microbial consortia". In: *PLOS Biology* 17.12 (Dec. 2019). Ed. by Wenying Shou, e3000550.

[158] L. Scardovi, A. Sarlette, and R. Sepulchre. "Synchronization and balancing on the N-torus". In: *Systems and Control Letters* 56.5 (2007), pp. 335–341.

[159] Fanni M. Sélley and Matteo Tanzi. "Synchronization for Networks of Globally Coupled Maps in the Thermodynamic Limit". In: *Journal of Statistical Physics* 189.1 (Oct. 2022), p. 16.

[160] Per Sebastian Skardal and Alex Arenas. "Higher order interactions in complex networks of phase oscillators promote abrupt synchronization switching". In: *Communications Physics* 3.1 (Nov. 2020), p. 218.

[161] Per Sebastian Skardal, Edward Ott, and Juan G. Restrepo. "Cluster synchrony in systems of coupled phase oscillators with higher-order coupling". In: *Physical Review E - Statistical, Nonlinear, and Soft Matter Physics* 84.3 (2011), pp. 1–10.

[162] Steven H. Strogatz. "From Kuramoto to Crawford: Exploring the onset of synchronization in populations of coupled oscillators". In: *Physica D: Nonlinear Phenomena* 143.1-4 (2000), pp. 1–20.

[163] Steven H. Strogatz. *Sync: The Emerging Science of Spontaneous Order.* New York: Hyperion, 2003, p. 338.

[164] Steven H. Strogatz, Daniel M. Abrams, Allan McRobie, Bruno Eckhardt, and Edward Ott. "Theoretical mechanics: Crowd synchrony on the Millennium Bridge". In: *Nature* 438.7064 (2005), pp. 43–44.

[165] Steven H. Strogatz and Renato E. Mirollo. "Stability of incoherence in a population of coupled oscillators". In: *Journal of Statistical Physics* 63.3-4 (1991), pp. 613–635.

[166] Steven H. Strogatz and Ian Stewart. "Coupled oscillators and biological synchronization". In: *Scientific American* 269.6 (1993), pp. 102–109.

[167] Hanlin Sun and Ginestra Bianconi. "Higher-order percolation processes on multiplex hypergraphs". In: *Physical Review E* 104.3 (Sept. 2021), p. 034306.

[168] Marina V. Sysoeva, Ilya V. Sysoev, Mikhail D. Prokhorov, Vladimir I. Ponomarenko, and Boris P. Bezruchko. "Reconstruction of coupling structure in network of neuron-like oscillators based on a phase-locked loop". In: *Chaos, Solitons and Fractals* 142 (2021), p. 110513.

[169] Matteo Tanzi. "Uniformly Expanding Coupled Maps: Self-Consistent Transfer Operators and Propagation of Chaos". 2022. arXiv: 2209.13571.

[170] Gerald Teschl. *Ordinary Differential Equations and Dynamical Systems.* American Mathematical Society, 2012, p. 356.

[171] V. A. Traag, G. Krings, and P. Van Dooren. "Significant Scales in Community Structure". In: *Scientific Reports* 3.1 (Dec. 2013), p. 2930.

[172] John H. Vandermeer. "The Competitive Structure of Communities: An Experimental Approach with Protozoa". In: *Ecology* 50.3 (May 1969), pp. 362–371.

[173] E. Vasilyeva, A. Kozlov, K. Alfaro-Bittner, D. Musatov, A. M. Raigorodskii, M. Perc, and S. Boccaletti. "Multilayer representation of collaboration networks with higher-order interactions". In: *Scientific Reports* 11.1 (Mar. 2021), p. 5666.

[174] Thomas J. Walker. "Acoustic synchrony: Two mechanisms in the snowy tree cricket". In: *Science* 166.3907 (1969), pp. 891–894.

[175] Xiao Fan Wang and Jian Xu. "Cascading failures in coupled map lattices". In: *Physical Review E* 70.5 (Nov. 2004), p. 056113.

[176] Duncan J. Watts and Steven H. Strogatz. "Collective dynamics of 'small-world' networks". In: *Nature* 393.6684 (June 1998), pp. 440–442.

[177] Daniel A. Wiley, Steven H. Strogatz, and Michelle Girvan. "The size of the sync basin". In: *Chaos* 16.1 (2006).

[178] Arthur T. Winfree. "Biological Rhythms and the Behavior of Populations of Coupled Oscillators". In: *Journal of Theoretical Biology* 16.1 (1967), pp. 15–42.

[179] Arthur T. Winfree. *The Geometry of Biological Time.* Berlin, Heidelberg: Springer Berlin Heidelberg, 1980, pp. 1–23.

[180] Jianbo Xie, Edgar Knobloch, and Hsien-Ching Kao. "Multicluster and traveling chimera states in nonlocal phase-coupled oscillators". In: *Physical Review E* 90.2 (Aug. 2014), p. 022919.

[181] Can Xu and Per Sebastian Skardal. "Spectrum of extensive multiclusters in Kuramoto model with simplicial interaction". In: *arXiv* (2020), pp. 1–11.

[182] Zhao Yang, René Algesheimer, and Claudio J. Tessone. "A comparative analysis of community detection algorithms on artificial networks". In: *Scientific Reports* 6.March (2016).

[183] Yuanzhao Zhang, Maxime Lucas, and Federico Battiston. "Higher-order interactions shape collective dynamics differently in hypergraphs and simplicial complexes". In: *Nature Communications* 14.1 (Mar. 2023), p. 1605.

[184]   Dengyong Zhou, Jiayuan Huang, and Bernhard Schölkopf. "Learning with Hypergraphs: Clustering, Classification, and Embedding". In: *Proceedings of the 19th International Conference on Neural Information Processing Systems*. MIT Press, 2006, pp. 1601–1608.

Appendix A

Additional Calculations for the Derivation of Phase Reductions

This chapter is based on the publication [20], which is joint work with Christian Bick and Christian Kuehn. In particular, the technical parts are taken from this publication of which I am the main author.

In this section, we exemplify the $(2,1)$-phase reduction for arbitrary perturbations g. In particular, we state the solution $R_k^{(1,1)}$ of the PDE (4.3.12) when g is not just given by sin but consists of more harmonics. We explain how higher-harmonics in g influence the $(2,1)$-phase reduction and how these additional harmonics affect the stability of the synchronized orbit.

Whenever $g(\phi) = \sin(n\phi)$ for $n \in \mathbb{N}$, the solution[1] of the PDE (4.3.12) is given by

$$R_k^{(1,1)}(\phi) = \frac{1}{2M(m^2 + (n\omega)^2)} \sum_{l=1}^{M} s_1(\phi_k, \phi_l) \tag{A.0.1}$$

with

$$
\begin{aligned}
s_1(\phi_k, \phi_l) = n\omega\Big(& (n-2)\cos(n\phi_k - \alpha) - \cos(\phi_k - (n+1)\phi_l - \alpha) \\
& - (n-3)\cos((n+1)\phi_k - \phi_l - \alpha) - \cos(\phi_k + (n-1)\phi_l - \alpha) \\
& - (n+2)\cos(n\phi_k + \alpha) + (n+3)\cos((n-1)\phi_k + \phi_l + \alpha)\Big) \\
+ m\Big(& (n-2)\sin(n\phi_k - \alpha) + \sin(\phi_k - (n+1)\phi_l - \alpha) \\
& - (n-3)\sin((n+1)\phi_k - \phi_l - \alpha) - \sin(\phi_k + (n-1)\phi_l - \alpha)
\end{aligned}
$$

---

[1]This PDE can be solved with the MATHEMATICA code, which is available on GitHub, see [33].

$$- (n+2)\sin(n\phi_k + \alpha) + (n+3)\sin((n-1)\phi_k + \phi_l + \alpha)\Big).$$

Moreover, if $g(\phi) = \cos(n\phi)$ for $n \in \mathbb{N}$, the solution of (4.3.12) is given by (A.0.1) as well, but then

$$\begin{aligned}
s_1(\phi_k, \phi_l) = n\omega\Big(&- (n-2)\sin(n\phi_k - \alpha) - \sin(\phi_k - (n+1)\phi_l - \alpha) \\
&+ (n-3)\sin((n+1)\phi_k - \phi_l - \alpha) + \sin(\phi_k + (n-1)\phi_l - \alpha) \\
&+ (n+2)\sin(n\phi_k + \alpha) - (n+3)\sin((n-1)\phi_k + \phi_l + \alpha)\Big) \\
+ m\Big(&(n-2)\cos(n\phi_k - \alpha) - \cos(\phi_k - (n+1)\phi_l - \alpha) \\
&- (n-3)\cos((n+1)\phi_k - \phi_l - \alpha) - \cos(\phi_k + (n-1)\phi_l - \alpha) \\
&- (n+2)\cos(n\phi_k + \alpha) + (n+3)\cos((n-1)\phi_k + \phi_l + \alpha)\Big)
\end{aligned}$$

Now, a general sufficiently smooth function g can be constructed as a sum of the basis functions $\cos(n\phi)$ and $\sin(n\phi)$ with $n \in \mathbb{N}$. Due to the linearity of the PDE (4.3.12) its solution for a general sufficiently smooth function g can therefore be constructed using its solutions when g is a basis function.

To investigate how these higher harmonics influence the stability of the synchronized orbit in a $(2,1)$-phase-reduced system one first notes that the only part in this phase reduction, that depends on $R_k^{(1,1)}(\phi)$ is $P_k^{(2,1)}$ as defined in (4.3.15b). In particular, if g is given by a general Fourier sum

$$g(\phi) = \sum_{n=1}^{\Omega} (a_n \cos(n\phi) + b_n \sin(n\phi))$$

with real coefficients a_n, b_n, the general form of $P_k^{(2,1)}$ is

$$\begin{aligned}
P_k^{(2,1)}(\phi) = \nabla_R H_k^{(-,0)}(\mathbb{1}, \phi) \cdot \left(\sum_{n=1}^{\Omega} a_n R_{\cos(n\phi)}^{(1,1)}(\phi) + b_n R_{\sin(n\phi)}^{(1,1)}(\phi) \right) \\
+ \nabla_R H_k^{(-,1)}(\mathbb{1}, \phi) \cdot R^{(1,0)}(\phi),
\end{aligned}$$

where $R_{\cos(n\phi)}^{(1,1)} = (R_{\cos(n\phi),1}^{(1,1)}, \dots, R_{\cos(n\phi),M}^{(1,1)})^\top$ and $R_{\sin(n\phi)}^{(1,1)} = (R_{\sin(n\phi),1}^{(1,1)}, \dots, R_{\sin(n\phi),M}^{(1,1)})^\top$ are the solutions (A.0.1) of (4.3.12) when $g(\phi) = \cos(n\phi)$ and $g(\phi) = \sin(n\phi)$, respectively. In other words, one can say that whenever g consists of multiple harmonics, these harmonics contribute to the right-hand side of the $(2,1)$-phase reduction, each by one summand $\nabla_R H_k^{(-,0)}(\mathbb{1}, \phi) \cdot R_{\cos(n\phi)}^{(1,1)}(\phi)$ or $\nabla_R H_k^{(-,0)}(\mathbb{1}, \phi) \cdot R_{\sin(n\phi)}^{(1,1)}(\phi)$ with possible prefactors, only. Therefore, higher harmonics in g cause

more summands in the linearization of the right-hand side at a synchronized state. As explained in Section 4.4.1 this Jacobian is of the form $h(\gamma)\frac{1}{M}(J_M - M\mathrm{Id}_M)$, when linearized at $\phi_1 = \cdots = \phi_M = \gamma$ and each harmonic in g causes one summand in h. A calculation shows that this summand for the harmonic $\sin(n\phi)$ is

$$\frac{2K^2\delta \sin(\alpha)^2}{m^2 + (n\omega)^2}\Big(n\omega \cos(n\gamma) + m \sin(n\gamma)\Big)$$

and

$$\frac{2K^2\delta \sin(\alpha)^2}{m^2 + (n\omega)^2}\Big(m \cos(n\gamma) - n\omega \sin(n\gamma)\Big)$$

if $g(\phi) = \cos(n\phi)$. When integrating these summands over the synchronized orbit $\gamma \in \mathbb{T}$ one sees that they vanish. Therefore, they do not contribute to the Floquet exponent, which determines the stability of the synchronized orbit.

Appendix B

Supplementary Material for the Analysis of Twisted States

The content of this chapter is based on the publication [22], which is joint work together with Christian Bick and Christian Kuehn. In particular, the technical parts are taken from the publication [22] of which I am the main author.

B.1 Abbreviations

Coefficients $c_1, \ldots, c_6$ The coefficients $c_1, \ldots, c_6$ that appear in the derivative of F^q in (5.4.13)-(5.4.16) are used to calculate γ_1 and γ_2, which are the main parameters in the expansion (5.4.27). Given γ_1 and γ_2 one can determine when bifurcating equilibria exist, their stability, ect. Using the convention $\hat{W}_r(-k) := \hat{W}_r(k)$ and $p = (r, \lambda, \mu) \in \mathcal{P}$, the coefficients are given by

$$c_1(q, k, p) = \frac{1}{4}\Big(\hat{W}_r(q-k) + \hat{W}_r(q+k) - 2\hat{W}_r(q) - (4\lambda + 2\mu)\hat{W}_r(q)\Big)$$

$$c_2(q, k, p) = \frac{1}{8}\Big(-\hat{W}_r(q-2k) + 2\hat{W}_r(q-k) - 2\hat{W}_r(q+k)$$
$$+ \hat{W}_r(q+2k) - 2\lambda\hat{W}_r(q-k) + 2\lambda\hat{W}_r(q+k)\Big)$$

$$c_3(q, m, k, p) = \frac{1}{8}\Big(-\hat{W}_r(q-m) + \hat{W}_r(q-m+k) + \hat{W}_r(q-k)$$
$$- \hat{W}_r(q+k) - \hat{W}_r(q+m-k) + \hat{W}_r(q+m)\Big)$$

$$c_4(q, m, k, p) = \frac{1}{8}\Big(-\hat{W}_r(q-m-k) + \hat{W}_r(q-m) + \hat{W}_r(q-k)$$
$$- \hat{W}_r(q+k) - \hat{W}_r(q+m) + \hat{W}_r(q+m+k)\Big)$$

$$c_5(q, k, p) = \frac{1}{16}\Big(\hat{W}_r(q - 2k) - 4\hat{W}_r(q - k) + 6\hat{W}_r(q) - 4\hat{W}_r(q + k)$$
$$+ \hat{W}_r(q + 2k) + 4\lambda\hat{W}_r(q - k) + 32\lambda\hat{W}_r(q) + 4\lambda\hat{W}_r(q + k)$$
$$+ 2\mu\hat{W}_r(q - k) + 14\mu\hat{W}_r(q) + 2\mu\hat{W}_r(q + k) \Big)$$

$$c_6(q, k, p) = \frac{1}{16}\Big(\hat{W}_r(q - 3k) - 3\hat{W}_r(q - 2k) + 3\hat{W}_r(q - k) - 2\hat{W}_r(q)$$
$$+ 3\hat{W}_r(q + k) - 3\hat{W}_r(q + 2k) + \hat{W}_r(q + 3k) - 12\lambda\hat{W}_r(q - k)$$
$$- 16\lambda\hat{W}_r(q) - 12\lambda\hat{W}_r(q + k) - 2\mu\hat{W}_r(q) \Big)$$

Note that c_2 does not depend on μ, c_3 does not depend on λ and μ and c_3 satisfies $c_3(q, m, k, p) = -c_3(q, k, m, p)$. Moreover, c_4 does not depend on λ and μ.

Note that these coefficients are chosen such that they fulfill the derivative conditions (5.4.13)-(5.4.16). They can be derived by evaluating the first, second and third derivatives of $F(\Psi, p)$, that is given in Section B.3, at a q-twisted state. As an example, we show the derivation of the first derivative condition (5.4.13) when $\lambda = \mu = 0$, see also [177] for a similar derivation. If $\lambda \neq 0$ and $\mu \neq 0$, the calculations only become longer but not more difficult. Therefore, we omit these calculations. Moreover, we recommend to use symbolic integrating software to compute higher-order derivatives of F.

By the calculation from Section B.3, the first derivative $F_\Psi(\Psi^q, p)$ is given by

$$F_\Psi(\Psi^q, p)[\eta](x) = \int_\mathbb{S} W_r(x - y)(\eta(y) - \eta(x)) \cos(\Psi^q(y) - \Psi^q(x)) \, \mathrm{d}y$$
$$- \int_\mathbb{S} W_r(y)\eta(y) \cos(\Psi^q(y)) \, \mathrm{d}y.$$

We insert $\eta = u_k$, use the Fourier series representation of W_r and evaluate each integral separately to obtain

$$\int_\mathbb{S} W_r(x - y)(\sin(2\pi k y) - \sin(2\pi k x)) \cos(\Psi^q(y) - \Psi^q(x)) \, \mathrm{d}y$$
$$= \int_\mathbb{S} \left(\frac{1}{2}\hat{W}_r(0) + \sum_{j=1}^\infty \hat{W}_r(j) \cos(2\pi j(x - y)) \right)$$
$$\cdot (\sin(2\pi k y) - \sin(2\pi k x)) \cos(2\pi q(y - x)) \, \mathrm{d}y$$
$$= \frac{1}{2}\hat{W}_r(0) \int_\mathbb{S} (\sin(2\pi k y) - \sin(2\pi k x)) \cos(2\pi q(y - x)) \, \mathrm{d}y$$
$$+ \sum_{j=1}^\infty \hat{W}_r(j) \int_\mathbb{S} \cos(2\pi j(x - y))(\sin(2\pi k y) - \sin(2\pi k x)) \cos(2\pi q(y - x)) \, \mathrm{d}y$$

Using trigonometric identities, we infer

$$2(\sin(2\pi ky) - \sin(2\pi kx))\cos(2\pi q(y - x))$$
$$= -\sin(2\pi(x(k + q) + y(-q))) + \sin(2\pi(xq + y(k - q)))$$
$$- \sin(2\pi(x(k - q) + yq)) + \sin(2\pi(-qx + y(k + q)))$$

Thus, integrating this quantity over y yields

$$\frac{1}{2}\hat{W}_r(0)\int_{\mathbb{S}}(\sin(2\pi ky) - \sin(2\pi kx))\cos(2\pi q(y - x))\ \mathrm{d}y$$
$$= \begin{cases} 0 & \text{if } k \neq q \\ \frac{1}{4}\hat{W}_r(0)\sin(2\pi kx) & \text{if } k = q \end{cases}. \tag{B.1.1}$$

Similarly, we obtain

$$4\cos(2\pi j(x - y))(\sin(2\pi ky) - \sin(2\pi kx))\cos(2\pi q(y - x))$$
$$= -\sin(2\pi(x(k - j + q) + y(j - q))) + \sin(2\pi(x(-j + q) + y(k + j - q)))$$
$$- \sin(2\pi(x(k + j + q) + y(-j - q))) + \sin(2\pi(x(j + q) + y(k - j - q)))$$
$$- \sin(2\pi(x(k - j - q) + y(j + q))) + \sin(2\pi(x(-j - q) + y(k + j + q)))$$
$$- \sin(2\pi(x(k + j - q) + y(-j + q))) + \sin(2\pi(x(j - q) + y(k - j + q)))$$

and after integrating over y

$$\int_{\mathbb{S}}\cos(2\pi j(x - y))(\sin(2\pi ky) - \sin(2\pi kx))\cos(2\pi q(y - x))\ \mathrm{d}y$$
$$= \frac{1}{4}\sin(2\pi kx)\begin{cases} -1 & \text{if } j - q = 0 \\ 1 & \text{if } k + j - q = 0 \\ -1 & \text{if } -j - q = 0 \\ 1 & \text{if } k - j - q = 0 \\ -1 & \text{if } j + q = 0 \\ 1 & \text{if } k + j + q = 0 \\ -1 & \text{if } -j + q = 0 \\ 1 & \text{if } k - j + q = 0 \\ 0 & \text{else} \end{cases}. \tag{B.1.2}$$

Now, note that there is no $j \in \mathbb{N}$ such that the third, fifth and sixth case of (B.1.2) occur. Moreover, when $k \geq q$ the second case cannot appear and when

$k \leq q$ the fourth case cannot appear. Multiplying with $\hat{W}_r(j)$ and then summing over j from 1 to ∞ yields

$$\frac{1}{4}\sin(2\pi kx)\Big(-\hat{W}_r(q) + \hat{W}_r(k-q) - \hat{W}_r(q) + \hat{W}_r(k+q)\Big),$$

which is valid for all $k, q \in \mathbb{N}$ with $k \neq q$ using the convention $\hat{W}_r(-k) = \hat{W}_r(k)$. Combining it with (B.1.1) shows that

$$\int_{\mathbb{S}} W_r(x-y)(\sin(2\pi ky) - \sin(2\pi kx))\cos(\Psi^q(y) - \Psi^q(x))\, \mathrm{d}y \qquad \text{(B.1.3)}$$

$$= \frac{1}{4}\sin(2\pi kx)\Big(-\hat{W}_r(q) + \hat{W}_r(k-q) - \hat{W}_r(q) + \hat{W}_r(k+q)\Big) \qquad \text{(B.1.4)}$$

for all $q, k \in \mathbb{N}$. Finally,

$$\int_{\mathbb{S}} W_r(y)\eta(y)\cos(\Psi^q(y))\, \mathrm{d}y = 0,$$

since this integral coincides with (B.1.3) evaluated at $x = 0$. Note that $W_r(-y) = W_r(y)$. Alltogether, this shows the derivation of the coefficient $c_1(q, k, p)$ when $\lambda = \mu = 0$ in the derivative condition (5.4.13).

Calculation of $\iota(\upsilon)$ Suppose that $\hat{W}_r(k)$ is given by (5.2.7). Rewriting this relation yields

$$\hat{W}_r(k) = \frac{2}{\pi k}\sin(2\pi kr) = \frac{1}{k}f(kr),$$

if $k \neq 0$ and $f\colon \mathbb{R} \to \mathbb{R}$ is given by $f(r) = \frac{2}{\pi}\sin(2\pi r)$. Moreover, note that

$$\hat{W}_r(0) = k\hat{W}_{\frac{r}{k}}(0).$$

We use this to calculate:

$$H(q, r) = \frac{\hat{W}_r(0) + \hat{W}_r(2q) - 2\hat{W}_r(q)}{\hat{W}_r(q)} = u(qr),$$

where $u\colon \mathbb{R} \to \mathbb{R}$ is defined by

$$u(\upsilon) = \frac{4\upsilon + \frac{1}{2}f(2\upsilon) - 2f(\upsilon)}{f(\upsilon)}.$$

Moreover,

$$c_1(q, 2q, p^0(0)) = \frac{1}{4}\left(\frac{1}{-q}f(-qr) + \frac{1}{3q}f(3qr) - \frac{2}{q}f(qr) - H(q, r)\frac{1}{q}f(qr)\right)$$

$$= \frac{1}{q} g(qr),$$

with $g\colon \mathbb{R} \to \mathbb{R}$,

$$g(v) = \frac{1}{4}\left(f(v) + \frac{1}{3}f(3v) - 2f(v) - u(v)f(v) \right).$$

Furthermore,

$$c_3(q, 2q, q, p^0(0)) = \frac{1}{8}\left(\frac{-1}{q}f(qr) + 8r - \frac{1}{q}f(2qr) + \frac{1}{3q}f(3qr) \right)$$

$$= \frac{1}{q}h(qr),$$

with $h\colon \mathbb{R} \to \mathbb{R}$,

$$h(v) = \frac{1}{8}\left(-f(v) + 8v - f(2v) + \frac{1}{3}f(3v) \right).$$

Finally, we can put everything together and calculate

$$X(q, r) = -\frac{1}{4q}f(qr) + \frac{h(qr)}{4g(qr)}\left(-4r + \frac{1}{2q}f(2qr) \right)$$

$$= \frac{1}{q}\iota(qr),$$

with

$$\iota(v) = -\frac{1}{4}f(v) + \frac{h(v)}{4g(v)}\left(-4v + \frac{1}{2}f(2v) \right).$$

In conclusion, we have

$$\iota(v) = \frac{1}{8}\left(-\sin(2\pi v) + 4\pi v - \sin(4\pi v) + \frac{1}{3}\sin(6\pi v) \right)\left(-4v + \frac{1}{\pi}\sin(4\pi v) \right)$$

$$\cdot \left(-\sin(2\pi v) + \frac{1}{3}\sin(6\pi v) - (2\pi v + \frac{1}{2}\sin(4\pi v) - 2\sin(2\pi v)) \right)^{-1}$$

$$+ \frac{-1}{2\pi}\sin(2\pi v)$$

B.2   Supplementary Calculations

B.2.1   Fourier Expansion in H_0^1

Lemma B.2.1. *The functions $u_k(x) = \sin(2\pi k x)$ and $w_k(x) = 1 - \cos(2\pi k x)$ for $k \geq 1$ form a Schauder basis of $H_0^1 = H_0^1(\mathbb{S}, \mathbb{R})$. Consequently, each $\eta \in H_0^1$ can*

be written as an infinite sum

$$\eta = \sum_{k=1}^{\infty} a_k u_k + b_k w_k, \tag{B.2.1}$$

that converges in H_0^1.

Proof. Let $\eta \in H_0^1$. Since for every $\eta \in H_0^1$, there is $\tilde{\eta} \in C(\mathbb{S})$ with $\eta = \tilde{\eta}$ almost everywhere [67, Section 5.6, Theorem 4], we assume η to be continuous, without loss of generality. Now, note that $D\eta \in L^2 = L^2(\mathbb{S}, \mathbb{R})$. Due to the Fourier theory in L^2, $D\eta$ can be expanded as

$$D\eta = \alpha_0 + \sum_{k=1}^{\infty} \alpha_k \cos(2\pi k x) + \beta_k \sin(2\pi k x),$$

where the convergence is in L^2. Defining a series

$$S_N(x) := \sum_{k=1}^{N} a_k \sin(2\pi k x) + b_k(1 - \cos(2\pi k x)),$$

with $a_k = \alpha_k/(2\pi k)$ and $b_k = \beta_k/(2\pi k)$, one can see that the partial sums of $D\eta$ agree with DS_N up to α_0. Thus, $\alpha_0 + DS_N \to D\eta$ in L^2. Next, by [40, Theorem 8.2], we can integrate this weak derivative to obtain η as

$$\eta(x) = \eta(0) + \int_0^x D\eta(\tilde{x}) \, d\tilde{x}. \tag{B.2.2}$$

Parseval's identity implies $\sum \alpha_k^2 < \infty$ and $\sum \beta_k^2 < \infty$. Therefore, the partial sums of $D\eta$ are bounded by

$$|\alpha_0 + DS_N| \leq |a_0| + \sum_{k=1}^{\infty} (\alpha_k^2 + \beta_k^2)$$

Consequently, we can invoke the dominated convergence theorem to integrate the summands of $D\eta$ separately. Using that $\eta(0) = 0$, we then arrive at

$$\eta(x) = \eta(0) + \int_0^x \lim_{N\to\infty} DS_N(\tilde{x}) \, d\tilde{x}$$
$$= \lim_{N\to\infty} \int_0^x DS_N(\tilde{x}) \, d\tilde{x} = \lim_{N\to\infty} S_N(x),$$

which is a Fourier series for η. Since this Fourier Series is unique and $\eta \in H_0^1 \subset L^2$, the convergence takes place in L^2. Moreover, evaluating (B.2.2) at $x = 1$, using that η is periodic, i.e. $\eta(0) = \eta(1)$ and applying the dominated convergence theorem again yields that $\alpha_0 = 0$. Therefore, $DS_N \to D\eta$ in L^2 and $S_N \to \eta$ in L^2. Combining these two convergences shows $S_N \to \eta$ in H^1.

$\square$

B.2.2   Maximal Eigenvalue

Lemma B.2.2. *For all $k \in \mathbb{Z} \setminus \{0\}$ and all r with $0 \le r \le \frac{1}{2}$ we have*

$$\hat{W}_r(1) \ge \hat{W}_r(k) \tag{B.2.3}$$

Proof. Because $\hat{W}_r(k) = \hat{W}_r(-k)$ this inequality only needs to be shown for $k \in \mathbb{N}, k \ge 2$. The derivative of $\hat{W}_r(k)$ with respect to r is given by

$$\frac{\mathrm{d}}{\mathrm{d}r} \hat{W}_r(k) = 4 \cos(2\pi k r).$$

Since cos is decreasing in $[0, \pi/2]$ we get $\frac{\mathrm{d}}{\mathrm{d}r} \hat{W}_r(1) = 4 \cos(2\pi r) \ge 4 \cos(2\pi r k) = \frac{\mathrm{d}}{\mathrm{d}r} \hat{W}_r(k)$ for all $r \in [0, \frac{1}{4k}]$. Since $\hat{W}_0(k) = 0$, equation (B.2.3) follows for all $r \in [0, \frac{1}{4k}]$. On the one hand, since this holds in particular for $r = \frac{1}{4k}$ and $\frac{\mathrm{d}}{\mathrm{d}r} \hat{W}_r(1) \ge 0$ for all $r \le \frac{1}{4}$ we have $\hat{W}_r(1) \ge \hat{W}_{\frac{1}{4k}}(1) \ge \hat{W}_{\frac{1}{4k}}(k) = \frac{2}{\pi k}$ for all $r \in [\frac{1}{4k}, \frac{1}{4}]$. On the other hand, $\hat{W}_r(k) \le \frac{2}{\pi k}$. Therefore the inequality (B.2.3) extends to all $r \in [0, \frac{1}{4}]$. By a symmetry argument one can see that it even holds for all $r \in [0, \frac{1}{2}]$. $\square$

Theorem B.2.3. *If $\frac{2}{\pi q} \le 2r - \frac{1}{\pi} \sin(2\pi r)$, the largest eigenvalue of the linearization of (5.3.5) with $\lambda = \mu = 0$ around a q-twisted state is attained for $k = q$, i.e., $\max_k c_1(q, k, (r, 0, 0)) = c_1(q, q, (r, 0, 0))$.*

Proof. Let $k \in \mathbb{N}$, $k \ne q$ be fixed and $r \in [0, \frac{1}{2}]$, $q \in \mathbb{N}$ such that the assumption in the theorem is fulfilled. Then,

$$\begin{aligned}
\hat{W}_r(q+k) - \hat{W}_r(2q) &\le \frac{2}{\pi} \left(\frac{1}{q+k} + \frac{1}{2q} \right) \\
&\le \frac{4}{\pi q} \\
&\le 4r - \frac{2}{\pi} \sin(2\pi r) \\
&= \hat{W}_r(0) - \hat{W}_r(1).
\end{aligned}$$

since $k - q \in \mathbb{Z} \setminus \{0\}$, we obtain by Lemma B.2.2

$$\hat{W}_r(q+k) - \hat{W}_r(2q) \le \hat{W}_r(0) - \hat{W}_r(k-q).$$

After rearranging this inequality and subtracting $2\hat{W}_r(q)$ to both sides it reads as

$$\hat{W}_r(2q) + \hat{W}_r(0) - 2\hat{W}_r(q) \ge \hat{W}_r(q+k) + \hat{W}_r(k-q) - 2\hat{W}_r(q).$$

This is equivalent to $c_1(q, q, (r, 0, 0)) \ge c_1(q, k, (r, 0, 0))$ for all $k \ne q$. Thus, the proof is complete. $\square$

B.2.3 γ Ratio in the Attractive Kuramoto Model

Here, we consider the bifurcation in the attractive Kuramoto model studied in Section 5.5.1. We show that $\gamma_1/\gamma_2 > 0$ when the q-twisted state looses its stability. To do this, we assume the following statements, which mainly follow from an analysis in [177]:

- At $r = r_0$ the first eigenvalue $c_1(q, 1, (r, 0, 0))$ passes through 0 from below when increasing r. Moreover, at the bifurcation the other eigenvalues are negative, i.e., $c_1(q, \ell, (r_0, 0, 0)) < 0$ for all $\ell \geq 2$.

- $c_1(q + 1, 1, (r_0, 0, 0)) > 0$.

From the first statement, it immediately follows that $\gamma_2 > 0$. It remains to show that $\gamma_1 > 0$. In particular, using the abbreviations from Appendix B.1 and $p_0 = (r_0, 0, 0)$, it follows from these statements that

$$c_1(q, 1, p_0) = \frac{1}{4}(\hat{W}_{r_0}(q-1) - 2\hat{W}_{r_0}(q) + \hat{W}_{r_0}(q+1)) = 0 \tag{B.2.4}$$

$$c_1(q, 2, p_0) = \frac{1}{4}(\hat{W}_{r_0}(q-2) - 2\hat{W}_{r_0}(q) + \hat{W}_{r_0}(q+2)) < 0 \tag{B.2.5}$$

$$c_1(q+1, 1, p_0) = \frac{1}{4}(\hat{W}_{r_0}(q) - 2\hat{W}_{r_0}(q+1) + \hat{W}_{r_0}(q+2)) > 0 \tag{B.2.6}$$

Using (B.2.4) we then get

$$16c_5(q, 1, p_0) = \hat{W}_{r_0}(q-2) - 4\hat{W}_{r_0}(q-1) + 6\hat{W}_{r_0}(q) - 4\hat{W}_{r_0}(q+1) + \hat{W}_{r_0}(q+2)$$
$$= \hat{W}_{r_0}(q-2) - 2\hat{W}_{r_0}(q) + \hat{W}_{r_0}(q+2) =: q_1.$$

Moreover, we note that

$$c_2(q, 1, p_0) = c_3(q, 2, 1, p_0)$$
$$= -\hat{W}_{r_0}(q-2) + 2\hat{W}_{r_0}(q-1) - 2\hat{W}_{r_0}(q+1) + \hat{W}_{r_0}(q+2) =: q_2.$$

Then, we obtain

$$32\gamma_1 = 16\left(c_5(q, 1, p_0) - \frac{c_2(q, 1, p_0)c_3(q, 2, 1, p_0)}{c_1(q, 2, p_0)}\right)$$
$$= q_1 - \frac{q_2^2}{q_1}$$
$$= \frac{1}{q_1}(q_1 + q_2)(q_1 - q_2).$$

By (B.2.5) we have $q_1 < 0$. Furthermore, using (B.2.4) and (B.2.6) we obtain

$$
\begin{aligned}
q_1 + q_2 &= 2(\hat{W}_{r_0}(q-1) - \hat{W}_{r_0}(q) - \hat{W}_{r_0}(q+1) + \hat{W}_{r_0}(q+2)) \\
&= 2(\hat{W}_{r_0}(q) - 2\hat{W}_{r_0}(q+1) + \hat{W}_{r_0}(q+2)) \\
&> 0.
\end{aligned}
$$

Consequently, $q_2 > 0$. Thus, we conclude $q_1 < 0$, $q_1 + q_2 > 0$ and $q_1 - q_2 < 0$ and therefore $\gamma_1 > 0$.

B.3 Differentiability of the Right-Hand Side

In this section we show that F is indeed Fréchet differentiable. We give the operator that represents the Fréchet derivative but only show this without higher-order interactions, i.e., when $\lambda = \mu = 0$, since that does not complicate but only lengthen the calculations.

We claim, that the n-th Fréchet derivative of $F(\Psi, p)$ around a state $\tilde{\Psi}$ is given by a n-linear operator $A^{\tilde{\Psi}} \colon (H_0^1)^n \to H_0^1$ with

$$
\begin{aligned}
&(A^{\tilde{\Psi}}[\eta_1, \dots, \eta_n])(x) \\
&= \int_{\mathbb{S}} W_r(x-y) \prod_{i=1}^{n} (\eta_i(y) - \eta_i(x)) \sin^{[n]}(\tilde{\Psi}(y) - \tilde{\Psi}(x)) \, \mathrm{d}y \\
&\quad - \int_{\mathbb{S}} W_r(y) \prod_{i=1}^{n} \eta_i(y) \sin^{[n]}(\tilde{\Psi}(y)) \, \mathrm{d}y \\
&\quad + \lambda \left[\int_{\mathbb{S}} \int_{\mathbb{S}} W_r(z+y-2x) \prod_{i=1}^{n} (\eta_i(z) + \eta_i(y) - 2\eta_i(x)) \right. \\
&\quad\quad\quad \cdot \sin^{[n]}(\tilde{\Psi}(z) + \tilde{\Psi}(y) - 2\tilde{\Psi}(x)) \, \mathrm{d}y\mathrm{d}z \\
&\quad\quad \left. - \int_{\mathbb{S}} \int_{\mathbb{S}} W_r(z+y) \prod_{i=1}^{n} (\eta_i(z) + \eta_i(y)) \sin^{[n]}(\tilde{\Psi}(z) + \tilde{\Psi}(y)) \, \mathrm{d}y\mathrm{d}z \right] \\
&\quad + \mu \left[\int_{\mathbb{S}} \int_{\mathbb{S}} \int_{\mathbb{S}} W_r(z-y+w-x) \prod_{i=1}^{n} (\eta_i(z) - \eta_i(y) + \eta_i(w) - \eta_i(x)) \right. \\
&\quad\quad\quad \cdot \sin^{[n]}(\tilde{\Psi}(z) - \tilde{\Psi}(y) + \tilde{\Psi}(w) - \tilde{\Psi}(x)) \, \mathrm{d}w\mathrm{d}y\mathrm{d}z \\
&\quad\quad \left. - \int_{\mathbb{S}} \int_{\mathbb{S}} \int_{\mathbb{S}} W_r(z-y+w) \prod_{i=1}^{n} (\eta_i(z) - \eta_i(y) + \eta_i(w)) \right. \\
&\quad\quad\quad \left. \cdot \sin^{[n]}(\tilde{\Psi}(z) - \tilde{\Psi}(y) + \tilde{\Psi}(w)) \, \mathrm{d}w\mathrm{d}y\mathrm{d}z \right],
\end{aligned}
$$

where $\sin^{[n]}$ denotes the n-th derivative of sin.

The main estimations needed to prove that this is indeed a n-linear operator and the n-th Fréchet derivative of F are

$$|\eta(y) - \eta(x)|^2 = \left| \int_x^y \partial\eta(z) \, \mathrm{d}z \right|^2 \leq \int_{\mathbb{S}} \partial\eta(z)^2 \, \mathrm{d}z = \|\partial\eta\|_{L^2}^2 , \tag{B.3.1}$$

for the part without higher-order interactions and

$$|\eta(z) + \eta(y) - 2\eta(x)|^2 \leq 4 \|\partial\eta\|_{L^2}^2 , \tag{B.3.2}$$

$$|\eta(z) - \eta(y) + \eta(w) - \eta(x)|^2 \leq 4 \|\partial\eta\|_{L^2}^2 \tag{B.3.3}$$

for the parts involving higher-order interactions. Due to the similarity of the main estimations (B.3.1),(B.3.2) and (B.3.3) regarding the parts with and without higher-order interactions, respectively, we only consider parts without higher-order interactions in the following. That means we only proof the boundedness of $A^{\tilde{\Psi}}$ and its derivative property for $\lambda = \mu = 0$.

B.3.1 Boundedness of $A^{\tilde{\Psi}}$

First, we show that $A^{\tilde{\Psi}}$ is bounded. To do this, we denote

$$f(x) = \int_{\mathbb{S}} W_r(x - y) \prod_{i=1}^n (\eta_i(y) - \eta_i(x)) \sin^{[n]}(\tilde{\Psi}(y) - \tilde{\Psi}(x)) \, \mathrm{d}y$$

and

$$g(x) \equiv \int_{\mathbb{S}} W_r(y) \prod_{i=1}^n \eta_i(y) \sin^{[n]}(\tilde{\Psi}(y)) \, \mathrm{d}y,$$

which is actually independent of x. It then follows that

$$(A^{\tilde{\Psi}}[\eta_1, \ldots, \eta_n])(x) = f(x) - g(x).$$

Using $\left\|\sin^{[n]}\right\|_\infty \leq 1$ and $\|W_r\|_\infty \leq 1$ we estimate

$$\|f\|_{L^2}^2 = \int_{\mathbb{S}} \left(\int_{\mathbb{S}} W_r(x - y) \prod_{i=1}^n (\eta_i(y) - \eta_i(x)) \sin^{[n]}(\tilde{\Psi}(y) - \tilde{\Psi}(x)) \, \mathrm{d}y \right)^2 \mathrm{d}x$$

$$\leq \int_{\mathbb{S}} \int_{\mathbb{S}} \prod_{i=1}^n (\eta_i(y) - \eta_i(x))^2 \, \mathrm{d}y\mathrm{d}x$$

$$= \prod_{i=1}^n \|\partial\eta_i\|_{L^2}^2 .$$

Moreover, a similar estimation yields

$$\|g\|_{L^2}^2 \le \prod_{i=1}^n \|\eta_i\|_{L^2}^2 \,.$$

Further, we calculate the derivative of f:

$$D_x f(x) = D_x \left(\int_{x-r}^{x+r} \prod_{i=1}^n (\eta_i(y) - \eta_i(x)) \sin^{[n]}(\tilde{\Psi}(y) - \tilde{\Psi}(x)) \; \mathrm{d}y \right)$$

$$= \prod_{i=1}^n (\eta_i(x+r) - \eta_i(x)) \sin^{[n]}(\tilde{\Psi}(x+r) - \tilde{\Psi}(x))$$

$$- \prod_{i=1}^n (\eta_i(x-r) - \eta_i(x)) \sin^{[n]}(\tilde{\Psi}(x-r) - \tilde{\Psi}(x))$$

$$+ \int_{x-r}^{x+r} \sum_{j=1}^n \prod_{\substack{i=1 \\ i \ne j}}^n (\eta_i(y) - \eta_i(x))(-\partial \eta_j(x)) \sin^{[n]}(\tilde{\Psi}(y) - \tilde{\Psi}(x)) \; \mathrm{d}y$$

$$+ \int_{x-r}^{x+r} \prod_{i=1}^n (\eta_i(y) - \eta_i(x)) \sin^{[n+1]}(\tilde{\Psi}(y) - \tilde{\Psi}(x))(-\partial \tilde{\Psi}(x)) \; \mathrm{d}y.$$

To simplify the notation, let us write

$$h_1(x) = \prod_{i=1}^n (\eta_i(x+r) - \eta_i(x)) \sin^{[n]}(\tilde{\Psi}(x+r) - \tilde{\Psi}(x))$$

$$h_2(x) = -\prod_{i=1}^n (\eta_i(x-r) - \eta_i(x)) \sin^{[n]}(\tilde{\Psi}(x-r) - \tilde{\Psi}(x))$$

and

$$u_j(x) = \int_{x-r}^{x+r} \prod_{\substack{i=1 \\ i \ne j}}^n (\eta_i(y) - \eta_i(x))(-\partial \eta_j(x)) \sin^{[n]}(\tilde{\Psi}(y) - \tilde{\Psi}(x)) \; \mathrm{d}y,$$

$$q(x) = \int_{x-r}^{x+r} \prod_{i=1}^n (\eta_i(y) - \eta_i(x)) \sin^{[n+1]}(\tilde{\Psi}(y) - \tilde{\Psi}(x))(-\partial \tilde{\Psi}(x)) \; \mathrm{d}y$$

Then, $D_x(A^{\tilde{\Psi}}[\eta_1, \dots, \eta_n])(x) = D_x f(x) = h_1(x) + h_2(x) + \sum_{j=1}^n u_j(x) + q(x)$. An estimation shows that

$$\|h_1\|_{L^2}^2 = \int_{\mathbb{S}} \left[\prod_{i=1}^n (\eta_i(x+r) - \eta_i(x)) \sin^{[n]}(\tilde{\Psi}(x+r) - \tilde{\Psi}(x)) \right]^2 \; \mathrm{d}x$$

$$\leq \int_{\mathbb{S}} \prod_{i=1}^{n} (\eta_i(x+r) - \eta_i(x))^2 \, \mathrm{d}x$$

$$\leq \prod_{i=1}^{n} \|\partial \eta_i\|_{L^2}^2 \, .$$

Similarly, we obtain $\|h_2\|_{L^2}^2 \leq \prod_{i=1}^{n} \|\partial \eta_i\|_{L^2}^2$. Moreover,

$$\|u_j\|_{L^2}^2 = \int_{\mathbb{S}} \left(\int_{x-r}^{x+r} \prod_{\substack{i=1 \\ i \neq j}}^{n} (\eta_i(y) - \eta_i(x))(-\partial \eta_j(x)) \sin^{[n]}(\tilde{\Psi}(y) - \tilde{\Psi}(x)) \, \mathrm{d}y \right)^2 \, \mathrm{d}x$$

$$\leq \int_{\mathbb{S}} \int_{\mathbb{S}} \prod_{\substack{i=1 \\ i \neq j}}^{n} \|\partial \eta_i\|_{L^2}^2 \, (\partial \eta_j(x))^2 \, \mathrm{d}y \, \mathrm{d}x$$

$$= \prod_{i=1}^{n} \|\partial \eta_i\|_{L^2}^2$$

and

$$\|q\|_{L^2}^2 = \int_{\mathbb{S}} \left(\int_{x-r}^{x+r} \prod_{i=1}^{n} (\eta_i(y) - \eta_i(x)) \sin^{[n+1]}(\tilde{\Psi}(y) - \tilde{\Psi}(x))(-\partial \tilde{\Psi}(x)) \, \mathrm{d}y \right)^2 \, \mathrm{d}x$$

$$\leq \int_{\mathbb{S}} \int_{\mathbb{S}} \prod_{i=1}^{n} \|\partial \eta_i\|_{L^2}^2 \, (\partial \tilde{\Psi}(x))^2 \, \mathrm{d}y \, \mathrm{d}x$$

$$\leq \prod_{i=1}^{n} \|\partial \eta_i\|_{L^2}^2 \left\| \partial \tilde{\Psi} \right\|_{L^2}^2 \, .$$

All together, we obtain

$$\left\| A^{\tilde{\Psi}}[\eta_1, \ldots, \eta_n] \right\|_{H^1}^2$$

$$= \left\| A^{\tilde{\Psi}}[\eta_1, \ldots, \eta_n] \right\|_{L^2}^2 + \left\| D_x(A^{\tilde{\Psi}}[\eta_1, \ldots, \eta_n]) \right\|_{L^2}^2$$

$$= \|f - g\|_{L^2}^2 + \left\| h_1 + h_2 + \sum_{j=1}^{n} u_j + q \right\|_{L^2}^2$$

$$\leq 2 \|f\|_{L^2}^2 + 2 \|g\|_{L^2}^2$$

$$+ (n+3) \left(\|h_1\|_{L^2}^2 + \|h_2\|_{L^2}^2 + \sum_{j=1}^{n} \|u_j\|_{L^2}^2 + \|q\|_{L^2}^2 \right)$$

$$\leq 2 \prod_{i=1}^{n} \|\partial \eta_i\|_{L^2}^2 + 2 \prod_{i=1}^{n} \|\eta_i\|_{L^2}^2$$

$$+ (n+3) \left((n+2) \prod_{i=1}^{n} \|\partial \eta_i\|_{L^2}^2 + \prod_{i=1}^{n} \|\partial \eta_i\|_{L^2}^2 \left\| \partial \tilde{\Psi} \right\|_{L^2}^2 \right)$$

$$\leq 4 \prod_{i=1}^{n} \|\eta_i\|_{H^1}^2$$

$$+ (n+3) \left((n+2) \prod_{i=1}^{n} \|\eta_i\|_{H^1}^2 + \prod_{i=1}^{n} \|\eta_i\|_{H^1}^2 \left\| \tilde{\Psi} \right\|_{H^1}^2 \right)$$

$$\leq c \prod_{i=1}^{n} \|\eta_i\|_{H^1}^2 \,,$$

where c is a constant that can be chosen as

$$c = 4 + (n+3) \left(n + 2 + \left\| \tilde{\Psi} \right\|_{H^1}^2 \right).$$

Even though some estimations are far from being tight, this proves that $A^{\tilde{\Psi}}[\eta_1, \ldots, \eta_n]$ is a bounded n-linear operator.

B.3.2   Derivative Property

To inductively show that $A^{\tilde{\Psi}}[\eta_1, \ldots, \eta_n]$ is the n-th Fréchet derivative of F around $\tilde{\Psi}$ we need to confirm that

$$\lim_{\|\eta_n\|_{H^1} \to 0} \frac{1}{\|\eta_n\|_{H^1}} \left\| A^{\tilde{\Psi}+\eta_n}[\eta_1, \ldots, \eta_{n-1}] - A^{\tilde{\Psi}}[\eta_1, \ldots, \eta_{n-1}] - A^{\tilde{\Psi}}[\eta_1, \ldots, \eta_n] \right\|_{H^1} = 0.$$

$$(\text{B.3.4})$$

To achieve that, we first rewrite

$$A^{\tilde{\Psi}+\eta_n}[\eta_1, \ldots, \eta_{n-1}] - A^{\tilde{\Psi}}[\eta_1, \ldots, \eta_{n-1}] - A^{\tilde{\Psi}}[\eta_1, \ldots, \eta_n]$$

$$= \int_{\mathbb{S}} W_r(x-y) \prod_{i=1}^{n-1} (\eta_i(y) - \eta_i(x)) \sin^{[n-1]}(\tilde{\Psi}(y) - \tilde{\Psi}(x) + \eta_n(y) - \eta_n(x)) \, \mathrm{d}y$$

$$- \int_{\mathbb{S}} W_r(y) \prod_{i=1}^{n-1} \eta_i(y) \sin^{[n-1]}(\tilde{\Psi}(y) + \eta_n(y)) \, \mathrm{d}y$$

$$- \int_{\mathbb{S}} W_r(x-y) \prod_{i=1}^{n-1} (\eta_i(y) - \eta_i(x)) \sin^{[n-1]}(\tilde{\Psi}(y) - \tilde{\Psi}(x)) \, \mathrm{d}y$$

$$+ \int_{\mathbb{S}} W_r(y) \prod_{i=1}^{n-1} \eta_i(y) \sin^{[n-1]}(\tilde{\Psi}(y)) \, \mathrm{d}y$$

$$- \int_{\mathbb{S}} W_r(x-y) \prod_{i=1}^{n} (\eta_i(y) - \eta_i(x)) \sin^{[n]}(\tilde{\Psi}(y) - \tilde{\Psi}(x)) \, \mathrm{d}y$$

$$+ \int_{\mathbb{S}} W_r(y) \prod_{i=1}^{n} \eta_i(y) \sin^{[n]}(\tilde{\Psi}(y)) \, \mathrm{d}y$$

$$= \int_{\mathbb{S}} W_r(x-y) \prod_{i=1}^{n-1} (\eta_i(y) - \eta_i(x))$$

$$\cdot \left[\sin^{[n-1]}(\tilde{\Psi}(y) - \tilde{\Psi}(x) + \eta_n(y) - \eta_n(x)) - \sin^{[n-1]}(\tilde{\Psi}(y) - \tilde{\Psi}(x)) \right. \tag{B.3.5}$$

$$\left. - (\eta_n(y) - \eta_n(x)) \sin^{[n]}(\tilde{\Psi}(y) - \tilde{\Psi}(x)) \right] \, \mathrm{d}y$$

$$- \int_{\mathbb{S}} W_r(y) \prod_{i=1}^{n-1} \eta_i(y) \left[\sin^{[n-1]}(\tilde{\Psi}(y) + \eta_n(y)) \right.$$

$$\left. - \sin^{[n-1]}(\tilde{\Psi}(y)) - \eta_n(y) \sin^{[n]}(\tilde{\Psi}(y)) \right] \, \mathrm{d}y \tag{B.3.6}$$

Now, we introduce the notation $g_1(x)$ for (B.3.5) and $g_2(x)$ for (B.3.6) such that we recover

$$A^{\tilde{\Psi}+\eta_n}[\eta_1, \ldots, \eta_{n-1}] - A^{\tilde{\Psi}}[\eta_1, \ldots, \eta_{n-1}] - A^{\tilde{\Psi}}[\eta_1, \ldots, \eta_n] = g_1(x) + g_2(x).$$

Note that by Taylor's Theorem we have

$$f(x_0 + a) = f(x_0) + a f'(x_0) + \frac{f''(\xi)}{2} a^2$$

for each twice continuously differentiable function f and some $\xi \in (x_0, x_0 + a)$ if $a > 0$ and $\xi \in (x - 0 - a, x_0)$ if $a < 0$. By applying this theorem to $f = \sin^{[n-1]}$ it follows that

$$| \sin^{[n-1]}(x_0 + a) - \sin^{[n-1]}(x_0) - a \sin^{[n]}(x_0) | \leq \frac{a^2}{2}. \tag{B.3.7}$$

Using this inequality we can estimate

$$\|g_1\|_{L^2}^2 = \int_{\mathbb{S}} \left\{ \int_{\mathbb{S}} W_r(x-y) \prod_{i=1}^{n-1} (\eta_i(y) - \eta_i(x)) \right.$$

$$\cdot \left[\sin^{[n-1]}(\tilde{\Psi}(y) - \tilde{\Psi}(x) + \eta_n(y) - \eta_n(x)) - \sin^{[n-1]}(\tilde{\Psi}(y) - \tilde{\Psi}(x)) \right.$$

$$- (\eta_n(y) - \eta_n(x)) \sin^{[n]}(\tilde{\Psi}(y) - \tilde{\Psi}(x)) \Big] \, \mathrm{d}y \Bigg\}^2 \, \mathrm{d}x$$

$$\leq \prod_{i=1}^{n-1} \|\partial \eta_i\|_{L^2}^2 \int_{\mathbb{S}} \left(\int_{\mathbb{S}} \frac{1}{2} (\eta_n(y) - \eta_n(x))^2 \, \mathrm{d}y \right)^2 \mathrm{d}x$$

$$= \frac{1}{4} \prod_{i=1}^{n-1} \|\partial \eta_i\|_{L^2}^2 \, \|\partial \eta_n\|_{L^2}^4 \, .$$

Furthermore, also by using (B.3.7), we obtain

$$\|g_2\|_{L^2}^2 = \int_{\mathbb{S}} \Bigg\{ \int_{\mathbb{S}} W_r(y) \prod_{i=1}^{n-1} \eta_i(y) \Big[\sin^{[n-1]}(\tilde{\Psi}(y) + \eta_n(y))$$

$$- \sin^{[n-1]}(\tilde{\Psi}(y)) - \eta_n(y) \sin^{[n]}(\tilde{\Psi}(y)) \Big] \, \mathrm{d}y \Bigg\}^2 \, \mathrm{d}x$$

$$\leq \prod_{i=1}^{n-1} \|\eta_i\|_{L^2}^2 \int_{\mathbb{S}} \left\{ \int_{\mathbb{S}} \frac{1}{2} |\eta_n(y)|^2 \, \mathrm{d}y \right\}^2 \mathrm{d}x$$

$$= \frac{1}{4} \prod_{i=1}^{n-1} \|\eta_i\|_{L^2}^2 \, \|\eta_n\|_{L^2}^4 \, .$$

Now, we calculate the derivative

$$D_x(A^{\tilde{\Psi}+\eta_n}[\eta_1, \ldots, \eta_{n-1}] - A^{\tilde{\Psi}}[\eta_1, \ldots, \eta_{n-1}] - A^{\tilde{\Psi}}[\eta_1, \ldots, \eta_n])$$

$$= D_x g_1(x)$$

$$= D_x \left(\int_{x-r}^{x+r} \prod_{i=1}^{n-1} (\eta_i(y) - \eta_i(x)) \Big[\sin^{[n-1]}(\tilde{\Psi}(y) - \tilde{\Psi}(x) + \eta_n(y) - \eta_n(x)) \right.$$

$$\left. - \sin^{[n-1]}(\tilde{\Psi}(y) - \tilde{\Psi}(x)) - (\eta_n(y) - \eta_n(x)) \sin^{[n]}(\tilde{\Psi}(y) - \tilde{\Psi}(x)) \Big] \, \mathrm{d}y \right)$$

$$= \prod_{i=1}^{n-1} (\eta_i(x+r) - \eta_i(x)) \Big[- \sin^{[n-1]}(\tilde{\Psi}(x+r) - \tilde{\Psi}(x))$$

$$+ \sin^{[n-1]}(\tilde{\Psi}(x+r) - \tilde{\Psi}(x) + \eta_n(x+r) - \eta_n(x)) \tag{B.3.8}$$

$$- (\eta_n(x+r) - \eta_n(x)) \sin^{[n]}(\tilde{\Psi}(x+r) - \tilde{\Psi}(x)) \Big]$$

$$- \prod_{i=1}^{n-1} (\eta_i(x-r) - \eta_i(x)) \Big[- \sin^{[n-1]}(\tilde{\Psi}(x-r) - \tilde{\Psi}(x))$$

$$+ \sin^{[n-1]}(\tilde{\Psi}(x-r) - \tilde{\Psi}(x) + \eta_n(x-r) - \eta_n(x)) \tag{B.3.9}$$

$$- (\eta_n(x-r) - \eta_n(x)) \sin^{[n]}(\tilde{\Psi}(x-r) - \tilde{\Psi}(x)) \Big]$$

$$+ \sum_{j=1}^{n-1} \int_{x-r}^{x+r} \prod_{\substack{i=1 \\ i \neq j}}^{n-1} (\eta_i(y) - \eta_i(x))(-\partial \eta_j(x))$$

$$\cdot \Big[\sin^{[n-1]}(\tilde{\Psi}(y) - \tilde{\Psi}(x) + \eta_n(y) - \eta_n(x)) - \sin^{[n-1]}(\tilde{\Psi}(y) - \tilde{\Psi}(x))$$

$$- (\eta_n(y) - \eta_n(x)) \sin^{[n]}(\tilde{\Psi}(y) - \tilde{\Psi}(x)) \Big] \, \mathrm{d}y \tag{B.3.10}$$

$$+ \int_{x-r}^{x+r} \prod_{i=1}^{n-1} (\eta_i(y) - \eta_i(x))$$

$$\cdot \Big[\sin^{[n]}(\tilde{\Psi}(y) - \tilde{\Psi}(x) + \eta_n(y) - \eta_n(x))(-\partial \tilde{\Psi}(x) - \partial \eta_n(x))$$

$$- \sin^{[n]}(\tilde{\Psi}(y) - \tilde{\Psi}(x))(-\partial \tilde{\Psi}(x))$$

$$+ (\partial \eta_n(x)) \sin^{[n]}(\tilde{\Psi}(y) - \tilde{\Psi}(x))$$

$$- (\eta_n(y) - \eta_n(x)) \sin^{[n+1]}(\tilde{\Psi}(y) - \tilde{\Psi}(x))(-\partial \tilde{\Psi}(x)) \Big] \, \mathrm{d}y. \tag{B.3.11}$$

We use the abbreviations $u_1(x)$ for the summand (B.3.8), $u_2(x)$ for the summand (B.3.9), $u_3^j(x)$ for the j-th summand in (B.3.10) and $u_4(x)$ for the summand (B.3.11) such that $D_x(A^{\tilde{\Psi}+\eta_n}[\eta_1, \ldots, \eta_{n-1}] - A^{\tilde{\Psi}}[\eta_1, \ldots, \eta_{n-1}] - A^{\tilde{\Psi}}[\eta_1, \ldots, \eta_n]) = u_1(x) + u_2(x) + \sum_j u_3^j(x) + u_4(x)$. Further, we split u_4 into $u_{4,1}(x) + u_{4,2}(x)$ as

$$u_{4,1}(x) = \int_{x-r}^{x+r} \prod_{i=1}^{n-1} (\eta_i(y) - \eta_i(x))(-\partial \tilde{\Psi}(x)) \Big[\sin^{[n]}(\tilde{\Psi}(y) - \tilde{\Psi}(x) + \eta_n(y) - \eta_n(x))$$

$$- \sin^{[n]}(\tilde{\Psi}(y) - \tilde{\Psi}(x)) - (\eta_n(y) - \eta_n(x)) \sin^{[n+1]}(\tilde{\Psi}(y) - \tilde{\Psi}(x)) \Big] \, \mathrm{d}y$$

$$u_{4,2}(x) = \int_{x-r}^{x+r} \prod_{i=1}^{n-1} (\eta_i(y) - \eta_i(x))(-\partial \eta_n(x)) \Big[\sin^{[n]}(\tilde{\Psi}(y) - \tilde{\Psi}(x) + \eta_n(y) - \eta_n(x))$$

$$- \sin^{[n]}(\tilde{\Psi}(y) - \tilde{\Psi}(x)) \Big] \, \mathrm{d}y$$

Then, again by using Taylor's theorem, we can estimate

$$\|u_1\|_{L^2}^2 \leq \prod_{i=1}^{n-1} \|\partial \eta_i\|_{L^2}^2 \int_{\mathbb{S}} \Big(\sin^{[n-1]}(\tilde{\Psi}(x+r) - \tilde{\Psi}(x) + \eta_n(x+r) - \eta_n(x))$$

$$- \sin^{[n-1]}(\tilde{\Psi}(x+r) - \tilde{\Psi}(x))$$

$$- (\eta_n(x+r) - \eta_n(x)) \sin^{[n]}(\tilde{\Psi}(x+r) - \tilde{\Psi}(x)) \Big)^2 \, \mathrm{d}x$$

$$\leq \prod_{i=1}^{n-1} \|\partial \eta_i\|_{L^2}^2 \int_{\mathbb{S}} \Big(\frac{1}{2}(\eta_n(x+r) - \eta_n(x))^2 \Big)^2 \, \mathrm{d}x$$

$$\leq \frac{1}{4} \prod_{i=1}^{n-1} \|\partial\eta_i\|_{L^2}^2 \|\partial\eta_n\|_{L^2}^4 \,.$$

Similarly, $\|u_2\|_{L^2}^2 \leq \frac{1}{4} \prod_{i=1}^{n-1} \|\partial\eta_i\|_{L^2}^2 \|\partial\eta_n\|_{L^2}^4$. Moreover,

$$
\begin{aligned}
\left\|u_3^j\right\|_{L^2}^2 &\leq \prod_{\substack{i=1\\i\neq j}}^{n-1} \|\partial\eta_i\|_{L^2}^2 \int_{\mathbb{S}}\int_{\mathbb{S}} (\partial\eta_j(x))^2 \Big[\sin^{[n-1]}(\tilde{\Psi}(y)-\tilde{\Psi}(x)+\eta_n(y)-\eta_n(x)) \\
&\qquad - \sin^{[n-1]}(\tilde{\Psi}(y)-\tilde{\Psi}(x)) - (\eta_n(y)-\eta_n(x))\sin^{[n]}(\tilde{\Psi}(y)-\tilde{\Psi}(x)) \Big]^2 \; \mathrm{d}y\mathrm{d}x \\
&\leq \prod_{\substack{i=1\\i\neq j}}^{n-1} \|\partial\eta_i\|_{L^2}^2 \int_{\mathbb{S}}\int_{\mathbb{S}} (\partial\eta_j(x))^2 \left[\frac{1}{2}(\eta_n(y)-\eta_n(x))^2\right]^2 \; \mathrm{d}y\mathrm{d}x \\
&\leq \frac{1}{4} \prod_{\substack{i=1\\i\neq j}}^{n-1} (\|\partial\eta_i\|_{L^2}^2) \|\partial\eta_n\|_{L^2}^4 \|\partial\eta_j\|_{L^2}^2 \\
&= \frac{1}{4} \prod_{i=1}^{n-1} (\|\partial\eta_i\|_{L^2}^2) \|\partial\eta_n\|_{L^2}^4
\end{aligned}
$$

and

$$
\begin{aligned}
\|u_{4,1}\|_{L^2}^2 &\leq \prod_{i=1}^{n-1} \|\partial\eta_i\|_{L^2}^2 \int_{\mathbb{S}}\int_{\mathbb{S}} \left((-\partial\tilde{\Psi}(x))\frac{1}{2}(\eta_n(y)-\eta_n(x))^2\right)^2 \; \mathrm{d}y\mathrm{d}x \\
&\leq \frac{1}{4} \prod_{i=1}^{n-1} \|\partial\eta_i\|_{L^2}^2 \|\partial\eta_n\|_{L^2}^4 \left\|\partial\tilde{\Psi}\right\|_{L^2}^2, \\
\|u_{4,2}\|_{L^2}^2 &\leq \prod_{i=1}^{n-1} \|\partial\eta_i\|_{L^2}^2 \int_{\mathbb{S}}\int_{\mathbb{S}} [(-\partial\eta_n(x))(\eta_n(y)-\eta_n(x))]^2 \; \mathrm{d}y\mathrm{d}x \\
&\leq \prod_{i=1}^{n-1} \|\partial\eta_i\|_{L^2}^2 \|\partial\eta_n\|_{L^2}^4
\end{aligned}
$$

Finally, we can combine the estimations to obtain

$$
\begin{aligned}
&\left\|A^{\tilde{\Psi}+\eta_n}[\eta_1,\ldots,\eta_{n-1}] - A^{\tilde{\Psi}}[\eta_1,\ldots,\eta_{n-1}] - A^{\tilde{\Psi}}[\eta_1,\ldots,\eta_n]\right\|_{H^1}^2 \\
&\leq \left\|A^{\tilde{\Psi}+\eta_n}[\eta_1,\ldots,\eta_{n-1}] - A^{\tilde{\Psi}}[\eta_1,\ldots,\eta_{n-1}] - A^{\tilde{\Psi}}[\eta_1,\ldots,\eta_n]\right\|_{L^2}^2 \\
&\quad + \left\|D_x(A^{\tilde{\Psi}+\eta_n}[\eta_1,\ldots,\eta_{n-1}] - A^{\tilde{\Psi}}[\eta_1,\ldots,\eta_{n-1}] - A^{\tilde{\Psi}}[\eta_1,\ldots,\eta_n])\right\|_{L^2}^2
\end{aligned}
$$

$$\leq \|g_1 + g_2\|_{L^2}^2 + \left\| u_1 + u_2 + \sum_{j=1}^{n-1} u_3^j + u_{4,1} + u_{4,2} \right\|_{L^2}^2$$

$$\leq 2(\|g_1\|_{L^2}^2 + \|g_2\|_{L^2}^2)$$
$$+ (n+3)\left(\|u_1\|_{L^2}^2 + \|u_2\|_{L^2}^2 + \sum_{j=1}^{n-1} \|u_3^j\|_{L^2}^2 + \|u_{4,1}\|_{L^2}^2 + \|u_{4,2}\|_{L^2}^2 \right)$$

$$\leq \prod_{i=1}^{n-1} \|\eta_i\|_{H^1}^2 \|\eta_n\|_{H^1}^4$$
$$+ (n+3)\left(\frac{n+6}{4} \prod_{i=1}^{n-1} \|\eta_i\|_{H^1}^2 \|\eta_n\|_{H^1}^4 + \frac{1}{4} \prod_{i=1}^{n-1} \|\eta_i\|_{H^1}^2 \|\eta_n\|_{H^1}^4 \left\| \tilde{\Psi} \right\|_{H^1} \right)$$
$$\leq c \|\eta_n\|_{H^1}^4 ,$$

where c is a constant that can be chosen to be

$$c = \prod_{i=1}^{n-1} \|\eta_i\|_{H^1}^2 \left(1 + (n+3)\left(\frac{n+6}{4} + \frac{1}{4} \left\| \tilde{\Psi} \right\|_{H^1} \right) \right)$$

This confirms (B.3.4) and therefore concludes this section.

Appendix C

Additional Illustrations of Community Integration Algorithms

This chapter is based on two publications [37, 36] which are both joint work with Mechthild Thalhammer and Christian Kuehn. In particular, the technical parts are taken from the publication [37] of which I am the main author. The comparison of community detection algorithms is based on [36] of which I am the main author.

C.1 Network Models

In this section we describe the pre-simulation steps (P1)-(P2) and the CIA Evaluation steps (E1)-(E2) in technical detail for several different network models. In a general network model of the form

$$\dot{x}_k = f_k(x_k) + \frac{1}{M} \sum_{l=1}^{M} a_{kl} \ g(x_l, x_k), \quad k = 1, \dots, M \qquad \text{(C.1.1)}$$

the steps (P2) and (E1) are quite abstract and general. When considering a specific network model, the function g is often not just an abstract function but one that exhibits more structure that can be exploited in those two steps. The steps (P1) and (E2), however, do not depend on the specific network model. Even though we have only described (E2) in Section 6.3 for a specific example this step is exactly the same for all other network models. Therefore, we shortly describe the community detection process (P1) in Subsection C.1.1 such that we have covered the steps (P1) and (E2), which are mostly independent of the particular network model. In the following subsections we then do not further touch upon these steps

but only describe (P2) and (E1) for specific network models. In particular, our fast CIAs work on block matrices with dense or fully occupied blocks. We shall explain below, why for illustration purposes, we may assume to illustrate the computation in the easiest case of just one full block. Hence, we assume for the subsections following Subsection C.1.1 that A is a full matrix with $A = (a_{kl})_{k,l=1,\ldots,M}$ and $a_{kl} = 1$ for all k, l. Table C.1 lists several examples of coupling functions of a wide variety of network models from different applications that are of the form (C.1.1); in fact, there are many more application examples having a form identical or very similar to (C.1.1) such as continuous Hopfield-type neural network models or the Hegselmann–Krause model for opinion formation.

Network Model	State Space ($\mathcal{X}$)	Coupling Functions
(DZ)	$\mathbb{R}$	$f_k(x) = f(x) = -\nabla V(x)$ $h(\xi) = \xi$
(K)	$\mathbb{T} = \mathbb{R}/(2\pi\mathbb{Z})$	$f_k(x) = \omega_k$ $h(\xi) = \sin(\xi)$
(CS)	$\mathbb{R}^{2d}$	$f_k(x) = (v, 0)^\top,\ x = (s, v)$ $h(\xi) = K\,(\alpha^2 + \|\hat{s}\|_2^2)^{-\beta}\,(0, \hat{v})^\top,\ \xi = (\hat{s}, \hat{v})$
(V)/(FN)	$\mathbb{R}^2$	$f_k(x) = f(x_1, x_2) = (x_2 - \frac{1}{3}x_1^3 + x_1, -\varepsilon\,x_1)^\top$ $h(\xi) = \xi$

Table C.1: Desai–Zwanzig (DZ), Kuramoto (K), Cucker–Smale (CS), Van-der-Pol (V) as well as FitzHugh–Nagumo (FN) systems are relevant examples for continuous-time dynamical systems that can be cast into the form (6.2.1) with coupling functions $g(x, y) = h(x - y)$.

C.1.1 Community Detection (P1)

In general, our CIAs can quickly evaluate the right-hand side of (C.1.1), when the interaction matrix $A = (a_{kl})_{k,l=1,\ldots,M} \in \{0, 1\}^{M \times M}$ is fully occupied by ones and so all nodes of the underlying graph form one large community. But CIAs can also quickly evaluate the right-hand side if the adjacency matrix has block structure such that the underlying graph is partitioned into smaller communities, within which each node is connected to every other node. Obviously, the adjacency matrices of most networks consist not only of blocks fully occupied by ones, but there may be a zero-entry of A at a position (k, l) that is in a larger block of ones. In other words, there is not always an all-to-all coupling inside communities but two nodes k, l belonging to the same community might be uncoupled (missing

intra-population links). Similarly, there may be a one-entry of A at (k, l) while nodes k and l do not belong to the same block in adjacency matrix A, meaning that two nodes k and l can be coupled even though they do not belong to the same community (additional inter-population links). Our CIA nevertheless assumes that A has block structure, calculates the right-hand side of (C.1.1) using this assumption in step (E1), and corrects this calculation by individually adding or subtracting $g(x_l, x_k)$ depending on whether (k, l) is an additional inter-population link or a missing intra-population link of the graph in step (E2).

In synthetically created benchmark graphs, the communities of the graph, or the block structure of the associated adjacency matrix, respectively, is already known from the construction. However, when dealing with real-world networks, communities first have to be found.

CIAs can quickly evaluate the right-hand side for blocks in A but the evaluation of many summands $g(x_l, x_k)$ is very costly. The aim of a community detection algorithm is to partition the graph into communities such that there are as few missing intra-population links and additional inter-population links as possible. In other words, the matrix S defined in Section 6.3 (see also Figure 6.2) has to be as sparse as possible. It can be seen as a feature of a community detection algorithm to achieve exactly that. However, not all community detection algorithms pursue to optimize on that feature [154]. Apart from existing comparisons of community detection algorithms for numerical simulations from [129, 60, 182], we analyze and compare different community detection algorithms with respect to that feature [36]. In particular, the tested algorithms are GREEDY_MODULARITY [54] from the PYTHON package NETWORKX [84] and the algorithms LOUVAIN [29], RBER_POTS [147, 148], RB_POTS [113, 148], SIGNIFICANCE_COMMUNITIES [171], WALKTRAP [145] from the PYTHON package CDLIB [152].

To compare these algorithms, we create a test scenario with synthetically created networks as follows: First, we consider a block matrix D that consists of four communities and a total of $M = 100$ nodes, as can be seen in Figure 6.2. Then, we choose a parameter $\hat{p} \in [0, .5]$ and create a random matrix $S = (s_{kl})_{k,l=1,\ldots,M}$ by choosing independent sample parameters $\mathfrak{s}_{kl} = 1$ with probability $\hat{p}$ and $\mathfrak{s}_{kl} = 0$ else, for $k, l = 1, \ldots, M$. Then, we define $s_{kl} := \mathfrak{s}_{kl}$ if the nodes k, l belong to different communities and $s_{kl} := -\mathfrak{s}_{kl}$ if k and l belong to the same community, see also matrix S in Figure 6.2. Then, we define the matrix $B := D + S$, such that B has an apparent block structure, see Figure C.1. Next, we create a random permutation $\kappa \colon [M] \to [M]$ and define an adjacency matrix A as $A := P^{\top} B P$, where P is the permutation matrix induced by the permutation κ. This is the adjacency matrix that we feed into all community detection algorithms. The output of these algorithms will be a decomposition of the node set into communities. We then order the nodes such that consecutive nodes are in the same community and
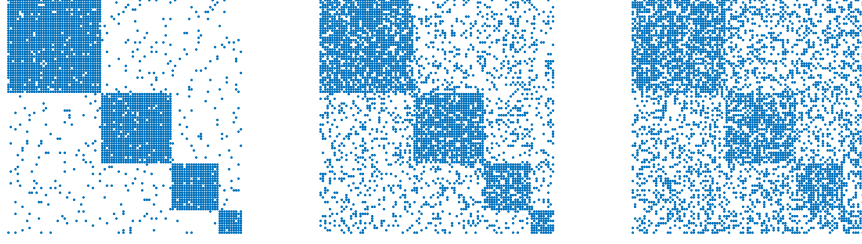
Figure C.1: Illustration of matrices B for different parameters of $\hat{p}$. Here, $\hat{p} = .05, 0.2, 0.3$ from left to right.

nodes, which are in bigger communities, come first. This ordering corresponds to a permutation matrix $\tilde{P}$, such that $\tilde{B} := \tilde{P}A\tilde{P}^\top$ has apparent block structure. The better the performance of the community detection algorithm, the more apparent this block structure should be. Then, we split this matrix $\tilde{B}$ into two matrices $\tilde{D}$ and $\tilde{S}$ such that $\tilde{B} = \tilde{D} + \tilde{S}$ and $\tilde{D}$ reflects the community structure found by the algorithm. As explained above, the matrix $\tilde{S}$ should be as sparse as possible. We measure this sparsity by the counting the number of non-zero entries of $\tilde{S}$. In particular, as we have created the graph from matrices S and D, we calculate

$$\mathfrak{r} := \sum_{k,l=1}^{M} |\tilde{s}_{kl}| - \sum_{k,l=1}^{M} |s_{kl}| \,,$$

which measures how much worse the output of the community detection algorithm is in comparison with the community structure from which the matrix A has been created. The lower this value the better the community detection algorithm suits our purposes. Apart from testing these algorithms only for $M = 100$ nodes, we also apply them to synthetically created test graph with more nodes, but the same community structure. The results can be seen in Figure C.2.

As one can see, the algorithms RBER_POTS and LOUVAIN perform very well when both $\hat{p}$ and M are varied. Moreover, we also took record of the computation time the algorithms take to find the communities, see Figure C.3.

While the computation time of all algorithms scales quadratically in M, the algorithms RBER_POTS, RB_POTS and SIGNIFICANCE_COMMUNITIES are among the fastest.

Our tests showed that RBER_POTS detects communities in a way such that the matrix S has the fewest non-zero entries. Moreover, this algorithm is one of the fastest ones. Consequently, it is best suitable for our applications. Knowing the theory behind this algorithm, it is no surprise that it performs well, since it
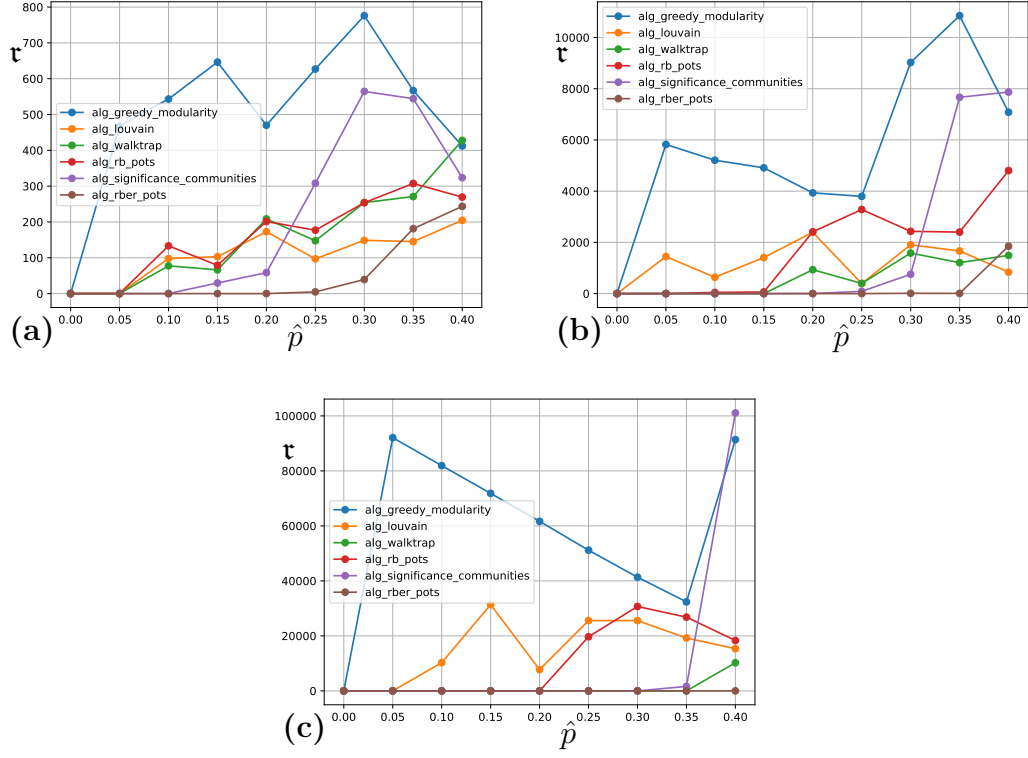
Figure C.2: Quantity $\mathfrak{r}$ for different community detection algorithms and different values of $\hat{p}$. The number of particles is $M = 100$ in part (a), $M = 400$ in part (b) and $M = 1600$ in part (c).
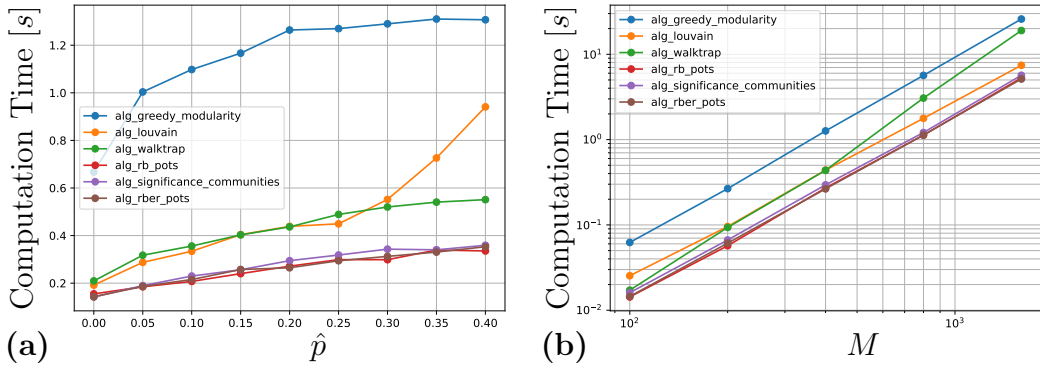

Figure C.3: Computation time of the community detection algorithms. Part (a) shows the dependence on $\hat{p}$ for $M = 400$ and part (b) depicts the dependence on the system size M for $\hat{p} = 0.2$.

is specifically optimized to reward existing intra-population links, punish missing intra-population links, reward missing inter-population links and punish existing inter-population links [148]. This results in a Hamiltonian

$$\mathcal{H}(\{\sigma\}) = -\sum_{k \neq l}(a_{kl} - \gamma p_{kl})\delta(\sigma_k, \sigma_l),$$

that the algorithm tries to minimize [148]. Here, a_{kl} are the entries of the adjacency matrix of the graph and p_{kl} is the probability that a link between node k and l exists. This probability is normalized such that $\sum_{k \neq l} p_{kl} = 2M$. It can be chosen as $p_{kl} = \mathfrak{p}_k \mathfrak{p}_l/(2M)$, where $\mathfrak{p}$ denotes the degree distribution of the network, or one can just take $p_{kl} = |E|/((M-1)M)$, where $|E|$ is the total amount of edges in the network. Further, σ_k is an index of the community to which node k belongs such that $\delta(\sigma_k, \sigma_l) = 1$ if nodes k and l belong to the same community and $\delta(\sigma_k, \sigma_l) = 0$ otherwise. Finally, there is a parameter γ that determines the ratio of how much a missing intra-population link should be punished in comparison with the reward of a non-existing inter-population link. In the standard case $\gamma = 1$, a missing intra-population link or an additional inter-population link negatively effects the Hamiltonian by the same amount as an existing intra-population link or a missing inter-population link positively effects it. Since we need to evaluate the coupling function $g(x_l, x_k)$ for each missing intra-population link and each existing inter-population link exactly once, $\gamma = 1$ is reasonable for our application.

Finally, we want to remark that all tested community detection algorithms do not take into account that the numerical evaluation of the right-hand side of (6.3.6) takes some time, too. Since this evaluation time scales with the number of communities it is sometimes better to have fewer but larger communities, especially if the order p of the expansion is high. The optimal community structure thus depends on the specific network model including its parameters such as the order p of the expansion and the dimension of the model.

C.1.2 General Network Model - Fourier Expansion

Having established a community structure, here, we focus on just one community. For the sake of a clear notation, we take $(a_{kl})_{k,l=1,\dots,M} = (1)_{k,l=1,\dots,M}$, i.e., we consider the network model

$$\dot{x}_k = \frac{1}{M}\sum_{l=1}^{M} g(x_l, x_k), \quad k = 1, \dots, M. \tag{C.1.2}$$

A naive computation of the right-hand side of (C.1.2) for all $k = 1, \dots, M$ requires M^2 evaluations of g and thus the required time scales quadratically with M.

Our aim is to reduce that to linear complexity. For simplicity we first assume that the coupling function g takes two inputs x_l and x_k from a one-dimensional space, e.g., the real line $\mathbb{R}$ or the circle $\mathbb{T}$ and maps into $\mathbb{R}$.

Complex Fourier Series   A general Fourier expansion of g is then of the form

$$g(x,y) = \sum_{\alpha \in \mathbb{Z}} \sum_{\beta \in \mathbb{Z}} c_{\alpha,\beta} e^{\frac{\pi i}{L} \alpha x} e^{\frac{\pi i}{L} \beta y} \tag{C.1.3}$$

$$\approx \sum_{\alpha=-p}^{p} \sum_{\beta=-p}^{p} c_{\alpha,\beta} e^{\frac{\pi i}{L} \alpha x} e^{\frac{\pi i}{L} \beta y}, \tag{C.1.4}$$

where $c_{\alpha,\beta}$ are the Fourier coefficients of g, $L > 0$ sets the size of the area $[-L, L] \times [-L, L]$ on which the Fourier expansion is valid and $p \in \mathbb{N}$ is an indicator for the approximation order. Inserting this representation into (C.1.2), we get

$$\dot{x}_k = \frac{1}{M} \sum_{l=1}^{M} g(x_l, x_k)$$

$$\approx \frac{1}{M} \sum_{l=1}^{M} \sum_{\alpha=-p}^{p} \sum_{\beta=-p}^{p} c_{\alpha,\beta} e^{\frac{\pi i}{L} \alpha x_l} e^{\frac{\pi i}{L} \beta x_k}$$

$$= \sum_{\alpha=-p}^{p} \sum_{\beta=-p}^{p} c_{\alpha,\beta} e^{\frac{\pi i}{L} \beta x_k} \underbrace{\left(\frac{1}{M} \sum_{l=1}^{M} e^{\frac{\pi i}{L} \alpha x_l} \right)}_{=: r_\alpha}.$$

Therefore, if one precomputes certain well-chosen observables, namely the so-called generalized order parameters

$$r_\alpha = \frac{1}{M} \sum_{l=1}^{M} e^{\frac{\pi i}{L} \alpha x_l}, \tag{C.1.5}$$

for all $\alpha = -p, \ldots, p$, the computation of the right-hand side reduces to

$$\dot{x}_k \approx \sum_{\alpha=-p}^{p} \sum_{\beta=-p}^{p} c_{\alpha,\beta} \, r_\alpha \, e^{\frac{\pi i}{L} \beta x_k}. \tag{C.1.6}$$

Now, note that the precomputation complexity of the generalized order parameters (C.1.5) scales linearly in M and so does the computation of (C.1.6), since it has to be computed for all $k = 1, \ldots, M$. The total complexity thus has come down to $\mathcal{O}(M)$. The constant in front of the M can be further improved by noting

that $c_{\alpha,\beta} = \overline{c_{-\alpha,-\beta}}$ in (C.1.4), where $\bar{c}$ denotes the complex conjugate of c. This has to hold to guarantee that g is a real function. Similarly, $r_\alpha = \overline{r_{-\alpha}}$ in (C.1.5). Using these relations, the computation time can be further reduced by a constant factor, even if it still scales linearly with M. However, since these improvements would make the notation more elaborate and thus worsen the readability, we do not mention them further below.

There still remains the question about how to choose L and p in the Fourier approximation. Unfortunately, there is no general answer to this question, but in specific cases the range of x is restricted to a region $[-L, L]$ anyway, so then L can be chosen such that the Fourier approximation is valid on the whole domain, see for example Section C.1.4 and C.1.7. Furthermore, in some cases, the coupling function is already a finite Fourier series, so (C.1.4) is exact for small $p \in \mathbb{N}$ from which a choice of p can be made. In general, L should be chosen large enough such that $x_k(t) \in [-L, L]$ for all k and all t in the simulation time range. This can either numerically be tested or ensured by theoretical results that guarantee the boundedness of $x_k(t)$.

To summarize, the important steps are as follows:

(P1) Before starting the simulation, determine Fourier-coefficients $c_{\alpha,\beta}$, such that the coupling function g can be represented as or well approximated by a finite series

$$g(x,y) \approx \sum_{\alpha=-p}^{p} \sum_{\beta=-p}^{p} c_{\alpha,\beta} e^{\frac{\pi i}{L}\alpha x} e^{\frac{\pi i}{L}\beta y}.$$

(E1) In each time step, precompute generalized order parameters

$$r_\alpha = \frac{1}{M} \sum_{l=1}^{M} e^{\frac{\pi i}{L}\alpha x_l},$$

for $\alpha = -p, \dots, p$ and calculate the right-hand side of (C.1.2) based on the formula

$$\dot{x}_k \approx \sum_{\alpha=-p}^{p} \sum_{\beta=-p}^{p} c_{\alpha,\beta} \, r_\alpha \, e^{\frac{\pi i}{L}\beta x_k}.$$

Real Fourier Series Alternatively from the approach using complex approximations, we can also start with an approximation involving sin and cos. Then, we first have to determine Fourier coefficients $c_{\alpha,\beta}^{11}, c_{\alpha,\beta}^{12}, c_{\alpha,\beta}^{21}, c_{\alpha,\beta}^{22}$ such that

$$g(x, y) \approx \sum_{\alpha=0}^{p} \sum_{\beta=0}^{p} \left(c_{\alpha,\beta}^{11} \cos\left(\frac{\pi}{L}\alpha x\right) \cos\left(\frac{\pi}{L}\beta y\right) + c_{\alpha,\beta}^{12} \cos\left(\frac{\pi}{L}\alpha x\right) \sin\left(\frac{\pi}{L}\beta y\right) \right.$$

$$\text{(C.1.7a)}$$

$$\left. + c_{\alpha,\beta}^{21} \sin\left(\frac{\pi}{L}\alpha x\right) \cos\left(\frac{\pi}{L}\beta y\right) + c_{\alpha,\beta}^{22} \sin\left(\frac{\pi}{L}\alpha x\right) \sin\left(\frac{\pi}{L}\beta y\right) \right).$$

$$\text{(C.1.7b)}$$

Using this representation, the right-hand side of (C.1.2) reads as

$$\dot{x}_k = \frac{1}{M} \sum_{l=1}^{M} g(x_l, x_k)$$

$$\approx \frac{1}{M} \sum_{l=1}^{M} \sum_{\alpha=0}^{p} \sum_{\beta=0}^{p} \left[c_{\alpha,\beta}^{11} \cos\left(\frac{\pi}{L}\alpha x_l\right) \cos\left(\frac{\pi}{L}\beta x_k\right) \right.$$

$$+ c_{\alpha,\beta}^{12} \cos\left(\frac{\pi}{L}\alpha x_l\right) \sin\left(\frac{\pi}{L}\beta x_k\right)$$

$$+ c_{\alpha,\beta}^{21} \sin\left(\frac{\pi}{L}\alpha x_l\right) \cos\left(\frac{\pi}{L}\beta x_k\right)$$

$$\left. + c_{\alpha,\beta}^{22} \sin\left(\frac{\pi}{L}\alpha x_l\right) \sin\left(\frac{\pi}{L}\beta x_k\right) \right]$$

$$= \sum_{\alpha=0}^{p} \sum_{\beta=0}^{p} \left[c_{\alpha,\beta}^{11} \left(\frac{1}{M} \sum_{l=1}^{M} \cos\left(\frac{\pi}{L}\alpha x_l\right)\right) \cos\left(\frac{\pi}{L}\beta x_k\right) \right.$$

$$+ c_{\alpha,\beta}^{12} \left(\frac{1}{M} \sum_{l=1}^{M} \cos\left(\frac{\pi}{L}\alpha x_l\right)\right) \sin\left(\frac{\pi}{L}\beta x_k\right)$$

$$+ c_{\alpha,\beta}^{21} \left(\frac{1}{M} \sum_{l=1}^{M} \sin\left(\frac{\pi}{L}\alpha x_l\right)\right) \cos\left(\frac{\pi}{L}\beta x_k\right)$$

$$\left. + c_{\alpha,\beta}^{22} \left(\frac{1}{M} \sum_{l=1}^{M} \sin\left(\frac{\pi}{L}\alpha x_l\right)\right) \sin\left(\frac{\pi}{L}\beta x_k\right) \right].$$

Therefore, in each time step, we need to precompute

$$r_\alpha^{\cos} := \frac{1}{M} \sum_{l=1}^{M} \cos\left(\frac{\pi}{L}\alpha x_l\right) \quad \text{and} \quad r_\alpha^{\sin} := \frac{1}{M} \sum_{l=1}^{M} \sin\left(\frac{\pi}{L}\alpha x_l\right) \qquad \text{(C.1.8)}$$

for all $\alpha = 0, \ldots, p$. Having done that, the right-hand side of (C.1.2) can be rewritten as

$$\dot{x}_k \approx \sum_{\alpha=0}^{p} \sum_{\beta=0}^{p} \left[c_{\alpha,\beta}^{11} r_{\alpha}^{\cos} \cos\left(\frac{\pi}{L} \beta x_k\right) + c_{\alpha,\beta}^{12} r_{\alpha}^{\cos} \sin\left(\frac{\pi}{L} \beta x_k\right) \right.$$
$$\left. + c_{\alpha,\beta}^{21} r_{\alpha}^{\sin} \cos\left(\frac{\pi}{L} \beta x_k\right) + c_{\alpha,\beta}^{22} r_{\alpha}^{\sin} \sin\left(\frac{\pi}{L} \beta x_k\right) \right].$$

To summarize, the important steps when using a real expansion are

(P1) Before starting the simulation, determine Fourier-coefficients $c_{\alpha,\beta}^{11}, c_{\alpha,\beta}^{12}, c_{\alpha,\beta}^{21}, c_{\alpha,\beta}^{22}$, such that the coupling function g can be represented as or well approximated by a finite series

$$g(x,y) \approx \sum_{\alpha=0}^{p} \sum_{\beta=0}^{p} \left(c_{\alpha,\beta}^{11} \cos\left(\frac{\pi}{L} \alpha x\right) \cos\left(\frac{\pi}{L} \beta y\right) \right.$$
$$+ c_{\alpha,\beta}^{12} \cos\left(\frac{\pi}{L} \alpha x\right) \sin\left(\frac{\pi}{L} \beta y\right)$$
$$+ c_{\alpha,\beta}^{21} \sin\left(\frac{\pi}{L} \alpha x\right) \cos\left(\frac{\pi}{L} \beta y\right)$$
$$\left. + c_{\alpha,\beta}^{22} \sin\left(\frac{\pi}{L} \alpha x\right) \sin\left(\frac{\pi}{L} \beta y\right) \right).$$

(E1) In each time step, precompute

$$r_{\alpha}^{\cos} := \frac{1}{M} \sum_{l=1}^{M} \cos\left(\frac{\pi}{L} \alpha x_l\right) \quad \text{and} \quad r_{\alpha}^{\sin} := \frac{1}{M} \sum_{l=1}^{M} \sin\left(\frac{\pi}{L} \alpha x_l\right)$$

for $\alpha, \beta = 0, \ldots, p$ and calculate the right-hand side of (C.1.2) based on the formula

$$\dot{x}_k \approx \sum_{\alpha=0}^{p} \sum_{\beta=0}^{p} \left[c_{\alpha,\beta}^{11} r_{\alpha}^{\cos} \cos\left(\frac{\pi}{L} \beta x_k\right) + c_{\alpha,\beta}^{12} r_{\alpha}^{\cos} \sin\left(\frac{\pi}{L} \beta x_k\right) \right.$$
$$\left. + c_{\alpha,\beta}^{21} r_{\alpha}^{\sin} \cos\left(\frac{\pi}{L} \beta x_k\right) + c_{\alpha,\beta}^{22} r_{\alpha}^{\sin} \sin\left(\frac{\pi}{L} \beta x_k\right) \right].$$

Difference based coupling function - Complex Fourier Series   Even though we have already reduced the complexity from being quadratic in M to being only linear in M, the constant scales with p^2. In many network models the coupling

function g is of the special form $g(x, y) = h(x - y)$, such that we are facing the system

$$\dot{x}_k = \frac{1}{M} \sum_{l=1}^{M} h(x_l - x_k), \quad k = 1, \dots, M. \tag{C.1.9}$$

This helps to reduce the dependence on p^2 to just p. Again, we assume that the coupling function h has an Fourier approximation

$$h(x) = \sum_{\alpha \in \mathbb{Z}} d_\alpha e^{\frac{\pi i}{L} \alpha x} \approx \sum_{\alpha=-p}^{p} d_\alpha e^{\frac{\pi i}{L} \alpha x}, \tag{C.1.10}$$

where d_α are the Fourier coefficients, $L > 0$ indicates the size of the domain $[-L, L]$ in which the approximation is valid and p gives the approximation order. Then, the right-hand side of (C.1.2) can be written as

$$\dot{x}_k = \frac{1}{M} \sum_{l=1}^{M} h(x_l - x_k)$$

$$\approx \frac{1}{M} \sum_{l=1}^{M} \sum_{\alpha=-p}^{p} d_\alpha e^{\frac{\pi i}{L} \alpha (x_l - x_k)}$$

$$= \sum_{\alpha=-p}^{p} d_\alpha \left(\frac{1}{M} \sum_{l=1}^{M} e^{\frac{\pi i}{L} \alpha x_l} \right) e^{-\frac{\pi i}{L} \alpha x_k} \tag{C.1.11}$$

$$= \sum_{\alpha=-p}^{p} d_\alpha r_\alpha e^{-\frac{\pi i}{L} \alpha x_k}, \tag{C.1.12}$$

where r_α are the generalized order parameters (C.1.5). While the general formula (C.1.6) involves two sums with indices running from $-p$ to p, the formula (C.1.12), which relies on the assumption of a difference based coupling, involves only one such sum.

Difference based coupling function - Real Fourier Series   Again, instead of expanding h in a complex Fourier series, one can also use a real Fourier series

$$h(x) = d_0^{\cos} + \sum_{\alpha=1}^{\infty} \left(d_\alpha^{\sin} \sin \left(\frac{\pi}{L} \alpha x \right) + d_\alpha^{\cos} \cos \left(\frac{\pi}{L} \alpha x \right) \right)$$

$$\approx d_0^{\cos} + \sum_{\alpha=1}^{p} \left(d_\alpha^{\sin} \sin \left(\frac{\pi}{L} \alpha x \right) + d_\alpha^{\cos} \cos \left(\frac{\pi}{L} \alpha x \right) \right) \tag{C.1.13}$$

Having precomputed the quantities $r_\alpha^{\sin}$ and $r_\alpha^{\cos}$ from (C.1.8), the right-hand side of (C.1.9) is given by

$$
\begin{aligned}
\dot{x}_k &= \frac{1}{M} \sum_{l=1}^{M} h(x_l - x_k) \\
&\approx \frac{1}{M} \sum_{l=1}^{M} \left[d_0^{\cos} + \sum_{\alpha=1}^{p} \left(d_\alpha^{\sin} \sin\left(\frac{\pi}{L}\alpha(x_l - x_k)\right) + d_\alpha^{\cos} \cos\left(\frac{\pi}{L}\alpha(x_l - x_k)\right) \right) \right] \\
&= d_0^{\cos} + \frac{1}{M} \sum_{l=1}^{M} \sum_{\alpha=1}^{p} \left[d_\alpha^{\sin} \sin\left(\frac{\pi}{L}\alpha x_l\right) \cos\left(\frac{\pi}{L}\alpha x_k\right) \right. \\
&\qquad\qquad - d_\alpha^{\sin} \cos\left(\frac{\pi}{L}\alpha x_l\right) \sin\left(\frac{\pi}{L}\alpha x_k\right) \\
&\qquad\qquad + d_\alpha^{\cos} \sin\left(\frac{\pi}{L}\alpha x_l\right) \sin\left(\frac{\pi}{L}\alpha x_k\right) \\
&\qquad\qquad \left. + d_\alpha^{\cos} \cos\left(\frac{\pi}{L}\alpha x_l\right) \cos\left(\frac{\pi}{L}\alpha x_k\right) \right] \\
&= d_0^{\cos} + \sum_{\alpha=1}^{p} \left[d_\alpha^{\sin} r_\alpha^{\sin} \cos\left(\frac{\pi}{L}\alpha x_k\right) - d_\alpha^{\sin} r_\alpha^{\cos} \sin\left(\frac{\pi}{L}\alpha x_k\right) \right. \\
&\qquad\qquad \left. + d_\alpha^{\cos} r_\alpha^{\sin} \sin\left(\frac{\pi}{L}\alpha x_k\right) + d_\alpha^{\cos} r_\alpha^{\cos} \cos\left(\frac{\pi}{L}\alpha x_k\right) \right].
\end{aligned}
$$

This last equation represents a the formula that one should use to compute the right-hand side of (C.1.9) when preferring real Fourier approximations.

Extensions In the above calculations we assumed that g or h take inputs form a one-dimensional space and map into a one-dimensional space. However, we want to remark that this approach also works if the inputs x_l and x_k are higher-dimensional objects, for example, when $g \colon \mathbb{R}^d \times \mathbb{R}^d \to \mathbb{R}^d$. In this case, α and β have to be thought of being multi-indices rather than integers. Quantities of the form $e^{\frac{\pi i}{L}\alpha x}$ have to be replaced with $e^{\frac{\pi i}{L}\langle \alpha, x \rangle}$, where $\langle \cdot, \cdot \rangle$ is a scalar product. Further, sums over $\alpha, \beta = -p, \ldots, p$ are then sums over $\alpha, \beta \in \mathbb{Z}(p)^d := \{-p, \ldots, p\}^d$. Moreover, the order parameter (C.1.5) or its real equivalents need to be precomputed for all $\alpha \in \mathbb{Z}(p)^d$.

C.1.3   General Network Model - Polynomial Expansion

Again, we consider the general network model

$$\dot{x}_k = \frac{1}{M} \sum_{l=1}^{M} g(x_l, x_k), \quad k = 1, \ldots, M. \tag{C.1.14}$$

Again, our goal is to reduce the computational complexity from M^2 to just M. We assume for simplicity that g takes two inputs from a one-dimensional space such as $\mathbb{R}$ or $\mathbb{T}$ and maps to $\mathbb{R}$. However, it should be said that our approach works as well when the inputs of g are from a higher-dimensional space.

Polynomial Approximation   However, instead of approximating the coupling function by a Fourier series, this time we approximate it by polynomials

$$g(x, y) = \sum_{\alpha=0}^{\infty} \sum_{\beta=0}^{\infty} c_{\alpha,\beta} x^\alpha y^\beta \approx \sum_{\alpha=0}^{p} \sum_{\beta=0}^{p} c_{\alpha,\beta} x^\alpha y^\beta. \tag{C.1.15}$$

Here, $c_{\alpha,\beta}$ are the coefficients of the approximation and $p \in \mathbb{N}$ indicates the approximation order. This approximation does not necessarily need to be a Taylor approximation. Rather, it is often more useful to consider a polynomial approximation of g with respect to a L^2 or a supremum norm on a domain $[-L, L] \times [-L, L]$. For numerical reasons it sometimes make sense to replace x and y in (C.1.15) by $(x - x_0)$ and $(y - y_0)$, respectively. Combining this approximation with (C.1.14), we obtain

$$\dot{x}_k = \frac{1}{M} \sum_{l=1}^{M} g(x_l, x_k)$$

$$\approx \frac{1}{M} \sum_{l=1}^{M} \sum_{\alpha=0}^{p} \sum_{\beta=0}^{p} c_{\alpha,\beta} x_l^\alpha x_k^\beta$$

$$= \sum_{\alpha=0}^{p} \sum_{\beta=0}^{p} c_{\alpha,\beta} \underbrace{\left(\frac{1}{M} \sum_{l=1}^{M} x_l^\alpha \right)}_{=:w_\alpha} x_k^\beta.$$

Therefore, if one precomputes the α-th moments

$$w_\alpha := \frac{1}{M} \sum_{l=1}^{M} x_l^\alpha \tag{C.1.16}$$

for $\alpha = 0, \ldots, p$, the computation of the right-hand side reduces to

$$\dot{x}_k \approx \sum_{\alpha=0}^{p} \sum_{\beta=0}^{p} c_{\alpha,\beta} w_\alpha x_k^\beta. \tag{C.1.17}$$

To summarize, the important steps are as follows:

(P1) Before starting the simulation, determine coefficients $c_{\alpha,\beta}$, such that the coupling function g can be represented as or well approximated by a finite series

$$g(x, y) \approx \sum_{\alpha=0}^{p} \sum_{\beta=0}^{p} c_{\alpha,\beta} x^\alpha y^\beta.$$

(E1) In each time step, precompute the moments

$$w_\alpha := \frac{1}{M} \sum_{l=1}^{M} x_l^\alpha$$

for $\alpha = 0, \ldots, p$ and calculate the right-hand side of (C.1.14) based on the formula

$$\dot{x}_k \approx \sum_{\alpha=0}^{p} \sum_{\beta=0}^{p} c_{\alpha,\beta} w_\alpha x_k^\beta.$$

As one can see, the complexity of an evaluation of the right-hand side (C.1.17) is only linear in M, since it has to be evaluated for each $k = 1, \ldots, M$. The dependence of this complexity on p^2 can be reduced in special cases, for example if the coupling function g depends only on differences.

Difference based coupling function - Polynomial Approximation Even though we have already reduces the complexity from being quadratic in M to being only linear in M, the constant scales with p^2. In many network models the coupling function g is of the special form $g(x, y) = h(x - y)$, such that we are facing the system

$$\dot{x}_k = \frac{1}{M} \sum_{l=1}^{M} h(x_l - x_k), \quad k = 1, \ldots, M. \tag{C.1.18}$$

Such a representation is helpful when one wants to further reduce the computational complexity. Now, we assume that the coupling function h can be well approximated by a polynomial

$$h(x) = \sum_{\alpha=0}^{\infty} c_\alpha x^\alpha \approx \sum_{\alpha=0}^{p} c_\alpha x^\alpha.$$

Again, for numerical reasons it is sometimes better to replace x in the above formula with $(x - x_0)$. However, for the sake of simplicity we do not incorporate this technical detail. Given this polynomial approximation and the α-th moments (C.1.16), we can rewrite the right-hand side of (C.1.18) to

$$
\begin{aligned}
\dot{x}_k &= \frac{1}{M} \sum_{l=1}^{M} h(x_l - x_k) \\
&\approx \frac{1}{M} \sum_{l=1}^{M} \sum_{\alpha=0}^{p} c_\alpha (x_l - x_k)^\alpha \\
&= \sum_{\alpha=0}^{p} c_\alpha \frac{1}{M} \sum_{l=1}^{M} \sum_{j=0}^{\alpha} \binom{\alpha}{j} x_l^j \, (-x_k)^{\alpha-j} \\
&= \sum_{\alpha=0}^{p} c_\alpha \sum_{j=0}^{\alpha} \binom{\alpha}{j} \left(\frac{1}{M} \sum_{l=1}^{M} x_l^j \right) (-x_k)^{\alpha-j} \\
&= \sum_{\alpha=0}^{p} c_\alpha \sum_{j=0}^{\alpha} \binom{\alpha}{j} w_j \, (-x_k)^{\alpha-j}.
\end{aligned}
\tag{C.1.19}
$$

This representation further reduces the computational complexity.

C.1.4   Kuramoto Model

The classical Kuramoto model [107] is given by

$$
\dot{\theta}_k = \omega_k + \frac{1}{M} \sum_{l=1}^{M} \sin(\theta_l(t) - \theta_k(t)), \quad k = 1, \dots, M,
$$

where $\theta_k \colon [0, T] \to \mathbb{T} = \mathbb{R}/(2\pi\mathbb{Z})$ is the phase and ω_k the intrinsic frequency of oscillator k. The coupling function g is hence given by $g(x, y) = h(x - y) = \sin(x - y)$.

Classical Kuramoto model   Following the difference based approach from Section C.1.2, we choose $L = \pi$, $p = 1$ and write h as

$$
h(x) = \sin(x) = \frac{-1}{2\mathrm{i}} e^{-\mathrm{i}x} + \frac{1}{2\mathrm{i}} e^{\mathrm{i}x},
$$

so $d_{-1} = -1/(2\mathrm{i}), d_0 = 0$ and $d_1 = 1/(2\mathrm{i})$ in (C.1.10) and this approximation is exact. After calculating the order parameters

$$
r_{-1} = \frac{1}{M} \sum_{l=1}^{M} e^{-\mathrm{i}\theta_l},
$$

$$r_0 = 1,$$

$$r_1 = \frac{1}{M} \sum_{l=1}^{M} e^{i\theta_l}, \tag{C.1.20}$$

the equation to evaluate the right-hand side (C.1.12) turns into

$$\dot{\theta}_k = \omega_k + \frac{-1}{2i} r_{-1} e^{i\theta_k} + \frac{1}{2i} r_1 e^{-i\theta_k}. \tag{C.1.21}$$

However, since $d_{-1} = \overline{d_1}$ and $r_{-1} = \overline{r_1}$ we can further simplify:

$$\dot{\theta}_k = \omega_k - \mathrm{Re}\left(i r_1 e^{-i\theta_k}\right) \tag{C.1.22}$$

$$= \omega_k + \mathrm{Im}(r_1 e^{-i\theta_k}). \tag{C.1.23}$$

One can also write $r_1 = |r_1| e^{i\psi}$ for some $\psi \in \mathbb{T}$. Then,

$$\dot{\theta}_k = \omega_k + \mathrm{Im}(r_1 e^{-i\theta_k})$$

$$= \omega_k + |r_1| \mathrm{Im}(e^{i(\psi - \theta_k)}) \tag{C.1.24}$$

$$= \omega_k + |r_1| \sin(\psi - \theta_k). \tag{C.1.25}$$

Alternatively, one can also prefer to work with real numbers only. Then, one has to precompute

$$r_1^{\cos} = \frac{1}{M} \sum_{l=1}^{M} \cos(\theta_l), \quad \text{and} \quad r_1^{\sin} = \frac{1}{M} \sum_{l=1}^{M} \sin(\theta_l). \tag{C.1.26}$$

According to the derivation in Section C.1.2, for the right-hand side we obtain

$$\dot{\theta}_k = \omega_k + r_1^{\sin} \cos(x_k) - r_1^{\cos} \sin(x_k). \tag{C.1.27}$$

To summarize, the important steps are given by

(P1) In this step nothing has to be done, since the coupling function is already a finite Fourier series.

(E1) In each simulation step, first calculate the complex order parameter (C.1.20) and then evaluate the right-hand side by using either of the formulas (C.1.21), (C.1.22), (C.1.23), (C.1.24), (C.1.25). Alternatively, calculate the real order-parameters (C.1.26) and then evaluate the right-hand side using the formula (C.1.27).

Higher-Harmonics Kuramoto Model   An easy generalization of the classical Kuramoto model additionally includes higher harmonics in the coupling function. The network model is then given by

$$\dot{\theta}_k = \omega_k + \frac{1}{M} \sum_{l=1}^{M} h(\theta_l - \theta_k),$$

with a coupling function $h\colon \mathbb{T} \to \mathbb{R}$ defined by

$$h(x) = \sum_{\alpha=1}^{p} (d_\alpha^{\sin} \sin(\alpha x) + d_\alpha^{\cos} \cos(\alpha x)).$$

Obviously, this is already of the form (C.1.13) for $L = \pi$, so we can directly follow this section. Having precomputed the quantities $r_\alpha^{\cos}$ and $r_\alpha^{\sin}$ from (C.1.8) for all $\alpha = 0, \ldots, p$, the right-hand side for the higher-harmonics Kuramoto model can be written as

$$\dot{\theta}_k = \omega_k + d_0^{\cos} + \sum_{\alpha=1}^{p} \Big[d_\alpha^{\sin} r_\alpha^{\sin} \cos(\alpha x_k) - d_\alpha^{\sin} r_\alpha^{\cos} \sin(\alpha x_k)$$
$$+ d_\alpha^{\cos} r_\alpha^{\sin} \sin(\alpha x_k) + d_\alpha^{\cos} r_\alpha^{\cos} \cos(\alpha x_k) \Big].$$

C.1.5   Desai–Zwanzig Model

The Desai–Zwanzig model [61] is given by the following set of equations:

$$\dot{x}_k = -\nabla V(x_k) + \frac{1}{M} \sum_{l=1}^{M} (x_l - x_k), \tag{C.1.28}$$

where $V\colon \mathbb{R} \to \mathbb{R}$ is a potential and $\nabla V = \frac{\mathrm{d}}{\mathrm{d}x} V(x)$. Following the difference based procedures in Section C.1.3, the coupling function h is given by just $h(x) = x$. Therefore, to match the notation in this section, $p = 1, c_0 = 0$ and $c_1 = 1$. After having computed the first moment w_1 from (C.1.16) and by using (C.1.19), we can write the right-hand side as

$$\dot{x}_k = -\nabla V(x_k) + (-x_k + w_1).$$

Even though this is an easy application of the theory from Section C.1.3 and could have easily derived from (C.1.28) without the general theory from this section, it helps to reduce the computational cost significantly and thereby lowers the complexity from $\mathcal{O}(M^2)$ to just $\mathcal{O}(M)$.

C.1.6 Cucker–Smale Model

The continuous Cucker–Smale model [57] is given by the dynamical system

$$\dot{s}_k = v_k \tag{C.1.29a}$$

$$\dot{v}_k = \frac{1}{M} \sum_{l=1}^{M} \frac{K}{(\sigma^2 + \|s_l - s_k\|^2)^\beta} \, (v_l - v_k), \tag{C.1.29b}$$

for $k = 1, \ldots, M$, where $s_k(t)$ represents the current position of the k-th bird, $v_k(t)$ is its velocity and K, σ and β are coupling constants. Here, $s_k(t), v_k(t) \in \mathbb{R}^d$, where typically $d = 1, 2, 3$. Putting this into the form (C.1.1) with $x = (s, v)^\top$, $f_k(x) := (v, 0)^\top$ would be functions mapping from $\mathbb{R}^{2d}$ to $\mathbb{R}^{2d}$ and similarly, $g \colon \mathbb{R}^{2d} \times \mathbb{R}^{2d} \to \mathbb{R}^{2d}$, with $g(\hat{x}, \tilde{x}) = (g_s(\hat{x}, \tilde{x}), g_v(\hat{x}, \tilde{x}))^\top$. Here, the first d components of g are given by $g_s(\hat{x}, \tilde{x}) = 0$ and the last d components of g are given by

$$g_v(\hat{x}, \tilde{x}) = \eta(\|\hat{s} - \tilde{s}\|^2) \, (\hat{v} - \tilde{v}), \quad \text{with } \eta(y) = \frac{K}{(\sigma^2 + y)^\beta}.$$

If we directly applied the algorithm described in previous section C.1.2 or C.1.3, the high dimension of the Cucker–Smale model would impact the performance of these algorithms, since they do not account for the special structure of the model. However, by exploiting this special structure, a more efficient algorithm can be constructed. In particular, a more efficient algorithm has to take into account that $g_s = 0$, so there is no need to expand this part either in a Fourier or a polynomial series. Furthermore, $g(\hat{x}, \tilde{x})$ only depends on the difference $\hat{x} - \tilde{x}$, which should be exploited. Moreover, $g_v(\hat{x}, \tilde{x})$ depends on $\hat{v} - \tilde{v}$ only linearly, so a polynomial expansion up to a degree higher than 1 is unnecessary. Last but not least, the fraction in the sum of (C.1.29b) is independent of the coordinate direction, which makes it superfluous to expand this fraction for each coordinate direction.

Let us start developing a fast algorithm by denoting $\tilde{\eta}(y) \colon \mathbb{R}^d \to \mathbb{R}$, with $\tilde{\eta}(y) := \eta(\|y\|^2)$ and expanding this in a Fourier series

$$\tilde{\eta}(y) = \sum_{\alpha \in \mathbb{Z}^d} \tilde{c}_\alpha e^{\frac{i\pi}{L}\langle \alpha, y\rangle} \approx \sum_{\alpha \in \mathbb{Z}(p)^d} \tilde{c}_\alpha e^{\frac{i\pi}{L}\langle \alpha, y\rangle}, \tag{C.1.30}$$

where $\alpha \in \mathbb{Z}(p)^d \subset \mathbb{Z}^d$ is a multi-index, $\mathbb{Z}(p) = \{-p, \ldots, p\}$, $\tilde{c}_\alpha$ are the Fourier coefficients of $\tilde{\eta}$, $L > 0$ is a parameter that denotes the region $[-L, L]^d$ on which the expansion is valid and $\langle \alpha, x\rangle = \sum_{l=1}^{d} \alpha_l x_l$ denotes the standard scalar product. In this new notation the second component of the right-hand side of (C.1.29b) reads as

$$\dot{v}_k = \frac{1}{M} \sum_{l=1}^{M} \tilde{\eta}(s_l(t) - s_k(t)) \, (v_l(t) - v_k(t)).$$

Inserting the approximation (C.1.30) into this formula yields

$$
\dot{v}_k \approx \frac{1}{M} \sum_{l=1}^{M} \sum_{\alpha \in \mathbb{Z}(p)^d} \tilde{c}_\alpha e^{\frac{i\pi}{L} \langle \alpha, s_l(t) - s_k(t) \rangle} (v_l(t) - v_k(t))
$$

$$
= \sum_{\alpha \in \mathbb{Z}(p)^d} \tilde{c}_\alpha e^{\frac{i\pi}{L} \langle \alpha, -s_k(t) \rangle} \left(\frac{1}{M} \sum_{l=1}^{M} e^{\frac{i\pi}{L} \langle \alpha, s_l(t) \rangle} v_l(t) - \frac{1}{M} \sum_{l=1}^{M} e^{\frac{i\pi}{L} \langle \alpha, s_l(t) \rangle} v_k(t) \right).
$$

Therefore, if one precomputes

$$
u_\alpha = \frac{1}{M} \sum_{l=1}^{M} e^{\frac{i\pi}{L} \langle \alpha, s_l \rangle} \in \mathbb{R}, \tag{C.1.31a}
$$

$$
h_\alpha = \frac{1}{M} \sum_{l=1}^{M} e^{\frac{i\pi}{L} \langle \alpha, s_l \rangle} v_l \in \mathbb{R}^d \tag{C.1.31b}
$$

for each $\alpha \in \mathbb{Z}(p)^d$, the right-hand side is finally given by

$$
\dot{v}_k \approx \sum_{\alpha \in \mathbb{Z}(p)^d} \tilde{c}_\alpha \, e^{\frac{i\pi}{L} \langle \alpha, -s_k(t) \rangle} (h_\alpha - u_\alpha v_k(t)) . \tag{C.1.32}
$$

To summarize, the important steps are given by

(P1) Before starting the simulation, determine Fourier-coefficients $\tilde{c}_\alpha$, such that the function $\tilde{\eta}$ is well approximated by a finite series of the form (C.1.30).

(E1) In each time step, precompute the quantities (C.1.31) for all $\alpha \in \mathbb{Z}(p)^d$ and calculate the right-hand side of (C.1.29b) by using the formula (C.1.32).

C.1.7   Higher-order Kuramoto Models

Higher-order Kuramoto models are generalizations from the classical Kuramoto model. While in the classical Kuramoto model the particle interactions are pairwise, in higher-order Kuramoto models, interactions of triplets, quadruplets, etc. determine the dynamics. We are going to show below that the CIA approach naturally generalizes to higher-order coupling, and is even more powerful in this case. The higher-order Kuramoto network model we use as an illustration for this generalization is given by

$$
\dot{\theta}_k = \frac{1}{M^d} \sum_{l \in [M]^d} \sin \left(\sum_{i=1}^{d} \lambda_i \theta_{l_i} + \lambda_{d+1} \theta_k \right) .
$$

Here, M is the number of oscillators, $[M] = \{1, \ldots, M\}$, $d + 1$ is amount of oscillators that interact with each other, $\theta_k(t)$ are the phases of oscillators $k = 1, \ldots, M$ and $\lambda_1, \ldots, \lambda_{d+1} \in \mathbb{Z}$ are integer valued coefficients that typically sum up to 0, see also Section 5.6. In the classical Kuramoto model $d = 1$, $\lambda_1 = 1$, $\lambda_2 = -1$. To make the presentation simple, we restrict ourselves to the model higher-order model

$$\dot{\theta}_k = \frac{1}{M^3} \sum_{l_1,l_2,l_3=1}^{M} \sin\left(\lambda_1\theta_{l_1} + \lambda_2\theta_{l_2} + \lambda_3\theta_{l_3} + \lambda_4\theta_k\right). \tag{C.1.33}$$

The computational complexity to naively evaluate the right-hand side of (C.1.33) is $\mathcal{O}(M^4)$ since there are three sums and they have to be evaluated for each $k = 1, \ldots, M$. The following calculation shows how to reduce this complexity:

$$\begin{aligned}
\dot{\theta}_k &= \frac{1}{M^3} \sum_{l_1,l_2,l_3=1}^{M} \sin\left(\lambda_1\theta_{l_1} + \lambda_2\theta_{l_2} + \lambda_3\theta_{l_3} + \lambda_4\theta_k\right) \\
&= \mathrm{Im}\left(\frac{1}{M^3} \sum_{l_1,l_2,l_3=1}^{M} e^{\mathrm{i}(\lambda_1\theta_{l_1} + \lambda_2\theta_{l_2} + \lambda_3\theta_{l_3} + \lambda_4\theta_k)}\right) \\
&= \mathrm{Im}\left(\frac{1}{M^3} \sum_{l_1,l_2,l_3=1}^{M} e^{\mathrm{i}\lambda_1\theta_{l_1}} \, e^{\mathrm{i}\lambda_2\theta_{l_2}} \, e^{\mathrm{i}\lambda_3\theta_{l_3}} \, e^{\mathrm{i}\lambda_4\theta_k}\right) \\
&= \mathrm{Im}\left(\left(\frac{1}{M}\sum_{j_1=1}^{M} e^{\mathrm{i}\lambda_1\theta_{l_1}}\right)\left(\frac{1}{M}\sum_{j_2=1}^{M} e^{\mathrm{i}\lambda_2\theta_{l_2}}\right)\left(\frac{1}{M}\sum_{j_3=1}^{M} e^{\mathrm{i}\lambda_3\theta_{l_3}}\right) e^{\mathrm{i}\lambda_4\theta_k}\right) \\
&= \mathrm{Im}\left(r_{\lambda_1} \, r_{\lambda_2} \, r_{\lambda_3} \, e^{\mathrm{i}\lambda_4\theta_k}\right). \tag{C.1.34}
\end{aligned}$$

As in (C.1.5) with $L = \pi$, r_α is the α-th order parameter

$$r_\alpha = \frac{1}{M} \sum_{l=1}^{M} e^{\mathrm{i}\alpha\theta_l}.$$

As can easily be seen precomputing the order parameters r_α for $\alpha = \lambda_1, \lambda_2, \lambda_3$ requires a $\mathcal{O}(M)$ function evaluations. Subsequently evaluating the right-hand side according to the formula (C.1.34) takes another $\mathcal{O}(M)$ operations. Thus, in summary the complexity of this algorithm is linear in M, which is a significant reduction from the naive algorithm that scales with M^4. This shows the power of our approach: as long as one can exploit dense coupling structure, even higher-order (or polyadic, or hypergraph) interactions can be reduced from a high polynomial computational complexity in M to linear complexity.

Even though there exist formulas that give a fast evaluation of the right-hand side only by using real numbers, deriving these formulas requires addition theorems on $\sin(\alpha_1 + \alpha_2 + \alpha_3 + \alpha_4)$ and consequently these formulas tend to be very long, which is why we recommend the complex formula (C.1.34).

C.1.8   Bornholdt–Rohlf Model

The Bornholdt–Rohlf model [39] on a static all-to-all network is a discrete-time dynamical system with the iteration rule

$$f_k^n = \sum_{l=1}^{M} v_l^n + \mu v_k^n + \sigma r_k^n, \quad r_k^n \sim \mathcal{N}(0,1),$$

$$v_k^{n+1} = \mathrm{sgn}[f_k^n],$$

where $n \in \mathbb{N}$ is the discrete time, v_k^n is the state of the k-th node at time n, $\sigma \geq 0$ is a parameter for the noise and $\mathcal{N}(0,1)$ denotes the standard normal distribution. Here, one needs to observe that the decisive sum in the definition of f_k is independent of k. Therefore, this sum can be precomputed and then reused for each calculation of f_k^n. In this way one can construct an algorithm whose complexity is linear in M. This example aims to illustrate in a simple setting that the neither the continuous-time assumption, nor the assumption about a particular ordinary differential equation structure matter. What does matter for being able to the CIA approach is that the computational bottleneck in a naive approach arises due to summing at each node over all its inputs.

C.2   Accuracy of CIAs in a Cucker–Smale Model

Having studied the accuracy of CIAs in phase oscillator models in Section 6.5.2, we now analyze an $d = 2$ dimensional Cucker–Smale model, that we have introduced Appendix C.1.6.

We simulate the Cucker–Smale model, both directly with a naive approach and with our CIA. We reuse the network from Section 6.5.2 consisting of four communities with $M = 500$ nodes. As in the Section 6.5.2, we use an explicit Euler scheme on an equidistant time grid $0, \Delta t, 2\Delta t, \ldots, T$ with $\Delta t = 1/10$ and $T = 20$.

Again, we denote the exact reference solution by $s_{k,t}^{\mathrm{ref}}$ and the solution obtained by the CIA described in Appendix C.1.6 by $s_{k,t}^{\mathrm{CIA}}$. Note that this time $s_{k,t} \in \mathbb{R}^2$, which is why we need to take the norm instead of the absolute value in the definition of the error:

$$z = \max_{k=1,\ldots,M} \max_{t=0,\Delta t, 2\Delta t, \ldots, T} \| s_{k,t}^{\mathrm{ref}} - s_{k,t}^{\mathrm{CIA}} \|.$$

We consider two cases. First, the function η is given by the algebraic function

$$\eta(y) = \frac{K}{(\sigma^2 + y)^\beta} \tag{C.2.1}$$

as in Appendix C.1.6 and second, the coupling function η is given by an exponential

$$\eta(y) = e^{-y/4}. \tag{C.2.2}$$

Recall from Appendix C.1.6 that pre-simulation step (P2) approximates the function $\tilde{\eta}(y) := \eta(\|y\|^2)$ on the domain $y \in [-L, L]^2$, where we chose $L = 10$. Moreover, the initial conditions for s are randomly chosen in the square $[-\frac{1}{2}, \frac{1}{2}]^2$, while each component of the initial velocity is normally distributed with mean 0 and standard deviation $1/20$. Figure C.4 shows the integration error z for the coupling functions (C.2.1) and (C.2.2) for different orders of approximation p. As one can see the rate with which the accuracy increases upon varying p is much better for the exponential coupling function. This is because Fourier coefficients of a Gaussian are decaying much faster than the ones of an algebraic function.
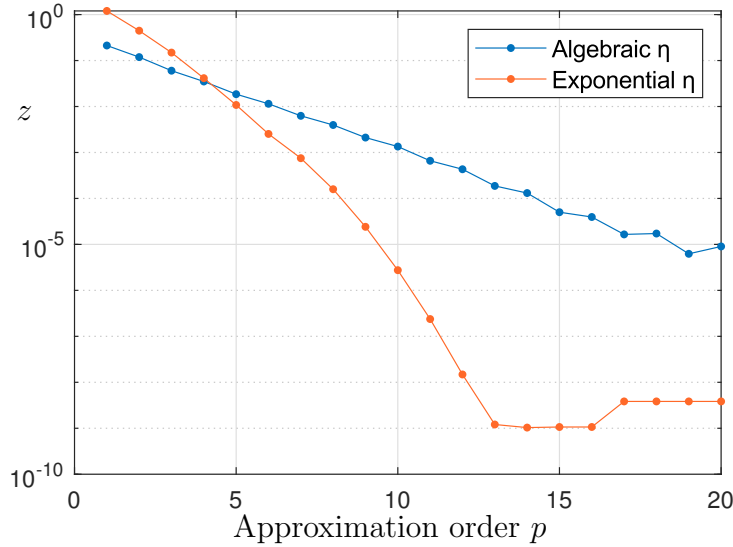

Figure C.4: Integration error z independence of the approximation order p and the coupling function η. The blue curve shows the integration error when choosing the exponential coupling function (C.2.2). The red curve depicts the same error when η is given by the standard algebraic function (C.2.1). The parameters are given by $K = 1$, $\sigma = 1$, $\beta = 0.2$.

Lastly, we point out that the rate of convergence in the Cucker–Smale model seems to be faster than the one for phase oscillator models. We believe that this

is because we simulate the phase oscillator system near an unstable set whereas the Cucker–Smale model exhibits flocking.